

DISSERTATION

THE EFFECTS OF SEDIMENT SUPPLY, WIDTH VARIATIONS, AND UNSTEADY
FLOW ON RIFFLE-POOL DYNAMICS

Submitted by

Jacob A. Morgan

Department of Civil and Environmental Engineering

In partial fulfillment of the requirements

For the Degree of Doctor of Philosophy

Colorado State University

Fort Collins, Colorado

Spring 2018

Doctoral Committee:

Advisor: Peter A. Nelson

Brian P. Bledsoe

Pierre Y. Julien

Ellen Wohl

Copyright by Jacob A. Morgan 2018

All Rights Reserved

ABSTRACT

THE EFFECTS OF SEDIMENT SUPPLY, WIDTH VARIATIONS, AND UNSTEADY FLOW ON RIFFLE-POOL DYNAMICS

Channel geometry, water discharge, and sediment supply work together to influence gravel-bed morphodynamics. How these forcings change and interact affects instream meso-scale geomorphic units, such as riffles and pools, which are often important habitat areas for aquatic organisms. Riffles and pools, defined as vertical undulations in the longitudinal bed profile, are often co-located with variations in channel width and their maintenance in natural systems is often attributed to unsteady flow effects. However, little work has been done to investigate the interaction between unsteady flow and the periodic width variations that often accompany riffle-pool morphology. Surficial sediment sorting, which is largely dependent on sediment supply, is also invoked as an important factor for riffle-pool maintenance. However, there is a lack of studies exploring how riffles and pools respond, or are maintained, in the case of increased sediment supply, such as might be experienced due to dam removal. In general, little is known about how constriction-forced riffles and pools interact with unsteady flow and changes to sediment supply.

This dissertation investigates the interplay between channel geometry, discharge, and sediment supply using numerical methods, laboratory experiments, and field exploration. Chapter 2 presents a one-dimensional morphodynamic model which was used to investigate the controls on sediment pulse evolution in coarse-bed rivers. The model uses the standard step backwater method to compute hydrodynamics, calculates bedload, and simulates elevation changes. A stratigraphy submodel retains data related to vertical grain size sorting in the channel subsurface. The results suggest that sediment pulses move downstream with

a greater degree of translation with smaller pulse sizes, longer pulse feed times, finer pulse grain sizes, and prolonged higher discharges.

In Chapter 3, a two-dimensional morphodynamic model was used to systematically investigate the influence of width variations, unsteady flow, and changing sediment supply rates on equilibrium morphodynamics. Multiple channels with various amplitudes and wavelengths of sinusoidal width variations were modeled under conditions of steady and unsteady discharge and different sediment supply rates. Results suggest that the amplitude of width variations exerts a primary control on riffle-pool relief and that under cycled hydrographs a reversal in the location of maximum shear stress occurs providing a riffle-pool maintenance mechanism.

Complementary flume experiments are presented in Chapter 4, where two geometries (constant- and variable-width) were subjected to the same sequential phases of steady flow and constant sediment supply, unsteady flow and constant sediment supply, and unsteady flow and increased sediment supply. Results show that the variable-width channel adjusts to an increased sediment supply by reducing the elevation relief between adjacent riffles and pools and decreased cross-sectional elevation variability, effectively reducing the form drag, rather than increasing the overall bed slope.

Finally, Chapter 5 presents a field investigation of the Elwha River downstream of the former Glines Canyon Dam site, using the dam removal as a natural experiment. Three annual topographic surveys were conducted along with hydrodynamic modeling to investigate the impact of increased sediment supply to a natural channel with riffle-pool morphology. Results show aggradation and channel widening have resulted in shallower, slower flows. Field surveys were complemented with historical aerial image analysis which suggests that channel widening and lateral migration rates have increased substantially since dam removal.

ACKNOWLEDGEMENTS

Primary thanks goes to Peter Nelson, who brought me on without the certainty of funding and has provided guidance, motivation, and assistance throughout my time at CSU. Thanks also to my committee members, Drs. Brian Bledsoe, Pierre Julien, and Ellen Wohl who provided helpful input that has increased the clarity and value of my work.

During my first year I was financially supported through the startup funds of Peter and my remaining time has been supported by National Science Foundation grant EAR-1425067.

I would like to thank Delft3D users and developers who are active on the online Message Board. There is a steep learning curve with relatively few resources available for creating somewhat complex fluvial models. The activity and assistance provided by more experienced users, both by directly answering my questions and indirectly through answering the questions of others, made creating the simulations in Chapter 3 possible. Aaron Schoelkopf provided valuable assistance during the F01 series of experiments presented in Chapter 4. The temporary flume walls were designed and constructed by Matt Szydłowski and installed by the ERC laboratory technicians. Taylor Hogan and the technicians also provided support in excavating and weighing sediment trapped in the flume tailbox. Moslem Kazemi helped us set up our computer-controlled flume cart. Special thanks are due to Dan Brogan who participated in each of the Elwha River surveys presented in Chapter 5. He also provided invaluable assistance in the operation of the Topcon surveying equipment. He also aided in the processing and analysis of field data. Andy Brew provided assistance during the 2014 survey, Peter Nelson provided assistance during the 2015 survey, and Travis Hardee provided assistance during the 2016 survey. I am grateful to Olympic National Park for allowing us to conduct our surveys in the park. Amy East, Jennifer Bountry, Tim Randle, and Andy Ritchie all were helpful in sharing information and resources related to the Elwha.

I appreciate the lab mates that have provided good company and thoughtful conversations: Andy Brew, Dan Brogan, Andy Bankert, Ryan Brown, Tess Hanson, Mike Gieschen,

and Robbie Queen. Through many days spent in collaborative field, laboratory, and office work, Dan Brogan has become a good friend and a much appreciated colleague.

I am most grateful for my family. My parents fostered a sense of curiosity and a value of life-long learning that continues to be a part of me. Special appreciation goes to my wife and son. I was once told by Dennis George at Tennessee Technological University that recognition for a graduate degree belongs not the recipient alone, but to their spouse as well. Certainly, this dissertation is as much a result of the hard work of my wife, Laura, as it is of my own efforts. So thank you, Laura, for being patient and understanding and enduring more schooling than you thought you were bargaining for, and our son Jude, for bringing new meaning and purpose to my life.

TABLE OF CONTENTS

ABSTRACT	ii
ACKNOWLEDGEMENTS	iv
LIST OF TABLES	viii
LIST OF FIGURES	ix
Chapter 1 Introduction	1
Chapter 2 Morphodynamic modeling of sediment pulse dynamics	8
2.1 Introduction	8
2.2 Methods	10
2.2.1 One-Dimensional Model	10
2.2.2 Analysis of sediment pulse evolution	15
2.2.3 Model Calibration	19
2.2.4 Numerical Run Procedure	19
2.3 Results	23
2.4 Discussion	26
2.4.1 Pulse mass and feed time	31
2.4.2 Pulse grain size	32
2.4.3 Unsteady flow	34
2.4.4 Width variability	35
2.4.5 Consideration for management/restoration applications	37
2.5 Conclusions	39
Chapter 3 Numerical simulations on the morphodynamics of variable-width gravel-bed rivers	41
3.1 Introduction	41
3.2 Methods	46
3.2.1 Numerical model	46
3.2.2 Numerical geometry set-up	47
3.2.3 Numerical run procedure	48
3.3 Results	51
3.3.1 Steady flow series: A–C	51
3.3.2 Unsteady flow series: D–J	57
3.4 Discussion	61
3.4.1 Morphology of variable-width channels	61
3.4.2 Sediment pulses and bedforms in variable width channels	63
3.4.3 Effects of unsteady flow on the morphodynamics of variable-width channels	65
3.4.4 Implications for riffle-pool dynamics	70
3.5 Conclusions	74

Chapter 4	Flume experiments on gravel-bed variable-width morphodynamics	77
4.1	Introduction	77
4.2	Methods	80
4.2.1	Experimental setup	80
4.2.2	Flume operation and measurements	83
4.2.3	Experimental procedure	84
4.3	Results	87
4.3.1	F01: Straight-Walled Channel	87
4.3.2	F02: Variable-Width Channel	94
4.4	Discussion	96
4.4.1	Steady versus Unsteady Flow	96
4.4.2	Effect of Increased Sediment Supply	99
4.4.3	Variable-width Gravel-bed Morphodynamics	102
4.5	Conclusions	103
Chapter 5	Hydro-geomorphology of the middle Elwha River, Washington, following dam removal	104
5.1	Introduction	104
5.2	Methods	106
5.2.1	Study site	106
5.2.2	Ground surveys	112
5.2.3	Measuring geomorphic changes	115
5.2.4	Aerial imagery surveys	116
5.2.5	Hydrodynamic modeling	117
5.2.6	Riffle-pool delineation	120
5.3	Results	122
5.3.1	Ground surveys	122
5.3.2	Geomorphic changes	126
5.3.3	Aerial imagery surveys	130
5.3.4	Hydrodynamic modeling	133
5.3.5	Riffle-pool delineation	135
5.4	Discussion	135
5.4.1	Effects of increased sediment supply on channel morphology	135
5.4.2	Dam removal effects on sedimentology	141
5.4.3	Hydrodynamics and geomorphic units	143
5.4.4	Implications for geomorphic unit maintenance	144
5.5	Conclusions	148
Chapter 6	Summary and Conclusions	150
References	153
Appendix A	Riffle-pool delineation details	186
A.1	Fuzzy c -means clustering	186
A.2	Cluster validity	187

LIST OF TABLES

3.1	General results from Series A, B, and C. S_0 = mean downstream bed slope; Bar mode C = central bars; Bar mode S = side bars; I_d = pulse dispersion index	52
3.2	General results from unsteady flow Series D–J. S_0 = mean downstream bed slope; Bar mode C = central bars; Bar mode S = side bars. Slopes and reliefs are all averaged over a complete hydrograph period.	58
5.1	Geomorphic Change Detection results.	128
5.2	Areas occupied by geomorphic units delineated using fuzzy logic for each survey geometry at the mean annual discharge ($Q_{\text{avg}} = 44 \text{ m}^3/\text{s}$). Units were numbered by ranking the mean shear stress.	136

LIST OF FIGURES

1.1 Typical riffle-pool morphology longitudinal (top), planform (middle), and cross-sectional (bottom) profiles.	2
2.1 Set-up for stratigraphy nodes and bookkeeping.	15
2.2 Idealized dispersive sediment pulses of the same shape but different sizes.	17
2.3 Measures of dispersion and translations for idealized dispersive sediment pulses shown in Figure 2.2. (a) Absolute IQR and C values, (b) values normalized per Sklar <i>et al.</i> (2009), and (c) values normalized per our recommendation.	17
2.4 Pulse mass, feed time, and feed rate for Runs 1–31. Each run number in this series is displayed on its corresponding marker.	21
2.5 Grain size distribution of bulk sediment and pulse sediment for Runs 16 and 32–35.	21
2.6 Time-series discharge for Runs 16 and 36–39.	22
2.7 Variable channel widths for (a) Runs 40–43, (b) Runs 44–47, (c) Runs 48–51, and (d) Runs 52–55. The dotted line in each plot represents the mean width, which is the channel width for Run 16.	23
2.8 Comparison of (a) measured bed profile and computed bed profile at the end of runs 1 through 4 in Nelson <i>et al.</i> (2015) and (b) measured and computed bedload exiting the flume throughout the experimental procedure of Nelson <i>et al.</i> (2015).	24
2.9 Model output from Run 32, 32 minutes after the beginning of the introduction of the sediment pulse, showing the stratigraphic grain size data.	24
2.10 Example of normalized pulse interquartile range versus normalized pulse center location for sediment pulses of the same shape but different masses.	25
2.11 Pulse dispersion index vs. sediment pulse mass. (a) Pulse dispersion indices grouped by pulse feed rates, representing pulses of different masses but the same shape, see Figure 2.10. (b) Pulse dispersion indices grouped by pulse feed time. Data points corresponding to feed rates or times where there is only one representative point are shown as single dots.	27
2.12 Pulse dispersion index vs. sediment pulse feed time. (a) Pulse dispersion indices grouped by pulse feed rates. (b) Pulse dispersion indices grouped by pulse mass, representing pulses of the same mass but different initial distributions (higher feed times correspond to a more dispersed initial condition). Data points corresponding to feed rates or times where there is only one representative point are shown as single dots.	28
2.13 (a) Interquartile range growth vs. distance traveled by pulse center for Runs 16 and 32–35; (b) Pulse dispersion index vs. sediment pulse median grain diameter. Light colored lines in (a) correspond to fitted lines.	29
2.14 (a) Interquartile range growth vs. distance traveled by pulse center for Runs 16 and 36–39; (b) Pulse dispersion index vs. hydrograph amplitude; and (c) Pulse dispersion index vs. hydrograph period.	30
2.15 (a) Pulse dispersion index vs. dimensionless amplitude of width variations; and (b) Pulse dispersion index vs. dimensionless wavenumber of width variations.	31

2.16 (a) Pulse dispersion index vs. average Froude number calculated over the sediment pulse only. (b) Pulse dispersion index vs. average Froude number calculated over the entire channel length. (c) Pulse dispersion index vs. relative pulse size.	33
2.17 Pulse dispersion index vs. average Froude number calculated over the entire channel length for pulses composed of different grain sizes. The pulse size is calculated as the quotient of the maximum pulse height above the antecedent bed and the channel width.	34
2.18 (a) Time-series of cycled hydrographs for unsteady flow runs, (b) time-series of instantaneous pulse dispersion index for unsteady flow runs, and (c) time-series of instantaneous pulse dispersion index with time normalized by hydrograph period. Breaks in lines indicate times for which there was no bedload movement.	36
2.19 Pulse dispersion index vs. average Froude number calculated over the entire channel length for pulses in channels with varying amplitudes and wavelengths of width variations.	37
3.1 General planform geometry of a channel with sinusoidal width variations.	48
3.2 Order of series runs, indicating which series' final conditions correspond to which series' initial conditions.	50
3.3 (a) Grain size distributions used in the numerical procedure. (b) Steady flow discharge and cycled hydrographs used in unsteady flow series.	50
3.4 Detrended elevation maps for Series A (equilibrium sediment supply) and Series B (no sediment supply) variable-width geometries. All axes are drawn to scale with tick marks every 0.5 m. Contours are in 0.5 cm increments. Flow is from left to right.	53
3.5 Detrended elevation and velocity profiles for A Series (equilibrium sediment supply) and B Series (no sediment supply) variable-width geometries. Color is constant per wavenumber and opacity increases with amplitude of width variations. Flow is from left to right.	54
3.6 (a) Average pulse dispersion indices versus dimensional amplitude of width variations for C Series runs. (b) Instantaneous pulse dispersion index versus time since end of pulse feed. (c–e) Instantaneous pulse dispersion index versus 25 th , 50 th , and 75 th percentiles of the cumulative elevation difference profile, respectively.	56
3.7 Differences between the maximum and minimum cross-sectional average detrended elevations for unsteady flow Series D–G.	58
3.8 Times series of bedform characteristics for J Series runs.	60
3.9 Differences in elevation from the mean of all times for each time in unsteady flow Series D–G. Note: $L_c = 6.84$ m for geometry 10 and $L_c = 3.42$ m for geometry 16.	67
3.10 Differences in elevation from the mean of all times for each time in unsteady flow Series D, H–J. Note: $L_c = 6.84$ m for geometry 10 and $L_c = 3.42$ m for geometry 16.	68
3.11 Velocity magnitude, shear velocity, and bedload transport rate over a complete hydrograph period for G10. Δ symbols correspond to sections where the maximum occurs. \circ symbols correspond to sections where the minimum occurs.	73

4.1	(a) Flume set up and planform channel geometry for (b) F01, straight-walled channel and (c) F02, varibale width channel	82
4.2	(a) Straight-walled flume geometry and (b) variable-width flume geometry. Camera view is oriented downstream in both images.	85
4.3	(a) Bulk grain size distribution used for initial bed composition and sediment supply during all phases. Gray lines are individual samples. The dark dotted line is the mean of all samples. (b) Stepped hydrograph used in unsteady flow phases. Dotted line corresponds to the steady flow discharge.	86
4.4	Time series of hydraulic conditions and bedload characteristics during all three phases of both geometries. For the unsteady flow phases, data points reflect variable values at the beginning/end of the hydrograph, when the flow equaled the mean discharge. μ is the mean and σ is the standard deviation.	88
4.5	Time-series box plots of flow depth for (a) F01 and (b) F02. Lighter or darker colored boxes correspond to lower or higher discharges, respectively. Hydrograph maximum occurs at 30 minutes and minimum occurs at 90 minutes.	89
4.6	Time-series box plots of shear stress for (a) F01 and (b) F02. Lighter or darker colored boxes correspond to lower or higher discharges, respectively. Hydrograph maximum occurs at 30 minutes and minimum occurs at 90 minutes.	90
4.7	Equilibrium detrended bed elevation maps for all phases in both geometries. Maps from the mean discharge are shown for unsteady flow phases.	91
4.8	Discharge-slope relationships for unsteady flow phases in both F01 and F02. The legend in subplot (b) applies to all subplots. Error bars encompass the calculated slope \pm the standard error.	93
4.9	Relief between bar top elevation and pool bottom elevation throughout variable-width channel phases. Circles represent mean values and error bars represent minimum/maximum values.	95
4.10	Standard deviation of elevations for each downstream cross-section for each of the phases in F02.	100
4.11	Mean bar-pool relief for unsteady F02 phases.	101
5.1	Location of the Elwha River on the Olympic Pensinsula and the location of the study site on the middle Elwha River, just within Olympic National Park. . . .	108
5.2	(a) Annual peak discharge versus return interval for the middle Elwha River from 1897 to 2016. (b) Annual trends in mean daily discharge between 1920 and 2017 for the middle Elwha River. The black line represents the mean for each day of the calendar year. The upper and lower limits represent the maximum mean daily discharge and the 5th percentile, respectively. (c) Mean daily discharge in the middle Elwha River between 1980 and 2017. The gray shaded box indicates the duration of removal for Glines Canyon Dam. The vertical lines indicate the dates of surveys reported in this paper. Flowrate data for each plot were collected at USGS gage 12045500 on the Elwha River at McDonald Bridge (available at http://waterdata.usgs.gov).	109
5.3	Study area reach on the middle Elwha River, showing the extent of the area of interest and the locations of other data of interest. Flow is from bottom to top.	111

5.4	Map of the area of interest, showing the general surveying methodology. Example from the 201506 survey. Flow is from bottom to top.	113
5.5	Aerial photographs used to delineate active channel margins and centerlines. Flow is from bottom to top.	118
5.6	Field and photo derived pebble count grain size distributions.	124
5.7	Summarized grain size data, showing also data from <i>Department of the Interior</i> (1996) and <i>Free</i> (2015). Error bars for the current study denote the interquartile range (Q1–Q3), square markers denote mean values.	125
5.8	Cross section comparisons between <i>Department of the Interior</i> (1995a) data and our survey results. Location of cross-sections are shown in Figure 5.3.	126
5.9	Cross section comparisons between 2011 pre-removal data and our survey results. Location of cross-sections are shown in Figure 5.3.	127
5.10	(a) and (b) Thresholded difference maps, using geomorphic change detection, covering the spans between the three survey dates. Flow if from bottom to top. (c) Area and (d) volume histograms for the first survey period, showing both raw (gray) and thresholded (colors) values, binned by elevation change. (e) Area and (f) volume histograms for the second survey period, showing both raw (gray) and thresholded (colors) values, binned by elevation change.	129
5.11	Raw and thresholded values of erosion, deposition, and net changes for (a) the first two surveys and (b) the second two surveys.	130
5.12	(a) Discharge over aerial photo period, (b) average migration rates between aerial photo dates, (c) active channel width distributions from aerial photos, and (d) sinuosity measured from active channel width centerlines.	131
5.13	Lateral migration of active channel centerlines delineated from aerial photos. Flow is from bottom to top.	132
5.14	Hydrodynamic variable distribution statistics for the modeled discharges through each survey geometry.	134
5.15	(a) Geographical distribution of clusters shown for each survey geometry. Units were numbered by ranking the mean shear stress. Flow is from bottom to top. (b) Results from fuzzy c -means clustering shown in variable-space. Note that all three surveys-worth of velocity and shear data points are included. Clusters were numbered by ranking the mean shear stress. (c) Aerial sums of each cluster for all survey geometries.	136
5.16	Cumulative estimated particle travel distances from Glines Canyon Dam based on grain size. Lighter colored lines represent a starting time of the beginning of dam removal in Sept. 2011 rather than the beginning of bedload passing in Oct. 2012. Dotted horizontal line represents the approximate distance from the site of former Glines Canyon Dam to our study area. Dotted vertical lines represent our surveys reported here.	139
5.17	Distribution statistics for shear stress grouped by cluster for each discharge and survey geometry. Box bounds represents the inter-quartile range (Q3–Q1), horizontal bar through box represents median, and upper and lower dots represent maximum and minimum, respectively.	146

- 5.18 Spatial distribution of calculated shear stress in a riffle-pool couplet at increasing discharges. Shear stress increases substantially in the pool from 44 m³/s to 760 m³/s, and only moderately in the riffle. Overall pool shear stress values for the higher discharges are greater than overall riffle shear stress values for the same discharges. Flow is from bottom to top. 147
- A.1 FCM clustering validation, where larger markers correspond to optimum values for the curve. (a) Separate-compactness index of *Zahid et al.* (1999), where darker colors correspond to higher m weighting exponents; (b) Cluster validity index of *Xie and Beni* (1991), where darker colors correspond to a higher number of clusters. 189

Chapter 1

Introduction

Alternating undulations of shallow and deep flow in rivers are commonly called riffle-pool sequences (Figure 1.1). Riffle-pool sequences are near-ubiquitous morphological features in both straight and meandering coarse-bedded rivers with slopes less than 2% (*Knighton*, 1998; *Leopold et al.*, 1964; *Thompson*, 2013). Riffles are defined as areas of higher relative elevation with a symmetrical cross-section and coarser bed material. Conversely, pools have relatively low topography and characteristically have finer bed material (*Keller*, 1971a; *Richards*, 1976b). Riffles are commonly co-located with wide portions of the channel or valley while pools are often forced by constrictions to downstream flow, either in the form of width variations or obstructions (*Brew et al.*, 2015; *Richards*, 1976b; *White et al.*, 2010). The heterogeneity in flow and bed surface conditions coincident with riffles and pools make these geomorphological features important habitat areas for aquatic organisms (*Brown and Brussock*, 1991; *Yarnell et al.*, 2006). Because of their ecological benefits, the reestablishment or maintenance of riffle-pool sequences is a major component in river restoration or management objectives (e.g., *Biron et al.*, 2012; *Pasternack and Brown*, 2013; *Rodríguez et al.*, 2004).

Individual riffles and pools are commonly classified based on bed topography (*Milne*, 1982; *O'Neill and Abrahams*, 1984; *Richards*, 1976a). Most often this method defines riffles as positive residuals of the difference between the thalweg elevation and a reach-averaged slope, and pools as negative residuals. *Leopold et al.* (1964) present a method for riffle-pool characterization using the energy-grade line, where steeper energy gradients correspond to riffles, and milder to pools. Other methods for riffle-pool delineation rely on hydrodynamic metrics such as flow depth, water surface slope, mean flow velocity, and Froude number (*Jowett*, 1993). The naturally variability of discharge in a river creates a potential issue with using hydraulic measures to identify riffles and pools, as these metrics are often changing de-

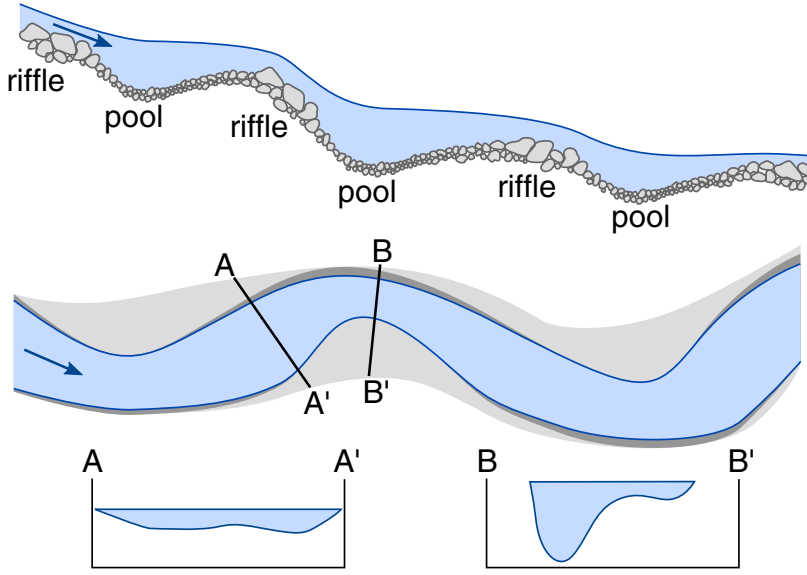


Figure 1.1: Typical riffle-pool morphology longitudinal (top), planform (middle), and cross-sectional (bottom) profiles.

pending on the flow. There is certainly no shortage of definition methods for riffles and pools and some suggest that the binary “riffle-pool” sequence overlooks the lateral heterogeneity inherent to natural channel morphology (*Wyrick and Pasternack, 2014*).

The issue of natural riffle-pool genesis and maintenance has been a topic of discussion and theorization nearly since the beginning of the study of geomorphology (*Gilbert, 1914*). One theory that has generated a lot of attention over the past few decades is the so-called “velocity reversal hypothesis” (*Keller, 1971b; Thompson, 2011*). According to this model, at low flow near-bed velocities in pools are lower than near-bed velocities in adjacent riffles. However, as stage increases the difference between the two near-bed velocities decreases until at some point a “reversal” occurs. That is, at an increased flow rate, the near-bed velocity in a pool is greater than that in an adjacent riffle. The hypothesis of some sort of reversal (near-bed velocity, mean flow velocity, boundary shear stress, etc.) has been the subject of numerous subsequent studies (e.g., *Caamaño et al., 2009; Keller and Florsheim, 1993; Lisle, 1979*). Although presupposed by the velocity reversal hypothesis, it should be noted that a reversal in velocity or shear stress does not necessarily indicate a similar reversal in bedload transport

(*Bayat et al.*, 2016). Additional hypotheses and revisions to the velocity reversal hypothesis have been made including the differential sediment entrainment hypothesis (*Clifford*, 1993; *Hodge et al.*, 2013; *Sear*, 1992), flow convergence routing hypothesis (*MacWilliams et al.*, 2006; *Sawyer et al.*, 2010), and others (e.g., *Caamaño et al.*, 2012; *Clifford and Richards*, 1992; *Strom et al.*, 2016; *Thompson et al.*, 1996, 1999).

Some of the hypotheses for natural riffle-pool maintenance, especially flow convergence routing, require the presence of longitudinal width variations. Indeed, the co-location of riffles and pools with wider and narrower lengths of channel, respectively, is well documented (*Brew et al.*, 2015; *Richards*, 1976b). A number of studies have used field measurements and hydrodynamic modeling to explore the structure of flow convergence into pools (*Harrison and Keller*, 2007; *MacVicar and Roy*, 2007a,b). There have been a handful of both flume and numerical studies exploring the effect of sinusoidal width variations on channel hydro- and morphodynamics (*Bittner*, 1994; *Jang*, 2014; *Nelson et al.*, 2015; *Repetto et al.*, 2002; *Tsujimoto*, 1987; *Wohl et al.*, 1999; *Wu and Yeh*, 2005; *Wu et al.*, 2011). Most of these have been in the context of braided channel morphology with very few in the context of riffle-pool sequences (but see *Nelson et al.* (2015), *Brown et al.* (2016), and *Chartrand* (2017)). These studies, most of which use uniform sediment, constant sediment supply (but see *Nelson et al.* (2015) and *Chartrand* (2017)), and steady flow, show that width variations create deep areas in width constrictions and shallow areas in width expansions. The combination of channel geometry, through the wavelength and amplitude of width variations, along with discharge (resulting in a certain aspect, or width-to-depth, ratio) have been hypothesized to be a control on whether a central bar or side bars develop in the widest sections of the channel (*Repetto et al.*, 2002; *Wu and Yeh*, 2005). There remains a wide knowledge gap in how nonuniform sediment, changes in sediment supply, and unsteady flow influence the hydrodynamics, bed topography, and material sorting in the development of riffles and pools forced by width variations. These topics are especially important as natural systems often

experience these conditions, and because changing sediment and hydrologic regimes are often inherent in problems faced by river managers and restoration professionals.

Sediment supply from upstream reaches is a major factor controlling a number of morphological features in alluvial/coarse-bedded streams including bed armoring (*Dietrich et al.*, 1989), grain size patches (*Nelson et al.*, 2009), and bedforms (*Kleinhans et al.*, 2002; *Venditti et al.*, 2017), including pool depth and variations in the amplitude of bed elevation through riffle-pool sequences (*Lisle*, 1982; *Wohl and Cenderelli*, 2000). Because sediment supply greatly affects sediment sorting patterns (*Lisle et al.*, 1993; *Venditti et al.*, 2012), and because bed sorting is generally thought to be an important component of riffle-pool maintenance (*Lisle*, 1979), it is likely that sediment supply has important feedbacks on riffle-pool dynamics. Studies have also shown that riffle-pool sequences sometimes persist in the same locations following sudden changes in sediment supply (*Brew et al.*, 2015). Sudden increases to sediment supply, either temporary or permanent, can result from both natural and anthropogenic causes (*Ferguson et al.*, 2015; *Pizzuto*, 2002; *Sutherland et al.*, 2002; *Zinger et al.*, 2011). Researchers have used field (*Brummer and Montgomery*, 2006; *Madej*, 2001; *Wohl and Cenderelli*, 2000), flume (*Cui et al.*, 2003a; *Humphries et al.*, 2012; *Sklar et al.*, 2009; *Venditti et al.*, 2010a), and numerical (*Cui and Parker*, 2005; *Cui et al.*, 2003, 2008; *Lisle et al.*, 2001) methods to explore how sediment pulses evolve and affect channel morphology under different conditions. With the growing popularity of dam removal as a restoration technique (*Bellmore et al.*, 2017; *Tullos et al.*, 2016), it is all the more important to understand how large fluctuations in sediment supply may affect downstream reaches and associated habitat.

Unsteady flow has been shown to have a significant effect on bedload transport (*Humphries et al.*, 2012; *Wong and Parker*, 2006), grain size sorting and armoring (*Hassan et al.*, 2006), and channel morphology (*Pasternack and Wyrick*, 2017). Previous studies on riffle-pool dynamics have concluded that unsteady flow is an important component of riffle-pool maintenance (*Knighton*, 1998; *Leopold and Wolman*, 1960). The riffle-pool maintenance hypothe-

ses generally rely on varying stage to explain the preservation of bed undulations (*Keller*, 1971b; *MacWilliams et al.*, 2006; *Vetter*, 2011) as well as sorting between riffles and pools (*de Almeida and Rodríguez*, 2011, 2012). Accordingly, the effects of unsteady flow have been inherent to both field and numerical studies of riffle-pool morphodynamics, however there has been little research on unsteady flow effects on riffles and pools in the laboratory.

In Chapter 2, sediment pulse dynamics are investigated. Sediment pulses, defined as discrete, temporary increases in sediment supply, enter channels through both natural and anthropogenic means. The movement of pulses in coarse-bedded channels are generally characterized by some combination of translation and dispersion. How pulses under move certain conditions is still poorly understood and the ability to predict how certain sediment pulses will evolve downstream under different conditions is important for management and restoration efforts. Here we present a one-dimensional morphodynamic model to explore how different pulse characteristics or channel configurations affect pulse movement. Our one-dimensional model uses the standard step backwater method to compute hydrodynamics, and determines morphodynamics by computing bedload transport, and retaining vertical grain-size stratigraphy. We explore the effect of pulse characteristics (pulse size, timing, and grain-sizes) as well as external forces (unsteady flow and width variations). In general, our results suggest more translation with smaller pulse sizes, longer pulse feed times, finer pulse grain sizes, and prolonged higher discharges. Our findings have implications for stream managers and restoration professionals in systems with sediment pulse concerns.

Channel geometry, water discharge, and sediment supply are primary influences governing the hydro- and morphodynamics of gravel bed rivers. The relative importance of these parameters on mesoscale bedforms such as riffles and pools, however, remains largely unexplored. In Chapter 3 we use a two-dimensional morphodynamic model to explore the interactions between width variations, steady vs. unsteady flow, and changes to sediment supply. Our results suggest that topographic relief between riffles and pools forced by width variations is governed by the amplitude of width variations. Increased sediment supply con-

ditions primarily result in an overall steepening of the downstream bed slope, in both steady flow and unsteady flow runs. Sediment pulses in variable width channels do not evolve with any more dispersion than an equivalent straight-walled channel. In variable width channels overall slope and riffle-pool relief are invariant to hydrograph shape as long as hydrograph maxima are the same. Under cycled hydrographs with constant sediment supply a series of alternating “hydrograph boundary layers” develop at each wavelength of width variation. Unsteady flow, coupled with width variations, provides conditions that facilitate the self-maintenance of riffles and pools through the upstream/downstream shifting of the location of maximum shear stress and bedload transport.

In Chapter 4 we present results from a laboratory flume experiment complementing the work in Chapter 3. Two flume geometries were used, a constant-width and variable-width. The width variations in the second channel were characterized by a sinusoidal pattern with a mean width equal to that of the first channel. Three phases were conducted in each flume geometry: 1) steady flow, constant sediment supply; 2) unsteady flow, constant sediment supply; and 3) unsteady flow, doubled sediment supply. Unsteady flow was implemented in the form of symmetrical triangular stepped hydrographs which were repeated for the duration of the phase. Hydrographs had a mean discharge equal to that in the steady flow phase. In all phases the bed and supply were composed of sediment grains between 1 and 8 mm. Results suggest that hydrograph averaged flow parameters for a variable-width channel vary little from parameters in steady discharge conditions. Our results indicate that our variable-width channel under unsteady flow conditions adjusted to an increase in sediment supply by reducing form drag in the form of reduced bar-pool relief and smaller cross-sectional elevation variability. Fluctuations in bar-pool relief over repeat discharge hydrographs indicate a mechanism for riffle-pool self-maintenance in the presence of width variations.

In Chapter 5, the removal of Glines Canyon Dam on the Elwha River serves as a natural experiment to investigate how downstream reaches respond to increased sediment supply.

Dam removal occurred in stages, beginning in 2011 and completed in 2014. Annual ground surveys were conducted from 2014 to 2016 to quantify channel bathymetry and topography and collect data related to surface sediment grain sizes. These surveys, combined with airborne lidar and uncertainty propagation, allow us to quantify the topographic changes throughout the study reach following dam removal. We also analyze historical aerial imagery dating back to 1939 to place planform changes observed during the survey period in the context of historical changes during dam emplacement. Each survey was used as input into a two-dimensional hydrodynamic model to calculate the flow field for a range of discharges, and these hydrodynamic outputs are used to delineate geomorphic units, such as riffles and pools, for each survey. Our analysis shows that channel widening and lateral migration, which have been occurring since at least 1939, have dramatically increased following dam removal. Channel bed aggradation and widening have resulted in shallower, slower flows. While geomorphic unit areas remained relatively constant between the first two surveys, there was a dramatic decrease in both riffle and pool areas between the second and third survey. Hydrodynamics within geomorphic units suggest the potential for maintenance and possible reemergence of reduced riffle and pool areas through a reversal in the position of maximum shear stress.

Chapter 2

Morphodynamic modeling of sediment pulse dynamics

2.1 Introduction

Sediment supply from upstream reaches is an important factor controlling a number of morphological features in alluvial coarse-bedded streams. Sediment supply rates and associated grain size distributions affect observed bed armoring (*Dietrich et al.*, 1989), surface patchiness (*Nelson et al.*, 2009), and bedforms (*Kleinhans et al.*, 2002). Sudden, temporary changes in sediment supply to a channel reach can be singular or episodic and often result from a number of causes. Sediment pulses (defined as short term significant increases in the sediment supply rate) can be introduced to a reach as a result of natural processes such as meander cutoffs (*Zinger et al.*, 2011), landslides or bank failure (*Sutherland et al.*, 2002), and wildfires (*Benda et al.*, 2003). Sediment pulse introduction can also result from anthropogenic causes such as land use changes (*Trimble*, 1997), mining operations (*Ferguson et al.*, 2015; *Pickup et al.*, 1983), restorative sediment augmentation (*Sklar et al.*, 2009), and dam removal (*Draut and Ritchie*, 2015; *Pizzuto*, 2002). Sediment pulses and associated spatial and temporal deposition patterns are of interest to river managers due to the possible effects on stream stability, habitat suitability, and in-stream infrastructure (*Nelson and Dubé*, 2016; *Wood and Armitage*, 1997). Additionally, some restoration techniques such as gravel augmentation rely on predicted pulse evolution patterns to achieve their desired effect (*Bunte*, 2004).

A number of field, flume, and numerical modeling studies have investigated sediment pulses, with a particular focus on the relative amount of translation and dispersion that occurs as a sediment pulse evolves and moves downstream. *Lisle et al.* (1997) showed that

coarse-grained pulses evolve primarily through dispersion, although some translation occurs as well. *Lisle et al.* (2001) used a numerical approach to determine that Froude numbers have to be low in order for coarse-grained pulses to experience significant translation. *Sklar et al.* (2009) found that larger volume pulses are more dispersive than smaller volume pulses and that finer-grained pulses evolve through translation more than coarser-grained pulses. Using flume experiments, *Humphries et al.* (2012) concluded that under unsteady flow larger magnitude hydrographs increase pulse translation and *Nelson et al.* (2015) concluded that width variations increase pulse dispersion.

Taken together, these studies suggest that the size of the sediment pulse, the Froude number of the flow, the grain size of the pulse material, the size of the hydrograph (if flow is unsteady), and channel width variations may act as controls on the relative translation and dispersion of a sediment pulse as it evolves. However, no study has systematically explored these potential controls and the relative importance of any of these factors remains unclear. The use of numerical modeling has the potential to increase our understanding of these important processes (*Cui and Wilcox*, 2008; *Cui et al.*, 2003, 2006a,b, 2008; *de Almeida and Rodríguez*, 2011; *Lisle et al.*, 2001).

In this study we present results from a 1D model used to explore sediment pulse dynamics as influenced by different pulse characteristics, hydrology, or channel geometry. The questions we wish to address are: 1) Can our 1D model effectively capture the pulse evolution trends shown by previous studies? 2) Under what conditions is dispersion/translation the favored form of pulse evolution? and 3) How is pulse evolution affected by pulse mass/timing, pulse grain size, unsteady discharge, and downstream variability in channel width? The model first is calibrated by reproducing the flume experiment of *Nelson et al.* (2015). Pulse characteristics, discharge, and channel geometry were then varied to understand how these variations affect pulse behavior and bed morphology.

2.2 Methods

In this section we introduce our model and provide details related to its development, we calibrate our model with results from a laboratory flume experiment, and then outline our experimental procedure to explore the controls on sediment pulse evolution.

2.2.1 One-Dimensional Model

Because of the wide parameter space required to consider the various controls on pulse evolution we needed a fast model capable of handling the dynamics important for pulse evolution and having the necessary user control to modify the boundary conditions and channel geometry as needed to explore these different channel and pulse characteristics. In lieu of using an existing model which may not have all of these necessary attributes, we chose to write our own 1D model. Despite the simplicity inherent to width- and depth-averaged models, *Lisle et al.* (1997) found that a 1D model effectively predicted pulse evolution in a channel with alternate bars, where secondary flow was not likely negligible. *Cui et al.* (2008) also had success using a 1D model to simulate flow in riffle-pool morphology forced by alternate bars. Additionally, (*de Almeida and Rodríguez*, 2011) used a 1D model to accurately reconstruct the thalweg profile in an nonuniform channel with riffles and pools forced by width variations.

Our model comprises four submodels which represent the processes in which we are interested: quasi-steady 1D hydraulics, mixed-size bedload transport, bed evolution/surface sorting, and vertical grain size sorting. Because the sediment pulses are often composed of material with a different size distribution than that of the antecedent bed, and because the surface and sub-surface composition may differ based on historical erosional/depositional processes, the stratigraphic submodel, recording the vertical sorting of grain diameters, is an important component of this model.

Hydraulics

Water flow was simulated using the standard step backwater method (*Chaudhry*, 2008), whereby the energy equation is iteratively solved to determine the flow depth at each successive position. We use a hydraulics model similar to that used by *Lisle et al.* (1997). This model also assumes total shear stress is accounted for by grain shear alone.

The total mechanical energy (E) at spatial index j is computed as the sum of the bed elevation, pressure head, and velocity head at that location

$$E_j = \eta_j + H_j + \frac{U_j^2}{2g} \quad (2.1)$$

where η is the local bed elevation, H is the flow depth, U is the mean flow velocity, and g is gravitational acceleration. Subcritical flow parameters are computed by solving the energy equation,

$$\frac{\partial E}{\partial x} = \frac{\partial}{\partial x} \left(\eta + H + \frac{U^2}{2g} \right) = S_f \quad (2.2)$$

where S_f is the friction, or energy, slope. The friction slope is related to a dimensionless friction coefficient (C_f) and the Froude number ($\text{Fr} = U(gH)^{-1/2}$) as

$$S_f = C_f \text{Fr}^2 \quad (2.3)$$

The friction coefficient can be determined using the Manning-Strickler relation (*Parker*, 2006)

$$C_f^{-1/2} = 8.1 \left(\frac{H}{k_s} \right)^{1/6} \quad (2.4)$$

where k_s is the roughness height ($k_s = 2D_{90}$, where D_{90} is the grain size on the bed surface for which 90 percent is finer) (*Parker*, 2006).

Additionally, due to the steep lee face associated with some of the pulse runs, and the degree of channel constriction associated with some of the variable width runs, a handling of transcritical flow was necessary. In order to do this, nodes of supercritical flow were

“flagged” during the original backwater profile calculations. The flagged nodes were then returned to and supercritical depths were computed in the downstream direction using a reduced momentum equation (*Brunner*, 2010)

$$\frac{2Q^2}{gA_j} + A_j H_j = \frac{2Q^2}{gA_{j+1}} + A_{j+1} H_{j+1} \quad (2.5)$$

These equations were solved simultaneously to determine the longitudinal distribution of flow depth, mean flow velocity, and associated shear stress (τ_b) (*Lisle et al.*, 1997; *Parker*, 2006)

$$\tau_b = \rho C_f U^2 \quad (2.6)$$

where ρ is the density of water.

Bedload Transport

Although bedload relations such as those developed by *Parker* (1990) and *Wilcock and Crowe* (2003) are well established, their applicability is more appropriate for larger grain size distributions than those considered here. For this reason we use the *Viparelli et al.* (2010a) variation of the *Ashida and Michiue* (1972) formula to model bedload transport. The grain size distribution from the experiment we use to calibrate our model (*Nelson et al.*, 2015) and the grain sizes used for our model are within the range of those used by *Ashida and Michiue* (1972) and *Viparelli et al.* (2010a). This formulation determines a dimensionless transport rate, or Einstein parameter, of grain size class i (q_{bi}^*), as a function of the Shields parameter referenced to grain size class i (τ_i^*) and a critical Shields parameter corresponding to the threshold of motion for grain size class i (τ_{ci}^*). The *Viparelli et al.* (2010a) modification of the *Ashida and Michiue* (1972) relation is specified as

$$q_{bi}^* = 17\alpha (\tau_i^* - \tau_{ci}^*) \left(\sqrt{\tau_i^*} - \sqrt{\tau_{ci}^*} \right) \quad (2.7)$$

where α is a coefficient calibrated to the data. The non-dimensional Shields parameter (τ^*) is determined by

$$\tau_i^* = \frac{\tau_b}{\rho R g D_i} \quad (2.8)$$

where R is the submerged specific gravity of the sediment, and D_i is the grain diameter in size class i .

In addition to the α coefficient, *Viparelli et al.* (2010a) presented a different hiding function from *Ashida and Michiue* (1972) to determine the critical Shields number for each grain size class

$$\frac{\tau_{ci}^*}{\tau_{scg}^*} = \begin{cases} \left(\frac{D_i}{D_{sg}}\right)^{-0.98} & \text{for } \frac{D_i}{D_{sg}} \leq 1 \\ \left(\frac{D_i}{D_{sg}}\right)^{-0.68} & \text{for } \frac{D_i}{D_{sg}} > 1 \end{cases} \quad (2.9)$$

where τ_{scg}^* is the threshold Shields stress referenced to the geometric mean of the bed surface, D_i is the grain size diameter, and D_{sg} is the surface geometric mean sediment size.

Viparelli et al. (2010a) used linear regression of measured bedload data to determine the value of $\alpha = 0.270$ and visually estimated $\tau_{scg}^* = 0.043$. We calibrated both α and τ_{scg}^* values using elevation profiles and bedload transport measured at the outlet of the flume in the *Nelson et al.* (2015) experiments. This resulted in $\alpha = 1$ and $\tau_{scg}^* = 0.03$. A value of unity for α indicates an agreement with *Ashida and Michiue* (1972) and $\tau_{scg}^* = 0.03$ is in agreement with laboratory results on the threshold of motion (*Parker et al.*, 2003).

Bed Evolution and Surface Sorting

Bed morphology was updated with the Exner equation for sediment continuity

$$\frac{\partial \eta}{\partial t} = -\frac{1}{(1 - \lambda_p)} \frac{\partial q_{bT}}{\partial x} \quad (2.10)$$

where q_{bT} is the dimensional bedload transport per unit width summed over all grain size classes and λ_p is the bed sediment porosity (here assumed to be 0.4) (*Parker*, 2006, 2008). Sorting of sediment grain sizes can be simulated by formulating the Exner equation for each

grain size class represented in the bedload and surface sediments. This is done using the active layer formulation of *Hirano* (1971)

$$(1 - \lambda_p) \left[f_{li} \frac{\partial}{\partial t} (\eta - L_a) + \frac{\partial}{\partial t} (F_i L_a) \right] = -\frac{\partial}{\partial x} (q_{bT} p_i) \quad (2.11)$$

where f_{li} is the fraction in grain size class i that is exchanged between the active layer and the substrate, F_i and p_i are the fractions in grain size class i of the surface and bedload, respectively, and L_a is the active layer thickness. The value of f_{li} depends on whether sediment is being deposited onto or degraded from the bed at the current timestep

$$f_{li} = \begin{cases} f_i|_{z=\eta-L_a} & \text{for } \frac{\partial \eta}{\partial x} < 0 \\ \alpha F_i + (1 - \alpha) p_i & \text{for } \frac{\partial \eta}{\partial x} > 0 \end{cases} \quad (2.12)$$

where f_i is the fraction in grain size class i of the substrate and α is a dimensionless exchange coefficient ($0 \leq \alpha \leq 1$), here taken as $\alpha = 0.7$ (*Cui et al.*, 1996; *Hoey and Ferguson*, 1994; *Toro-Escobar et al.*, 1996). Both equations (2.10) and (2.11) were discretized using a semi-implicit upwinding scheme with an upwinding coefficient of 0.75 (*Parker*, 2006).

Vertical Stratigraphic Sorting

In general our stratigraphy submodel follows that developed by *Viparelli et al.* (2010b). Each downstream node is assigned stratigraphy nodes underneath its active layer, numbered N_j , with the lowest vertical layer corresponding to the datum and the highest corresponding to the active layer-substrate interface. Each stratigraphy layer, save the topmost, has a uniform height of L_s . The topmost layer has a height of the difference between the active layer-substrate interface elevation and the next stratigraphy node elevation (see Figure 2.1). The number of substrate nodes, N_j , at each downstream location is modified appropriately due to aggradation or degradation. If the magnitude of aggradation/degradation is small the same number of stratigraphy nodes may exist. In the case of aggradation the deposited

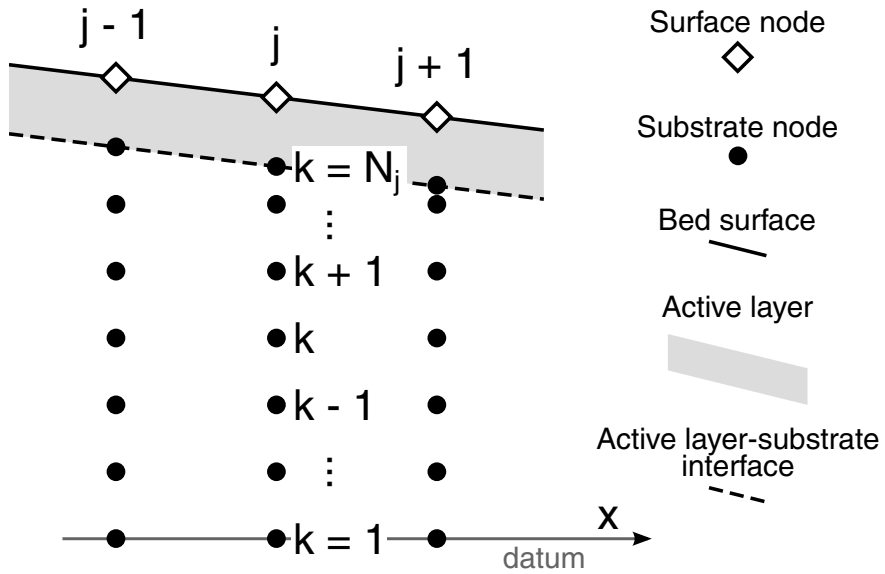


Figure 2.1: Set-up for stratigraphy nodes and bookkeeping.

sediment is mixed into the topmost substrate distribution using weighted averages. In the case of degradation the substrate remains the same. When aggradation occurs such that a new storage layer is created the antecedent topmost storage layer is mixed with the deposited grains and the new storage layer is composed entirely of the deposited sediment. See *Viparelli et al.* (2010b) for more details.

2.2.2 Analysis of sediment pulse evolution

Quantifying sediment pulse evolution has been a difficult problem. In their study examining the behavior of pulse movement in flume experiments, *Sklar et al.* (2009) proposed using the interquartile range (IQR) and pulse center (C) of the normalized cumulative elevation difference to characterize relative dispersion and translation. Elevation differences are computed by subtracting the initial, pre-pulse bed elevations from the time-specific bed elevation after the pulse has been introduced. From this the downstream-cumulative bed elevation difference is computed and normalized by the maximum cumulative elevation difference for each run. The pulse center (C) is calculated as the median of the normalized cumulative bed elevation difference distribution. The first (Q1) and third (Q3) quartiles are

calculated as the median locations of the lower and upper halves of the same distribution, respectively. The IQR is the difference between Q3 and Q1. Both IQR and C are calculated for each time step following the introduction of the sediment pulse. The slope of the line created by IQR versus C is used to determine the relative dispersiveness of a pulse, with higher slopes corresponding to a higher degree of dispersion.

Sklar et al. (2009) normalize the interquartile range by dividing each IQR value by the initial IQR value. They normalize the pulse center location by subtracting the initial C value from each subsequent C value, essentially resulting in the distance moved by the pulse center. While we believe both IQR and C are valuable parameters for quantifying pulse evolution, we recommend normalizing IQR in a similar fashion to C, by subtracting each value from the initial IQR. Imagine three idealized sediment pulses with exactly the same shape, but different sizes, that all evolve in a dispersive manner (Figure 2.2). For each of the different pulse sizes the subsequent elevation difference profiles have exactly the same relative position with its original distribution. Figure 2.3a shows the absolute values of the interquartile range and pulse center location for each of the three pulses. Normalization of IQR and C values according to *Sklar et al.* (2009) is shown in Figure 2.3b. Although the slopes of the three IQR versus C plots in Figure 2.3a are the same, they become different after this normalization method, showing the larger pulse to be more translational and the smaller pulse to be more dispersive. Normalization of IQR and C according to the methods we recommend is shown in Figure 2.3c. In this case the original slopes of the IQR versus C lines are retained, and the starting point of each line is translated to the origin of the plot. According to our method, the resulting value of the normalization of IQR is a measure of the IQR growth over time

$$IQR_n = IQR - IQR_{initial} \quad (2.13)$$

Similarly, the normalization of C is a measure of the distance moved by the pulse center over time

$$C_n = C - C_{initial} \quad (2.14)$$

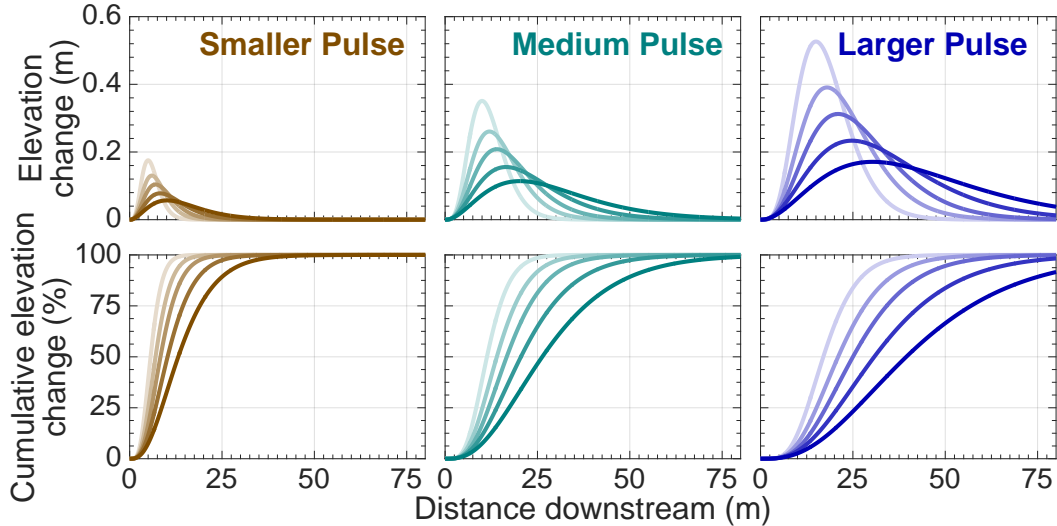


Figure 2.2: Idealized dispersive sediment pulses of the same shape but different sizes.

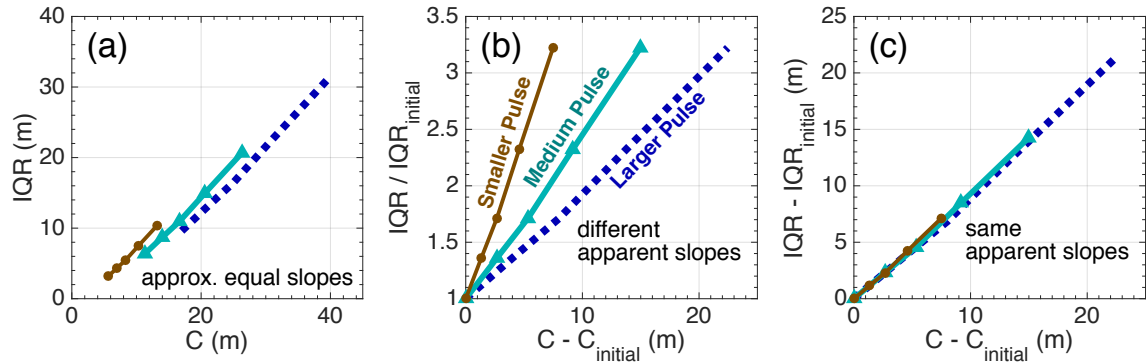


Figure 2.3: Measures of dispersion and translations for idealized dispersive sediment pulses shown in Figure 2.2. (a) Absolute IQR and C values, (b) values normalized per Sklar *et al.* (2009), and (c) values normalized per our recommendation.

For comparison of many different pulses it is beneficial to compute a single, non-dimensional parameter from these IQR_n and C_n values. In statistics there are a number of measures for the relative spread of a distribution, many of which are the quotient of some variable of spread (standard deviation, interquartile range, etc.) to some variable of the average (mean, median, etc.) (Lewis, 2012). From this, we introduce a parameter we call the “pulse dispersion index” (I_d), calculated as the quotient of normalized interquartile range and median of the normalized cumulative bed elevation difference distribution

$$I_d = \frac{\text{IQR}_n}{C_n} \quad (2.15)$$

For some occasions it is advantageous to see how this measure of the relative spread of a sediment pulse itself evolves over time. In such cases it is beneficial to calculate an instantaneous pulse dispersion index ($I_{d,\text{inst}}$):

$$I_{d,t} = \frac{d\text{IQR}_n}{dC_n} \quad (2.16)$$

where t is the time index. At other times, it is more useful to calculate a single value of the spread of a sediment pulse over the entire time range. The IQR_n and C_n (both of which are a series of values) can be used to calculate a normalized pulse dispersion index, I_{dn} .

$$I_{dn} = \frac{\sum_{t=1}^T (C_n \circ \text{IQR}_n)}{\sum_{t=1}^T (C_n \circ C_n)} \quad (2.17)$$

where the “ \circ ” operator denotes the Hadamard, or elementwise, product of two vectors or matrices and T denotes the total number of time steps. Equation 2.17 essentially calculates a best-fit line of the IQR_n versus C_n plot forcing the line to pass through the origin. A higher dispersion index corresponds to a more dispersive sediment pulse distribution. This is similar to the “ dZ/dX ” from *Sklar et al.* (2009), which is the slope of a line fitted to the $\text{IQR}/\text{IQR}_{\text{initial}}$ versus $C - C_{\text{initial}}$ plot in units of m^{-1} . Our parameter has the benefit of being dimensionless. Our pulse dispersion index is analogous to the ratio of the change in mean to the change in standard deviation of the pulse location used by *Pace et al.* (2017a). As *Sklar et al.* (2009) notes, it is also essentially the inverse of the Peclet number which has also been used to quantify pulse translation versus dispersion (*Lisle et al.*, 1997; *Pace et al.*, 2017a).

2.2.3 Model Calibration

Model calibration was performed using the flume results of *Nelson et al.* (2015). Their experiment took place in a $0.216\text{ m} \times 9.144\text{ m}$ flume with six sinusoidal width constrictions installed ($A_c = 0.33$, $\lambda_c = 1.2$, both parameters defined below). The bed and feed material consisted of unimodal mixture of sand and fine gravel (0.08 mm – 4 mm, $D_{50} = 0.84\text{ mm}$). The experimental procedure consisted of five runs all performed with the same discharge, 0.91 l/s. During the first run the sediment feed remained constant at 150 g/min and lasted 13 hours. The second run, intended to simulate dam installation, lasted 23.6 hours with no sediment feed. Run 3 was meant to represent dam removal and had the 150 g/min sediment feed reintroduced for 4.5 hours. In the fourth run the sediment feed was discontinued again, also intended to simulate dam installation, and was run for 28.6 hours. The last run consisted of the feeding of a sediment pulse. The pulse was of uniform grain diameter (0.83 mm – 1 mm) and was fed to the flume for 27 minutes at a rate of 600 g/min, after which no sediment was supplied to the flume. The pulse mass was chosen to be that which would fill the pools to create a plane bed condition and the timing was chosen so that the pulse was fed at a rate 4 times the equilibrium rate from Run 1. See *Nelson et al.* (2015) for more details on both their procedure and results. The computational model was subjected sequentially to each of these runs in the same way in which they were performed in the laboratory and the entire series of runs was used for the calibration of bedload parameters α and τ_{scg}^* mentioned above. Values were chosen which minimized the root mean squared error between measured and computed values for the bed profiles at the end of each run and bedload measurements throughout the experimental procedure.

2.2.4 Numerical Run Procedure

To explore sediment pulse dynamics under variable conditions (e.g., sediment pulse characteristics, channel geometry) we performed a number of numerical runs with nearly identical parameters. We explored the effect of pulse size, pulse mass, pulse feed rate, grain size, un-

steady discharge, and width variability on pulse movement. Each of the runs was identical with the exception of the parameter to be explored. The standard pulse parameters were the same as that of Run 5 in *Nelson et al.* (2015), a mass of 16.2 kg fed over a time period of 27 minutes, which corresponds to a feed rate of 600 g/min. The standard pulse grain size distribution was composed of grains between 0.841 and 1 mm with $D_{50} = 0.917$ mm. The standard channel geometry for the pulse runs consisted of a 0.185 m wide \times 20 m long rectangular channel. Each run was preceded by a ‘zeroing’ run whereby the simulation was performed without any sediment feed for a period of 9999 minutes. In each case, immediately following the ‘zeroing’ run the sediment pulse was fed to the upstream end of the spatial domain.

Total pulse mass and timing of pulse feed were simultaneously varied to explore the effect of the volume/mass of the pulse and its feed rate on pulse evolution. Pulse masses and times were chosen to encompass the mass and timing of the “standard” pulse run. This resulted in groupings of runs according to pulse mass, timing, and feed rate (Figure 2.4). Run 16 in this series corresponds to the “standard” pulse parameters. Therefore, for each series Run 16 serves as a sort of control.

For the purpose of determining the effect of pulse material grain size on pulse evolution, we simulated four pulses of differing grain sizes compositions (Figure 2.5). For all grain size runs the pulse was composed of either well-sorted sand or very fine gravel with D_{50} values ranging from 0.229 mm to 3.668 mm. The pulse grain size distributions for these runs are shown in F.

Unsteady discharge effects were modeled by simulating four different discharge hydrographs over the run time with the otherwise standard pulse parameters. All hydrographs were symmetrical (i.e. the rising limb and falling limb have the same slope). The first two of these runs (Runs 36 and 37) had hydrographs with periods (T_H) of 60 minutes and amplitudes (A_H) of 0.2275 and 0.6825 l/s, respectively. The second two unsteady flow runs (Runs

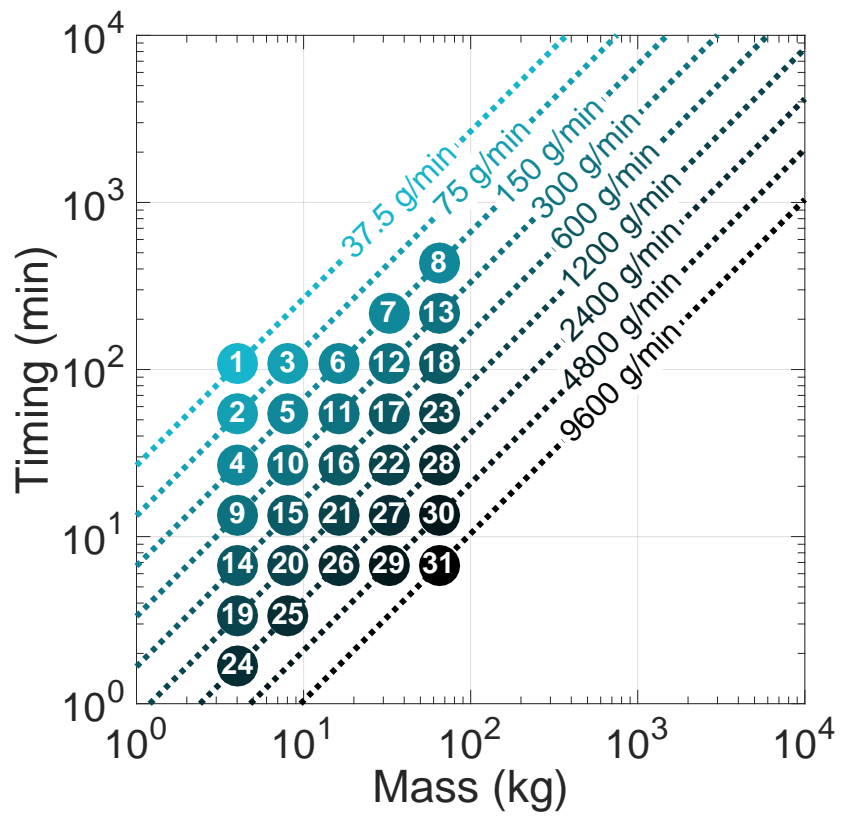


Figure 2.4: Pulse mass, feed time, and feed rate for Runs 1–31. Each run number in this series is displayed on its corresponding marker.

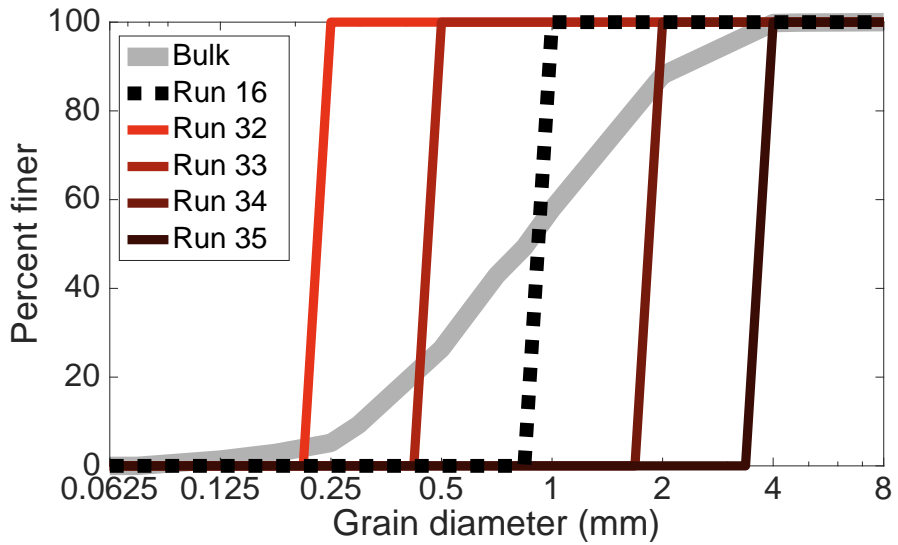


Figure 2.5: Grain size distribution of bulk sediment and pulse sediment for Runs 16 and 32–35.

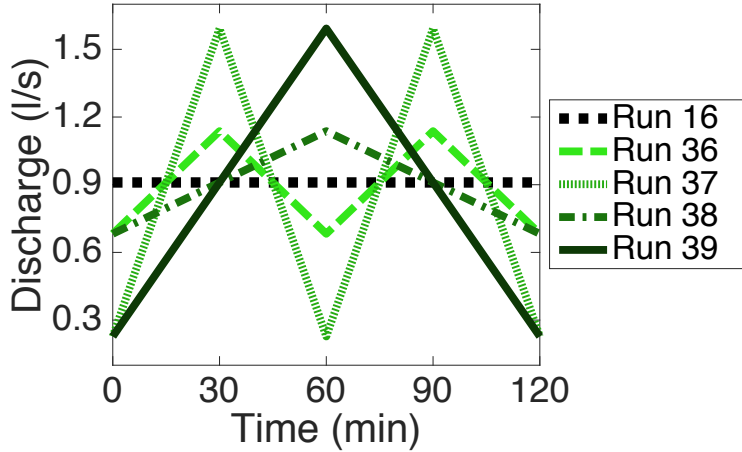


Figure 2.6: Time-series discharge for Runs 16 and 36–39.

38 and 39) had periods of 120 minute and amplitudes of 0.2275 and 0.6825 l/s, respectively. All unsteady flow runs have a mean discharge of 0.91 l/s (Figure 2.6).

Runs with variable width geometries were performed to not only discern the effect of a variable width channel versus a constant width channel, but also the effects of varying amplitudes and wavelengths of the width variations. A channel with a sinusoidally varying channel width can be described by the equation (*Wu et al.*, 2011)

$$B(x) = B_0 [1 + A_c \sin(\lambda_c x / B_0)] \quad (2.18)$$

where $B(x)$ is the local half channel width, B_0 is the mean channel half width, A_c is the dimensionless amplitude, and λ_c is the dimensionless wave number. The dimensional wavelength is calculated as

$$L_c = \frac{2\pi B_0}{\lambda_c} \quad (2.19)$$

Both A_c and λ_c were varied simultaneously with A_c values of 0.1, 0.167, 0.233, and 0.3 and λ_c values of 0.2, 0.4, 0.6, and 0.8 (Figure 2.7). In all cases $B_0 = 0.0925$ m.

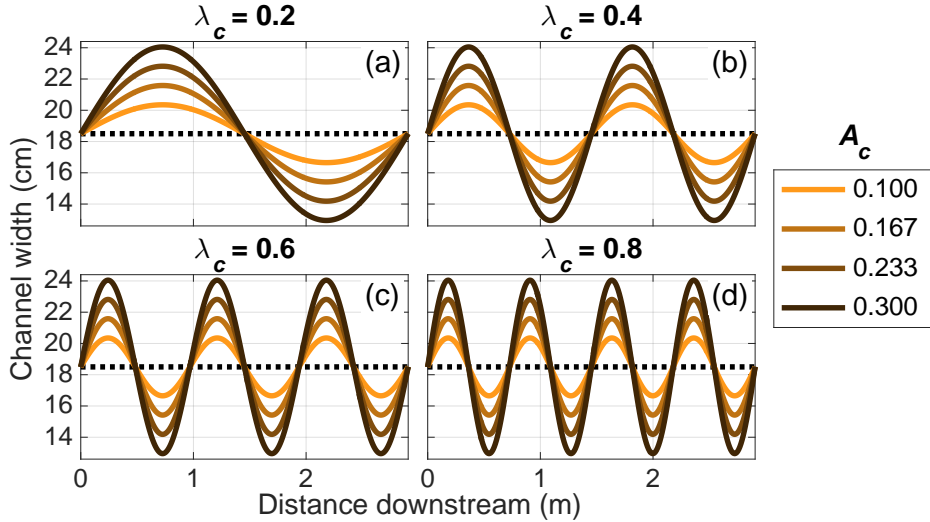


Figure 2.7: Variable channel widths for (a) Runs 40–43, (b) Runs 44–47, (c) Runs 48–51, and (d) Runs 52–55. The dotted line in each plot represents the mean width, which is the channel width for Run 16.

2.3 Results

For all simulations relevant data (elevations, grain size distributions, flow depths, etc.) were output from the Fortran90 model into comma-delimited ASCII files at simulated 1 minute intervals and analyzed using MATLAB. Model calibration resulted in elevation profiles and sediment transport calculations that were in good agreement with flume experiment results (Figure 2.8). Figure 2.9 shows example output from Run 32, highlighting the ability to track stratigraphic grain size data, which is potentially important when the pulse is composed of material of a different size than the antecedent surface. An example of the normalized pulse interquartile range and normalized pulse center location for Runs 9–13 is shown in Figure 2.10, where the slope of each curve is approximately that run’s pulse dispersion index (I_{dn}). The local slope of each position on a curve corresponds to the instantaneous pulse dispersion index ($I_{d,t}$).

The pulse dispersion index from Runs 1–31 are shown in Figures 2.11 and 2.12 plotted against the pulse mass and pulse feed time, respectively. Each grouping of points as shown in the legend of Figure 2.11a represents sediment pulses with similar shapes but different masses. In general, grouping by either pulse feed rate or pulse feed time, increased pulse

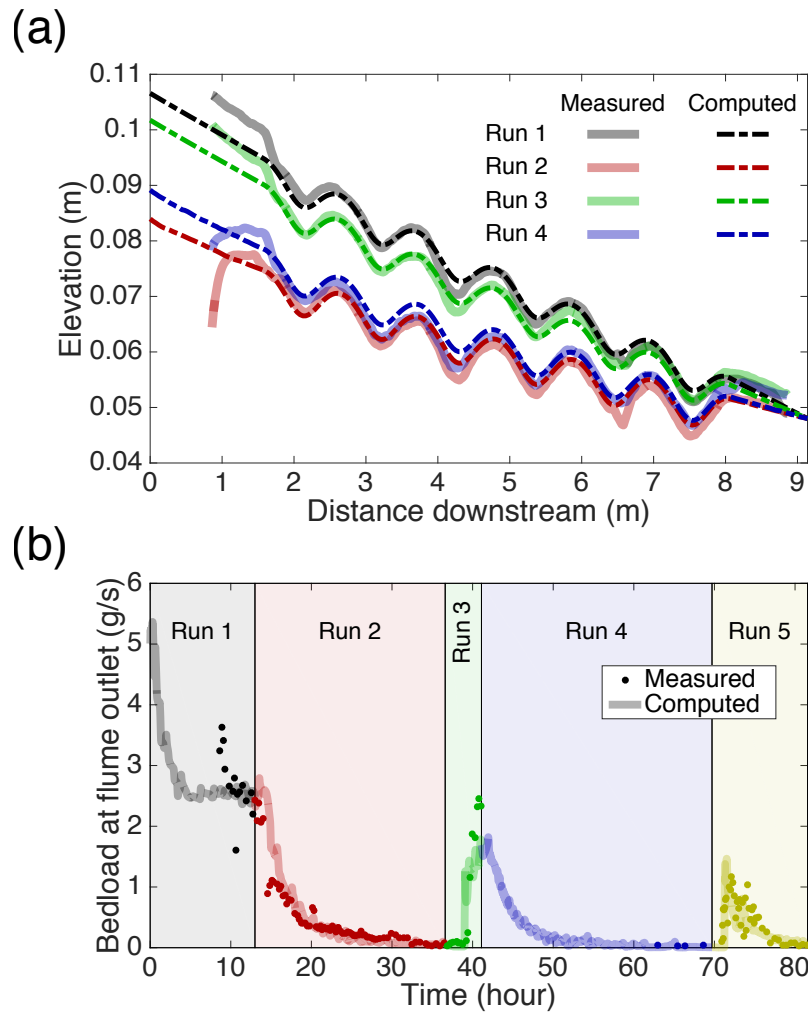


Figure 2.8: Comparison of (a) measured bed profile and computed bed profile at the end of runs 1 through 4 in *Nelson et al.* (2015) and (b) measured and computed bedload exiting the flume throughout the experimental procedure of *Nelson et al.* (2015).

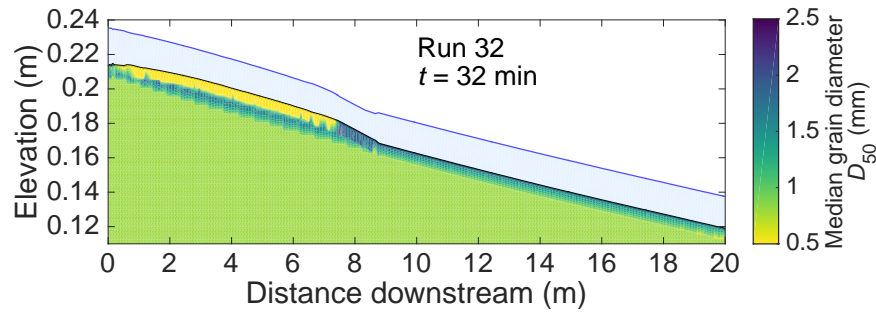


Figure 2.9: Model output from Run 32, 32 minutes after the beginning of the introduction of the sediment pulse, showing the stratigraphic grain size data.

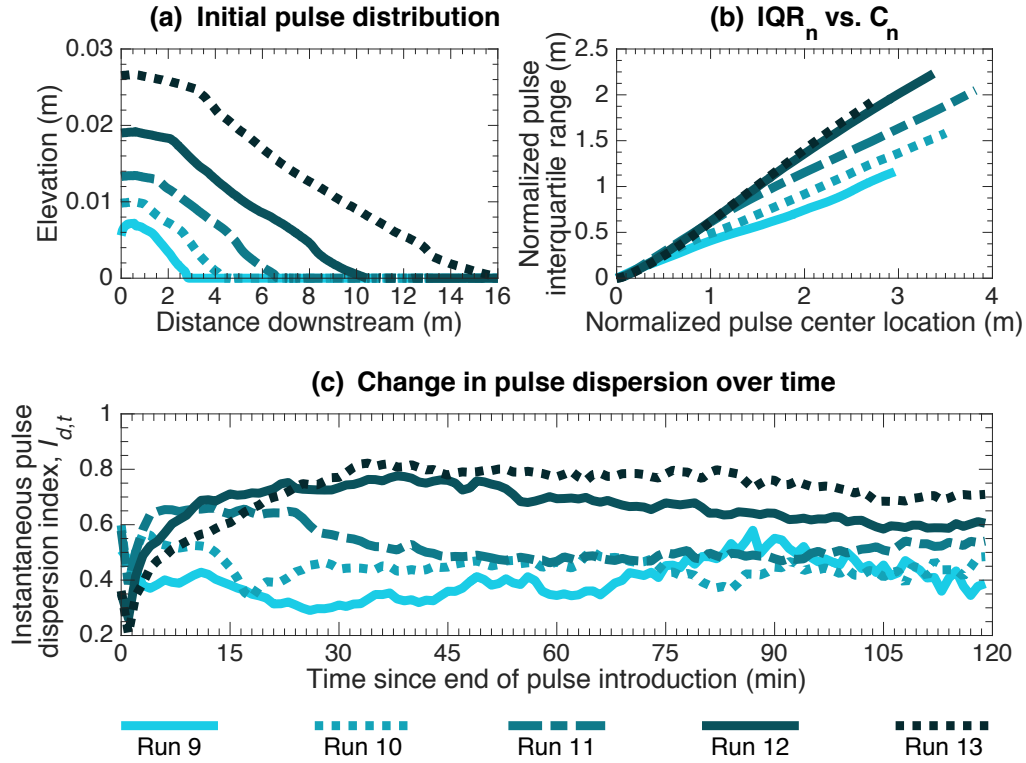


Figure 2.10: Example of normalized pulse interquartile range versus normalized pulse center location for sediment pulses of the same shape but different masses.

mass corresponds to a higher pulse dispersion index and therefore a more dispersive pulse. Conversely, each grouping of points in Figure 2.12b represents pulses of the same mass but different initial spatial distributions, where higher feed times create a more dispersed initial pulse distribution. In general these curves show a decrease in pulse dispersion index with increased feed time, suggesting that pulses with a more dispersed initial condition evolve through translation more than pulses of the same mass with a less dispersed initial distribution. Pulse dispersion indices for Runs 1–31, with variable pulse mass and timing, range between 0.2 and 1.2.

Results from Runs 33–35 show a clear increase in pulse dispersion with larger median grain diameters (Figure 2.13). The range of pulse dispersion indices in these runs vary from 0.3 to 1.6. Figure 2.14 shows the results from runs 36–39, simulating unsteady flow. In all cases, unsteady flow resulted in a more dispersive sediment pulse than the standard steady flow run (Run 16), but the pulse dispersion indices for unsteady flow runs varied only between 0.9 and 1.1, a much narrower range than any other set of runs. Calculated pulse dispersion indices for variable width runs (Runs 40–55), which range from 0.8 to 1.9, are shown in Figure 2.15. The only variable width simulations that resulted in significantly different pulse dispersion indices from the standard run (Run 16) were for those with a wavenumber, λ_c , of 0.2.

2.4 Discussion

In general, previous studies have related sediment pulse movement and behavior to Froude number (*Lisle et al.*, 1997; *Pace et al.*, 2017a; *Singh and Ojha*, 2008; *Sklar et al.*, 2009). Namely, research has shown that pulses experience a higher degree of translation with a lower Froude number (*Lisle*, 2007). We try to frame our discussion in the context of how Froude number is affected by pulse or channel configuration due to the fact that channel conditions, prior to the introduction of the sediment pulse, were exactly the same for most of the simulations (Runs 1–35). Additionally, once the pulse has been introduced, any change

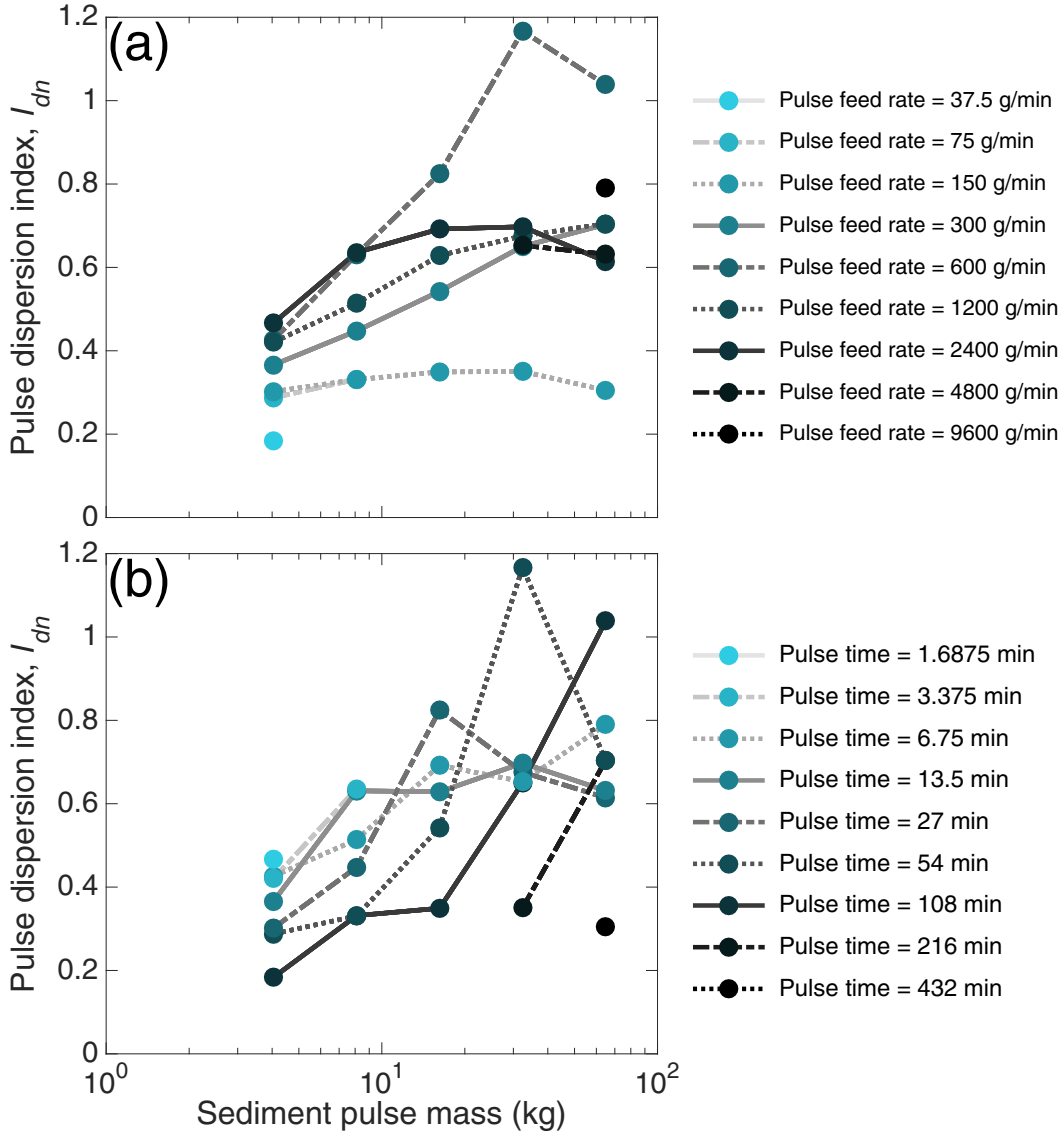


Figure 2.11: Pulse dispersion index vs. sediment pulse mass. (a) Pulse dispersion indices grouped by pulse feed rates, representing pulses of different masses but the same shape, see Figure 2.10. (b) Pulse dispersion indices grouped by pulse feed time. Data points corresponding to feed rates or times where there is only one representative point are shown as single dots.

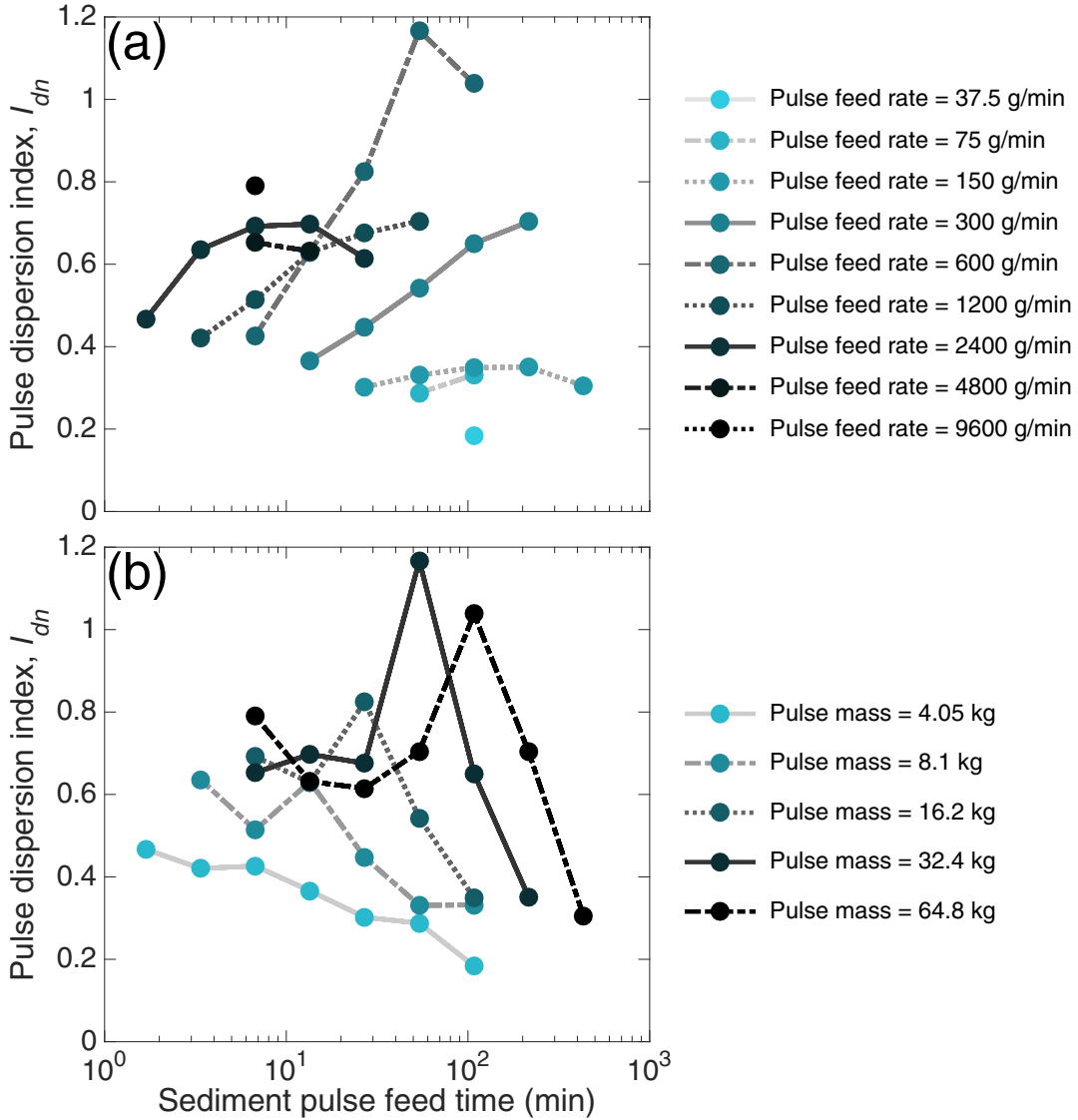


Figure 2.12: Pulse dispersion index vs. sediment pulse feed time. (a) Pulse dispersion indices grouped by pulse feed rates. (b) Pulse dispersion indices grouped by pulse mass, representing pulses of the same mass but different initial distributions (higher feed times correspond to a more dispersed initial condition). Data points corresponding to feed rates or times where there is only one representative point are shown as single dots.

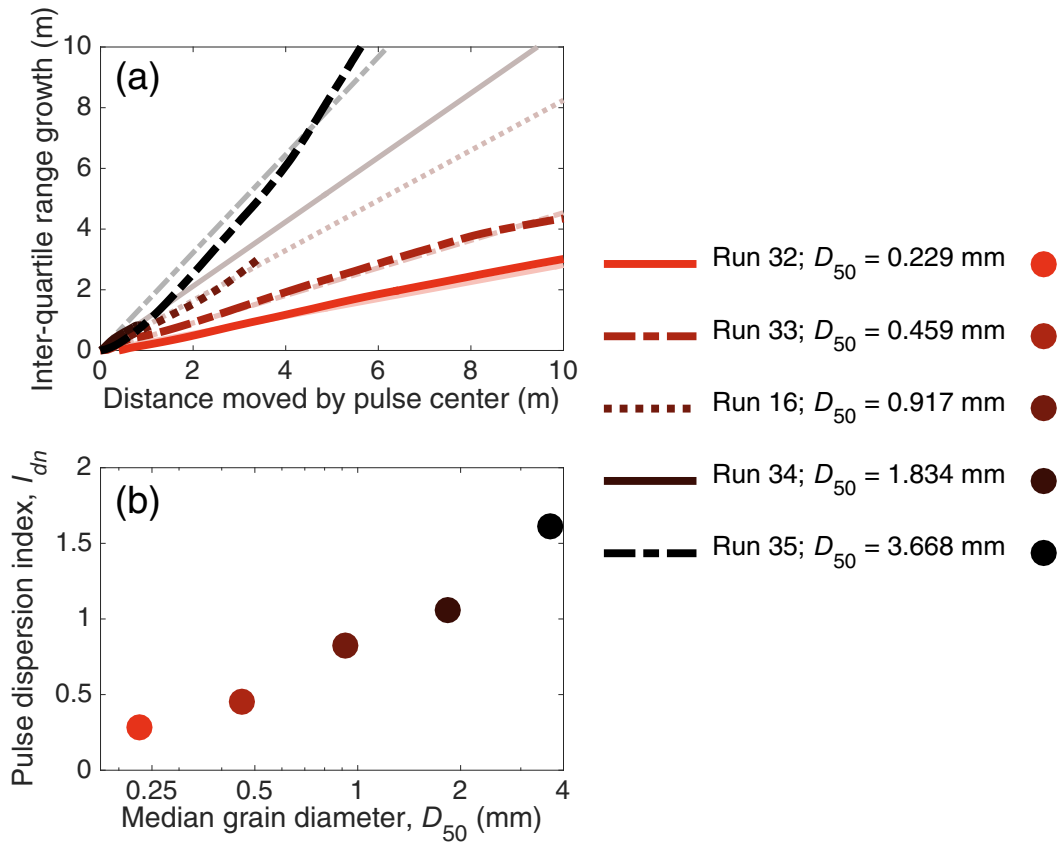


Figure 2.13: (a) Interquartile range growth vs. distance traveled by pulse center for Runs 16 and 32–35; (b) Pulse dispersion index vs. sediment pulse median grain diameter. Light colored lines in (a) correspond to fitted lines.

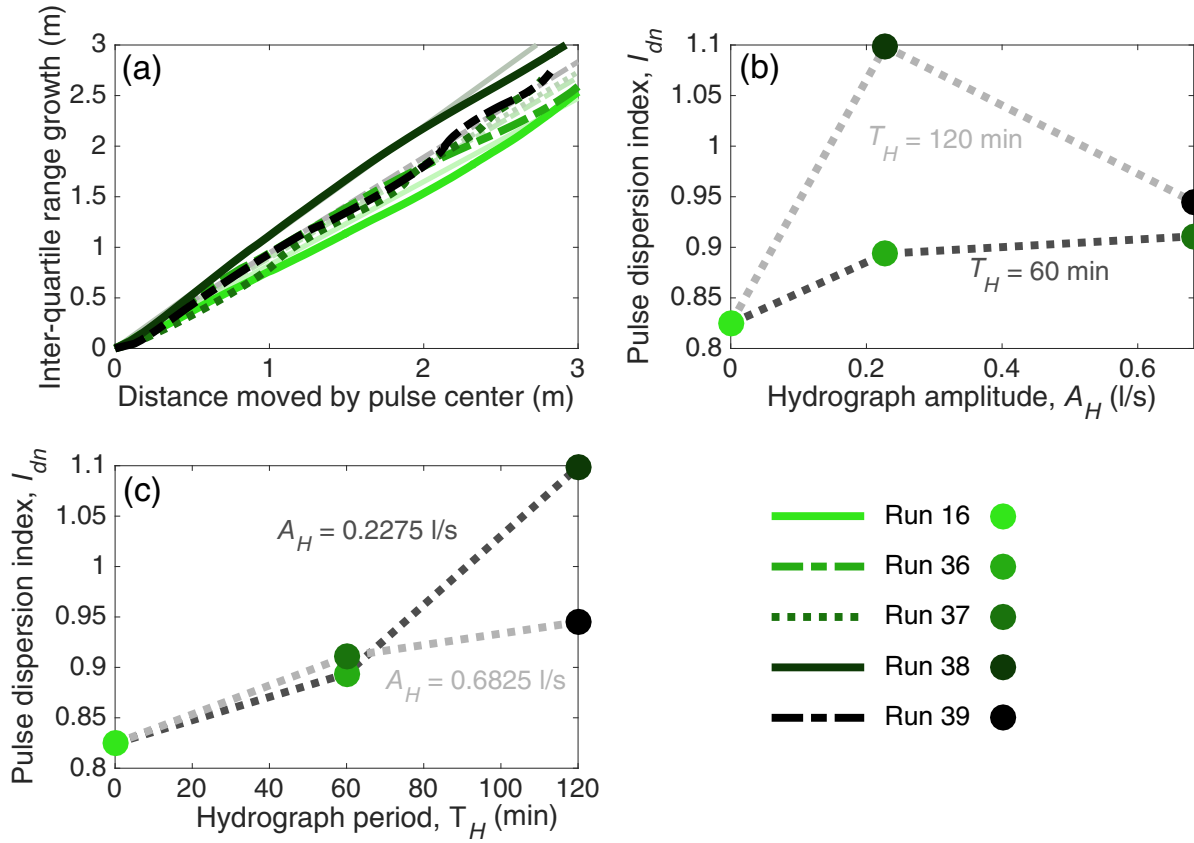


Figure 2.14: (a) Interquartile range growth vs. distance traveled by pulse center for Runs 16 and 36–39; (b) Pulse dispersion index vs. hydrograph amplitude; and (c) Pulse dispersion index vs. hydrograph period.

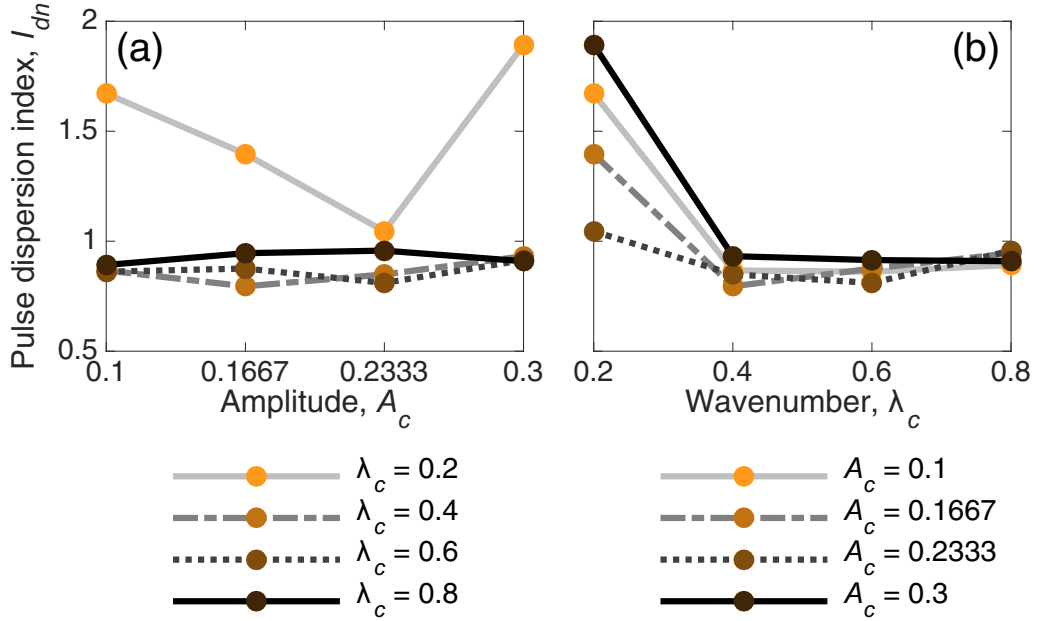


Figure 2.15: (a) Pulse dispersion index vs. dimensionless amplitude of width variations; and (b) Pulse dispersion index vs. dimensionless wavenumber of width variations.

in the Froude number is dependent on the conditions of the pulse itself (composition, shape, etc.). The influence of the Froude number is partly captured in these pulse characteristics for Runs 1-35, the changes in stage for Runs 36-39, and the width variations in Runs 40-55.

2.4.1 Pulse mass and feed time

In Runs 1–31 of our simulations, larger sediment pulses generally evolved through more dispersive means, agreeing with previous research conclusions (*Lisle et al.*, 2001; *Sklar et al.*, 2009). For a given pulse mass, a shorter feed time will correspond to a higher feed rate and therefore a steeper slope front. This will subsequently create higher Froude numbers over the pulse and presumably lower pulse dispersion indices (Figure 2.12b). When we view the relationship between the spatially-averaged Froude number over the pulse (calculated at the end of pulse introduction) and the pulse dispersion index, there is no clear relationship (Figure 2.16a). However, when we calculate the average Froude number for the entire channel length and replot, a clearer relationship emerges, echoing previous conclusions that lower

Froude numbers result in more translation (Figure 2.16b). This estimate of Froude number is understandably a better predictor of pulse dispersion since it inherently takes into account the size (length) of the pulse by using Froude numbers calculated for the entire length of the channel rather than over the pulse only. Figure 2.16b shows a trend of rapid increase in pulse dispersion over a very short Froude number range (0.6–0.7). Interestingly, our models predict significant pulse translation with Froude numbers in excess of 0.4, in contrast to *Lisle et al.* (1997, 2001), who observed translational behavior only when the Froude number was 0.4 or lower.

The size/mass of the sediment pulse is itself relevant, with larger pulses evolving in a more dispersive manner (Figure 2.11a). Previous studies have often considered the size (height) of a pulse relative to the channel dimensions (width) (*Pace et al.*, 2017a; *Sklar et al.*, 2009), showing that translation is maximized when the pulse size is small relative to the channel. Our results also corroborate this conclusion, with pulses having higher maximum pulse heights resulting in more dispersive evolution (Figure 2.16c).

2.4.2 Pulse grain size

Runs 32-35 explored the effect the grain diameters of the pulse material. Our results are consistent with previous studies (*Lisle et al.*, 2001; *Sklar et al.*, 2009), showing that translation is favored with finer pulse grain sizes (Figure 2.13). Since our sediment pulses were continuously added to the channel over a period of time, rather than placed in the channel all at once, it is conceivable that the differences in grain sizes of the pulses in Runs 32-35 may have resulted in differently shaped pulses. These different shapes will be manifested by different pulse geometries and affect the Froude number in the channel, both of which are parameters that can also apparently affect pulse movement. However, the average Froude number falls within a very narrow range for this series of runs (0.64-0.66, Figure 2.17), indicating that pulse material plays an important role in pulse movement even for channels at the same Froude number. However, the pulse size, defined as the ratio of the

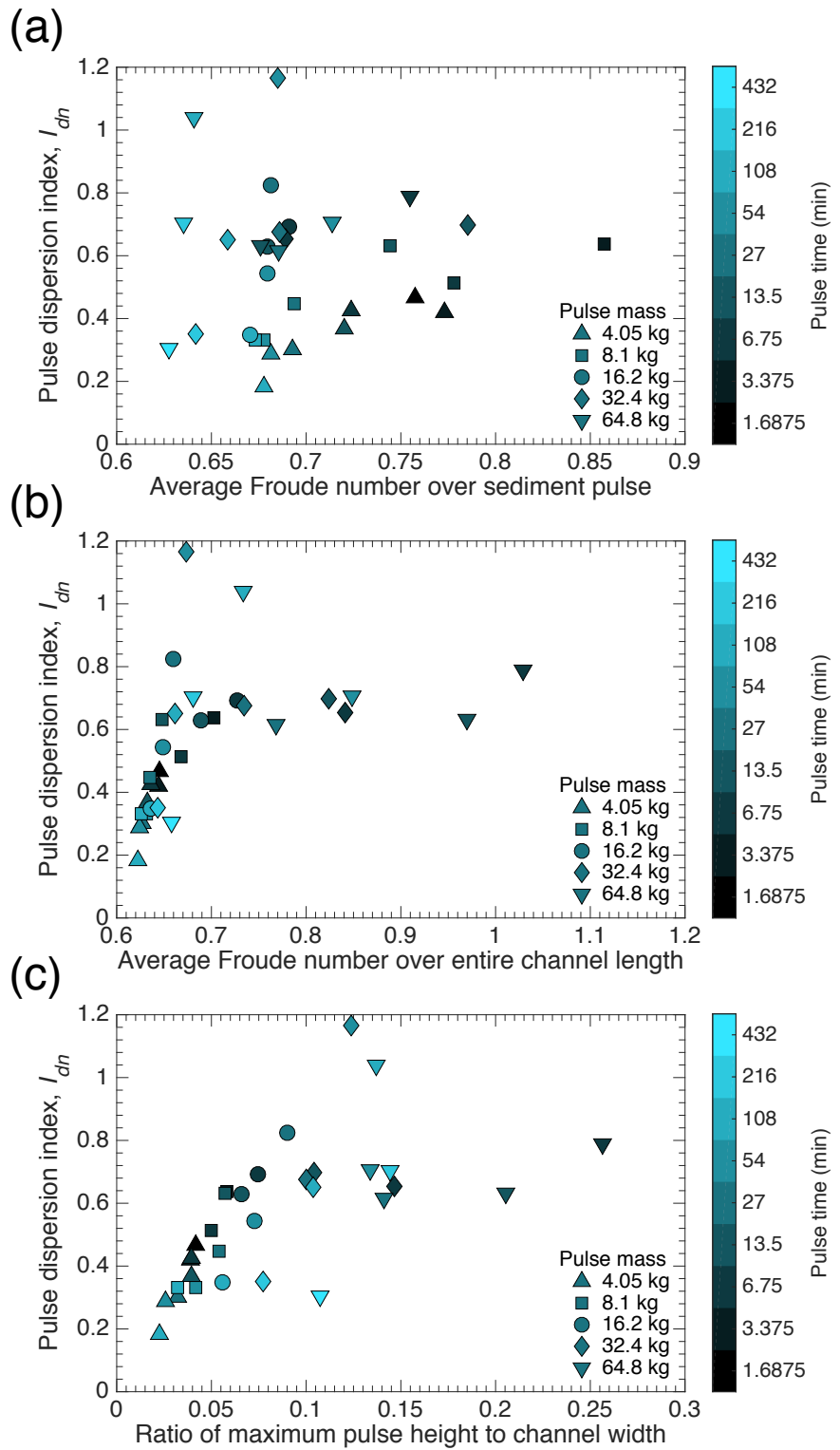


Figure 2.16: (a) Pulse dispersion index vs. average Froude number calculated over the sediment pulse only. (b) Pulse dispersion index vs. average Froude number calculated over the entire channel length. (c) Pulse dispersion index vs. relative pulse size.

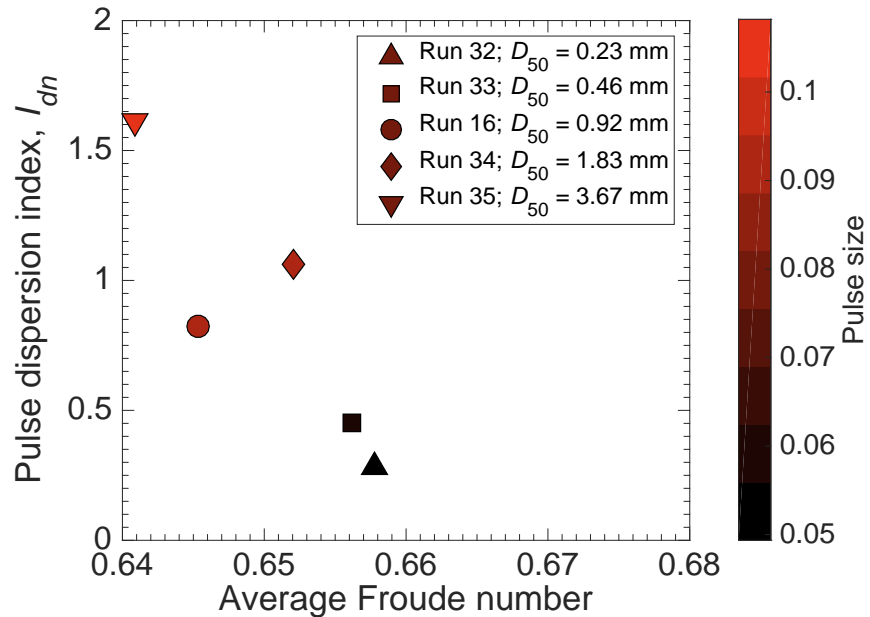


Figure 2.17: Pulse dispersion index vs. average Froude number calculated over the entire channel length for pulses of composed of different grain sizes. The pulse size is calculated as the quotient of the maximum pulse height above the antecedent bed and the channel width.

maximum pulse height to the channel width, varies from 0.05 to 0.11. The combined effects of pulse composition and geometry likely intensify the overall effect on pulse evolution and may explain the large magnitude of differences in pulse dispersion indices.

2.4.3 Unsteady flow

Unsteady flow simulations (Runs 36-39) indicate that changing discharge has the effect of increasing pulse dispersion, with all unsteady runs having a greater pulse dispersion index than Run 16 (Figure 2.14). As one might expect, the instantaneous pulse dispersion index is highly dependent on the flow conditions at that specific time, and higher discharges correspond to lower dispersion indices, or more translation (Figure 2.18a, b). In every case the lowest instantaneous pulse dispersion index occurs in coincidence with the peak of the hydrograph. Figure 2.18c indicates that the value of the peak discharge does not have a strong impact on the minimum pulse dispersion index, with each curve having nearly the same local minima at peak discharges. For unsteady flow runs with higher amplitude hydro-

graphs (Runs 37 and 39), during the lowest discharges of the hydrograph bedload transport ceases, shown as gaps in the curves in Figure 2.18b and c. Differences between Runs 36 and 38 in Figure 2.18 suggest that, regardless of the fact that each has the same minimum discharge, prolonged time at low discharges causes more pulse dispersion. When evaluating the overall, normalized pulse dispersion index, the differences in unsteady flow runs with one another and with a steady flow run are minimal (Figure 2.14), and for shorter wavelength hydrographs (Runs 36 and 37) there is no appreciable difference. Our results do not decisively corroborate the conclusions of *Humphries et al.* (2012), that larger peak discharges cause a greater degree of translation. We hypothesize that this may be due, at least in part, to the difference in hydrograph shapes between our runs (triangular, symmetrical) and those in *Humphries et al.* (2012) (lognormal distribution).

2.4.4 Width variability

Variable-width channel runs suggest that, in general, width variations have little effect on overall pulse evolution. Because each of the channel configurations has a constant-width inlet reach, there is no appreciable difference in the initial pulse distributions (ratio of maximum pulse heights to channel width range from 0.09 to 0.1). The average Froude number for the length of the channel, however, varies from 0.4 to 0.8, with higher Froude numbers generally occurring in configurations with lower wavenumbers (longer wavelengths). In contrast with previous research, and the indications from previous run series in this study, Froude number appears to have little effect on the movement of sediment pulses in variable-width channels (Figure 2.19). Also in contrast with the conclusions of *Nelson et al.* (2015), our results suggest that width variations do not increase sediment pulse dispersion. Because of the limitations of one-dimensional modeling, our model is not able to predict lateral distribution of pulse material, which may not be ideal for cases where lateral differences in elevation are important. Similar to the observations of *Nelson et al.* (2015), our variable-width simulations never showed the pool-filling and bed homogenization that has been reported in the field

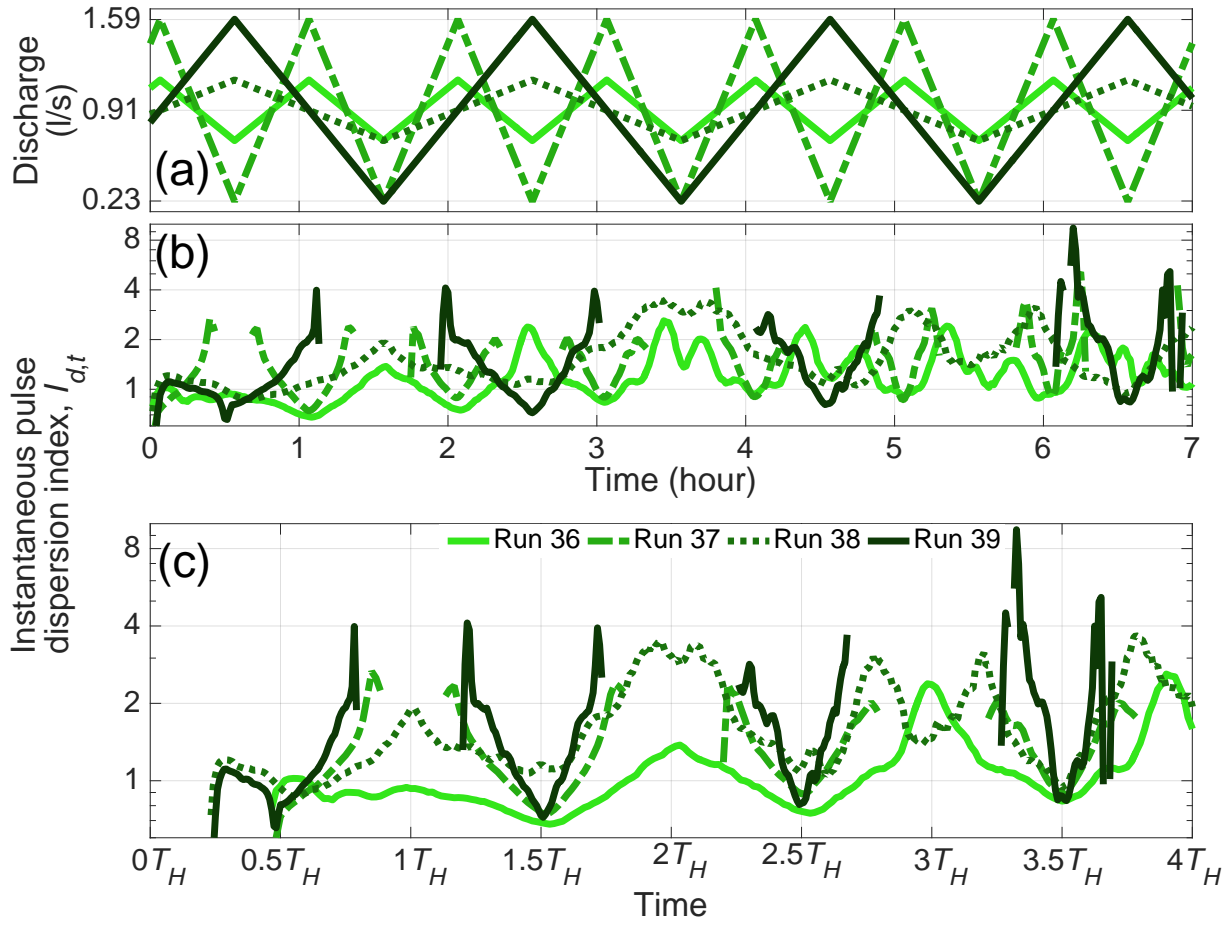


Figure 2.18: (a) Time-series of cycled hydrographs for unsteady flow runs, (b) time-series of instantaneous pulse dispersion index for unsteady flow runs, and (c) time-series of instantaneous pulse dispersion index with time normalized by hydrograph period. Breaks in lines indicate times for which there was no bedload movement.

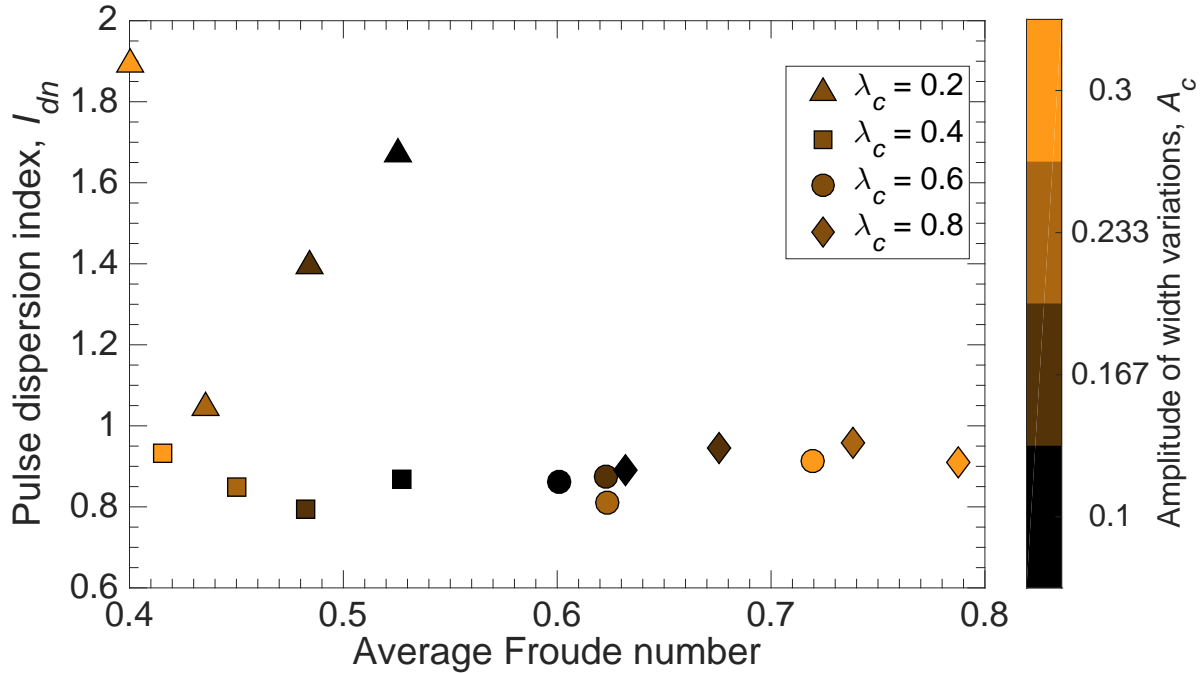


Figure 2.19: Pulse dispersion index vs. average Froude number calculated over the entire channel length for pulses in channels with varying amplitudes and wavelengths of width variations.

(Brew *et al.*, 2015; Madej, 2001), highlighting the fact that increased sediment supply alone is sometimes insufficient for pools to fill.

2.4.5 Consideration for management/restoration applications

Both natural and anthropogenically influenced rivers with introduced sediment pulses are likely to experience more complicated effects than are captured in our simulations. Because of the inherent complexity of available material and geometry, coarse-bed, full-scale rivers are rarely straight and plane bed. Natural systems are likely to experience more complicated planform conditions (e.g., meandering, braiding, confluences) as well as more complicated substrate materials (e.g., cohesive material, bedrock controls). Previous studies have shown that sediment pulse introduction can result in initial homogenization of the channel bed (Madej, 2001), local channel widening (Madej and Ozaki, 1996; Thomas *et al.*, 2015), increased sinuosity (East *et al.*, 2015), increased pool abundance and capacity (Madej, 2001; Wohl and Cenderelli, 2000), and degree of bedrock exposure (Bartley and Rutherford, 2005;

East et al., 2015; *Hoffman and Gabet*, 2007). Obviously these are all conditions that are not possible to capture in a simplified model such as the one presented here.

Despite these limitations there are applications from our study to management and restoration of sediment pulse dynamics in river systems. Addition of coarse-grained material to sediment-starved systems is often designed for the purpose of increasing habitat suitability for certain in-stream biota (*Zeug et al.*, 2014). Along with the studies of *Sklar et al.* (2009), *Venditti et al.* (2010a), and *Humphries et al.* (2012), our simulations can help managers determine appropriate masses and grain sizes for augmentation, as well as possible discharge regimes if control of reservoir releases upstream is possible. For example, our results suggest that if translation of augmented material downstream of the feed site is desired, there may be relatively little benefit to increasing discharge beyond some threshold. However, sustained high discharge may contribute to create the desired effect.

The movement of previously trapped sediment downstream of dam removal sites is also of importance to managers who must consider sensitive areas of both ecological importance (e.g., salmon habitat) and municipal interest (e.g., water intake structures). The method of dam removal can affect how this sediment pulse is introduced to the channel. For example, a “blow-and-go” approach, such as on Marmot Dam (*Zunka et al.*, 2015), will introduce the pulse of sediment nearly instantaneously. A stepped dam removal procedure, on the other hand, such as used on Glimes Canyon Dam (*East et al.*, 2015), will incrementally allow bedload to pass the former dam site, analogous to our runs with longer feed times. Our results suggest that for a given pulse mass, longer feed times generally result in a more translation-favored evolution regime. For example, a stepped dam removal strategy will likely prolong the temporal extent of pulse effects, but it will also result in a more dispersive sediment pulse, which may minimize the local effects of the sediment pulse on downstream locations. If rapid movement of the sediment pulse is desired, a faster removal regime may be more appropriate.

Legacy tailings from mining activities may also constitute a sediment pulse (*Ferguson et al.*, 2015; *Knighton*, 1989). Depending on the chemical composition of the tailing material, it may be incredibly important for managers to have an idea of how the pulse will move downstream and potentially affect water quality or ecology in other areas. Other causes of sediment pulse introduction can be uncontrolled introductions of sediment masses due to landslides, bluff collapse, or bank failure (*Benda et al.*, 2003; *Dethier et al.*, 2016; *Gran and Czuba*, 2017; *Nelson and Dubé*, 2016). Being able to predict whether these mass introductions will primarily disperse or translate downstream can help managers and restoration professionals develop a course of action to respond to the abrupt change in material available for fluvial transport.

2.5 Conclusions

In this study we developed a one-dimensional hydro- and morphodynamic model with the ability to retain and update vertical sediment stratigraphy in order to evaluate sediment pulse dynamics under a variety of conditions. We calibrated our model using the flume experiments of *Nelson et al.* (2015) and then used our model to simulate 55 different scenarios with varying pulse mass, timing, and grain size distribution, unsteady flow, and spatial width variations. Our results complement previous numerical (*Cui et al.*, 2008; *Lisle et al.*, 2001), laboratory (*Lisle et al.*, 1997; *Sklar et al.*, 2009; *Venditti et al.*, 2010a), and field studies involving sediment pulses. Our simulations show a trend of more translation with smaller pulse sizes, longer pulse feed times, finer pulse grain sizes, and prolonged higher discharges. Our results suggest that while Froude number and pulse movement are not unrelated, there are other controls that complicate what has sometimes been viewed as a clear relationship. Under certain circumstances pulses under a small range of Froude numbers behave quite differently or pulses under a wide range of Froude numbers behave quite similarly. Based on the parameters we used in our simulation runs, differences in pulse size or composition (grain

size) result in much larger differences in relative translation/dispersion than differences in unsteady flow parameters or channel width variations.

Chapter 3

Numerical simulations on the morphodynamics of variable-width gravel-bed rivers

3.1 Introduction

Natural rivers rarely experience uniform channel width for any appreciable distance downstream. There is often considerable variability in undulations around some mean channel width (*Moody and Troutman*, 2002). Width variations have been observed to influence the locations of bars (*Luchi et al.*, 2010) and channel stability (*Zolezzi et al.*, 2012) in meandering rivers. Variations in channel width have also been connected with suitable habitat regions for both terrestrial and aquatic organisms (e.g., *Hicks et al.*, 1991; *Krapu et al.*, 1984). Morphologically, variations in channel width are often responsible for the location of forced mesoscale bedforms (e.g., riffles and pools) and associated grain size sorting. The importance of width variations in the context of riffles and pools has long been recognized (*Richards*, 1976b) and flow convergence into pools is considered an important component of riffle-pool maintenance (*Harrison and Keller*, 2007; *MacVicar and Roy*, 2007a,b; *MacWilliams et al.*, 2006; *Thompson*, 2001, 2007, 2011; *Thompson and Hoffman*, 2001; *Thompson et al.*, 1998, 1999).

Flume experiments in sediment-supply limited channels have shown that constriction shape affects pool geometry and riffle location (*Thompson*, 2006; *Thompson and McCarrick*, 2010) and that higher flows result in constriction-forced pools with greater depths and lengths (*Thompson*, 2002). Field studies on the Colorado River have shown that width constrictions and expansions, associated with fans at incoming tributary mouths, result in flow separation and recirculating eddies that are important for bar characteristics, with bars forming beneath

recirculation zones (*Kieffer*, 1989; *Rubin et al.*, 1990; *Schmidt*, 1990). Deposition has been found to preferentially occur at locations of flow separation and reattachment and velocities (*Schmidt*, 1990). Related flume experiments by *Schmidt et al.* (1993) suggest that bars and channel irregularities downstream can influence eddy reattachment lengths, and associated bar deposition, upstream.

Physical experiments and numerical models have been used to explore sinusoidal width variations in the context of braided rivers (*Jang*, 2014; *Repetto et al.*, 2002; *Wu and Yeh*, 2005; *Wu et al.*, 2011), channels in extremely confined canyons (*Wohl et al.*, 1999), and in more general contexts (*Bittner*, 1994; *Tsujimoto*, 1987). These studies have all shown that for a channel with continuous, sinusoidal variations in channel width, sediment deposits to form bars coincident with the wider channel sections, while sediment scours out pools coincident with the narrower channel sections. These studies have also shown that greater amplitudes of width variation result in more topographic relief between bars and pools. Flume experiments in variable-width channels have documented the development of side bars (*Bittner*, 1994) or central bars (*Wu and Yeh*, 2005) in the widest sections of the channel, and *Wu et al.* (2011) concluded the amplitude of width variations controls vertical bar amplitude, while the wavenumber of width variations controls the bar mode (central or side). These previous studies with sinusoidally varied width were generally conducted using uniform grain sizes confined to the sand range (but see *Wohl et al.* (1999) who used a sand/clay mixture). There have been no physical experiments or numerical simulations, to our knowledge that consider sinusoidal width constrictions with non-uniform, non-cohesive sediment. Additionally, these studies have all employed steady flow and sediment supply. There remains a knowledge gap in how nonuniform sediment, changes in sediment supply, and unsteady flow interact with width variations and the bedforms they force.

The importance of unsteady flow and, in particular high flow events, on gravel bed fluvial geomorphology is universally recognized (*Baker*, 1977; *Costa and O'Connor*, 1995; *Wolman and Miller*, 1960). Numerical modeling and laboratory studies imposing designed

hydrographs on uniform and nonuniform channels have yielded helpful results in the context of gravel bed rivers. The characteristics and behavior of alternate bars, for example, have been shown to behave differently under varying flow regimes (*Tubino*, 1991). Unsteady flow has been shown to influence how bedload sediment pulses move downstream (*Humphries et al.*, 2012). Flow unsteadiness has also been shown to influence bedload transport rates and grain size sorting (*Bombar et al.*, 2011; *Powell et al.*, 2001). Results from flume experiments by *Ferrer-Boix and Hassan* (2015) suggest that duration of low flow conditions between flood hydrographs plays an important role in the surface sorting and bedload transport rates. Flume experiments by *Wang et al.* (2015) show that for beds composed of sediment of mixed grain diameters the coarser grains had increased transport rates on the rising limb of hydrographs, while finer sediments mobilized more during the falling limb.

Straight walled flume studies using cycled hydrographs suggest that hydrograph shape has little effect on morphodynamic parameters such as bed slope, surface grain size, and overall sediment transport rates (*Mao*, 2012; *Wong and Parker*, 2006). Under repeat discharge hydrographs with constant sediment supply, *Parker et al.* (2007) and *Wong and Parker* (2006) found that at “dynamic equilibrium” conditions, over a hydrograph cycle, changes in bed elevation and sorting patterns were confined to a relatively short reach immediately downstream of the sediment feed point, defined as the “hydrograph boundary layer”. Within the hydrograph boundary layer the elevation, slope, and surface size distribution fluctuate with the hydrograph. However, downstream of the hydrograph boundary layer these parameters adjust until at equilibrium they are invariant to the variable discharge of the repeated hydrographs (*Parker et al.*, 2007). In modeling gravel augmentation schemes for the Trinity river using a 1D model with stratigraphic record-keeping, *Viparelli et al.* (2011) observed a hydrograph boundary layer which responded to higher sediment feed rates by lengthening and extending further downstream. *An et al.* (2017a) found that when the sediment feed is composed of poorly sorted sediment, low amplitude sorting features (bedload sheets) develop and migrate downstream beyond the hydrograph boundary layer. *An et al.* (2017b)

introduced the concept of a “sedimentograph boundary layer”, where a channel subjected to repeated hydrographs and pulsed sediment inputs develops a similar phenomenon in the vicinity of the sediment pulse.

The importance of unsteady flows for the self-maintenance of riffles and pools in the field was first proposed a century ago (*Gilbert*, 1914) and formulated into the “velocity reversal” hypothesis by *Keller* (1971b). Since then the role that varied flow plays in the natural preservation of these mesoscale features has been the topic of many studies. Field studies have shown that at low flows sediment erodes from riffles and deposits in pools, but at high discharge pools erode and riffles aggrade, effectively maintaining the riffle-pool morphology (*Leopold and Wolman*, 1960; *Lisle*, 1979). Morphodynamic modeling by *de Almeida and Rodríguez* (2011, 2012) suggests that unsteady flow may enhance the sorting of grain sizes between riffles and pools, which has also been suggested as an important component of self-maintenance (*Clifford*, 1993; *Hodge et al.*, 2013). The interaction between flow unsteadiness and changes in channel geometry that often accompany riffles and pools, however, remains largely unexplored (but see (*Thompson*, 2002, 2006)).

Although the relationship between sediment supply and morphological features such as bed surface armoring or spatial sorting and alternate bar dynamics has been explored (*Dietrich et al.*, 1989; *Lisle et al.*, 1993; *Nelson et al.*, 2009; *Podolak and Wilcock*, 2013; *Venditti et al.*, 2012), the impact of sediment supply on riffle-pool dynamics is relatively uninvestigated. Sediment supply to a river reach is moderated by many potential factors. Local geology and the degree of continuity between the main channel and its adjacent floodplain and/or hillslopes, as well as upstream reaches, can greatly affect the characteristics (sizes and rates) of sediment that enter the channel. Punctuated sediment supply, resulting in a sediment wave or pulse, can be brought about by both natural and anthropogenic causes (*Benda et al.*, 2003; *Ferguson et al.*, 2015; *Pizzuto*, 2002; *Sutherland et al.*, 2002; *Zinger et al.*, 2011). How channels adjust to and convey sediment pulses has been explored using field (*Aigner et al.*, 2017; *Brummer and Montgomery*, 2006; *Madej*, 2001; *Wohl and Cen-*

derelli, 2000), flume (*Cui et al.*, 2003a; *Humphries et al.*, 2012; *Nelson et al.*, 2015; *Sklar et al.*, 2009; *Venditti et al.*, 2010a), and numerical (*Cui and Parker*, 2005; *Cui et al.*, 2003, 2008; *Lisle et al.*, 2001; *Rathburn and Wohl*, 2003, 2001) methods. However, the systematic exploration of how sediment pulse movement is potentially modulated by channel width variations and their associated forced bedforms has not been studied. In addition to punctuated sediment supplies that result in pulses of sediment waves, channels may experience a consistent increase to sediment supply that is sustained for long periods of time. The removal of a dam, for example, and the restored continuity of sediment supply from reaches upstream of the impoundment can lead to readjustment of downstream reaches. Other changes to environmental conditions, such as those related to climate change, urbanization, or deforestation can also cause sustained increases of sediment supplied to river channels. The effect of these kinds of changes on riffles and pools, particularly those forced by width constrictions, has not been studied in detail.

In this paper we investigate the effects of unsteady flow, changing sediment regimes, and channel width variations on gravel-bed morphodynamics. We use two-dimensional morphodynamic simulations to systematically explore how straight channels with downstream width variations respond to conditions of steady/unsteady flow and changes to sediment supply, including a sediment pulse. We are mainly interested in how width variations affect equilibrium channel morphology with and without sediment supply, manifested in parameters such as bar configuration, surface sorting patterns, and relief between pools and bars. We also seek to better understand sediment pulse dynamics relative to how their evolution is moderated by different degrees of downstream channel width variability. We also are interested in addressing the combined effects of unsteady flow on dynamic equilibrium conditions in variable-width channels, under different sediment supply conditions.

3.2 Methods

3.2.1 Numerical model

We investigated the effect of variable-width geometries using the open source, non-linear Delft3D model (*Deltires*, 2014). Although Delft3D is capable of solving the three-dimensional Navier Stokes equations for an incompressible fluid, under the shallow water and Boussinesq assumptions (*Deltires*, 2014), our use of the model implements a finite difference scheme to solve the depth-averaged momentum and continuity (shallow water) equations. Spiraling flow is parameterized using the methods introduced by *Struiksma et al.* (1985). Bedload sediment transport was simulated using the fractional *Wilcock and Crowe* (2003) transport model, which is well suited for the sand-gravel mixtures we use in this study. Bed elevations and morphology are dynamically updated by conserving the sediment mass and converting the specified dry bed density and sediment fractions into a bed level change (*Deltires*, 2014). Delft3D also has the ability to implement a layered bed stratigraphy, whereby a bookkeeping procedure is used to track the sediment fractions as they are deposited and subsequently eroded to simulate the vertical composition of grain size sorting. We decided to utilize this tool as stratigraphic feedbacks on bedload and surficial sorting are important for mixed-grain compositions, especially in the presence of bedforms subject to changing sediment regimes (*Bankert and Nelson*, 2017; *Brown*, 2017).

Two-dimensional, depth-averaged hydro- and/or morphodynamic models have been successfully used to simulate flow and morphology in variable-width channels (*Bittner*, 1994; *Repetto et al.*, 2002; *Wohl et al.*, 1999; *Wu and Yeh*, 2005; *Wu et al.*, 2011). While the detail provided by a fully 3D model would better resolve both the horizontal and vertical convergence/divergence of flow associated undulations in width and topography (*Repetto et al.*, 2002), the computational expense required by such a model is prohibitive. However, there is a significant advantage of depth-averaged modeling over more simplified one-dimensional models (e.g., Chapter 2), as the ability to account for the effects of width variation on the horizontal flow field is important for the calculation of cross-stream velocity, shear stress, and

bedload transport. Furthermore, *Wu and Yeh* (2005) found that morphodynamic modeling with the inclusion of helical flow greatly improved topographic results when compared with flume experiments. *Duró et al.* (2016) showed good agreement between a depth-averaged Delft3D model, which included spiraling flow, and experimental results of a variable-width channel from *Wu and Yeh* (2005).

3.2.2 Numerical geometry set-up

In order to explore the effect of downstream width-variations on gravel-bed morphodynamics under different flow and sediment supply conditions, we considered seventeen different channel geometries (one straight, sixteen variable-width), described by:

$$B(x) = B_0 [1 + A_c \sin(\lambda_c x / B_0)] \quad (3.1)$$

where $B(x)$ is the local channel half-width at downstream distance x , B_0 is the mean channel half-width, A_c is the dimensionless wave amplitude of width variations, and λ_c is the dimensionless wavenumber of width variations (see Figure 3.1). The dimensionless wavenumber (λ_c) is related to the dimensional wavelength (L_c) as $\lambda_c = 2\pi B_0 L_c^{-1}$. Each of the seventeen geometries was numbered (00 through 16), with 00 corresponding to a constant width channel. For all geometries the mean channel half-width was specified as $B_0 = 0.435$ m to correspond with associated flume experiments (Chapter 4). Geometries 01 through 16 were generated by simultaneously varying the dimensionless amplitude of width variations ($A_c = [0.1, 0.2, 0.3, 0.4]$) and the dimensionless wavenumber of width variations ($\lambda_c = [0.2, 0.4, 0.6, 0.8]$). In reference to the natural spacing of riffles and pools (5–7 channel widths) the general range of wavenumbers of width variation would be 0.45–0.62. Amplitudes of width variation for riffle-pool rivers are generally 0.07–0.14, however width differences that correspond to values as high as 0.33–0.43 have been reported (*Brew et al.*, 2015; *Brown and Pasternack*, 2017; *Wilkinson et al.*, 2004).

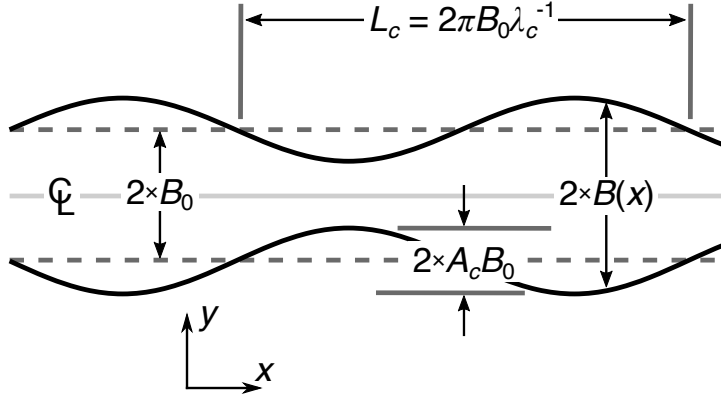


Figure 3.1: General planform geometry of a channel with sinusoidal width variations.

Each variable-width channel geometry was defined to have a width as described above and a length equal to six wavelengths of width variation for that geometry. The first and last wavelengths correspond to entrance and exit reaches with a constant width equal to the mean channel width ($B_0 = 0.435$ m). A channel-fitted quadrilateral mesh was constructed for each geometry with 16 grid cells in the cross-stream direction and a downstream spacing of 5.4 cm, resulting in generally square-shaped grids cells ($dy \approx dx = 5.4$ cm).

3.2.3 Numerical run procedure

Our computational strategy was composed of ten series of runs labeled A through J, summarized in Figure 3.2. The first three series (A–C), involving steady water discharge, included all of the channel geometries, while the others series (D–J), involving unsteady water discharge, included only three channel geometries (00, 10, and 16). All Series were run for 100 simulated hours with the exception of Series C which was run for 24 simulated hours. In all cases this duration was sufficient to achieve quasi-steady conditions defined as an unchanging bed slope and surface grain size distribution. Series A constitutes a sort of control series with steady flow ($Q_{bf} = 65$ ℓ/s) and steady “equilibrium” sediment supply ($Q_{se} = 9.94 \times 10^{-6}$ m³/s = 1580 g/min). The initial conditions for Series A for each geometry consists of a planar bed with a constant slope of $S_0 = 0.007$. Water and sediment feed rates

were chosen to maintain a bed slope of approximately 0.007, which is typical of gravel-bed rivers exhibiting riffle-pool sequences (*Brew et al.*, 2015). The bed was initialized to have a bed material composed of a bulk sediment size distribution of coarse sand to medium gravel (Figure 3.3(a), $D_{50} = 4.58$ mm, $D_g = 4.11$ mm, $\sigma_g = 2.04$ mm). This distribution was chosen to match available sediment used for complementary flume experiments (Chapter 4). The equilibrium sediment feed Q_{se} was also composed of the bulk sediment distribution. Initial conditions for the other series were dependent on final conditions of a previous series. The order path of this dependence is shown with arrows in Figure 3.2. Series B has as its initial conditions the final conditions of Series A and is also subject to steady water discharge (Q_{bf}). In contrast with Series A, Series B has no sediment supply and is meant to simulate the installation of a dam or some other obstruction that disrupts downstream sediment continuity. Series C, subject also to Q_{bf} , consists of a sediment pulse and represents sediment augmentation, dam removal, or some other event that provides a large, temporary influx of sediment to the upstream boundary. The sediment pulse has a total volume of 0.296 m^3 and is fed over a simulated period of 124 minutes. The pulse is composed of a more uniform and slightly finer distribution than the bulk sediment (Figure 3.3(a), $D_{50} = 4$ mm, $D_g = 4$ mm, $\sigma_g = 1$ mm), but with a similar median grain diameter (D_{50}). The pulse mass was calculated to be the average volume of sediment required to fill the pools that exist at the channel constrictions in the final conditions of Series B. The pulse feed rate ($Q_{sp} = 3.98 \times 10^{-5} \text{ m}^3/\text{s} = 6321 \text{ g/min}$) was calculated to be 4 times the “equilibrium” feed rate (*Nelson et al.*, 2015). Once the pulse feed ended, no bedload material was supplied to the upstream boundary. The run time for Series C (24 hours) was sufficient for the pulse to begin exiting the spatial domain.

Series D–J only include three geometries (00, 10, and 16) and involve unsteady water discharge. For Series D–G the three geometries were subjected to four different repeat discharge hydrographs (numbered 1–4, respectively, see Figure 3.3(b)). Each of the hydrographs has as its mean flow the steady discharge of $Q_{bf} = 65 \ell/\text{s}$. In all four series the initial conditions

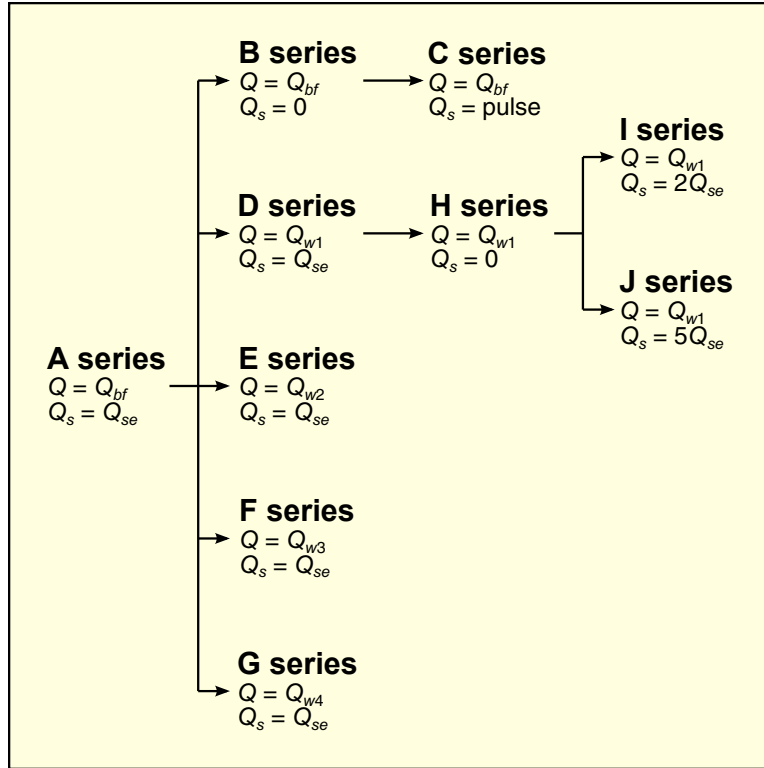


Figure 3.2: Order of series runs, indicating which series' final conditions correspond to which series' initial conditions.

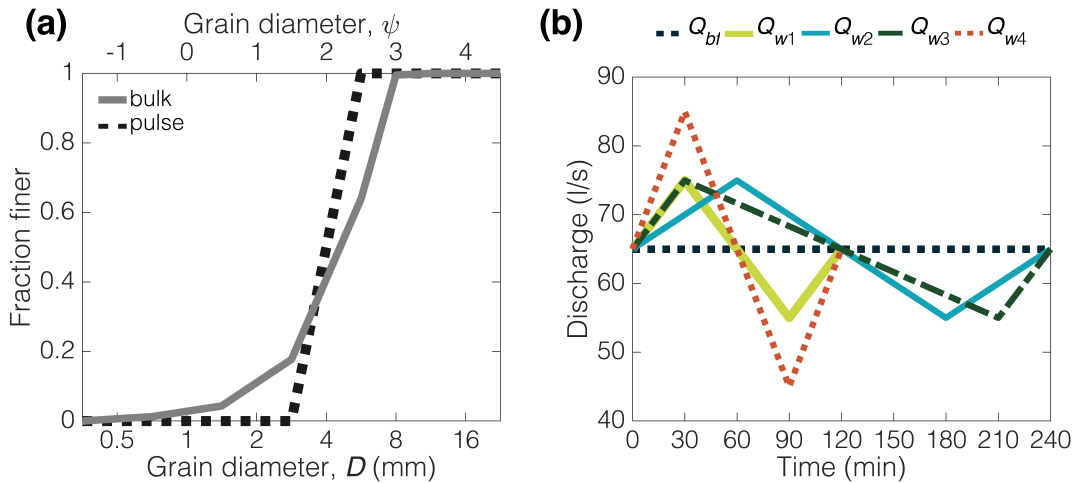


Figure 3.3: (a) Grain size distributions used in the numerical procedure. (b) Steady flow discharge and cycled hydrographs used in unsteady flow series.

correspond to the final conditions of Series A and sediment supply continues as Q_{se} . The hydrograph for Series D (Q_{w1}) varied linearly from 55 ℓ/s to 75 ℓ/s and back again over a symmetrical period of 120 minutes. For Series E the cycled hydrographs (Q_{w2}) had the same amplitude as in Q_{w1} , but a period of 240 minutes. Series F hydrographs (Q_{w3}) also had the same amplitude, but was asymmetric with the rising limb of the hydrographs lasting 60 minutes and the falling limb 180 minutes. Q_{w4} , used in Series G, was a symmetric hydrograph with a period of 120 minutes, but with an increased amplitude, varying linearly between 45 ℓ/s and 85 ℓ/s . Series H–J represent set of a series simulating sediment supply removal and reintroduction at a higher rate. The initial conditions of Series H are the final conditions of Series D. In Series H, repeat Q_{w1} hydrographs continue, but no sediment is supplied to the upstream boundary. Series I and J both have the final conditions of Series H as their initial conditions and continue the same cycled hydrograph pattern but with sediment supply reinstated at elevated rates of $2 \times Q_{se}$ and $5 \times Q_{se}$, respectively.

3.3 Results

3.3.1 Steady flow series: A–C

In Series A each geometry was subjected to steady water discharge ($Q_{bf} = 65 \ell/\text{s}$) and constant sediment supply ($Q_{se} = 1580 \text{ kg/min}$) for 100 simulated hours. Mean downstream bed slopes varied from 0.0069 to 0.0081 (Table 3.1). Higher bed slopes corresponded to increased width-variation amplitude and increased width-variation wavenumber (decreased wavelength). Predictably, accelerating flow into width constrictions created forced scour holes (pools) at or near the narrowest part of the channels. Conversely, decelerating flow associated with divergence at width expansions resulted in local topographic highs (bars or riffles) at or near the widest channel sections. Bed elevations can be detrended by subtracting the average downstream slope, calculating a deviation from the mean bed elevation (Figure 3.4). In general, detrended elevation maps for Series A in Figure 3.4 show side bars occurring in geometries with higher wavenumbers and central bars in geometries with lower

Table 3.1: General results from Series A, B, and C. S_0 = mean downstream bed slope; Bar mode C = central bars; Bar mode S = side bars; I_d = pulse dispersion index

		Series A			Series B			Series C
A_c	λ_c	S_0	Relief (m)	Bar mode	S_0	Relief (m)	Bar mode	I_d
00	0	—	0.0072	—	0.0041	—	—	1.11
01	0.1	0.2	0.0069	0.018	C	0.0058	0.019	C
02	0.1	0.4	0.0072	0.018	C	0.0050	0.019	C
03	0.1	0.6	0.0073	0.017	S	0.0045	0.019	S
04	0.1	0.8	0.0073	0.017	S	0.0041	0.020	S
05	0.2	0.2	0.0069	0.037	C	0.0059	0.038	C
06	0.2	0.4	0.0073	0.036	C	0.0051	0.039	C
07	0.2	0.6	0.0074	0.036	S	0.0046	0.040	S
08	0.2	0.8	0.0075	0.036	S	0.0042	0.040	S
09	0.3	0.2	0.0070	0.058	C	0.0059	0.060	C
10	0.3	0.4	0.0074	0.057	C	0.0052	0.061	C
11	0.3	0.6	0.0076	0.056	S	0.0048	0.062	S
12	0.3	0.8	0.0078	0.056	S	0.0045	0.063	S
13	0.4	0.2	0.0070	0.082	C	0.0060	0.084	C
14	0.4	0.4	0.0076	0.080	C	0.0054	0.086	C
15	0.4	0.6	0.0079	0.079	S	0.0050	0.088	S
16	0.4	0.8	0.0081	0.079	S	0.0047	0.089	S
								0.93

wavenumbers. Riffle-pool relief, calculated by differencing the maximum and minimum cross-sectional averaged detrended elevations averaged onto a single wavelength, show increased values for higher width-variation amplitudes. For a given amplitude relief decreases slightly with increasing wavenumber (Table 3.1). Figure 3.5 shows average downstream profiles over a wavelength of the cross-sectionally averaged deviation from mean bed elevation as well as cross-sectional- and depth-averaged velocity values. In every case the pools are farther from the mean bed than bars (i.e., bars are longer, pools are deeper). For Series A both relative elevation profiles and velocity profiles remain relatively close for geometries of the same amplitude. Although slight spatial patterns of grain size sorting developed, the magnitudes of differences were < 1 mm, and were deemed negligible. Overall the channels had an average D_{50} of 6.7 mm (approximately 2 mm coarser than the original bed material and bulk feed).

In Series B, the steady flow (Q_{bf}) continued from Series A, but the sediment supply was terminated ($Q_{se} = 0$). In general this resulted in degradation of the bed and lowering of the average downstream bed slope (Table 3.1). Average slopes varied from 0.0041 to 0.0060, with

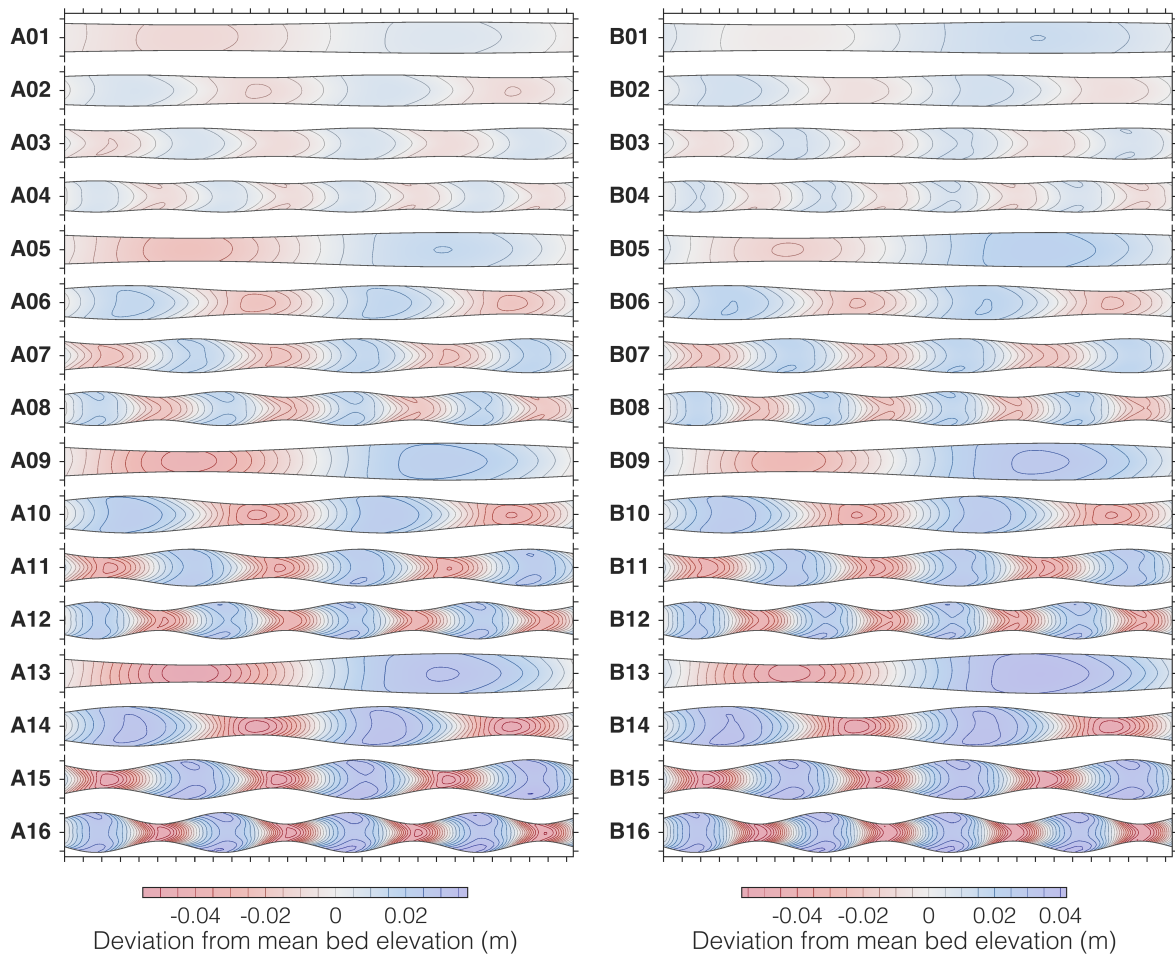


Figure 3.4: Detrended elevation maps for Series A (equilibrium sediment supply) and Series B (no sediment supply) variable-width geometries. All axes are drawn to scale with tick marks every 0.5 m. Contours are in 0.5 cm increments. Flow is from left to right.

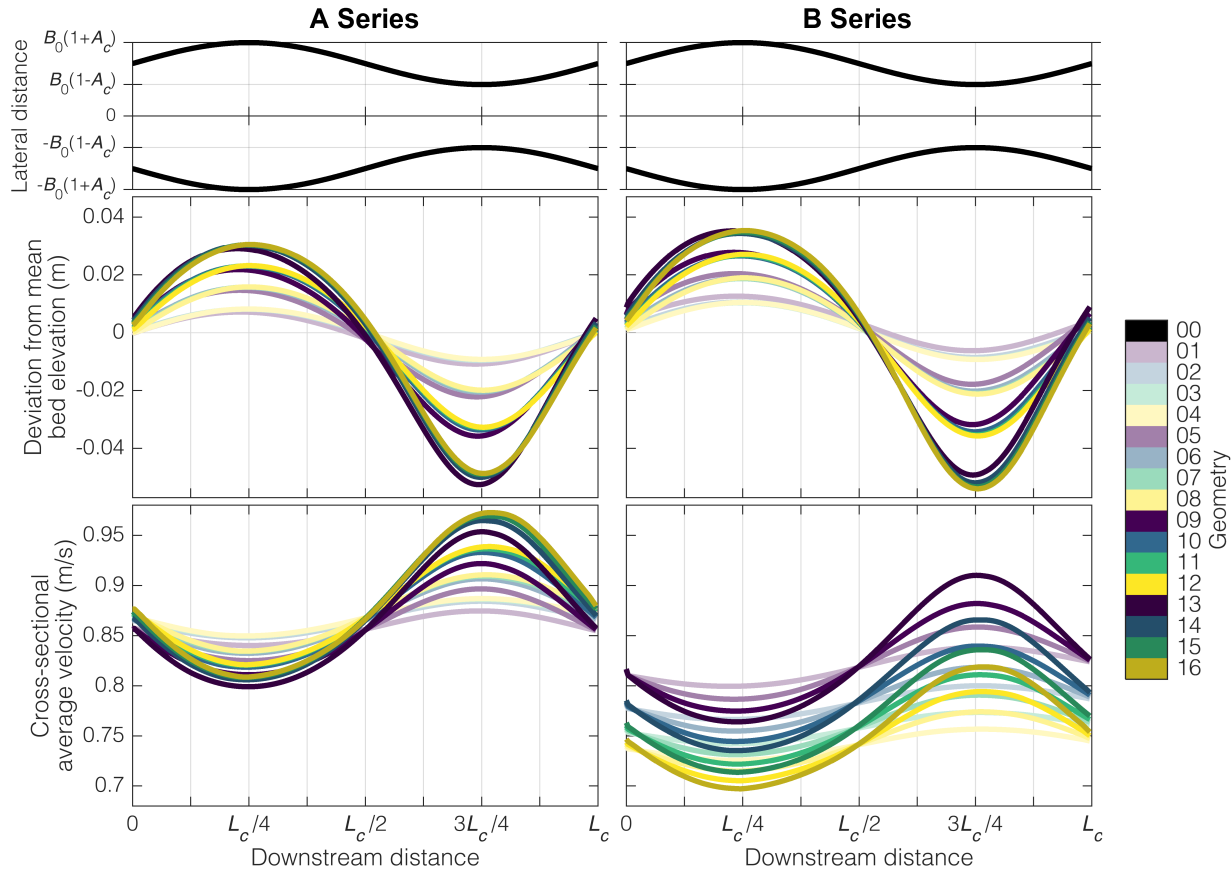


Figure 3.5: Detrended elevation and velocity profiles for A Series (equilibrium sediment supply) and B Series (no sediment supply) variable-width geometries. Color is constant per wavenumber and opacity increases with amplitude of width variations. Flow is from left to right.

increasing slopes again associated with increasing amplitude of width-variations. However, the relationship of slope and wavenumber reversed from Series A. Here, steeper slopes are associated with lower wavenumbers (longer wavelengths) of width-variations. Relief between low and high topography associated with adjacent channel constrictions and expansions increased from Series A. Once again greater riffle-pool relief occurs at higher amplitudes of width-variation, but in Series B there are slight decreases in relief values with increased wavenumber (Figure 3.5). Equilibrium velocities for Series B show strong stratification according to the wavenumber of width variations. While in Series A the “hinge point” (where the profile crosses over the 0 and $L_c/2$ points on the x-axis) for each of the geometries falls around the same value, regardless of amplitude or wavenumber, for Series B the crossing point velocities are arranged with increasing velocities clearly associated with lower wavenumber (longer wavelengths). Again, grain size differences on the surface are not of meaningful magnitudes. From Series A to Series B the overall bed median grain diameter coarsened approximately 0.1–0.5 mm.

In Series C the “sediment starved” conditions resulting from Series B were fed a sediment pulse. Pulse movement was quantified using the pulse dispersion index of Chapter 2 (similar also to *Sklar et al. (2009)*). The pulse dispersion index (I_d) is a measure of the relative pulse dispersion to pulse translation. It is essentially a measure of the rate of growth of the inter-quartile range of the cumulative elevation differences between the pulse topography and antecedent bed topography divided by the rate of movement of the median of the cumulative elevation differences between the pulse elevations and the original surface. Higher values of I_d correspond to a higher degree of dispersion relative to translation. The pulse dispersion index can be calculated either as an “instantaneous” value using each time step incrementally or an average value can be calculated using all time steps. Average pulse dispersion indices are shown in Table 3.1 and range from 0.93 to 1.23. These average values are graphically shown in Figure 3.6(a) and instantaneous values are shown in Figure 3.6(b). Instantaneous pulse dispersion indices show a relatively high degree of variability for most of the indices

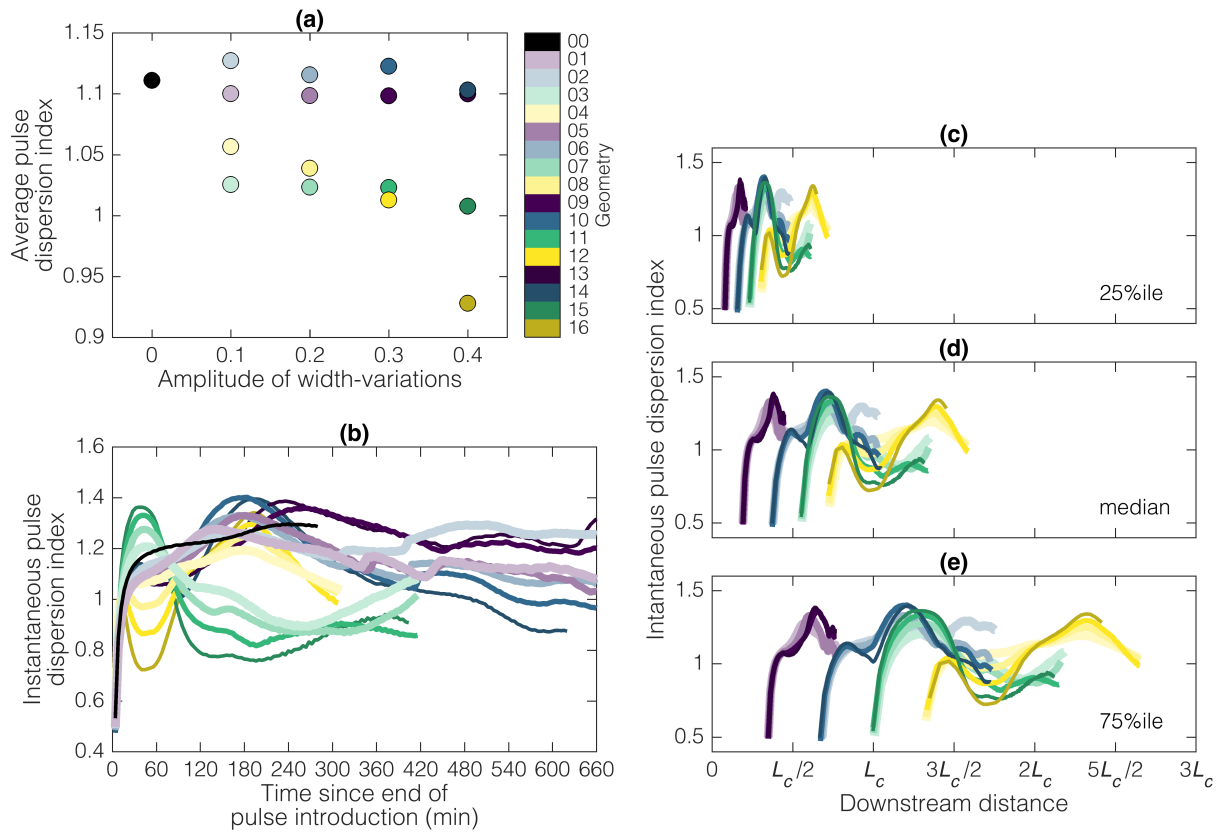


Figure 3.6: (a) Average pulse dispersion indices versus dimensional amplitude of width variations for C Series runs. (b) Instantaneous pulse dispersion index versus time since end of pulse feed. (c–e) Instantaneous pulse dispersion index versus 25th, 50th, and 75th percentiles of the cumulative elevation difference profile, respectively.

other than that for the straight-walled channel. Each curve in Figure 3.6(b) starts with a relatively low degree of dispersion. As time progresses, each dispersion index curve rises rapidly and then appears to become more consistent, although fluctuations remain for the variable-width geometries. Figure 3.6(c–e) shows the instantaneous pulse dispersion index plotted against the locations of the 25th percentile, median, and 75th percentile of cumulative elevation difference between the instantaneous pulse location and the initial pre-pulse bed for each variable width geometry.

3.3.2 Unsteady flow series: D–J

Unsteady flow Series D–G involved four different cycled hydrographs with varying amplitudes and periods. For Series D hydrograph Q_{w1} (Figure 3.3) was routed through geometries 00, 10, and 16 with constant, equilibrium sediment supply Q_{se} . At equilibrium, even over the changing discharge, slopes were practically constant, varying only from 0.0071, 0.0074, and 0.0080 near the peak of the hydrograph to 0.0072, 0.0074, and 0.0081 at the trough of the hydrograph for geometries 00, 10, and 16, respectively. Average bedslopes throughout the hydrograph cycle also did not substantially change from the steady flow results from Series A (cf. Table 3.1 and Table 3.2). Average riffle-pool relief was also equivalent to that under steady flow conditions; however, the time-series of riffle-pool relief shows variations around the average with peaks and troughs shortly lagging behind peaks and troughs in the discharge hydrograph (Figure 3.7). The average slopes and riffle-pool relief in Series E and F were similar to those of Series D (Table 3.2). Again, minimum and maximum slopes remained relatively constant throughout the hydrograph period. Time-series values of riffle-pool relief are shown also in Figure 3.7, with fluctuations lagging shortly behind hydrograph extrema. For Series D–F the average slopes and riffle-pool reliefs did not change substantially from the corresponding geometries in Series A and the minima and maxima of riffle pool relief also remained the same, undulating with discharge. In Figure 3.7, there is a slightly longer lag time for the lower wavenumber geometry (10) than for the geometry with higher wavenumber (16). Series G, which involved the routing of repeat hydgraphs of twice the magnitude of the other unsteady flow runs, shows an overall slight decrease in both time-averaged bed slope and a slight increase in time-averaged riffle-pool relief (Table 3.2). Time-series values for riffle-pool relief show greater deviations from the mean than the other unsteady flow series (Figure 3.7). For Series D–G the bar configurations that developed in the corresponding geometries in Series A persisted and did not change throughout the hydrographs.

Table 3.2: General results from unsteady flow Series D–J. S_0 = mean downstream bed slope; Bar mode C = central bars; Bar mode S = side bars. Slopes and reliefs are all averaged over a complete hydrograph period.

Series	00	10			16		
	S_0	S_0	Relief (m)	Bar mode	S_0	Relief (m)	Bar mode
D	0.0071	0.0074	0.057	C	0.0081	0.079	S
E	0.0071	0.0074	0.057	C	0.0081	0.079	S
F	0.0071	0.0074	0.057	C	0.0081	0.079	S
G	0.0068	0.0071	0.058	C	0.0077	0.080	S
H	0.0035	0.0047	0.065	C	0.0042	0.099	S
I	0.0085	0.0085	0.056	C	0.0096	0.077	S
J	0.0114	0.0115	0.054	C	0.0128	0.075	S

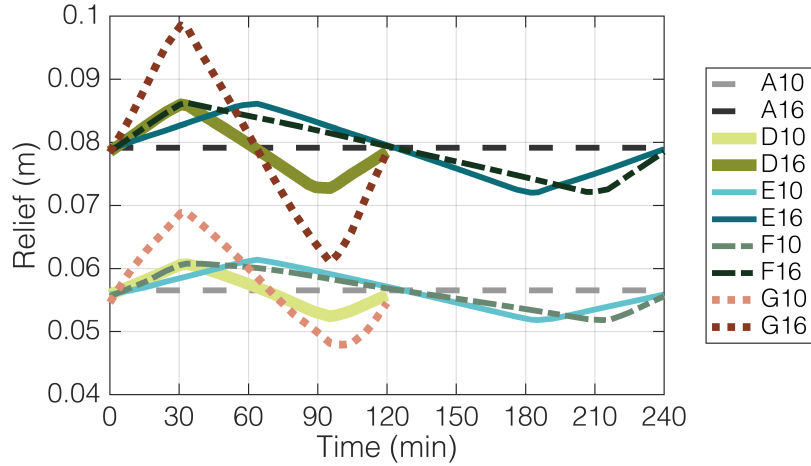


Figure 3.7: Differences between the maximum and minimum cross-sectional average detrended elevations for unsteady flow Series D–G.

Series H–J continued from Series D results with runs consisting of no sediment supply, $2 \times Q_{se}$ and $5 \times Q_{se}$, respectively. Table 3.2 also shows average downstream slope, riffle-pool relief, and bar mode for these series. In Series H, with no sediment supply, channel slopes reduced slightly while riffle-pool relief slightly increased. However, the magnitudes of these changes were not as dramatic as those that occurred for some geometries from Series A to B. Geometries 00 and 16 for Series B, which also consisted of no sediment feed, show steeper slopes and milder amplitudes than for the unsteady flow Series H. In Series I sediment supply was reinstated at a rate of $2 \times Q_{se}$. The beds steepened again, to higher grades than were originally present during equilibrium supply in Series D. Riffle-pool relief declined, but only slightly lower than in Series D. In Series J ($5 \times Q_{se}$) the slope increased and the riffle-pool relief decreased, but once again, only slightly. In this series the increased sediment supply, coupled with unsteady flow, created a constant migrating chain of low-relief, short-wavelength bedforms for each geometry. Bedform wavelength was calculated as the mean of the peak-to-peak and trough-to-trough distances. Amplitude was calculated as the mean of the elevation differences between adjacent peaks and troughs. For the straight-walled geometry (00) the bedform geometry remained relatively consistent in the downstream direction. For both variable-width channels (10 and 16) bedforms migrated through channel expansions, became suppressed in width constrictions, and re-emerged as the width increased again. Reach-average wavelengths and amplitudes of bedforms over a complete hydrograph period are shown in Figure 3.8.

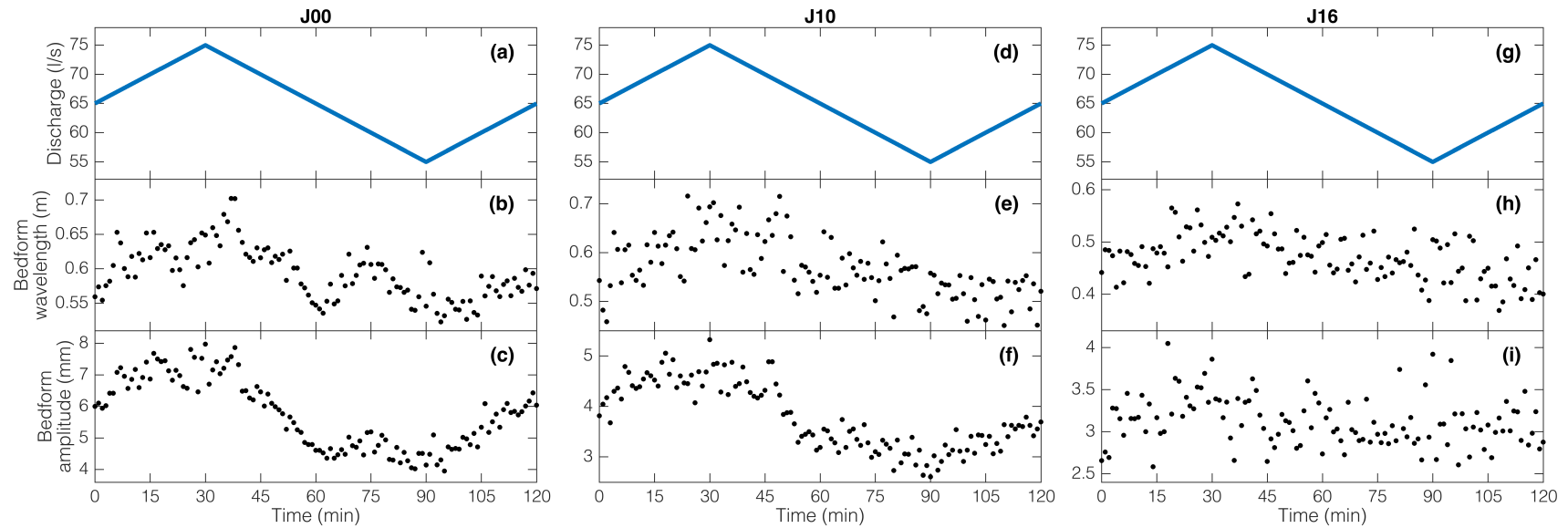


Figure 3.8: Times series of bedform characteristics for J Series runs.

Throughout these unsteady flow series the type of bars that formed (central or side) remained consistent, regardless of discharge or sediment supply. Additionally, although there were slight increases in the magnitude of the degree of sorting between low flows and high flows during the cycled hydrographs (and between hydrographs with lower amplitudes and higher), as with the steady flow series, the overall magnitude is small enough (< 1 mm) to be considered practically negligible.

3.4 Discussion

3.4.1 Morphology of variable-width channels

Along with others who have used physical experiments and numerical models to explore equilibrium conditions for variable-width channels (*Bittner, 1994; Repetto et al., 2002; Wu and Yeh, 2005; Wu et al., 2011*), our results show bed undulations coincident with width variations and the development of either central or side bars in the channel expansions. In the absence of an artificial perturbation, all bedforms were stationary and forced by the geometry (*Wu et al., 2011*). In agreement with *Wu and Yeh (2005)*, the wavenumber of width variations (λ_c) seems to exert the primary control on whether central or side bars develop. This especially becomes evident when bar configurations of Series A are compared with Series B. Although the two series have differences in average channel slope and cross-sectional average velocity the same bar configurations exist for a given geometry. It has been suggested that width-to-depth ratio is a principal variable controlling the bar mode (*Repetto et al., 2002; Wu and Yeh, 2005*). However, our results show a wide range of width-to-depth ratios for a given geometry without any changes in the bar mode. For example, geometry 10 has width-to-depth ratios that range from 8.1 (B10) to 18.9 (G10) but never develops side bars. Geometry 16 has width-to-depth ratios from 9.2 (B16) to 22.0 (G16), but side bars never give way to a central bar. Even under the same flow conditions (e.g., Series A), the width-to-depth ratios for geometries of a given amplitude remain relatively constant, yet the shorter wavelength geometries show central bars while the longer wavelength geometries

show side bars. These results may suggest that the differing degrees of secondary flow associated with different variable-width geometries may be a more important factor than width-to-depth ratio in the formation of central versus side bars.

Overall, varying degrees of width undulations seem to have a minor effect on reach-average morphology under steady flow, equilibrium conditions. Although there are differences in riffle-pool relief values for different amplitudes in Series A, average downstream slopes are not considerably different, varying only between 0.0069 and 0.0081. In Series A lower amplitude width variations are generally closer in slope to the straight-walled run. The higher slopes that develop in geometries with greater amplitudes and wavenumbers are likely due to a number of factors. Increasing wavenumbers correspond to shorter wavelengths, which decrease the length available to the channel for adjustment to the varied flow. With longer wavelengths the flow is able to follow the geometry of the channel more closely and distribute laterally. Shorter wavelengths effectively keep the flow concentrated along the middle part of the channel from constriction to constriction. A more extreme example of the same process would be through a series of abrupt channel expansions and constrictions, whereas our variations in channel width are smooth and relatively gradual. The associated relatively lower velocities and shear stress at the channel edges in width expansions is likely what drives the development of side bars for these geometries. The side bars, by elevating channel margins and deflecting flow back to the centerline of the channel, feedback into this same process.

Greater differences arise in Series B and, interestingly, the pattern is reversed. Table 3.1 shows that for a given amplitude of width variations, under conditions of no sediment supply, shorter wavelengths tend to create channels that have milder slope. Although, as we have mentioned, degrees of grain size sorting are very small in magnitude, we hypothesize that organization of coarser grains (and associated armoring, even if minor) on the bar tops may contribute to this pattern. Although the magnitude remains very weak it may be sufficient to reduce the erosive capacity on the bars. Additionally, Figure 3.5 shows clear differences in cross-sectional average velocity profiles between the A and B Series. In the

A Series it is channels with shorter wavelengths that experience across the board greater average velocities. In Series B that pattern is reversed and becomes much more dramatic.

3.4.2 Sediment pulses and bedforms in variable width channels

Although numerical models have been used to explore the evolution of sediment pulses (*Cui and Parker, 2005; Cui et al., 2003*) and some have even looked at pulse movement in irregularly shaped artificial channels (*Cui et al., 2008*) or in natural topography (*Ferguson et al., 2015*), there has been relatively little work systematically considering how channel geometry modulates pulse evolution (but see Chapter 2). *Nelson et al. (2015)* suggested that sinusoidal width variations serve to increase sediment pulse dispersion, but our depth-averaged modeling results here suggest that for even dramatic width variations (both in wavenumber and amplitude) there is relatively little increase to the pulse dispersion index in the presence of width-variations, and sometimes decreased dispersion is experienced. There are a number of factors, however, that complicate our treatment of pulse evolution. Firstly, because of the differences in the geometries, the “initial” pulse distribution (the distribution at the instant the pulse feed ended) had potentially different relative locations in each channel. For example, in Figure 3.6(c–e) the beginning point of the curves falls on four distinct locations per plot, depending on the wavenumber of width variations. Nevertheless, when considering the downstream location of the 75th percentile of the cumulative elevation difference (Figure 3.6(e)) there appears to be a pattern where the curves overlap. The 75th percentile of the cumulative elevation difference can serve as a sort of proxy for the pulse front location. As the pulse front moves through from L_c to $3L_c/2$, which constitutes a channel expansion (bar or riffle), the pulses show increased rates of dispersion relative to translation. Conversely, from $3L_c/2$ to $2L_c$, which is a channel constriction (pool), the pulse dispersion indices decrease, indicating a higher degree of translation. This indicates that under steady flow conditions bars or riffles serve as locations of temporary sediment storage as a sediment pulse moves downstream. *Wu et al. (2011)* found that the celerity

of migrating bedforms reduced as they moved through channel constrictions, indicating a reduction in translation. Field studies of sediment pulses in channels with bedforms (forced and free) generally show pools filling with sediment (i.e., sediment storage) and riffles with more translative conveyance (sometimes even net degradation) (e.g., *Madej*, 2001). As with the flume experiment reported by *Nelson et al.* (2015), this discrepancy is likely due to at least two factors: the need for a wider range of sediment sizes (particularly finer material in the pulse) and steady flow versus unsteady flow. It is hypothesized that periods of relatively low flow are important for observing pool filling by sediment pulses. Although, even in the beginning of the runs for Series I and J, when amplified sediment feed rates were supplied to sediment starved channels under unsteady water discharge, pools never filled. As the wedge of sediment making up the increased supply propagates downstream, riffle-pool relief is reduced first and remains consistent as the overall channel slope steepens. Our results on pulse movement, which show relatively little differences between pulse dispersion indices for a wide range of variable-width configurations, in agreement with Chapter 2, corroborate the conclusions of *Cui et al.* (2008), that one-dimensional numerical models can relatively accurately represent reach-averaged pulse movement. However, for natural channels, which are likely to exhibit a much greater degree of irregularity in channel width and topography, a one-dimensional model may not perform as well as a multi-dimensional approach. Indeed, even a two-dimensional approach may be insufficient to capture pulse dynamics in a natural system with more complex geometric boundaries (overhanging banks, banks with protruding roots, large wood, etc.) that would likely have a large influence on the flow field both laterally and vertically.

The bedforms that developed in each of the geometries of Series J spanned the entire channel width and were symmetrical. Their relatively short wavelength, and especially their low amplitude ($< 2 \times D_{84}$) may suggest that they are bedload sheets (*Qin et al.*, 2015). However, bedload sheets, or free patches, are usually defined by their spatial sorting pattern, which is not present here. Additionally, there appears to be a strong hydraulic

dependence on the bedform characteristics (Figure 3.8), which may be more indicative of gravel dunes. Nevertheless, for the straight-walled geometry, both bedform length and height (Figure 3.8(b and c)), follow closely with discharge, which is consistent with known dune dynamics (*Wijbenga and Klaassen*, 1983). Bedform characteristics in the variable width channels show similar trends, although to a lesser degree. This is especially true for J16 where a temporal trend is difficult to discern. In both variable width cases the wavelength and amplitude of bedforms are decreased from the straight-walled geometry. In J16 the bedforms are roughly half the amplitude as in J00. These results are in agreement with the results of *Wu et al.* (2011), mentioned also above, who reported that higher amplitudes of width variation decreased bar height, and to a lesser extent, bar length. Our results indicate that the dependence of bedform characteristics on flow (namely, discharge and flow depth) is also suppressed with more dramatic variations in channel width. *Wu et al.* (2011) also reports that bedform height peaked and length minimized at the channel constrictions. Their bedforms were never fully suppressed, but our results show suppression through, and then re-emergence after, channel constrictions, for both geometries modeled.

3.4.3 Effects of unsteady flow on the morphodynamics of variable-width channels

In straight channels, experiments with unsteady flow have found that the shape and duration of hydrographs does not generally have a strong influence on reach-scale parameters (*Humphries et al.*, 2012; *Mao*, 2012; *Wong and Parker*, 2006). In the case of hydrographs with periods of low flow between them, however, the duration of those periods can have a significant effect on sorting patterns (*Ferrer-Boix and Hassan*, 2015). Our results also show relative invariance of reach-scale average channel parameters to hydrograph characteristics. Although the values for both slope and riffle-pool relief are slightly different for Series G (where hydrograph maxima are twice as far from mean), the differences are small.

In the case of cycled hydrographs of durations shorter than typical scales for morphodynamic adjustments the local bedload flux quickly compensates for the changing discharge preventing excessive elevation changes or grain size sorting. Researchers examining cycled hydrographs with constant sediment supply have identified a length of channel extending downstream from the upper boundary within which aggradation and scour associated with disequilibrium are confined (*Parker et al.*, 2007; *Wong and Parker*, 2006). Downstream of this so-called “hydrograph boundary layer”, changes in discharge are entirely accommodated by changes in the rate and size distribution of the bedload material while the bed itself remains unchanged. Within the hydrograph boundary layer, however, the bed conditions fluctuate with the instantaneous discharge of the hydrograph. At higher discharges the bed erodes and becomes coarser near the upstream boundary, and at lower discharges the bed aggrades and becomes finer.

Our results confirm some of the general findings regarding the hydrograph boundary layer. Figures 3.9 and 3.10 show elevation profiles for the unsteady flow series with the hydrograph-averaged elevations subtracted. For the straight-walled runs under different discharge hydrographs (D00–G00, Figure 3.9), patterns emerge that corroborate flume experiments and one-dimensional modeling by *Wong and Parker* (2006) and *Parker et al.* (2007). A hydrograph boundary layer is especially evident for D00 where beyond ~10 m no changes occur. Fluctuations in the downstream-most area are likely an artifact of the downstream boundary (*Viparelli et al.*, 2011). The elevation profiles for both E00 and F00 (which have hydrograph durations of 240 minutes rather than 120) show a longer hydrograph boundary layer, practically extending to the downstream boundary of the domain (*Parker et al.*, 2007). Similarly, for G00, the morphological influence of the hydrographs is greatly reduced beyond ~12 m. For a longer spatial domain the effect would be clearer as there would be more length between the hydrograph boundary layer and the downstream boundary artifacts.

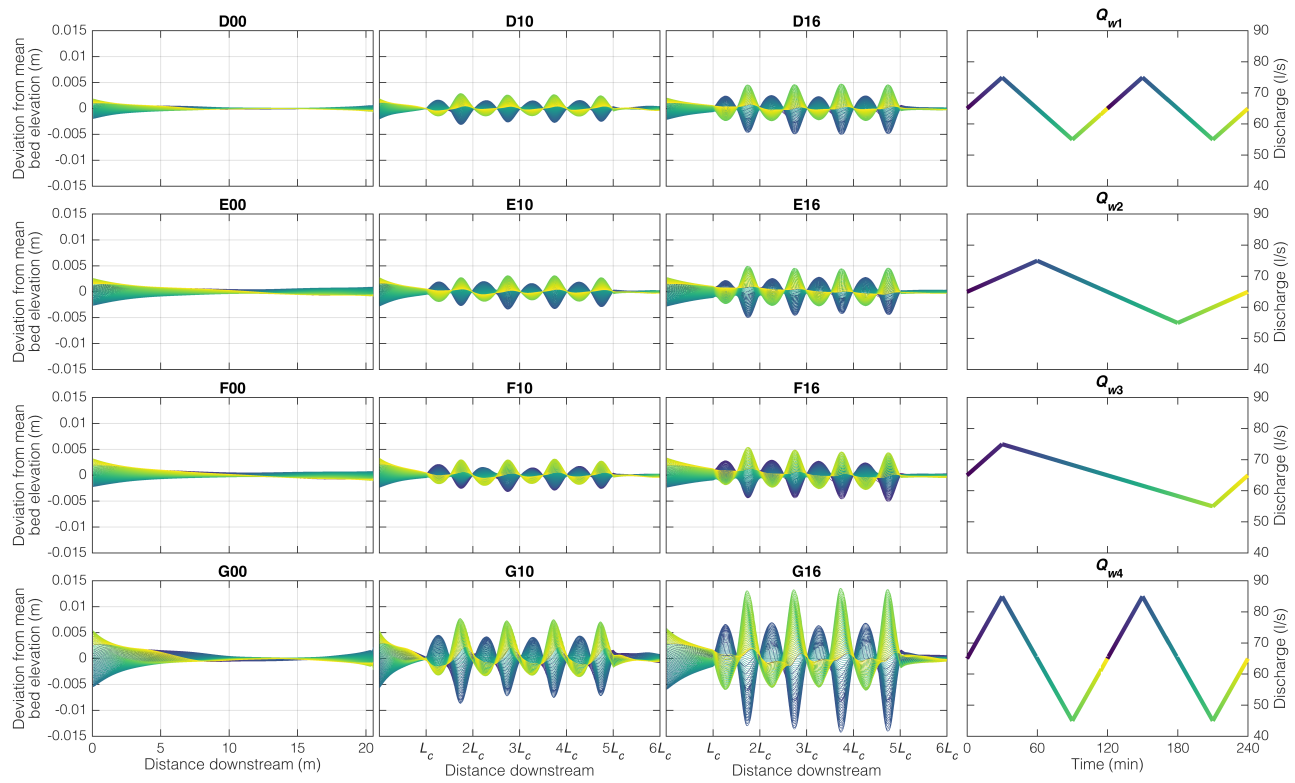


Figure 3.9: Differences in elevation from the mean of all times for each time in unsteady flow Series D–G. Note: $L_c = 6.84$ m for geometry 10 and $L_c = 3.42$ m for geometry 16.

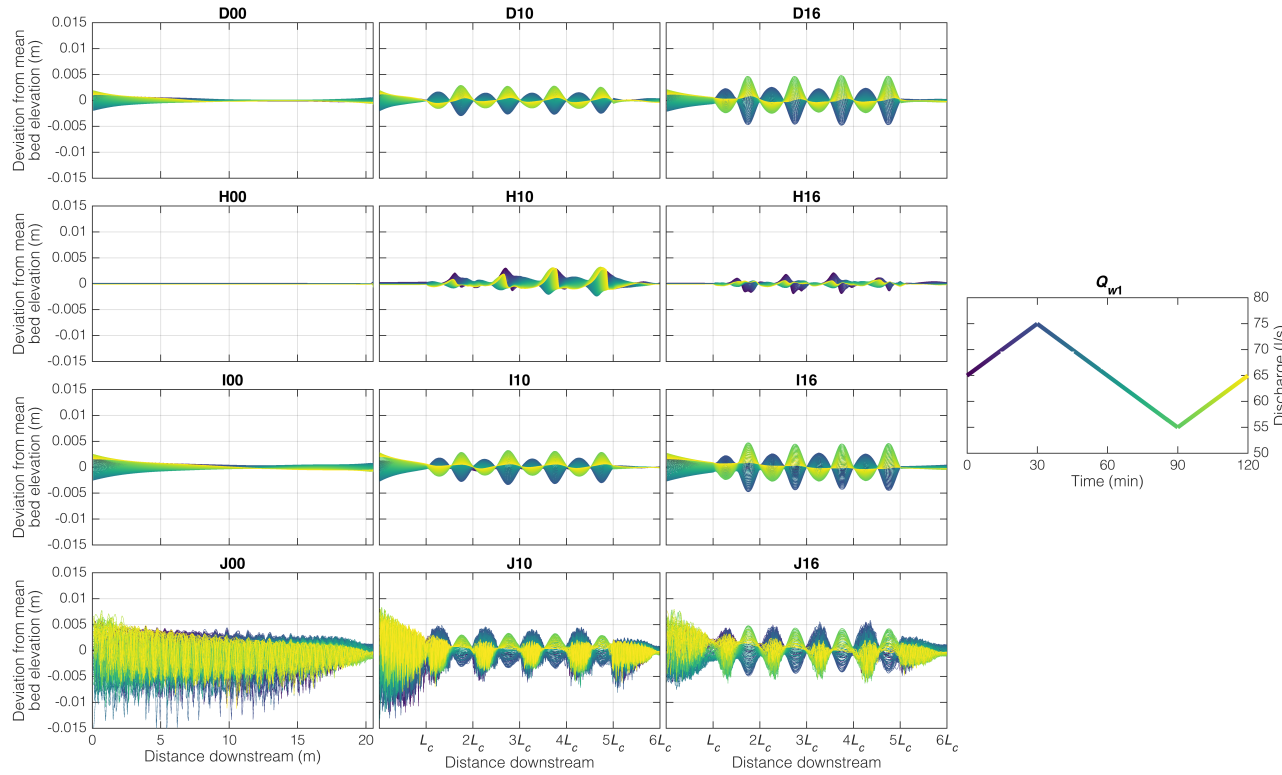


Figure 3.10: Differences in eleveation from the mean of all times for each time in unsteady flow Series D, H–J. Note: $L_c = 6.84$ m for geometry 10 and $L_c = 3.42$ m for geometry 16.

For the variable width geometries (10 and 16), an interesting phenomenon emerges, in which a series of alternating hydrograph boundary layers develops at each width variation period (Figure 3.9). Each wavelength (L_c) contains a single width variation (save the first and last which are straight-walled inlet and outlet reaches). Whole number multiples of L_c correspond to cross-over points, with the maximum width occurring at $L_c/4$ and minimum width occurring at $3L_c/4$. Centered at the maximum channel width in each case is coupled hydrograph boundary layer. In the expanding part of the channel, immediately upstream of the widest section, an “inverted” hydrograph boundary layer forms, where aggradation occurs with increasing discharge and degradation occurs with lower flows. Immediately downstream of the section of maximum channel width the trend reverses, with increasing discharges causing erosion and lower flows resulting in deposition. For all the variable-width geometries in Series D–G this pattern persists with inverted and regular boundary layers alternating every half multiple of L_c . These may be called “structural hydrograph boundary layers” as they are forced by a change in the channel geometry. They are analogous to the ‘sedimentograph boundary layer’ reported by *An et al.* (2017b) in the presence of sediment pulses present midway down the simulation domain. Interestingly, the inverted boundary layer that is centered at the widest channel section is always thinner than the boundary layer that is centered at the narrowest section.

As long as discharge magnitude is unaltered (Series D–F) the amplitude of the structural hydrograph boundary layer appears relatively unrelated to hydrograph duration. Although, for longer wavelengths a longer, more diffuse structural hydrograph boundary layer may become evident. Discharge magnitude, however, appears to have a clear impact on the amplitude of the boundary layer. Both entrance hydrograph boundary layers and structural boundary layers for the G Series show amplitudes over twice that for the D Series, indicating a strong control on boundary layer characteristics by hydrograph maxima. Under conditions of no sediment supply, if simulated for a sufficient duration, even under cycled hydrographs there should be no changes. Such a case exists for H00 (Figure 3.10). However, H10 and

H16 continue to show minor variations in bed elevation, which is likely an effect of an insufficient modeling time. *Parker et al.* (2007) and *Viparelli et al.* (2011) found that as sediment supply increased the hydrograph boundary layer amplitude increases and spreads further downstream. Our results from Series I–J partially support that conclusion. On the one hand, entrance reaches of I Series runs all show a higher amplitude boundary layer that protrudes further downstream. On the other hand, the amplitudes of the structural hydrograph boundary layers that develop in each width variation show for both Series D (Q_{se}) and Series I ($2 \times Q_{se}$) appear to be unaltered by sediment supply. This may suggest that where geometric changes occur, the associated boundary layers may exert more control than sediment supply conditions. In Series J ($5 \times Q_{se}$) a well defined hydrograph boundary layer never emerges for J00 and structural boundary layers are highly variable for J10 and J16. *An et al.* (2017a) found that the hydrograph boundary layer concept may not apply for sediment supplies of a sufficiently wide grain size distribution where bedload sheets develop. Our similar results for Series J are therefore likely attributable to the presence of migrating bedforms. This also may explain why the more consistent sections of structural boundary layers occur at the narrowest sections where bedforms are suppressed. Notice also that the amplitude of the structural boundary layer at these locations is generally equivalent to the amplitude at those same locations in both D series and I series. This again highlights that the amplitude of the structural boundary layer is invariant to sediment supply, having greater dependence on channel geometry and hydrograph maxima.

3.4.4 Implications for riffle-pool dynamics

One of the primary objectives of our study was to explore the combined effects of width variations, unsteady flow, and changing sediment supply in the context of riffle-pool dynamics. Both variable width and unsteady flow have been primary conditions upon which riffle-pool maintenance hypotheses have been developed. The most prominent hypothesis, velocity-reversal (*Keller*, 1971b), postulates that at low flow near-bed velocity values in riffles

are higher than in adjacent pools. However, as discharge increases the near-bed velocities of the two converge until at some point a reversal in the location of maximum near-bed velocity occurs. It is thus the high flows that are responsible for pool maintenance through scour and riffle maintenance through deposition. The hypothesis has had no shortage of critics (e.g., *Bhowmik and Demissie*, 1982), but many have confirmed the phenomenon or something analogous with shear stress (*Milan et al.*, 2001; *Sear*, 1996). In order to better explain the environmental controls that result in the phenomena of reversal, *MacWilliams et al.* (2006) proposed the flow convergence routing hypothesis. Rather than a rebuttal of the velocity reversal hypothesis, flow convergence routing builds on the revised reversal hypothesis of *Thompson et al.* (1996, 1998, 1999) and emphasizes the importance of obstructions (bedrock, boulders, logjams, point bars, etc.) which serve to cause converging flow into pools and diverging flow into riffles. The convergence and associated acceleration of flow into pools, *MacWilliams et al.* (2006) suggest, is a more comprehensive mechanism maintaining riffle-pool sequences. Others have since observed flow convergence routing specifically (*Sawyer et al.*, 2010) or the control of channel width on riffle-pool locations generally (*Brew et al.*, 2015; *Brown and Pasternack*, 2017). Variations in channel width have been shown to be required for reversal to occur (*Caamaño et al.*, 2009). It should be noted, however, that reversal in the location of maximum velocity or shear stress does not necessarily indicate a reversal in the location of bedload transport rates. There is evidence that bedload reversal may occur without velocity (or shear stress) reversal and, conversely, that bedload reversal may not occur despite the occurrence of velocity (or shear stress) reversal (*Bayat et al.*, 2017).

Figure 3.11 shows maps of depth-averaged velocity magnitude, shear velocity, and subsequent bedload transport rates for G10 over a complete hydrograph cycle. At the lowest flows, which may be most analogous to baseflow conditions in a natural system, maximum values of all three variables are about midway through the width variation wavelength. This point corresponds to the steepest local channel slope as the bar plunges into the pool. Minimum

values of all three variables at this lowest discharge occur roughly half a wavelength apart from the maximum, where the slope is rising out of the pool onto the bar. As discharge increases, the maxima of all three variables quickly move downstream to near the center of the width constriction, and they maintain a relatively stable position at the higher flows. At peak discharge the maximum velocity, shear velocity, and bedload occur just downstream from the narrowest channel section. Conversely, minimum values occur just downstream from the widest channel section. These results partly support the velocity/shear/bedload reversal concept with locations of maxima shifting back and forth with discharge. Similar patterns exist also for runs D10, D16, and G16, however to a lesser degree. Run G10, with the higher variability in discharge and channel dimensions that more closely match natural riffle-pool sequences is likely the most transferrable. Similarly, the fact that this process is more pronounced in geometry 10 over geometry 16 suggests that there may be some “optimum” variable width geometry (e.g., spacing of 5–7 channel widths) to achieve ideal riffle-pool maintenance.

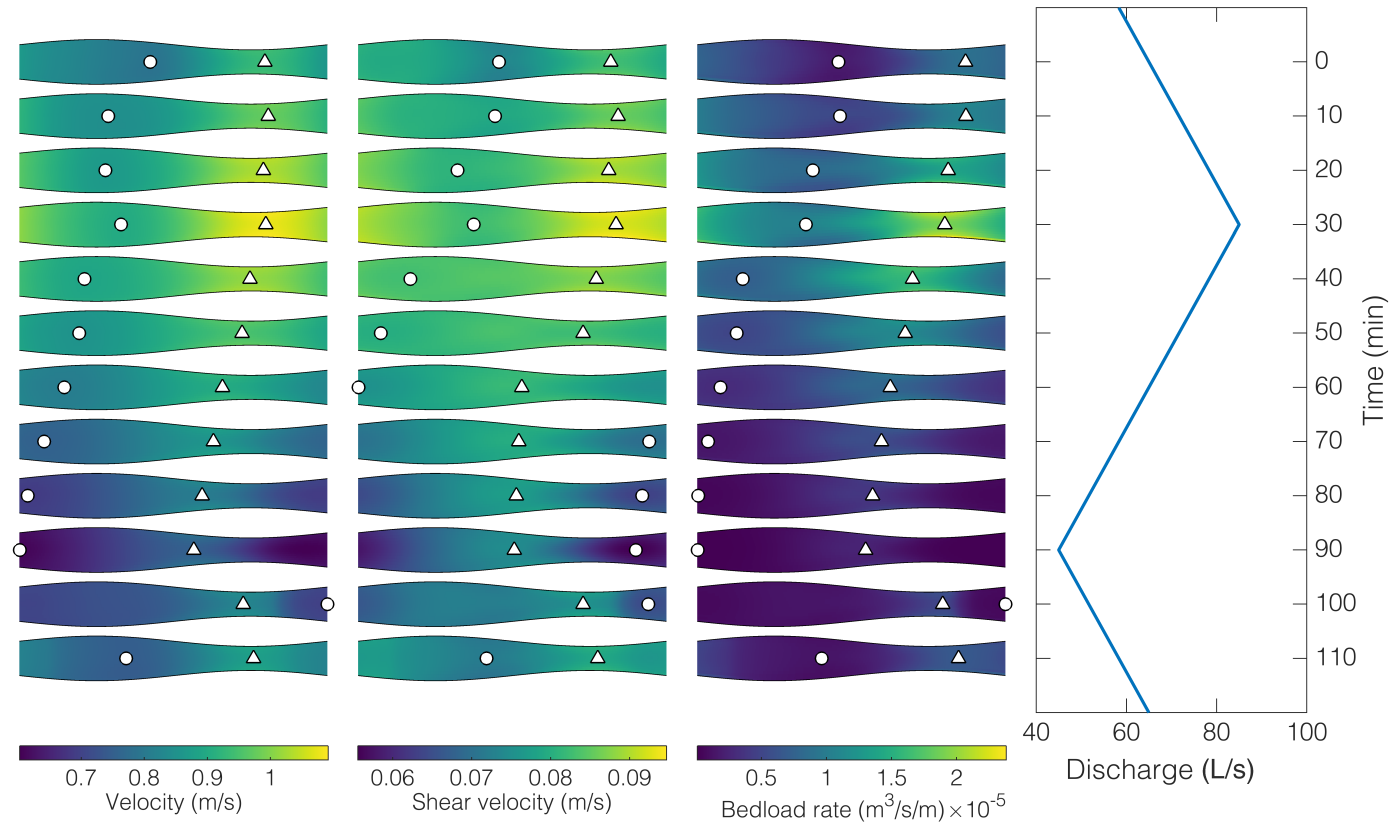


Figure 3.11: Velocity magnitude, shear velocity, and bedload transport rate over a complete hydrograph period for G10. △ symbols correspond to sections where the maximum occurs. ○ symbols correspond to sections where the minimum occurs.

The importance of width variations to this process is clear, as such reversal would not occur in a constant width channel. Indeed our results indicate that width variability exerts a primary control on certain reach-scale equilibrium parameters as well as morphology under unsteady flow and changing sediment supplies. Others have shown that constrictions associated with channel geometry play an important role in riffle-pool characteristics (pool depth and length, for example (*Wohl and Legleiter*, 2003)). Our results, corroborating the flume experiments of *Nelson et al.* (2015), indicate that while sediment supply controls overall channel slope, riffle-pool relief is primarily controlled by channel geometry. The notable example in our numerical simulations where riffle-pool relief differed the most from other runs is when there was no sediment supply. For both steady (B Series) and unsteady flows (H Series) when there was no sediment supply riffle-pool relief increased. Under other sediment regimes the equilibrium relief remained consistent. Additionally, our unsteady flow runs in Series D–G show the relative invariance of riffle-pool morphology to hydrograph duration, and to a certain extent magnitude. During the rising limb of the cycled hydrographs our models show deposition in wide channel sections and erosion in narrow sections. During the falling limb the trend is reversed. These findings highlight the importance of channel geometry and variations in channel width to the self-maintenance of riffles and pools.

3.5 Conclusions

In this study we have presented a set of depth-averaged numerical simulations we have conducted examining the interaction of unsteady flow and changing sediment regimes in straight channels with variable width. We conducted 10 series of runs where we systematically varied both the amplitude and wavelength of width variations and imposed different hydrological and sedimentological inputs. In Series A both discharge and sediment feed were held constant. Results showed pools forming in channel constrictions and bars developing in channel expansions. Riffle-pool relief is controlled by amplitude of width variations, while the wavelength of width variations controlled whether side bars or a central bar formed at

the widest section. In Series B the steady discharge continued but sediment supply was terminated causing slopes to decrease and riffle-pool relief to increase. In Series C a sediment pulse was fed into the sediment starved channels. There was relatively minor variability in the degree of dispersion in pulse evolution. However, there is evidence of fluctuations in relative dispersion-translation depending upon the location of the pulse. Dispersion increased in channel expansions and translation increased in channel constrictions. Series D–G continued from Series A with constant sediment supply but cycled hydrographs rather than steady discharge. Series D–F, which all had the same magnitude of hydrograph maxima, showed very little variations, with average slopes, reliefs, and bar modes all remaining the same as during Series A. In Series G, however, with higher magnitude maxima in the hydrograph the slope flattened and relief slightly decreased. Series H continued from Series D with the same cycled hydrographs, but sediment supply was terminated. Slopes reduced to about half of what they were in Series D and riffle-pool relief increased. Series I and J both continued from Series H with the same cycled hydrographs, but reinstated sediment supplies at twice and five times the previous feed rates. In both cases slopes steepened beyond what had been seen in Series D, and relief was reduced, but values were relatively consistent with relief values in Series A and Series D–G. In Series J consistent symmetric, transverse bedforms developed that were of low height and short wavelength.

Based on our results we draw several conclusions.

1. Under a certain steady discharge and sediment supply, average topographic relief in a variable-width channel is governed by the amplitude of width changes, with higher amplitudes corresponding to greater topographic relief. The bar mode that emerges in the widest section is controlled by the wavelength of width changes, with side bars developing in geometries with shorter wavelengths of width variation.
2. In the presence of sediment supply higher amplitude, shorter wavelength width variations result in an overall steeper bed slope. In the absence of sediment feed higher

amplitude, longer wavelength width variations result in steeper bed slope. This holds under steady and unsteady flow.

3. Sediment pulse translation is locally modulated by geometry with the pulse evolving through more dispersion through channel expansions and more translation through channel constrictions. However, overall relative dispersion-translation differs very little from that in a straight-walled channel having the same mean width.
4. Reach-averaged channel characteristics (slope and riffle-pool relief) are invariant to cycled hydrograph shape and duration. However, under cycled hydrographs with greater maxima slight reductions in slope occur.
5. Under consistent elevated sediment feed rates, slopes adjust to become steeper, but riffle-pool relief remains consistent, similar to that under lower supply conditions.
6. The concept of a “hydrograph boundary layer” is corroborated and partially expanded upon, with the introduction of the “structural hydrograph boundary layer” which occurs at changes in channel geometry. These structural variations disrupt the ability the channel has to create a bed relatively invariant to discharge from upstream.
7. The converging/diverging flow associated with width variations, and the resultant bed topography under cycled hydrographs and constant sediment supply, create conditions that facilitate the shifting of the location of maximum transport capacity from the riffle entrance during periods of low flow to the pool center during periods of high flow.

Chapter 4

Flume experiments on gravel-bed variable-width morphodynamics

4.1 Introduction

Rivers are often characterized by downstream variations in channel width (*Harman et al.*, 2008; *Moody and Troutman*, 2002; *Myers and Swanson*, 1997). Longitudinal variations in channel width have been observed to play an important role in habitat suitability (*Hicks et al.*, 1991; *Krapu et al.*, 1984), meandering dynamics (*Eke et al.*, 2014; *Zolezzi et al.*, 2012), braiding dynamics (*Repetto et al.*, 2002; *Wu and Yeh*, 2005), bar position and movement (*Duró et al.*, 2016; *Luchi et al.*, 2010; *Wu et al.*, 2011), and riffle-pool location and persistence (*Brew et al.*, 2015; *MacWilliams et al.*, 2006; *Richards*, 1976b). *Kazemipour and Apelt* (1980, 1983) performed flume experiments in a variable-width channel with uniform expansion and constriction rates. The bed in their experiments was fixed to produce a constant area below a plane parallel to the overall channel slope. They found that for a channel with nearly constant cross-sectional area, despite irregularities in channel width, there is little resistance due to form. However, for a channel whose cross-sectional area does not remain relatively constant form resistance can account for up to 90% of the energy loss. *Tsujimoto* (1987) conducted mobile-bed experiments in a channel with sinusoidally varying width and observed bed deformation that resulted in vertical undulations with a pool developing at the width contraction. He also observed multi-modal bar development in the width expansion. *Bittner* (1994) performed flume experiments and numerical modeling of channels with sinusoidally varying width and found for slight width variations migrating alternate bars form which are similar to those in constant-width channels. For more pronounced width variations migrating bedforms were suppressed entirely and instead stationary bars developed which were

alternate at low flow and centered at high flow. Using flume experiments to simulate width variations in bedrock channels, *Wohl et al.* (1999) concluded that width undulations create a condition of minimized energy expenditure and uniform energy expenditure at the reach scale. In the context of braided rivers, *Repetto et al.* (2002) performed flume experiments in variable-width channels of a range of constriction amplitudes and wavelengths. They also found migrating alternate bars in low amplitude width variations and the development of central bars at wide sections in channels of more significant width variations. Building on their work, *Wu and Yeh* (2005) explored the possible modes of forced bars that develop at wide sections, concluding that the aspect ratio is the primary control on bar mode. There are essentially two bar modes: central bars, which comprise a single bar in the expansion located in the middle of the channel; and side bars, which involve two bars on either side of the centerline in the widest section. Transition from central bars to side bars and back to central bars again was found to occur with increasing aspect ratios. *Wu et al.* (2011) continued this work, investigating the dynamics of free, or migrating bars, in channels with sinusoidal width variations. Shorter width variation wavelengths and amplitudes result in suppression of bar height and length. Bar celerity depends on the combination of wavelength and amplitude of width variations. More recently, *Brown et al.* (2016) used depth-averaged hydrodynamic modeling to evaluate riffle-pool flow parameters in channels where bed topography co-varied, both in phase and out of phase, with sinusoidal width variations, introducing the concept of geomorphic covariance structures. Despite these studies, relative to other controls on alluvial morphodynamics, the effect of downstream variation in channel width remains largely unstudied and poorly understood, particularly in the context of unsteady flow and changing sediment supply regimes. To our knowledge there are no studies that investigate periodic width variations with unsteady flow and/or changing sediment supplies (but see *Chartrand* (2017)).

Discharge is considered one of the dominating independent variables controlling alluvial morphodynamics and unsteady flow is the reality in natural systems. Variations in discharge

have been shown to play an important role in bedload transport rates (*Bombar et al.*, 2011; *Lee et al.*, 2004; *Mao*, 2012; *Phillips and Sutherland*, 1990; *Waters and Curran*, 2015) and grain size sorting and armoring (*Hassan et al.*, 2006; *Nouh*, 1990; *Strom et al.*, 2004). Unsteady flow has been observed to impact alternate bar morphology (*Rodrigues et al.*, 2015; *Tubino*, 1991) and has long been recognized as a dominant factor in riffle-pool maintenance (*Gilbert*, 1914; *Keller*, 1971b; *Leopold and Wolman*, 1960). Field studies and laboratory experiments in constant width flumes using unsteady flow have shown that there are often hysteresis effects between discharge and other flow variables (e.g., depth, velocity). Both clockwise and counterclockwise hysteresis patterns of bedload have been observed in field and flume results (*Guney et al.*, 2013; *Gunsolus and Binns*, 2018; *Kuhnle*, 1992; *Mao*, 2012; *Wang et al.*, 2015; *Waters and Curran*, 2015). *Guney et al.* (2013) found that antecedent surface armoring can control the bedload hysteresis direction. Others have also observed armor layer effects related to unsteady flow (*Ferrer-Boix and Hassan*, 2015; *Recking*, 2014). Using flume experiments *Wang et al.* (2015) found that bedload rates exhibited clockwise hysteresis in a channel with a coarser grained surface, while a finer gravel surface resulted in a counterclockwise bedload hysteresis. Many studies have been conducted using field, laboratory, and numerical methods to explore unsteady effects on gravel-bed dynamics, but little work has been done to specifically explore the interaction between unsteady flow and downstream variations in channel width.

Alluvial channels can adjust to changing sediment supplies through a combination of modifications to the channel slope, channel cross-section (e.g., width), or surface grain size distribution (*Blom et al.*, 2017; *Lane*, 1955). The grain size and rate of sediment supply is a major factor governing a number of morphological features in gravel-bed streams including bed sorting, armoring, and patchiness (*Buffington and Montgomery*, 1999; *Dietrich et al.*, 1989; *Hassan and Church*, 2000; *Nelson et al.*, 2009; *Pitlick et al.*, 2008) and bedform dynamics (*Kleinhans*, 2005; *Kleinhans et al.*, 2002; *Lisle et al.*, 1993; *Venditti et al.*, 2012). Channels experiencing an increased sediment supply have been observed to show sur-

face fining and enhanced grain mobilization (*Cui et al.*, 2003a; *Dietrich et al.*, 1989; *Jackson and Beschta*, 1984). Studies with increased rates of sediment supply in riffle-pool or bar-pool morphology have shown general pool filling resulting in a more homogeneous downstream bed profile (*Brew et al.*, 2015; *Lisle*, 1982; *Lisle and Hilton*, 1992; *Madej*, 2001; *Madej et al.*, 2009; *Pryor et al.*, 2011; *Sutherland et al.*, 2002; *Wohl and Cenderelli*, 2000). However, recent studies have found that for channels with stable width variations the response to increased sediment supply is characterized more by a change in total slope, rather than a decrease in riffle-pool relief (Chapter 3; *Nelson et al.*, 2015). Aside from these studies, very little has been done to explore the combined effects of width variations and changing sediment supplies.

How a constant-width channel and an equivalent variable-width channel comparatively respond to differences in steady versus unsteady flow or changes in sediment supply is not well understood. Previous studies considering flow and sediment changes in irregular channels have largely been field-based and therefore poorly constrained. Conversely, laboratory and numerical studies that have used variable-width channels have generally used steady flow and constant sediment supply. In our current understanding there is a gap on how these forcings interact to influence gravel-bed morphology.

In this paper we present results from a laboratory flume experiment used to explore the interactions between periodic variations in channel width, unsteady flow, and changing sediment supplies. Our goals were to characterize the differences in dynamic equilibrium conditions of a constant-width versus a variable-width channel under various water and sediment supply regimes.

4.2 Methods

4.2.1 Experimental setup

Flume experiments were conducted at the Hydraulics Laboratory at the Colorado State University Engineering Research Center using a straight, rectangular, sediment-feed flume

that is 1.21 m (4 ft) wide, 0.76 m (2.5 ft) deep, and 18.29 m (60 ft) long (Figure 4.1a). The laboratory floor is underlain by a sump and a 100 hp pump moves water from the sump to the flume headbox. Water discharge is regulated with a gate valve adjusted manually with a handwheel. A Rosemount Annubar Flowmeter is installed to measure the pressure differential in the pipe supplying the flume headbox. Volumetric discharge measurements, calculated from the pressure differential, were calibrated using a 90°, sharp-crested weir, and these were used to control the water discharge to the flume. A hopper, located above the flume headbox, supplies sediment to the upstream boundary of the flume. The sediment feed from the hopper is regulated by an auger-type feeder, enclosed in a PVC pipe situated above the flume entrance. The variable-speed motor controlling the auger, and thereby the volumetric sediment feed rate, was calibrated manually prior to the experiments. At the downstream end of the flume the water level is regulated by a tailgate which is manually adjusted. A tailbox, between the flume exit and the tailgate, facilitates the capture of all bedload exiting the flume while allowing water to pass over the tailgate. The tailbox must be manually excavated, while the water passing the tailgate returns to the sump underneath the laboratory. A motorized, computer-controlled instrumentation cart moves longitudinally along rails mounted to the top of the flume walls. The cart is outfitted with five Massa ultrasonic sensors, spaced in lateral increments of approximately 11 cm, used to semi-continuously measure water surface elevations along 5 parallel longitudinal profiles (*Venditti et al., 2016*).

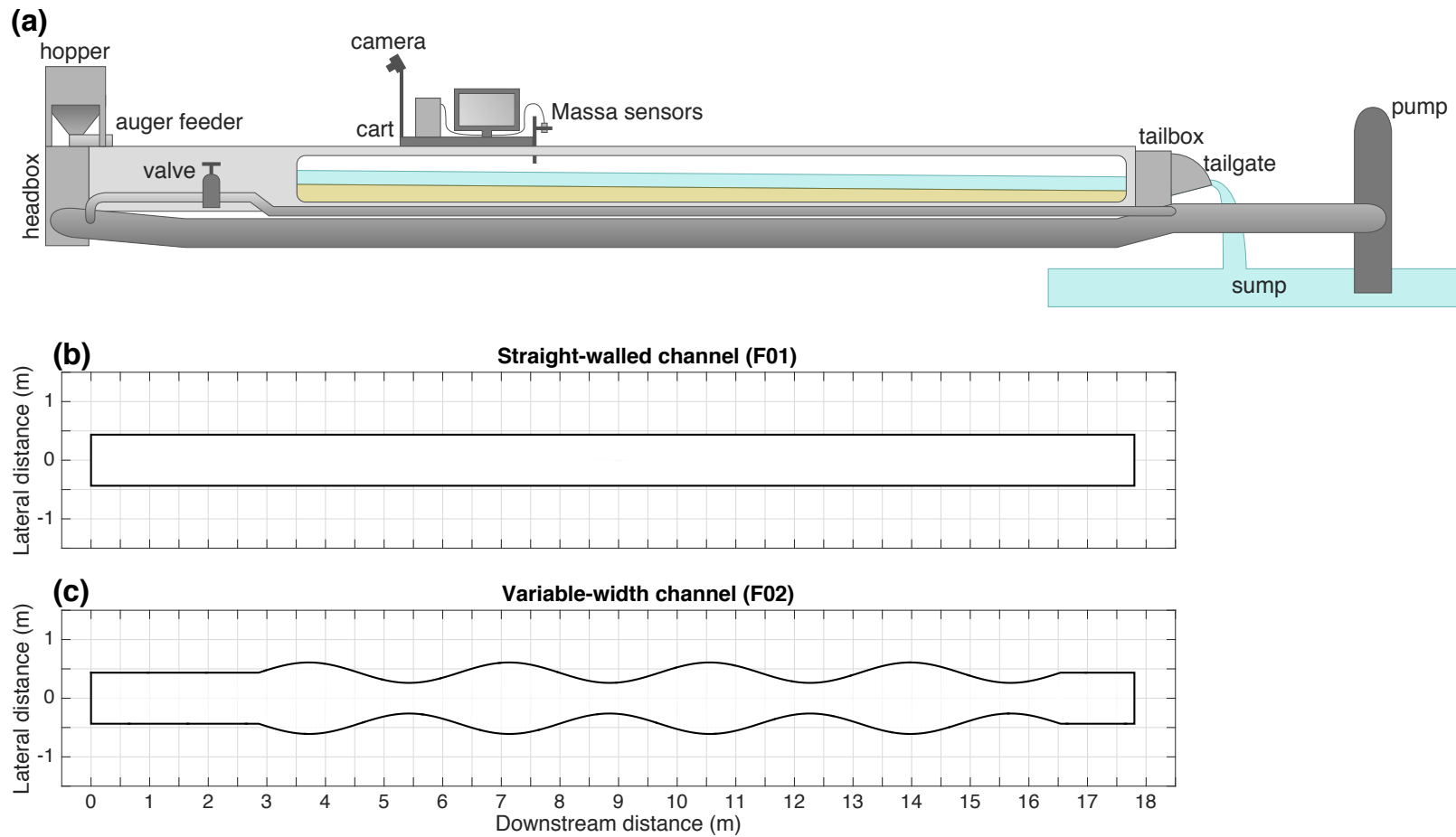


Figure 4.1: (a) Flume set up and planform channel geometry for (b) F01, straight-walled channel and (c) F02, variable width channel

4.2.2 Flume operation and measurements

While the flume was running quantitative measurements related to water surface elevations were made using the instrumentation described above and qualitative observations related to the bed surface conditions (e.g., bedforms) were made. Water surface elevations were used to calculate water surface slopes (S_w) by fitting a linear model to the data in the downstream-elevation plane. Flow depths (H) were estimated by subtracting the interpolated bed elevations (described below) from the water surface elevation coordinates. Estimates of the aspect ratio (β , i.e. width-to-depth ratio), shear stress ($\tau_0 = \rho g H S_w$, where ρ is the density of water and g is gravitational acceleration), and Froude number ($Fr = Qg^{-1/2}B^{-1}H^{-3/2}$, where Q is the discharge and B is the channel width) were subsequently made from the water surface data.

Care was taken during flume start up and shut down to minimize the effect on bed morphodynamics. Run periods between start up and shut down were generally governed by the filling of the tailbox with bedload exiting the flume. In general runs lasted 2–4 hours until the tailbox was full. However, at equilibrium for each phase finer temporal resolution of measurements was obtained by shutting down the flume after shorter periods. When the flume was shut down the tailbox was excavated and the material was dried and weighed to determine long-term bedload flux rates exiting the flume. Samples from the material were collected and manually sieved to obtain grain size distributions. Once the bed had drained digital imagery was collected to obtain bed topography. A Canon EOS Rebel T3i with an 18–55 mm IS II lens was mounted to the cart and oriented approximately 45° below horizontal. Imagery was collected in three passes. In the first pass 60 images were collected with the camera oriented upstream and the focal length set to 18 mm, resulting in a longitudinal image spacing of approximately 0.28 m. In the second pass, 100 images were collected with the camera oriented in the upstream direction and the focal length set to 55 mm, resulting in a longitudinal image spacing of approximately 0.17 m. In the third pass, 60 images were collected with the camera oriented in the downstream direction and the focal

length set again to 18 mm. Camera focal length and image intervals produced photosets with substantial overlap ($\geq 80\%$). For each photoset the 220 images were processed using Structure-from-Motion (SfM) photogrammetric methods (*Agisoft*, 2016). SfM methods have been shown to produce three-dimensional point clouds of comparable accuracy to standard laser scanning methods with much higher spatial resolution (*Morgan et al.*, 2017). SfM point clouds were scaled and referenced using eight checkerboard targets with known coordinates located on the top of the flume walls. The three dimensional point clouds were interpolated into 5 cm DEM grids using the natural neighbor algorithm. Detrended elevation maps were made by subtracting the mean downstream bed slope from the DEM grids. Bar-pool reliefs were calculated for the variable width runs as the difference of the mean elevation of the cross-section with the minimum elevation in a width variation wavelength and the mean elevation of the cross-section with the maximum elevation in a width variation wavelength.

4.2.3 Experimental procedure

Flume configurations

Two geometries were considered for our experiments: a straight-walled channel (F01), serving as a control, and a variable width channel (Figure 4.1b,c). The specific dimensions of these geometries were chosen to coincide with geometries used in related two-dimensional numerical morphodynamic modeling experiments that we have also been conducting. The straight-walled geometry had a width of 0.87 m (Figure 4.1b), which required a temporary wall be built within the 1.21 m wide flume. The wall was constructed using sheet metal attached to a wooden frame affixed to the interior of the flume (Figure 4.2a). The narrower inset channel extended for the entire length of usable flume. The variable-width channel (F02) consisted of a straight-walled inlet reach with a length of 2.86 m and a straight-walled outlet reach with a length of 1.26 m (Figure 4.1c). The width of both the entrance and exit reaches was 0.87 m. Between the inlet and exit reaches four sinusoidal width constrictions were installed. A channel with sinusoidal width constrictions may be described by speci-



Figure 4.2: (a) Straight-walled flume geometry and (b) variable-width flume geometry. Camera view is oriented downstream in both images.

fying mean channel half-width (B_0), a dimensionless amplitude (A_c), and a dimensionless wavenumber (λ_c).

$$B(x) = B_0 [1 + A_c \sin(\lambda_c x / B_0)] \quad (4.1)$$

where $B(x)$ is the local channel half-width at downstream location x . For our variable-width geometry an amplitude of $A_c = 0.4$ and a wavenumber of $\lambda_c = 0.8$ were chosen. This resulted in a maximum channel width of 1.21 m, a minimum channel width of 0.52 m, and a wavelength of width variations equaling $L_c = 3.42$ m ($L_c = 2\pi B_0 / \lambda_c$). These values correspond to the largest amplitude and shortest wavelength width variations considered for our related numerical simulations (Chapter 3). The sinusoidal width variations were also constructed using temporary walls made of sheet metal and wooden framing (Figure 4.2b).

Phase procedure

The experimental procedure for each channel geometry was set up to consist of three phases. For each geometry, before the first phase began, the flume was filled with the bulk sediment and the bed was screeded flat to a constant bed slope (S_0) around 0.7%. The

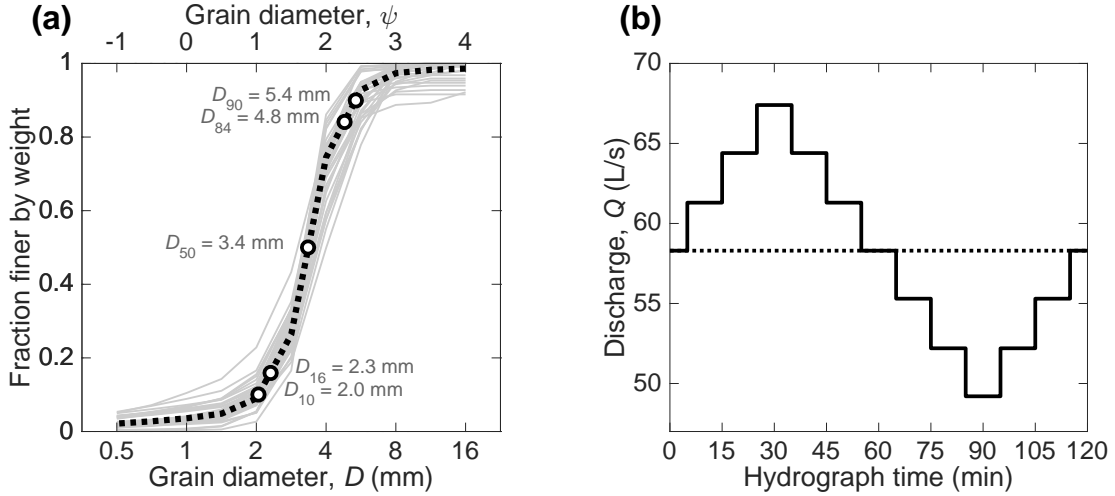


Figure 4.3: (a) Bulk grain size distribution used for initial bed composition and sediment supply during all phases. Gray lines are individual samples. The dark dotted line is the mean of all samples. (b) Stepped hydrograph used in unsteady flow phases. Dotted line corresponds to the steady flow discharge.

bulk sediment consisted of a unimodal distribution of coarse sand to fine gravel with median grain diameter of $D_{50} = 3.4$ mm and a geometric standard deviation of $\sigma_g = 1.6$ mm (Figure 4.3a). The distribution was chosen based on material already available and to ensure the full range would be mobile for the discharges modeled. The initial conditions of the second and third phases were the final conditions of the previous phase. Each phase of the experimental procedure was continued until steady-state, “dynamic equilibrium” conditions were attained. These conditions were indicated by consistent rates and grain size of bedload exiting the flume and consistent water and bed slopes. The first phase (P01) consisted of steady discharge ($Q = 58.3 \text{ } \ell/\text{s}$) and steady constant sediment supply ($Q_{bf} = 1580 \text{ g/min}$). In the second phase (P02) discharge was unsteady, in the form of repeated, stepped hydrographs, and sediment supply remained the same as in P01. The discharge hydrographs were triangular and symmetrical with a mean discharge of $58.3 \text{ } \ell/\text{s}$, minimum of 49.2 and maximum of $67.4 \text{ } \ell/\text{s}$, a period of 120 minutes, and a step length of 10 minutes (Figure 4.3b). The hydrograph was chosen to have a mean discharge equal to the steady flow from phase one. The maximum discharge was chosen as the maximum discharge the 6 inch bypass valve (which feeds water to the flume headbox) could carry. The minimum discharge was chosen

to be an equal difference from the mean as the maximum discharge, and a symmetrical shape was chosen for simplicity. The hydrograph duration was chosen to scale from 2 hours in lab to approximately 16–18 hours in the field, using the scaling relationship of *Parker et al.* (2003) and riffle width measurements reported by *Carling and Orr* (2000) and *Brew et al.* (2015). In the third phase (P03) the repeated hydrographs continued the same as in P02 but the sediment supply rate was doubled ($2 \times Q_{bf} = 3160$ g/min). In all phases the sediment feed was composed of the bulk material (Figure 4.3a).

4.3 Results

4.3.1 F01: Straight-Walled Channel

F01P01: Steady Flow, Steady Sediment Supply

The first phase of the straight-walled geometry lasted 4154 minutes (69.2 hours). The bed profile quickly relaxed from the initial slope of approximately 0.008 to a relatively consistent bed slope of approximately 0.004 (Figure 4.4). Bedload rates exiting the flume initially dropped steeply before evening out after several hours. Equilibrium water surface slopes were 0.0051. Equilibrium flow depths ranged from 9 to 12 cm with a mean of 10.5 cm (Figure 4.5a). Mean shear stresses are estimated to have been approximately 5.25 Pa (Figure 4.6a). Froude numbers were consistent and remained subcritical around 0.63 (Figure 4.4). During the straight-walled experiments dune-like migrating bedforms, which had an alternating pattern, developed almost immediately and continued throughout the duration of the F01 experimental phases (Figure 4.7a). The details and dynamics of these gravel bedforms are not discussed here, but are investigated elsewhere (*Nelson and Morgan, in review*).

F01P02: Unsteady Flow, Steady Sediment Supply

In the second phase the sediment supply remained constant at the same rate, while water discharge became unsteady. The total duration of the phase was 3000 minutes (50 hours). We observed minimal differences between steady and unsteady flow on hydraulic and sediment

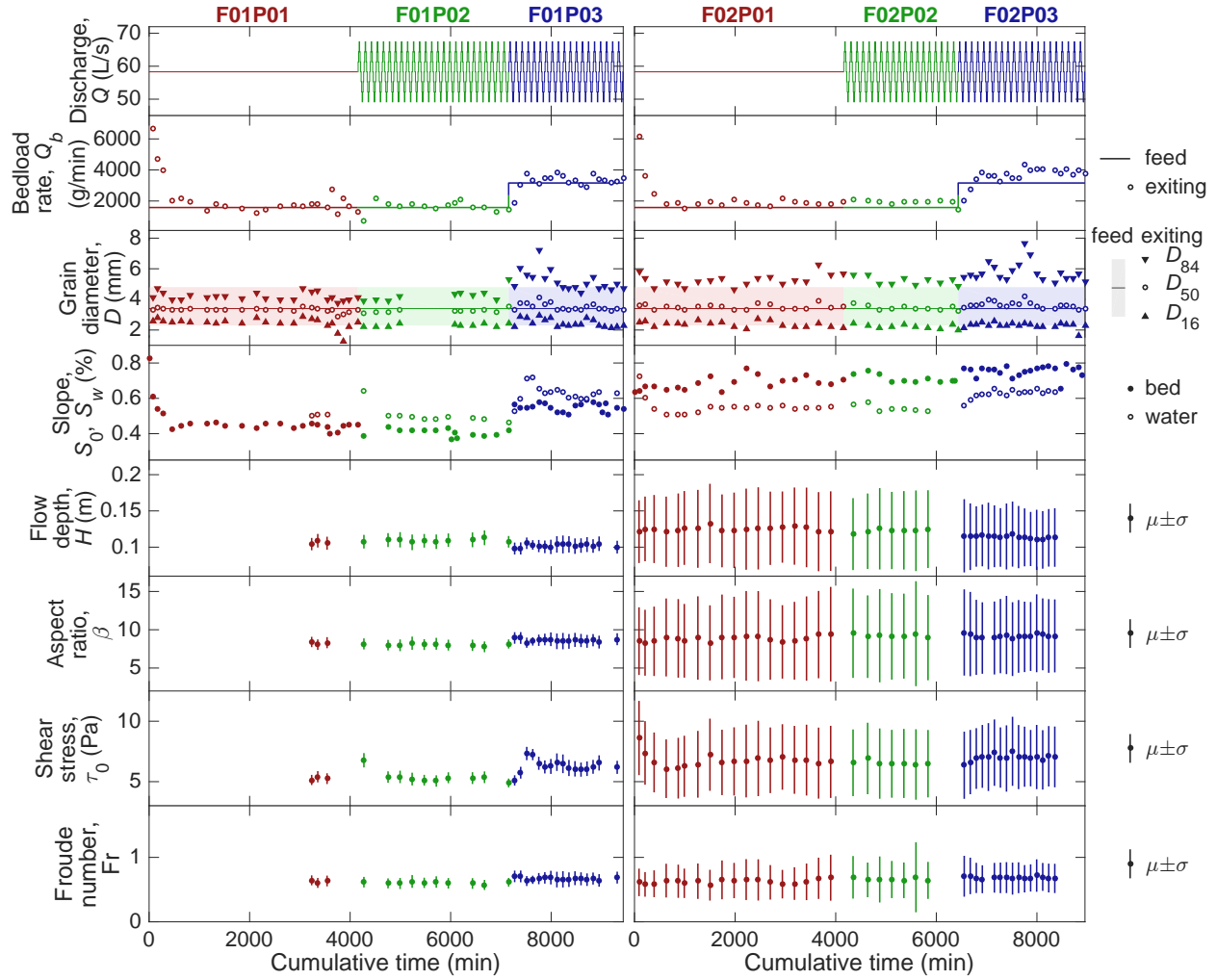


Figure 4.4: Time series of hydraulic conditions and bedload characteristics during all three phases of both geometries. For the unsteady flow phases, data points reflect variable values at the beginning/end of the hydrograph, when the flow equaled the mean discharge. μ is the mean and σ is the standard deviation.

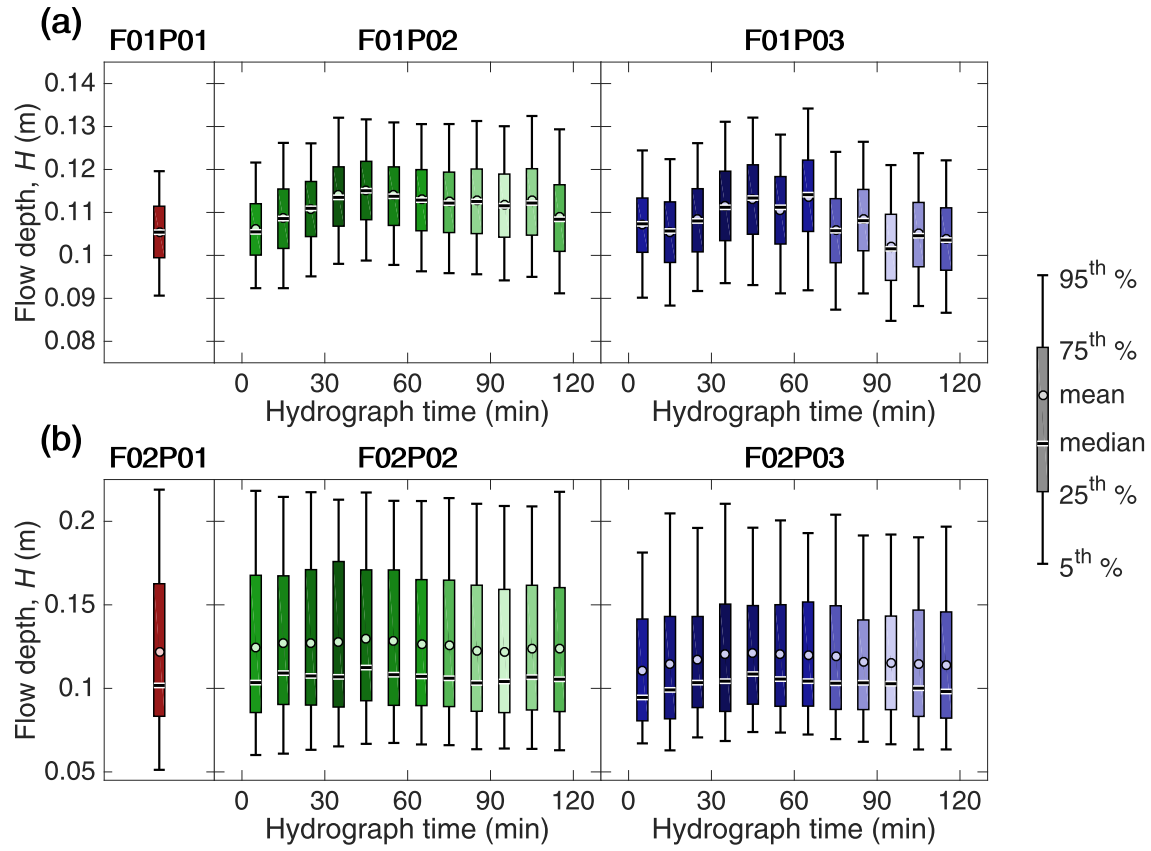


Figure 4.5: Time-series box plots of flow depth for (a) F01 and (b) F02. Lighter or darker colored boxes correspond to lower or higher discharges, respectively. Hydrograph maximum occurs at 30 minutes and minimum occurs at 90 minutes.

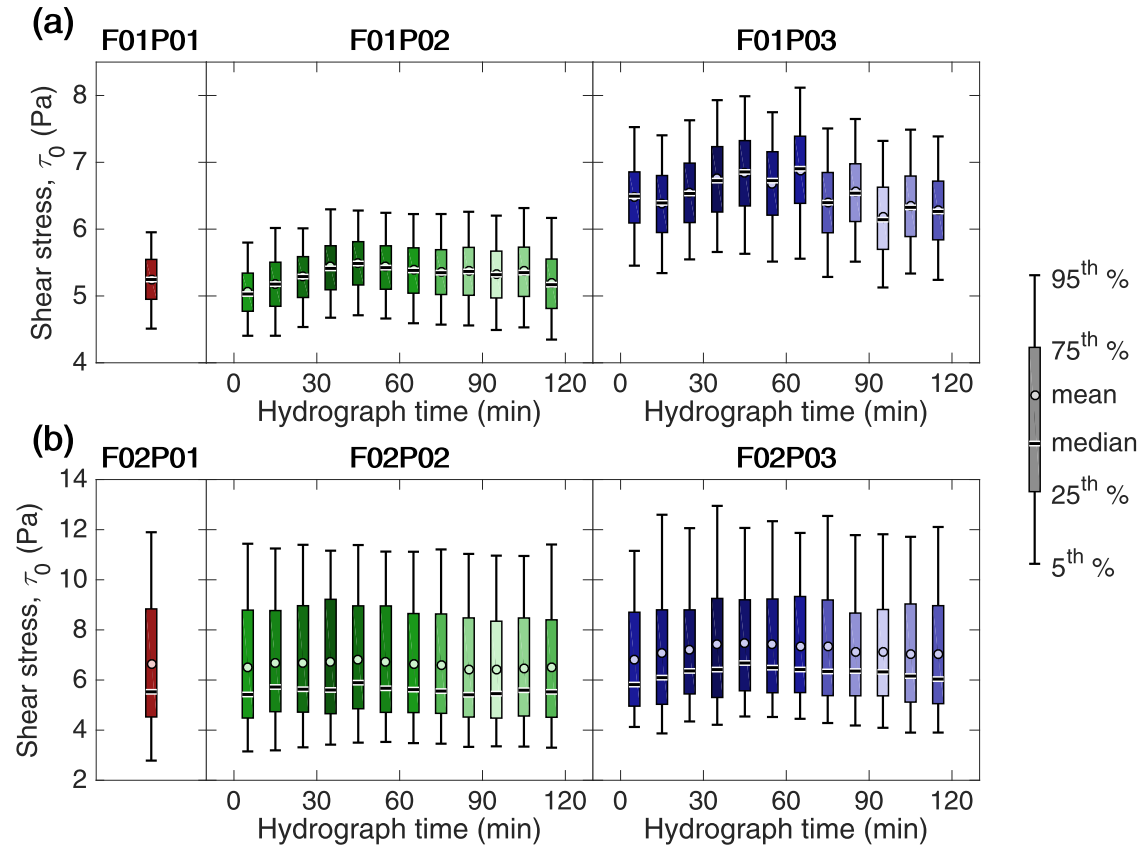


Figure 4.6: Time-series box plots of shear stress for (a) F01 and (b) F02. Lighter or darker colored boxes correspond to lower or higher discharges, respectively. Hydrograph maximum occurs at 30 minutes and minimum occurs at 90 minutes.

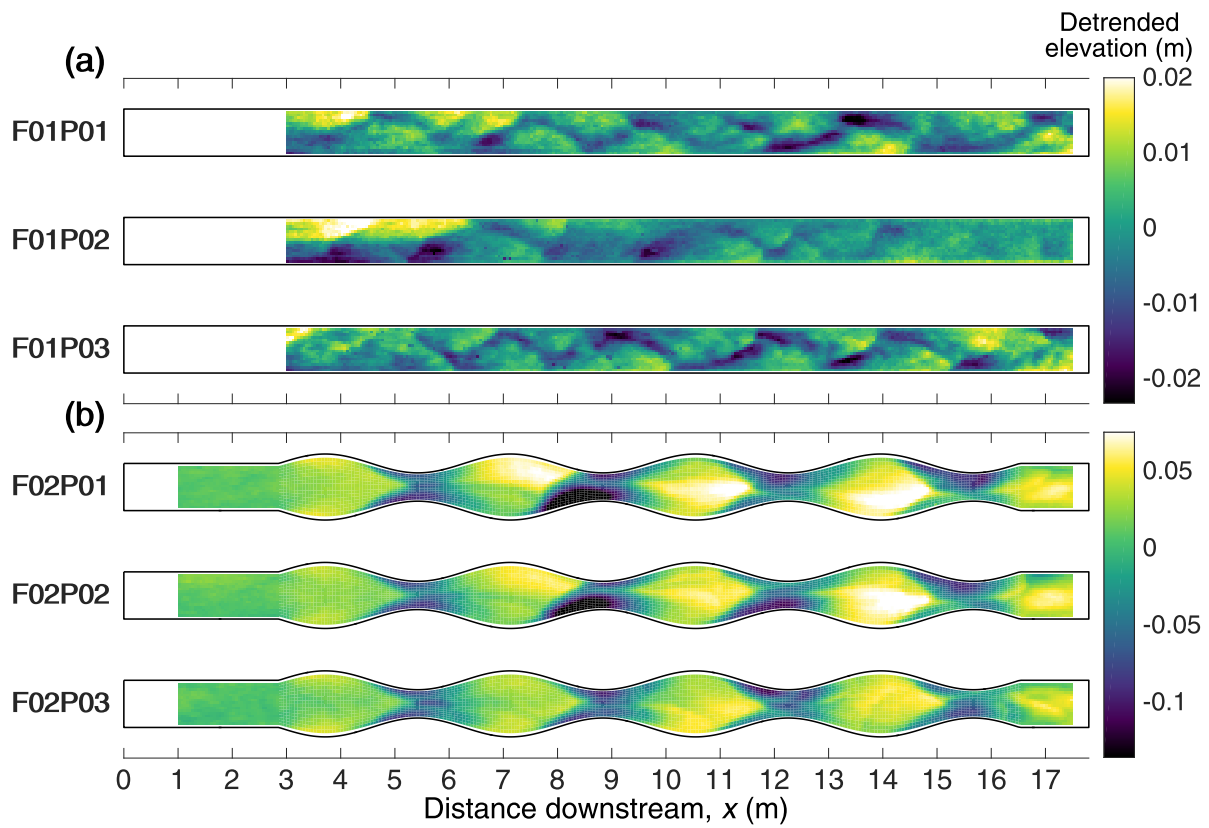


Figure 4.7: Equilibrium detrended bed elevation maps for all phases in both geometries. Maps from the mean discharge are shown for unsteady flow phases.

transport parameters at points in the hydrograph equaling the mean flow (Figure 4.4). Equilibrium bed slope varied slightly over the hydrograph, with the greatest difference seen not in relation to discharge, but in the rising versus falling limb of the hydrograph (Figure 4.8a). Bed slopes showed a general clockwise hysteresis with the discharge hydrograph, with rising limb bed slopes generally steeper than falling limb bed slopes for a given discharge. Weak counterclockwise hysteresis was also observed for the water surface slopes, but different values for a given discharge are within one another's error range (Figure 4.8a). Water surface slopes varied with discharge (from 0.0047 at low flow to 0.0052 at high flow) and, similar to F01P01, water surface slopes remained consistently steeper than bed slopes (Figures 4.4 and 4.8a). Flow depths at the mean discharge remained similar to depths in F01P01 (Figure 4.5a). Mean flow depths varied little over the hydrograph with a range from 10.5 cm to 11.5 cm and overall depth values more-or-less tracked with discharge. No hysteresis was discernible for flow depth relative to discharge. Mean shear stress values at the mean discharge were essentially the same as in F01P01 at around 5 Pa (Figures 4.4 and 4.6a). Shear stress values also tracked with discharge, without any appreciable degree of hysteresis.

F01P03: Unsteady Flow, Increased Sediment Supply

Sediment supply was doubled in the third phase, which lasted 2280 minutes (38 hours). Phase F01P03 saw a general increase in both bed and water surface slopes and a decrease in flow depths (Figure 4.4). Both bed and water surface slopes increased from those in F01P02 by approximately 0.0015 for each step of the discharge hydrograph (Figure 4.8b). Bed slopes varied inversely with discharge, although the greater relationship again appears to be with the rising versus the falling limb of the hydrograph. As in F01P02, bed slope shows a clockwise hysteresis with discharge. Water surface slopes show a very weak clockwise hysteresis, with different slopes for a given discharge once again falling within the other's error range (Figure 4.8b). Flow depths were initially slightly lower than in the previous phases although equilibrium mean flow depths were approximately the same (Figure 4.4). Equilibrium flow depths again generally varied with discharge without any clear hysteresis (Figure 4.5a) and

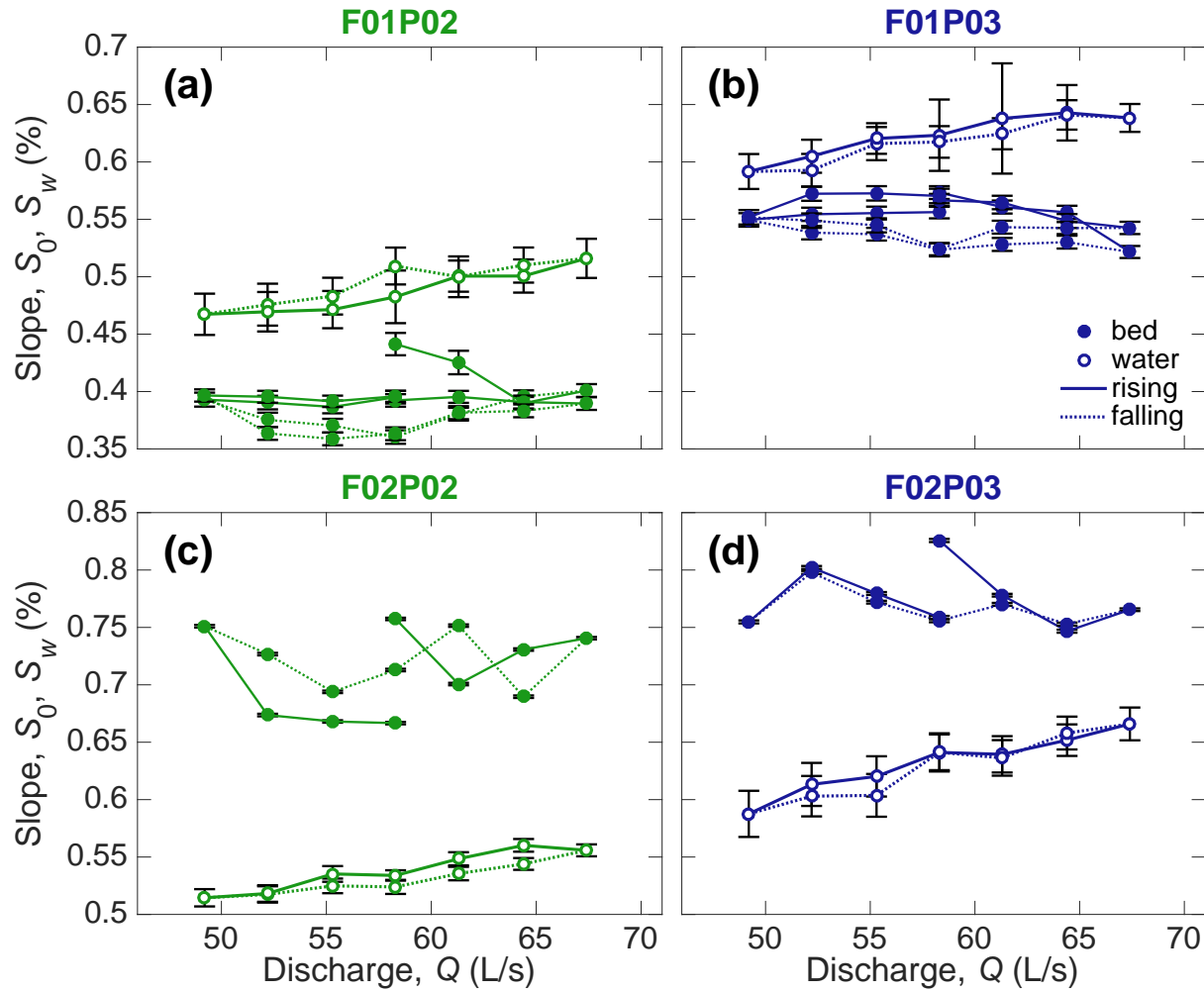


Figure 4.8: Discharge-slope relationships for unsteady flow phases in both F01 and F02. The legend in subplot (b) applies to all subplots. Error bars encompass the calculated slope \pm the standard error.

were approximately the same as in F01P02. Shear stress estimates increased from F01P02 by approximately 1.5 Pa and again generally followed discharge (Figure 4.6a).

Throughout the three phases for F01 the exiting grain diameters remained relatively constant (Figure 4.4). Initially during F01P03 the exiting bedload became slightly coarser than during the previous phases, but the subsequent characteristic grain sizes relaxed values more similar to the first two phases. Bed slopes increased and stabilized almost immediately, while several hours were needed for bedload rates exiting the flume and the water surface slopes to level out. Throughout the straight-walled phases the ranges of flow depths (and therefore subsequently derived parameters such as aspect ratio, shear stress, and Froude number) remained fairly limited (Figure 4.4), indicating that uniform flow approximations (such as are inherent to the depth-slope product for shear stress) are likely justified.

4.3.2 F02: Variable-Width Channel

F02P01: Steady Flow, Steady Sediment Supply

Phase F02P01 began from a screed-flat bed and consisted of steady water discharge and constant sediment supply, lasting 4155 minutes (69.3 hours). Bedload rates and water surface slopes initially dropped steeply for the first several hours, although the bed slope remained relatively unchanged (Figure 4.4). Forced bars and pools formed immediately during the phase, with bars located at width expansions and pools located at narrow sections, and remained through all three phases (Figure 4.7b). Relief between bar crest and pool trough elevations quickly developed and slightly increased to an equilibrium value of 13 cm (Figure 4.9). Equilibrium slope relationships were reversed from the straight-walled first phase, with bed slope consistently steeper than water surface slopes. The equilibrium bed slope was approximately 0.0069 and the water surface slope approximately 0.0055. Flow depths ranged from 5 cm to 22 cm with a mean of 12 cm. However, we should note that water surface elevations were collected along straight longitudinal profiles within the center 44 cm of the channel width. Accordingly, the outermost parts of the channel in the width

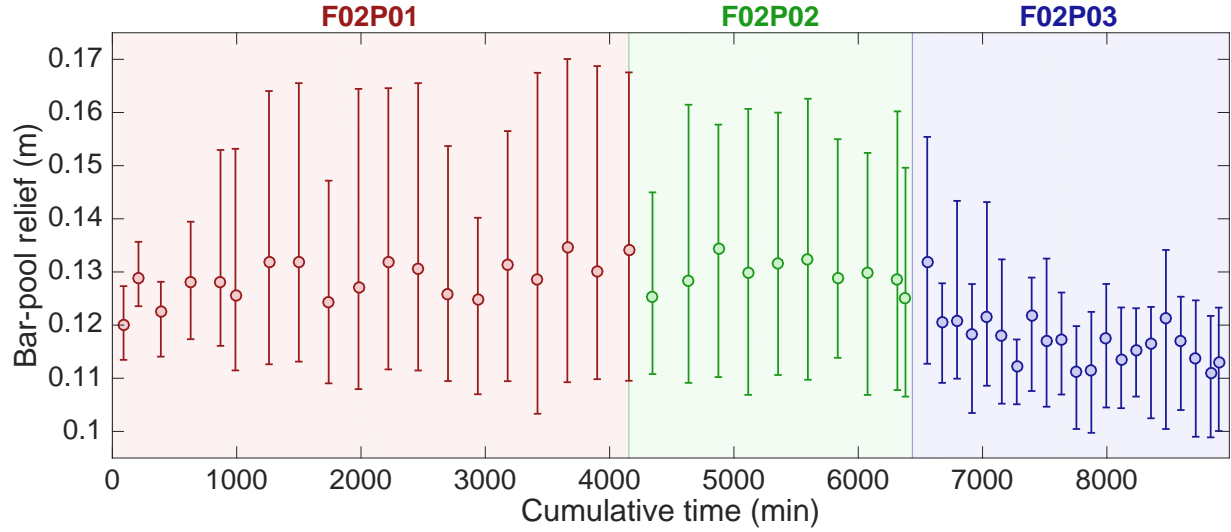


Figure 4.9: Relief between bar top elevation and pool bottom elevation throughout variable-width channel phases. Circles represent mean values and error bars represent minimum/maximun values.

expansions remained unsampled, potentially skewing data in favor of the narrower sections. Water surface elevations showed little lateral variability so water surface slopes are assumed to be relatively unaffected, but flow depth estimates exclude those outermost wide section areas. For this reason the median may be a more appropriate descriptor of the central tendency. Equilibrium median flow depth for F02P01 was 10 cm, approximately the same as for F01P01 (Figure 4.5b). Similarly, shear stress estimates ranged from 3 to 12 Pa, a range six-fold that of F01P01, but the median shear stress estimate, 5.5 Pa, was essentially the same (Figure 4.6b).

F02P02: Unsteady Flow, Steady Sediment Supply

Phase F02P02 lasted for 2280 minutes (38 hours) and saw very little overall changes from F02P01 (Figure 4.4). Throughout the phase bar-pool relief remained consistent and averaged around 13 cm (Figure 4.9). Equilibrium bed slope at the mean discharge was 0.007, approximately the same as in F02P01, and varied slightly throughout the hydrograph. In general rising limb bed slopes were shallower than falling limb bed slopes, but hysteresis was not clear (Figure 4.8c). Water surface slopes were approximately the same as in F02P01 and varied with discharge with a weak clockwise hysteresis. Median flow depths for the

mean discharge increased slightly from F02P01 with values around 11 cm and overall flow depths varied slightly with discharge (Figure 4.5b). Similarly, estimated shear stresses were approximately the same as in F01P01 with median shear stresses of 5.5 at the mean discharge of the hydrograph and overall shear stress estimates varying with discharge (Figure 4.6b).

F02P03: Unsteady Flow, Increased Sediment Supply

Phase F02P03, where the sediment supply was double, lasted 2520 minutes (42 hours). Mean bar-pool relief decreased from F02P02 by approximately 2 cm and ranges were halved (Figure 4.9). Bed slopes increased slightly from 0.007 in F02P02 to 0.0075 (Figure 4.4). Over the hydrograph there was very little variation in bed slope and there was no obvious relationship with discharge (Figure 4.8d). Water surface slopes saw a greater increase from 0.0055 in F02P02 to 0.0065 at the mean discharge. Water slopes varied with discharge and with very weak hysteresis (Figure 4.8d). Overall flow depths were slightly shallower than in F02P02, but the median values were approximately the same (Figure 4.5b). Shear stress estimates were slightly higher than in F02P02 with median values around 6.5 Pa at the mean discharge and varying with the hydrograph (Figure 4.6b).

4.4 Discussion

4.4.1 Steady versus Unsteady Flow

Although the shape and duration of unsteady flow hydrographs have been observed to have a minimal influence on overall reach-averaged morphological parameters (*Humphries et al., 2012; Wong and Parker, 2006*), variable discharge has been shown to result in differences in channel morphodynamics from equivalent steady flow conditions (*Nouh, 1990; Tubino, 1991*). In the straight-walled phases of our experiments neither hydraulic nor sediment transport parameters appeared to change much between the steady flow phase and the mean discharge during the first unsteady flow phase. Likewise, there was no appreciable difference in the general trend of grain sizes being transported (Figure 4.4). The migrating

bedforms that developed during F01P01 persisted through the unsteady flow phases without changes to bedform geometry, but their celerity under unsteady flow was approximately half of that under steady flow conditions (*Nelson and Morgan*, in review). The presence of bedforms and the fact that the entire distribution of grain sizes was mobile throughout the hydrograph suggests that surficial armoring never occurred. Additionally, because there were not prolonged periods of low flow between hydrographs there was likely little sediment settling, imbrication, or infiltration that could contribute to a higher initial threshold condition (*Ferrer-Boix and Hassan*, 2015). This lack of surface armoring may have contributed to the general trend of clockwise hysteresis in bed surface slope (Figure 4.8) (*Guney et al.*, 2013). Sand-bed streams are often reported to experience a clockwise hysteresis in bedload related to discharge over a hydrograph, while gravel-bed channels are often reported to experience a counterclockwise hysteresis, but such a relationship is not straightforward as there are many more factors involved (*Gunsolus and Binns*, 2018). Comparisons with studies reporting bedload hysteresis are difficult here because we were unable to make direct bedload measurements. For a constant-width channel water surface slope may be analogous to bedload, but the standard errors associated with our slope calculations negate any hysteretic trend in the slope values themselves. However, a clockwise hysteresis in bed slope may indicate a counterclockwise hysteresis in bedload. If we take $Q_s D_s \propto S_0 Q$, where Q_s is bedload and D_s is grain size (*Lane*, 1955), and assume D_s to be constant, for a given discharge only Q_s and S_0 would vary. Therefore, for a given discharge a steepening of the channel would correspond to a lower bedload rate, and vice versa. Therefore, our bed slope results for the unsteady flow runs in F01 (Figure 4.8) may suggest a counterclockwise bedload hysteresis in spite of the apparent absence of an armor layer.

Flow unsteadiness, a dimensionless parameter characterizing the magnitude and period of the hydrograph, has sometimes been used in attempts to determine trends in hysteretical relationships (*Song and Graf*, 1996; *Waters and Curran*, 2015). The unsteadiness is defined as the ratio of the change in flow depth and the time duration of the hydrograph scaled by

the inverse of shear velocity.

$$\Gamma_{HG} = \frac{1}{u_{*0}} \frac{\Delta H}{\Delta T} \quad (4.2)$$

where u_{*0} is the shear velocity at base flow, ΔH is the difference between flow depths at maximum discharge and minimum discharge, and ΔT is the hydrograph duration. It is clear from the above relation that higher differences in flow depth or shorter duration hydrographs produce a higher degree of unsteadiness. Our flow unsteadiness ($\Gamma_{HG} \approx 2 \times 10^{-5}$) remains relatively low compared to other unsteady flow experiments such as *Song and Graf* (1996) ($4 - 12 \times 10^{-3}$) and *Waters and Curran* (2015) ($0.4 - 1.1 \times 10^{-3}$), which may partly account for the weakness in hysteresis.

Numerical models and flume experiments with steady sediment supply and cycled hydrographs in constant-width channels have shown that at equilibrium channel adjustment over a hydrograph is confined to a limited reach immediately downstream from the feed boundary (*An et al.*, 2017a; *Parker et al.*, 2007; *Wong and Parker*, 2006). Downstream of this “hydrograph boundary layer” morphological parameters (e.g., bed elevation, surface sorting) are invariant to the variability of flow over the hydrograph. Although our associated depth-averaged modeling corroborate these studies (Chapter 3), our results here show no indication of a hydrograph boundary layer. *An et al.* (2017a) found that for wider grain size distributions, which can result in migrating sorting patches (bedload sheets), the concept of a hydrograph boundary layer is no longer applicable. Although effects of unsteady flow are diminished at greater distances downstream of the upstream boundary they are not negligible. In our experiments the grain size distribution was sorted too well for the development of bedload sheets. However, the presence of migrating low amplitude bedforms (*Nelson and Morgan*, in review) may create a nonlinear advection effect in bed material such as that observed by *An et al.* (2017a).

4.4.2 Effect of Increased Sediment Supply

For the straight-walled geometry of our experiments there was an obvious bed and water surface slope adjustment following the increased sediment supply in F01P03 (Figure 4.4 and 4.8). Channels are often expected and have often been reported to respond in this way (*Blom et al.*, 2017; *Lane*, 1955). Interestingly although the slope increased and the channel was able to convey the doubled sediment supply, indicated by the bedload rate exiting the flume, there was no significant change to bedform dimensions or dynamics (*Nelson and Morgan*, in review). There was a temporary increase in the sizes of grains exiting the flume, accompanied by an initially greater water surface slope (Figure 4.4). There was no indication that the distribution of grain sizes on the surface changed, although fining has been reported following a sediment supply increase, which may partly explain the temporary increase in exiting grain diameters. The increased bedslope resulted in slightly shallower flow depths and steeper water surface slopes, contributing to higher estimated shear stress values.

Unlike the straight-walled geometry, the variable-width channel did not experience a noticeable steepening with increased sediment supply (Figure 4.4 and 4.8). Although there have been few studies exploring changing sediment supplies in variable-width channels, this result is in contrast with them (Chapter 3; *Nelson et al.*, 2015). Additionally, as in F01P03, there was not any noticeable change in surficial sediment texture. Without a substantial change in slope or grain size the question arises regarding the mechanism by which the channel was able to reach a new equilibrium capable of transferring the increased sediment load. We should also note that shear stress estimates for the variable-width channel are not as reliable as for the straight-walled channel because reach-averaged uniform flow is not a valid assumption. Therefore the modest increases in estimated shear stress from F02P02 to F02P03 shown in Figures 4.4 and 4.6 are likely underestimations. Another parameter available to be adjusted to compensate for the increased sediment load is cross-sectional geometry (e.g., width per *Blom et al.* (2017)). Because our width was fixed, changes in cross-sectional geometry were made through changes in the lateral bed profile. The variation

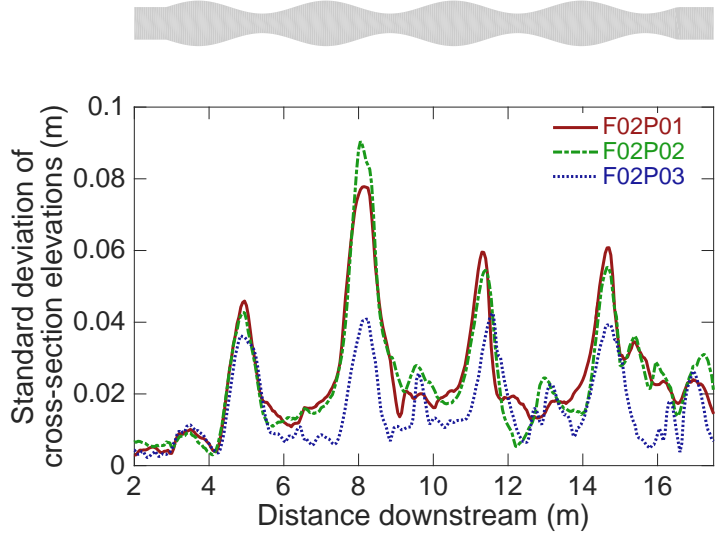


Figure 4.10: Standard deviation of elevations for each downstream cross-section for each of the phases in F02.

in lateral elevation for given cross-sections decreased in F02P03 from the previous phases, especially in sections where the width was decreasing (Figure 4.10). Furthermore, reductions in bar-pool relief (Figure 4.9) are likely to be accompanied by reduced form drag (similar to the reduction in roughness with reduced bedform steepness (*van Rijn*, 1984)). In the case of potential eddies forming at the pool entrance (such as occur on the lee side of dunes (*Nelson and Smith*, 1989)) the eddy region would also be reduced with a reduction in relief. Mean bar-pool relief remained lower for the increased sediment supply phase for all steps of the hydrograph (Figure 4.11). This decreased relief is also in contrast with other studies (Chapter 3; *Nelson et al.*, 2015) which suggest that bar-pool relief is invariant to sediment supply. *Nelson et al.* (2015) hypothesized that unsteady flow was likely necessary to fill pools under increased sediment supply; however, numerical modeling results from Chapter 3 show relief varying over the hydrograph, such as in Figure 4.11, with mean relief largely invariant to sediment supply. The discrepancies highlight the need for further exploration into the controls on forced bar features under conditions of unsteady flow and sediment supply.

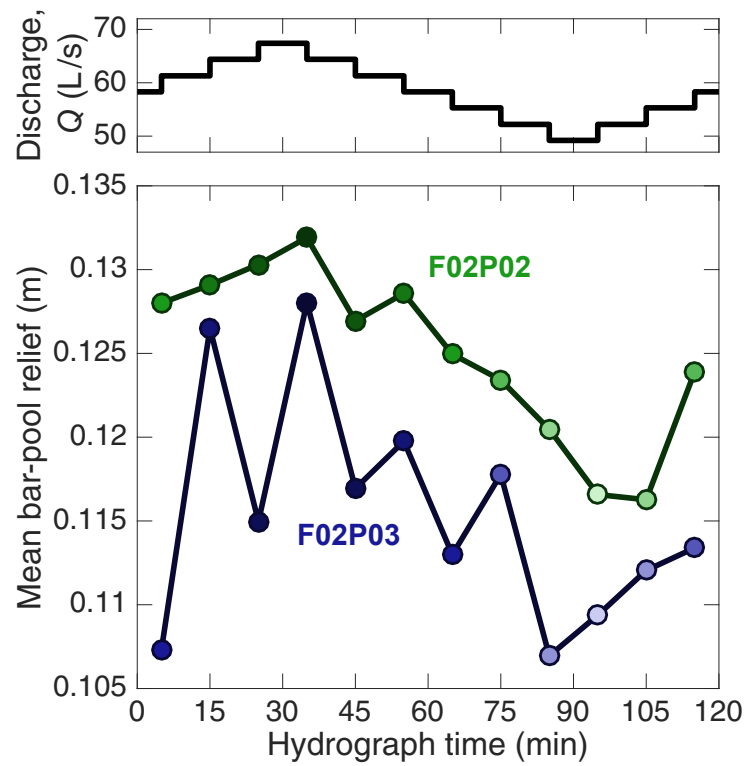


Figure 4.11: Mean bar-pool relief for unsteady F02 phases.

4.4.3 Variable-width Gravel-bed Morphodynamics

Previous studies have explored morphodynamics in channels with sinusoidal width variations (*Bitner*, 1994; *Jang*, 2014; *Repetto et al.*, 2002; *Tsujimoto*, 1987; *Wu and Yeh*, 2005; *Wu et al.*, 2011), however, few explicitly compare with a comparable constant-width channel (but see Chapter 3). Relative to a channel with a constant downstream width, Chapter 3 showed that bed slopes vary in channels with variable width depending on the wavelength and amplitude of width variations. More dramatic width changes (i.e., higher amplitudes and shorter wavelengths) result in steeper reach-averaged channel gradients. For width variations having the same amplitude and wavelength as we used in the flume, Chapter 3 also showed a mean bed slope greater than in an equivalent constant-width channel. Although, for other variable-width geometries Chapter 3 showed bed slopes shallower than for a constant-width channel.

Downstream variations in channel width in the field are often associated with the development of riffles and pools co-located with those width transitions. Our results corroborate field studies that have noted the infilling of pools following increased sediment loading (*Brew et al.*, 2015; *Madej*, 2001). It is often reported that increased sediment supply serves to homogenize the downstream elevation profile (*Andrews*, 1982; *Kappesser*, 2002; *Lisle*, 1982; *Lisle and Hilton*, 1992). The reduced bar-pool relief between F02P02 and F02P03 shows a similar trend (Figure 4.9), even when substantial forcing elements (e.g., rigid width constrictions) are present. The tendency of relief to trend with the hydrograph (Figure 4.11) is also consistent with field studies related to riffle-pool maintenance mechanisms. Early on researchers noted that higher flows were important for maintenance of these features (*Gilbert*, 1914; *Leopold et al.*, 1964), and our results also show that relief is enhanced at higher discharges. In natural coarse-bed channels, very little bedload is transported during baseflow conditions and what deposition does occur is often in pools. Our results highlight the ability of higher discharges to maintain riffle-pool features in variable-width channels.

4.5 Conclusions

We performed a series of experiments in a straight, sediment-feed flume with a sand-gravel sediment mixture. The first experiments involved a constant-width channel and three phases were performed. 1) Steady discharge, constant sediment supply; 2) stepped hydrographs, constant sediment supply; and 3) stepped hydrographs, doubled sediment supply. The same phases were then performed in a variable-width channel whose mean width was the same as the constant width channel. The primary conclusions of our investigation may be summarized:

1. Similar to constant-width channels, mean flow parameters for variable-width channels vary little between unsteady flow and a comparable steady discharge.
2. Variable-width channels under unsteady flow respond to sediment supply increases through reduction in topographic relief between bars and pools and homogenization of cross-stream elevations, rather than an overall adjustment to bed slope.
3. Fluctuations in bar-pool relief over the course of a hydrograph corroborate theories related to riffle-pool maintenance which suggests that maintenance occurs at higher discharges.

Discrepancies between our results presented here and those from related numerical modeling (Chapter 3) emphasize the importance for further investigation into the relationship between channel response to increased sediment supply and width variability.

Chapter 5

Hydro-geomorphology of the middle Elwha River, Washington, following dam removal

5.1 Introduction

How fluvial systems respond and adjust to disturbances, both natural and anthropogenic, is a primary concern of river managers, stream restoration specialists, and stakeholders with special interest in specific streams or stream networks. Projects with the intent of restoring or rehabilitating river systems often incorporate goals associated with the physical, chemical, and/or biological integrity of the system to at least some semblance of “natural” or pre-anthropogenic conditions (*Bernhardt et al.*, 2005). A common goal in rehabilitation projects is the rejuvenation, creation, or maintenance of habitat for certain in-stream species. A common disturbance that managers and professionals must plan for is an altered sedimentological regime. The ability to understand and predict how stream channels adjust to these changing conditions, especially in the context of mesoscale geomorphic features that provide habitat, is an important component of planning.

River systems can be subjected to dramatically altered sedimentological regimes through a number of avenues. Natural processes like landslides (*Benda and Dunne*, 1997; *Schuerch et al.*, 2006; *Sutherland et al.*, 2002), meander cutoffs (*Zinger et al.*, 2011), and bank/bluff erosion (*Gran and Czuba*, 2017) can contribute to increased sediment supply. Human activities such as urbanization (*Chin and Gregory*, 2001; *Wolman and Schick*, 1967), deforestation (*Derose et al.*, 1993), and road construction (*Luce and Black*, 1999) often also have the effect of increasing the sediment delivered to river channels. Warming global temperatures associated with climate change are generally accepted to be accompanied by an increase in the frequency and magnitude of large landscape-scale disturbances like wildfires (*West-*

erling *et al.*, 2006) and floods (Knox, 2000) which are also potential sources of escalated sediment supplies. Restoration activities themselves often include increased sediment loads (e.g., gravel augmentation). In recent decades the restoration practice of dam removal has become increasingly common (Bellmore *et al.*, 2017; Foley *et al.*, 2017), and is a potential source for extremely large volumes of sediment in many systems.

The potential for dramatic changes to sediment inputs have led researchers to explore various aspects of channel response to pulsed, punctuated, and continuous increases in sediment supply. Sediment supply has been shown to be a controlling factor in a number of morphological stream features such as bed armoring (Dietrich *et al.*, 1989; Venditti *et al.*, 2010b), grain size patches (Nelson *et al.*, 2009) and sorting patterns (Lisle *et al.*, 1993; Venditti *et al.*, 2012), and bedforms (Kleinhans *et al.*, 2002; Venditti *et al.*, 2017). Specifically, researchers have used field expeditions, remote sensing, physical experimentation, and numerical modeling to explore the effect of sediment supply changes due to meander cutoffs (Zinger *et al.*, 2011), landslides/debris flows (Brummer and Montgomery, 2006; Hoffman and Gabet, 2007; Nelson and Dubé, 2016; Sutherland *et al.*, 2002), flood events (Lisle, 1982; Madej, 1999), sediment augmentation (Humphries *et al.*, 2012; Juez *et al.*, 2016; Nelson *et al.*, 2015; Sklar *et al.*, 2009), mining operations (Ferguson *et al.*, 2015; Pickup *et al.*, 1983), reservoir sediment releases (Rathburn and Wohl, 2003, 2001; Wohl and Cenderelli, 2000), and general supply increases (Jackson and Beschta, 1984; Lisle *et al.*, 1997, 2000; Madej, 2001; Maturana *et al.*, 2014; Podolak and Wilcock, 2013). Additionally, with the growing frequency of dam removal projects, studies related to subsequent geomorphic effects have been plentiful (Collins *et al.*, 2017; Cui *et al.*, 2014; Ibáñez *et al.*, 2016; Pace *et al.*, 2017b; Pearson *et al.*, 2011; Pizzuto, 2002; Zunka *et al.*, 2015).

Given the wide array of possible factors that can bring about an increase in sediment supply, the response of mesoscale geomorphic units (e.g., riffles and pools) to such changes has often been the topic of previous research. These studies have repeatedly shown increased sediment supplies resulting in pool-filling, homogenization of the bed topography, and bed

surface fining (*Lisle*, 1982; *Madej*, 1999; *Madej and Ozaki*, 1996; *Schmidt*, 1990; *Wohl and Cenderelli*, 2000). However, these studies have been largely one-dimensional and increased sediment supply rates were often modulated by extreme hydrological events. Additionally, the increase to sediment supply in these studies were often temporary in nature rather than sustained. How a natural channel with riffle-pool morphology may respond to a sustained elevated sediment supply level that is not coincident with increased discharge is not well understood.

The removal of Glines Canyon Dam on the Elwha River in Washington State, as a part of major restoration efforts that have been taking place there for the last several years, offers a unique opportunity to study the effect of dramatically increased sediment supply rates on a natural system. Of particular interest is how downstream reaches, which are important spawning habitat for salmonids, respond to the increased sediment loading. Because Glines Canyon Dam was operated as a run-of-the-river facility, the increased sediment supply to downstream reaches is disconnected from any major changes to hydrology. In this paper we explore how a gravel-bed river with riffle-pool morphology responds to an increased sediment supply that is not accompanied by changes to or extreme events related to hydrology. We seek to understand how sediment supply increases and resultant geomorphic changes adjust capacity for channel changes and how riffle-pool maintenance is potentially connected to sediment supply. We use repeat topographic surveys to characterize geomorphic changes, historic aerial imagery to quantify planform channel changes, and hydrodynamic modeling to estimate flow characteristics following dam removal.

5.2 Methods

5.2.1 Study site

The Elwha River is situated on the northern part of the Olympic Peninsula in Washington State, USA (Figure 5.1, bottom right inset). The river has its headwaters in the Olympic Mountains and flows northward approximately 70 km to its mouth at the Strait of Juan

de Fuca. Historically, two dams have impeded sediment continuity along the Elwha River. Elwha Dam, completed in 1913, was located at river kilometer 7.4 and stood 33 m high. Glines Canyon Dam, completed in 1927, was located at river kilometer 21.6 and stood 64 m high. Between 2011 and 2014 the Elwha River was the site of the largest dam removal, in terms of dam height and volume of impounded sediment, in history. Removal of both dams began in September 2011. By March 2012 the lower Elwha Dam was completely removed. On 14 October 2012 bedload began being transported over then-partially removed Glines Canyon Dam and by September 2014 the dam had been completely removed (see *Warrick et al.* (2015) for more details on the dam removal procedure). Lake Mills, the reservoir impounded by the upper Glines Canyon Dam, was estimated to have stored $21.6 \pm 3.0 \times 10^6$ m³ of sediment prior to dam removal (*Draut and Ritchie*, 2015).

Hydrology for the Elwha River is characterized by a bimodal distribution of flows over the hydrologic year. Flashy, higher peak flows occur with late fall and winter rain storms while sustained high flows due to snowmelt occur from late spring to mid-summer (Figure 5.2b). The USGS stream gage at McDonald Bridge (1204550) provides continuous discharge measurements of the middle Elwha River (Figure 5.1). Discharge return periods, computed with the Weibull plotting position method, generally follow a power-law function in semi-log space (Figure 5.2a). While not equal, the recurrence intervals in Figure 5.2a are in very close agreement with the results of *Mastin et al.* (2016). They also note that because Glines Canyon Dam was operated as run-of-the-river, dam operations had a negligible effect on peak flow values and so the entire period of record is usable. Furthermore, *Mastin et al.* (2016) report no trend in the magnitude of annual peak flows for the Elwha River through water year 2014. Throughout the period of dam removal (September 2011 to September 2014) the Elwha River experienced a relatively muted hydrologic regime, with neither mean daily flow nor instantaneous peak flow ever exceeding the two-year recurrence interval discharge ($Q_2 = 411$ m³/s; Figure 5.2c).

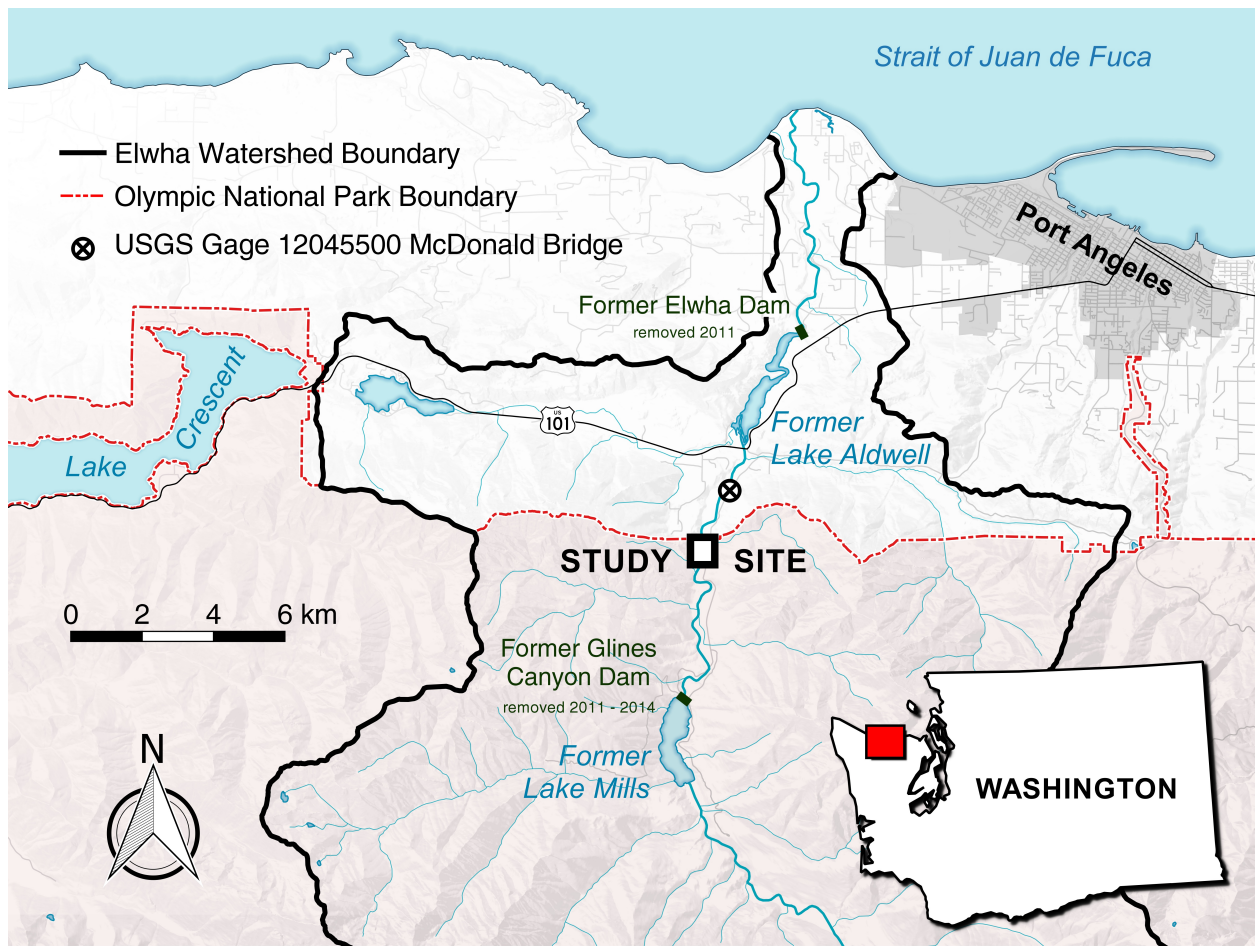


Figure 5.1: Location of the Elwha River on the Olympic Peninsula and the location of the study site on the middle Elwha River, just within Olympic National Park.

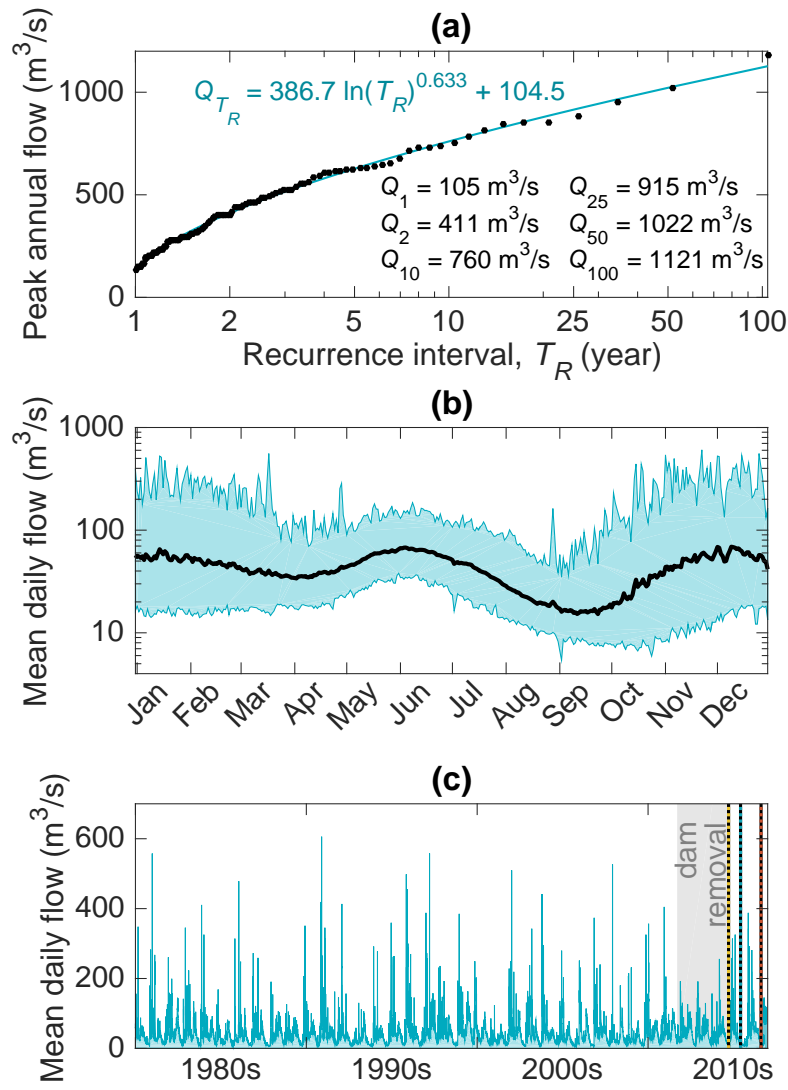


Figure 5.2: (a) Annual peak discharge versus return interval for the middle Elwha River from 1897 to 2016. (b) Annual trends in mean daily discharge between 1920 and 2017 for the middle Elwha River. The black line represents the mean for each day of the calendar year. The upper and lower limits represent the maximum mean daily discharge and the 5th percentile, respectively. (c) Mean daily discharge in the middle Elwha River between 1980 and 2017. The gray shaded box indicates the duration of removal for Glines Canyon Dam. The vertical lines indicate the dates of surveys reported in this paper. Flowrate data for each plot were collected at USGS gage 12045500 on the Elwha River at McDonald Bridge (available at <http://waterdata.usgs.gov>).

Our study reach is located on the middle Elwha River, between the two former dam sites. The reach is approximately 15 km upstream from the river mouth and 5 km downstream from the former Glines Canyon Dam site (Figure 5.1). The site is also approximately 1.5 km upstream from the McDonald Bridge USGS streamgage location. The study reach is approximately 900 m in length and is mostly located just within the Olympic National Park boundary (Figure 5.3). The reach is relatively straight (sinuosity of 1.06) with a slope of 0.007 and is composed of three riffle-pool sequences which are co-located with, and apparently forced by, variations in bankfull channel width (*Brew et al.*, 2015; *Morgan and Nelson*, 2016; *Nelson et al.*, 2015). The reach is coincident with two cross-sections surveyed in 1994 for the Environmental Impact Statement (*Department of the Interior*, 1995a) and seventeen cross-sections collected in 2011 as a part of the pre-removal terrain (Jennifer Bountry, USBR, personal communication). Located within the study area are also two locations of pebble counts collected in 1994 (*Department of the Interior*, 1996), whose locations are shown within the area of interest in Figure 5.3.

The reach immediately downstream from, and partially coincident with, our study site was studied by *Free* (2015) from September 2012 (before bedload began passing Glines Canyon Dam) to August 2014 (nearly coincident with our first survey date in September 2014). From 2012-2013 the area experienced net aggradation in the form of bar building and the filling of interstitial space between larger clasts by sands and silts, but no migration or planform changes were noted. From 2013-2014 the area underwent net degradation accompanied by a large influx of large wood within the bankfull channel. Throughout the 2012-2014 study period of *Free* (2015), surficial D_{84} diameters substantially fined from boulders to fine gravel and coarsened again to cobbles. Because of the dampened annual hydrological maxima from 2011-2014 the true effects of dam removal are difficult to evaluate during this period.

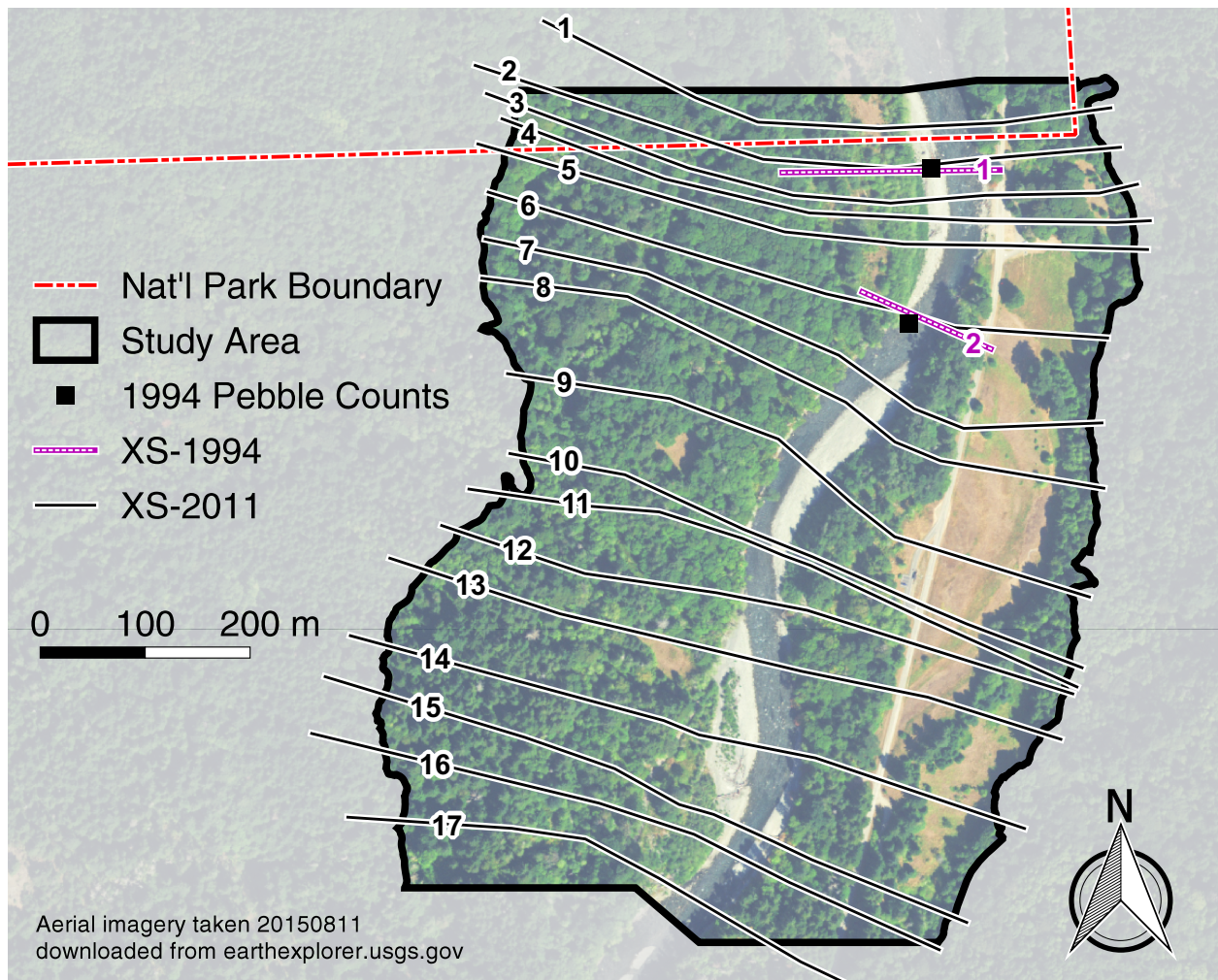


Figure 5.3: Study area reach on the middle Elwha River, showing the extent of the area of interest and the locations of other data of interest. Flow is from bottom to top.

5.2.2 Ground surveys

Three ground surveys were conducted for the study reach in consecutive years from 2014 to 2016. The first survey was conducted from 17 – 20 September 2014, the second from 29 May – 2 June 2015, and the third from 10 – 13 August 2016. Throughout this paper these surveys are referred to as 201409, 201506, and 201608, respectively (in general, data presented in this chapter are labeled by the date when they were collected as *yyyy*, *yyymm*, or *yyyymmdd*). Bathymetry and topography were measured using RTK-GNSS technology. Channel banks and shallower, slower-moving in-channel areas were surveyed using a rod-mounted Topcon GR-5 receiver coupled with a Topcon Tesla controller. The study reach was delineated into approximately 100 cross-sections, spaced 8–10 meters apart as shown in Figure 5.4 (*Morgan and Nelson, 2016*). Lateral point spacing in a single cross-section was generally < 1 m. Deeper, swifter in-channel areas were surveyed by coupling the Topcon equipment with a Seafloor Systems Inc. Sonarmite (Hydrolite TM) single-beam echosounder mounted on an inflatable kayak. Survey data were manually filtered to remove points with obviously erroneous elevation values. Data points collected in places not coincident with the ground surface (e.g. large wood) were also removed for the purpose of digital elevation model creation.

Due to dense vegetation on the floodplain, the RTK-GNSS receivers did not have adequate reception to extend our surveys far beyond the top of the channel banks. To create a continuous elevation surface of the valley bottom we combined our survey points with aerial lidar data collected in close temporal proximity to our survey dates. The 201409 survey was combined with lidar flown in October 2012¹. The 201506 and 201608 surveys were combined with lidar datasets flown in February 2015 and March 2016, respectively (both unpublished). The average point densities for the three lidar datasets were 1.67, 1.39, and 2.45 points per m², respectively. In each case the lidar point clouds were clipped to remove in-channel areas included in the ground survey. The survey point clouds were then combined with the lidar

¹downloadable from <http://nationalmap.gov>

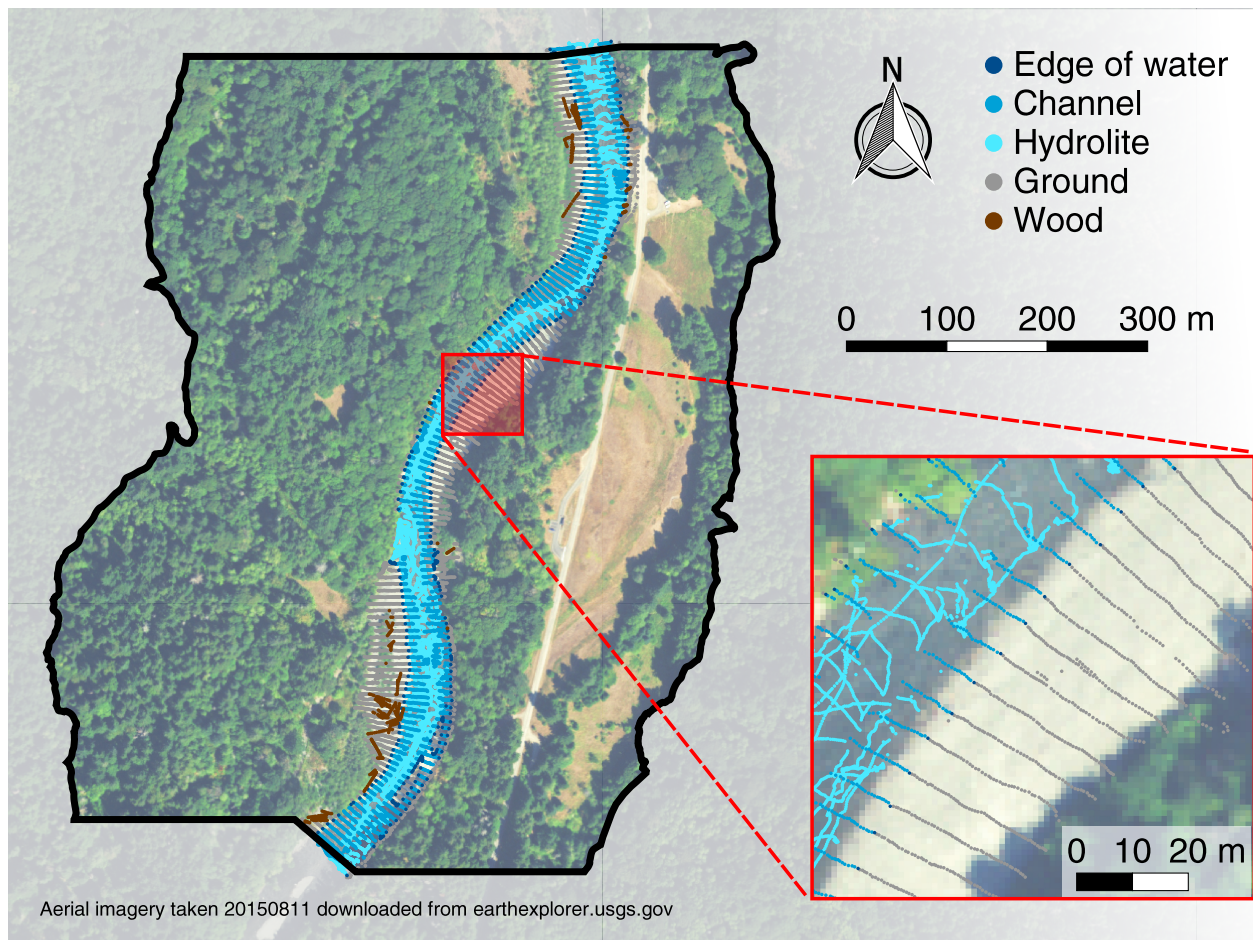


Figure 5.4: Map of the area of interest, showing the general surveying methodology. Example from the 201506 survey. Flow is from bottom to top.

point clouds and interpolated into rasters ($1\text{ m} \times 1\text{ m}$, using the natural neighbor algorithm) to produce three continuous surface digital elevation models (DEMs) corresponding to the three survey dates. The DEMs were finally clipped to include only the area of interest.

During each ground survey period data were also collected related to surficial sedimentology in the study reach. The 201409 survey included 19 images collected with a Canon EOS Rebel T3i camera (18.0 Megapixel) equipped with a EF-S 18-55mm f/3.5-5.6 IS Type II lens. Imagery was acquired by setting the lens focal length to 18mm, holding the camera at a height of approximately 2 m above the ground, and orienting the sensor approximately orthogonal to the ground surface. A gravelometer with square openings in $\frac{1}{2}\text{-}\psi$ units (*sensu Parker and Andrews, 1985*) from 2 mm to 128 mm ($1 \leq \psi \leq 7$) was included in the frame of each image for the purpose of determining the image resolution in mm/pixel. Because of time constraints and a limited number of surveyors, no explicit field measurements of grain sizes were collected during the 201409 survey. The 201506 survey included 56 images collected with a Canon EOS Rebel XSi camera equipped with a EF-S 10-22mm f/3.5-4.5 USM lens. Imagery was acquired in the same fashion as during the 201409 survey and two field Wolman-style pebble counts (*Wolman, 1954*) were also conducted. During the 201608 survey ~2500 images were collected with a Canon EOS Rebel T3i equipped with a EF-S 18-55mm f/3.5-5.6 IS Type II mounted to a hand-held painting pole. Images were acquired by holding the pole above the head and pointing the sensor at an oblique angle to the ground surface. The images were grouped into 10 different areas and processed using Agisoft Photoscan (*Agisoft, 2016*) to produce ortho-rectified images of the ten areas.

Each image from all three surveys was subject to a manual “digital pebble count”. The 201409 and 201506 images were each processed as a single sample, while each of the ten orthophotos from 201608 was separated into two or three smaller images, depending on the size of the area (resulting in 110 total grain size distributions spanning the three surveys). Equidistant grids, having approximately 100 nodes each, were superimposed over the images. At each node the diameter of the grain in the underlying image was measured at the medial

(or intermediate) axis. We make the assumption that the shortest axis is perpendicular to the camera and thus only the long and intermediate axes are visible. This diameter, measured in pixels, is multiplied by the image resolution to obtain grain diameters in mm. Rather than calculating distribution statistics on the measured diameters directly the lengths were separated into $\frac{1}{2}\psi$ bins, similar to how they would be in a field sampling method (e.g., pebble counts), in order to smooth any errors in pixel measurements that may have occurred. Following the “voidless cube” model of *Kellerhals and Bray* (1971) we consider the distributions obtained by our pebble counts to be interchangeable with distributions obtained by standard mass sieving procedures (all while noting the limitations discussed by *Bunte and Abt* (2001)).

5.2.3 Measuring geomorphic changes

Changes in the geomorphology of our study reach were evaluated using two different methods. First, the cross-section data collected in 1994 and 2011 provide an opportunity to compare discrete cut lines through the DEMs created with our datasets to pre-removal topography. With only two cross-sections from the 1994 dataset coincident with our study reach, it is difficult to draw any definitive patterns from these comparisons. The difficulties are exacerbated by the fact that the two cross-sections are relatively close together; however, these cross-sections nevertheless represent informative observations of channel conditions two decades before dam removal. With seventeen cross-sections from the 2011 dataset falling within our study reach the comparison of these data with our own provides a more complete picture of the differences between pre-removal and post-removal topography. These cross-sections are also well-spaced throughout the study reach and therefore provide a more thorough picture (in space and time) of the net character of geomorphic changes following dam removal.

Our detailed DEMs corresponding to each survey date and encompassing the entire valley bottom provide a method to compare topographic differences that are more spatially contin-

uous. Error analysis and DEM differencing was carried out using the Geomorphic Change Detection tool² (*Wheaton et al.*, 2010a,b). The tool allows for systematic propagation of elevation errors from the original input RTK-GNSS and lidar point clouds and the rasterization process through to the elevation rasters. The tool uses a fuzzy inference system (FIS) to incorporate user-defined errors and uncertainties associated with different parameters. For input into the FIS we used point quality, point density, and slope. The RTK-GNSS equipment provides estimates of vertical accuracy for each data point. These data, along with a blanket vertical accuracy of 20 cm for each lidar data point (a conservative value based on the 2012 lidar’s reported value of 15 cm, (*Woolpert, Inc.*, 2013)), were used to create the point quality raster. The point density raster was calculated as the points per each 1 m × 1 m raster cell. Slope rasters were generated from the DEM rasters. These input parameters are fed through the FIS to create an output raster of uncertainty associated with each survey’s DEM raster.

When differencing the DEMs to compute elevation changes between survey dates the uncertainty rasters are incorporated into a new uncertainty raster associated with the DEM of difference (DoD). If a DoD raster cell shows a magnitude difference that is exceeded by the uncertainty of that raster cell the DoD cell value can be discarded, thereby creating a “thresholded” DoD. Using the thresholded DoD, we computed spatial patterns of measurable erosion/deposition and the magnitudes of each. We also calculated estimates of the total area and volumetric changes between survey dates, including uncertainty.

5.2.4 Aerial imagery surveys

We place the topographic changes we measure during 2014–2016 in the context of historical channel conditions by making use of historical aerial imagery of our study reach. Images dating back to 24 July 1939 allow us to determine whether general characteristics of planform evolution we quantify for our study reach are longer term tendencies or are trends that

²downloadable from <http://gcd.joewheaton.org/>

appear following dam removal. Specifically, we are interested in determining how channel planform parameters such as migration rates, bankfull channel widths, and channel sinuosity have been changing long-term, under the influence of Glines Canyon Dam, and short-term, since dam removal.

Imagery was downloaded from USGS EarthExplorer and Google Earth from 12 dates between 1939 and 2016, with higher temporal resolution after 2006 (Figure 5.5). In each image “active channel” boundaries were manually delimited and defined as the unvegetated width, and analogous to bankfull channel width (*Brew et al.*, 2015). It is assumed that the lack of vegetation indicates frequent recent flows that would inundate the area (*Draut et al.*, 2011). From these essentially longitudinal banklines, the channel centerline was also defined as the midpoint between the active channel banks. Lateral channel migration was calculated as the area between consecutive centerlines divided by the mean length of the two centerlines, similar to *Gillespie and Giardino* (1996) and *Konrad et al.* (2011). From this length an average rate of migration was determined by dividing by the time between the two centerline images. Active channel widths were measured perpendicular to the channel centerline at 2 m longitudinal spacings. Channel sinuosity was calculated by dividing the length along the channel centerline by the straight-line distance between the centerline endpoints.

5.2.5 Hydrodynamic modeling

Detailed measurements of hydrodynamic variables are difficult and time-consuming to measure, and for higher discharges can be potentially very dangerous to collect. Therefore, we used a hydraulic model to characterize flow depth, velocity, and shear stress as the channel underwent geomorphic changes post dam removal. In this study we use the Nays2DH solver distributed freely as a part of the International River Interface Cooperative (iRIC, www.i-ric.org, *Nelson et al.*, 2016). Nays2DH approximates the two-dimensional, depth-averaged, shallow water equations for the horizontal flow field. Although fully three-dimensional models can potentially better capture the horizontal and vertical convergence and divergence

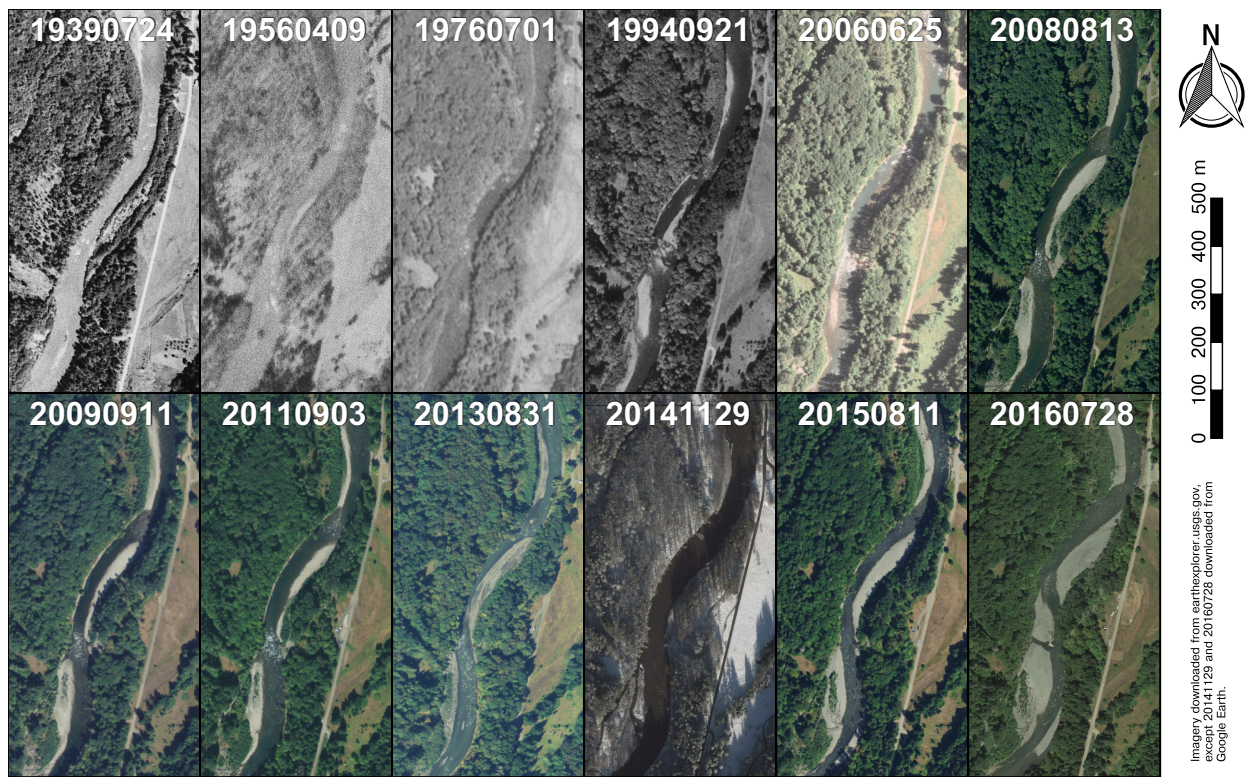


Figure 5.5: Aerial photographs used to delineate active channel margins and centerlines. Flow is from bottom to top.

of flow associated with riffles and pools, the degree of detail in the topographic data required as input, the detail of hydrodynamic data required for calibration, and the increased computational time made two-dimensional modeling the preferred choice.

Although Nays2DH has the ability to simulate flow on a general, non-orthogonal coordinate system, we discretized our domain into a rectangular grid with both a lateral and longitudinal spacing of 1 m (equivalent to the DEM raster grids). Elevations for the grid nodes were taken from the DEM grid which was calculated using only ground surface data points (e.g., no large wood or vegetation were rasterized or parameterized). The computational domain was extended beyond our area of interest in the upstream direction, but only results were considered for the grid cells located within the interest area. Nays2DH uses Manning's n for roughness closure, and this parameter was calibrated using each survey dataset. In Nays2DH the drag coefficient is calculated using both Manning's n and flow depth, such that the drag decreases with increasing depth; therefore, a single n value may be used for multiple discharges and flow depths. Calibration for Manning's n was performed by running models using each survey geometry with the discharge at the time of the survey and n values ranging from 0.01 to 0.09 in increments of 0.01. Results from the models were compared to measured "edge of water" locations from topographic surveying. The model corresponding to the lowest mean horizontal distance between the measured and calculated "edge of water" was considered to be the best Manning's n value. Although floodplain roughness often differs greatly from within-bankfull roughness, especially in the presence of thick vegetation, without data necessary to parameterize such a difference we imposed a single Manning's n for the entire spatial domain.

Ranges of discharges have been shown to be important for a number of geomorphological and sedimentological processes associated with channel morphodynamics. This is also the case for the maintenance of riffles and pools, for which one of the leading hypotheses, "velocity-reversal", is based on variable flows (*Keller*, 1971b). Our hydrodynamic modeling procedure included simulating flows ranging from a base flowrate ($Q_{low} = 8 \text{ m}^3/\text{s}$) to the

100-year recurrence interval discharge ($Q_{100} = 1121 \text{ m}^3/\text{s}$). Additionally, the mean annual discharge ($Q_{avg} = 44 \text{ m}^3/\text{s}$) was modeled. The discharges modeled, and their corresponding recurrence-intervals, are shown in Figure 5.2a. The range of discharges for a single geometry can be compared with one another to examine how the spatial distribution of hydrodynamic variables change over discharge, or a single discharge for each of the survey geometries can be compared with one another to explore how the spatial distribution of hydrodynamic parameters have changed over time as the channel has changed. Additionally, flow parameters (e.g., flow depth and velocity) can be used to aid in the delineation of riffles and pools or other geomorphologic units within the main channel.

5.2.6 Riffle-pool delineation

To characterize changing hydrogeomorphology related to riffles and pools it is necessary to spatially delimit these features. Numerous methods exist for riffle-pool delineation and many studies simply fail to report the methodology and criteria used to define their boundaries. In an attempt to alleviate the inherent subjectivity and unrepeatability of field mapping (*Poole et al.*, 1997; *Radinger et al.*, 2017; *Roper and Scarneccchia*, 1995), we delineated geomorphic features using fuzzy c -means (FCM) classification, a method common to pattern recognition and automatic typological analysis (*Legleiter and Goodchild*, 2005; *Tamminga*, 2016; *Wallis et al.*, 2012). FCM uses fuzzy logic (data points can have partial membership in multiple clusters) to group similar data points into “soft” clusters, having indefinite boundaries (*Bezdek*, 1981). More information related to the FCM algorithm is included in Appendix A.

Variables used as input for the FCM algorithm were model-predicted flow depth and shear stress. To ensure consistent depth and shear stress characteristics for each delineated geomorphic unit over time, we combined the variables from each survey dataset to create a single set of input variables (*Wallis et al.*, 2012) prior to the FCM classification. Performing the FCM algorithm on each survey separately would result in three different and distinct

fuzzy c -partitions which would be difficult to compare as the clusters from each survey would not necessarily be characterized by the same values (i.e., pools delineated from the 201409 survey would likely have different hydrodynamic characteristics than pools defined from the 201608 survey). Furthermore, hydrodynamic variables are highly dependent on discharge and so there is a need to determine which discharge to use. Other riffle-pool studies use data collected or calculated for low or baseflow conditions because these are the conditions generally used to describe riffles and pools (e.g., *Wyrick and Pasternack*, 2014). For rivers influenced by upstream impoundments such a specification may be easier as baseflows are often consistent, being controlled by dam operations. For our purposes we used hydrodynamic data modeled for $44 \text{ m}^3/\text{s}$, the mean annual flow measured between 1920 and 2017. This discharge is less than half the one-year flow ($Q_1 = 105 \text{ m}^3/\text{s}$) and is therefore assumed to be well below bankfull discharge and characteristic of low/base flow conditions.

Further input requirements for FCM include a specified number of clusters and a fuzzy weighting exponent. The weighting exponent controls the degree of fuzziness with greater exponents creating a fuzzier partition. The number of clusters and weighting exponent can be optimized using cluster validity techniques whose objective is to maximize the similarity within a cluster while minimizing the similarity between different clusters (*Bezdek*, 1981; *Gath and Geva*, 1989). Here, we used the separationcompactness indices introduced by *Zahid et al.* (1999) and *Xie and Beni* (1991) which produced optimized values for the number of clusters and the fuzzy weighting exponent of 5 and 1.9, respectively. More information related to cluster verification is included in Appendix A. Fuzzy membership information can be “defuzzified” using a number of different methods. One method is to simply assign a data point full membership into the cluster for which it has the highest degree of membership. Another method is to use an α -cut, where a threshold, α , is specified and a data point is assigned full membership in a cluster only if its degree of membership is greater than α . In this method some points, whose maximum degree of membership for any cluster does not exceed α , will not be assigned to a cluster. We used the α -cut method with a value of α

$\alpha = 0.5$, indicating that a datapoint would need at least half-membership in a cluster to be considered part of that cluster. Clearly, fewer data points would be associated with any specific cluster with higher values of α .

Because none of the input variables for the FCM algorithm include spatial information the output does not reflect the spatial distribution of the cluster or any points membership therein (*Nelson et al.*, 2014). However, these data points, and their associated membership in any cluster, can be viewed in their geographical locations to show the spatial arrangement of the clusters in geographical space. Using the original FCM output membership values we can create maps of cluster arrangement with “fuzzy” boundaries, or using the “defuzzification” technique described above we can delineate clusters, with each having a crisp boundary.

5.3 Results

5.3.1 Ground surveys

Between the 201409 survey and the 201506 survey the maximum instantaneous flow measured at the USGS McDonald Bridge gaging station was $447 \text{ m}^3/\text{s}$ (10 December 2014, 19:15:00), with approximately 6 hours of total time spent above the 2-year flow ($411 \text{ m}^3/\text{s}$) and approximately 20 days of total time above the 1-year flow ($105 \text{ m}^3/\text{s}$). The 2-year flow was exceeded by two different events (on 9 – 10 December 2014 and 6 February 2015). Between the 201506 and 201608 surveys the maximum instantaneous flow was $881 \text{ m}^3/\text{s}$ (17 November 2015, 15:15:00), with approximately 4 hours of total time spent above the 10-year flow, 2 days of total time spent above the 2-year flow, and 31 days of total time spent above the one-year flow. During this time period four events had peak instantaneous discharges that exceeded the 2-year event, and only one that exceeded the 10-year event (on 17 November 2015).

Comparisons of field pebble counts and digital photo pebble counts of the same areas are shown in Figure 5.6. In general the 201608 survey shows good agreement between field and photo pebble counts. The photo pebble counts for 201506 are consistently finer than the field

pebble counts. This can be attributed, at least in part, to a number of potential factors. First, field and photo pebble counts were performed by different operators and considerable variability has been shown among different surveyors sampling the same site (*Daniels and McCusker*, 2010; *Marcus et al.*, 1995). *Olsen et al.* (2005) estimate that for grain size data sampled by different observers changes less than 15% are not detectable. Furthermore, even experienced field surveyors are prone to operator bias toward sampling larger grains (*Bunte and Abt*, 2001). Other researchers have also found that image-based methods underestimate grain-sizes relative to field-based methods (*Strom et al.*, 2010; *Whitman et al.*, 2003). Additionally, photo-sieving methods necessarily assume that the intermediate axis of each sampled grain is measurable from the image. However, the medial axis may not be completely visible or adequately measurable due to partial grain burial or occlusion as well as particle angle orientation. Although “correction” techniques for photographic grain size analyses have been suggested (*Adams*, 1979; *Kellerhals and Bray*, 1971), we have elected to proceed with the original results from the photo-sieving technique.

There is a great deal of variability in the magnitude and spread of grain size distributions within each survey depending on the location of the sample image. There is no clear longitudinal trend in distributions, although images sampled farther away from the main channel show an increased proportion of finer grains. Figure 5.7 summarizes all grain size distributions calculated for each survey date. D_{84} (grain diameter for which 84% is finer) values from 201409 agree well with those reported by *Free* (2015) the previous month. There is a clear and dramatic fining from pre-removal distributions measured in 1994 with median grain diameter (D_{50}) values roughly 2–4 ψ -classes finer in our photo-sieved samples. Our sampled grain size distributions show overall fining from 201409 to 201506, followed by coarsening in 201608.

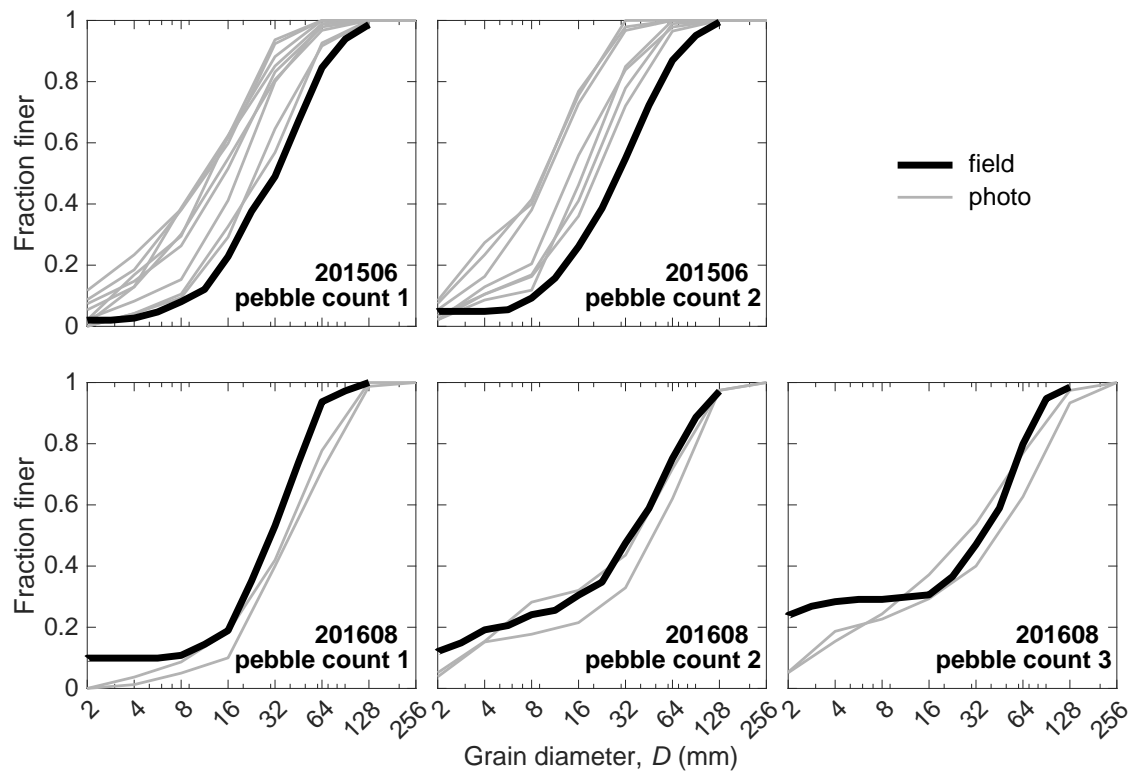


Figure 5.6: Field and photo derived pebble count grain size distributions.

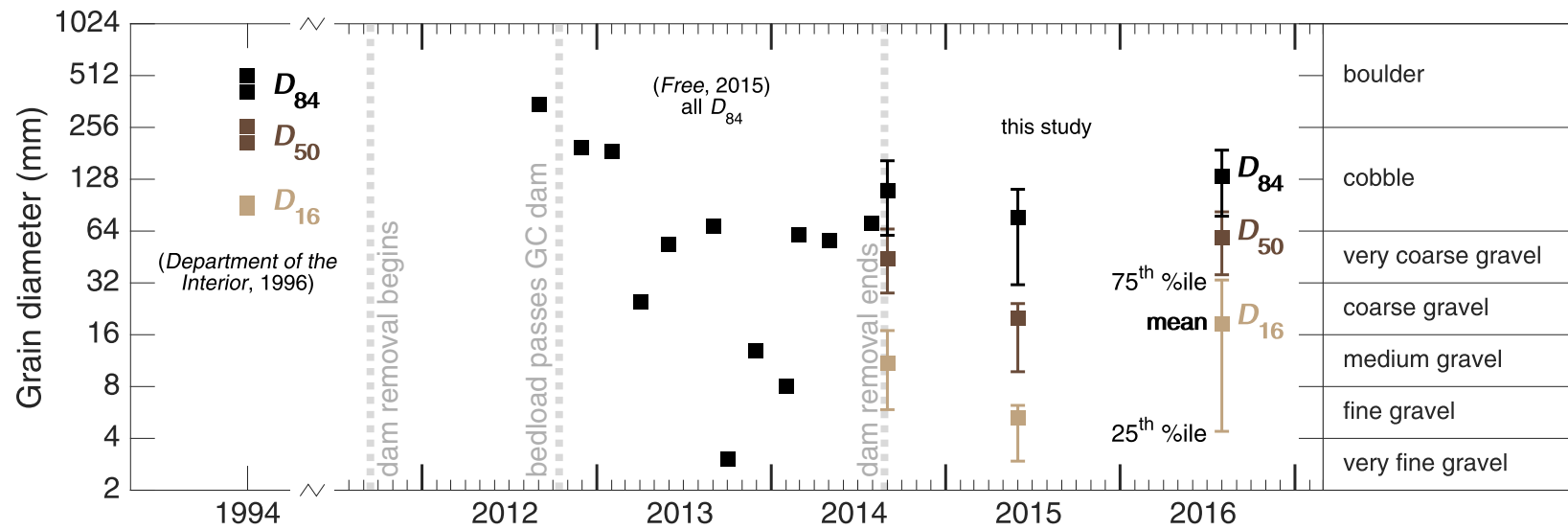


Figure 5.7: Summarized grain size data, showing also data from *Department of the Interior* (1996) and *Free* (2015). Error bars for the current study denote the interquartile range (Q1–Q3), square markers denote mean values.

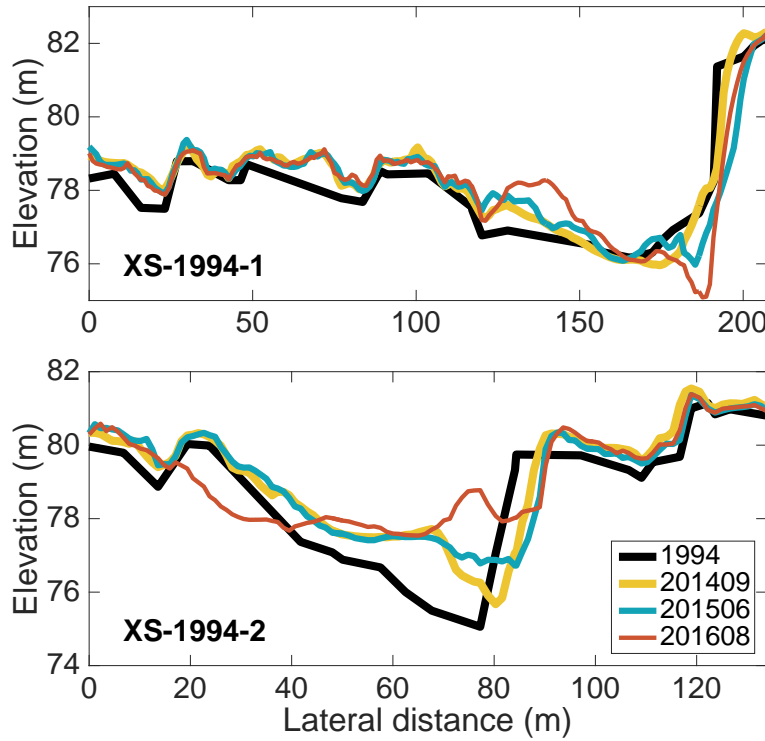


Figure 5.8: Cross section comparisons between *Department of the Interior* (1995a) data and our survey results. Location of cross-sections are shown in Figure 5.3.

5.3.2 Geomorphic changes

Cross-section comparisons between our survey data and the 1994 survey are shown in Figure 5.8. The lower cross section (XS-1994-1) shows relatively little change between 1994 and 2014. The 201506 and 201608 surveys show scour occurring at the foot of the outside bank. The bank shows slight lateral erosion, which reverses between 201506 and 201608 with National Park efforts to armor the bank to provide protection for the Madison Creek Falls parking lot. The upper cross section (XS-1994-2) shows slight retreat of the right bank from 1994-2015 and bar growth opposite the cut bank during the same period. The 201608 survey shows channel-wide bed aggradation and widening on the left bank at this cross-section.

Cross-section data from 2011 are compared with our survey data in Figure 5.9. The cross-section comparisons show general channel widening and lateral migration from pre-removal

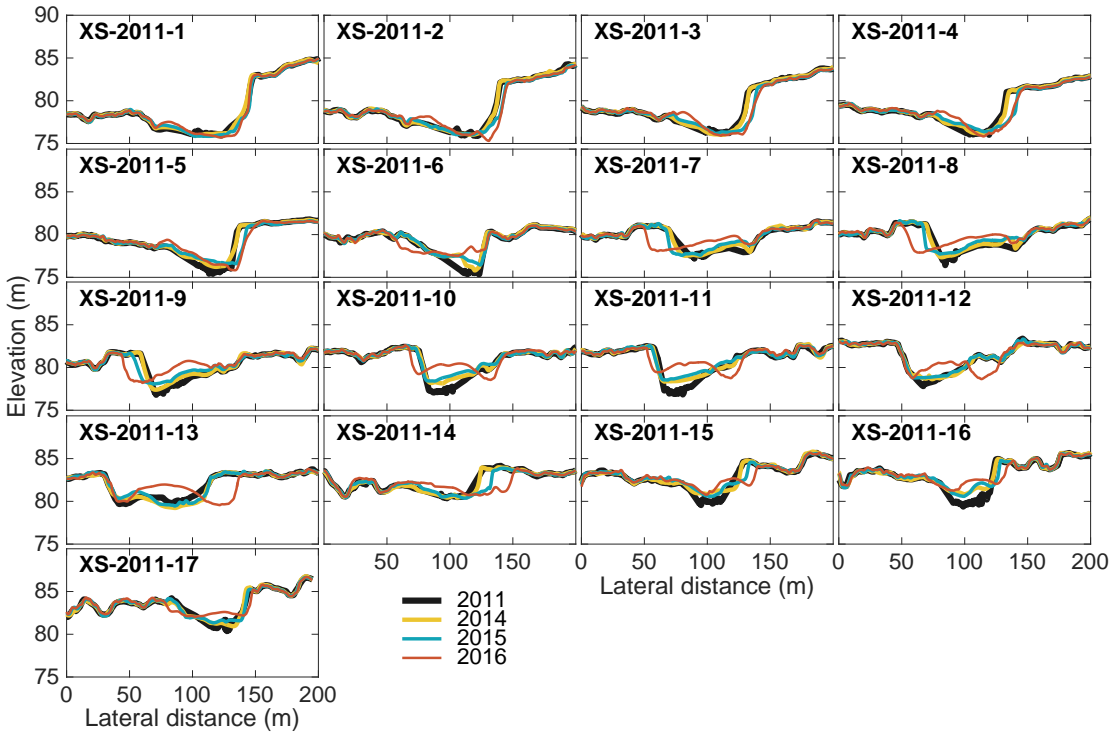


Figure 5.9: Cross section comparisons between 2011 pre-removal data and our survey results. Location of cross-sections are shown in Figure 5.3.

conditions. In some cross-sections bar building and outside bend erosion have occurred concurrently, resulting in relatively little change in channel width (e.g., XS-2011-5,9,14). For other cross-sections in-channel deposition has occurred and both banks have eroded, resulting in a wider, shallower channel (e.g., XS-2011-10,11,17). The cross-sections generally show deposition occurring in the channel bed, often on point bars, with erosion predominately in the form of bank migration.

Results from the Geomorphic Change Detection are summarized in Table 5.1 and Figures 5.10 and 5.11. The thresholded DoD maps (Figure 5.10a and b) show more areas of significant deposition than of significant erosion for both survey periods. The thresholded areas of erosion for the two time spans are approximately equivalent while the area of deposition for the second period is roughly 25% larger than for the first period (Figure 5.11). Thresh-

olded volumes of both erosion and deposition for the second two surveys are approximately double that for the first two surveys and the uncertainty values between the two periods are roughly equivalent. Thresholded net volume changes show net erosion in the first period and deposition in the second, although the uncertainty in both cases far exceeds the thresholded value.

Table 5.1: Geomorphic Change Detection results.

	201506 - 201409		201608 - 201506	
	Raw	Thresholded	Raw	Thresholded
Total area of erosion (m^2)	299,645	23,589	202,080	23,761
Total area of deposition (m^2)	164,910	32,487	262,464	40,665
Total volume of erosion (m^3)	48,853	$18,021 \pm 7,449$	43,392	$30,381 \pm 7,002$
Total volume of deposition (m^3)	30,348	$16,058 \pm 9,743$	51,680	$33,301 \pm 11,537$
Total volume of difference (m^3)	79,201	$34,079 \pm 17,192$	95,072	$63,682 \pm 18,539$
Total net volume difference (m^3)	-18,505	$-1,964 \pm 12,264$	8,289	$2,920 \pm 13,496$
Percent erosion	62	53	46	48
Percent deposition	38	47	54	52

Spatial distributions of thresholded erosion and deposition (Figure 5.10) corroborate the cross-section comparison results. Between the 201409 and 201506 surveys the channel experienced deposition mostly on bars on the inside of the slight bends in planform and erosion was focused on the banks on the outside of those bends. These changes result in channel migration and slightly increased channel sinuosity. Relatively little channel widening occurred between these surveys as bank retreat was offset by bar building. Between the 201506 and 201608 surveys the channel experienced more widespread aggradation within the bankfull channel, including both the bed and bars. Erosional areas are again concentrated at the outside banks of the slight curves in the planform. During this second period the channel experienced migration, widening, and slightly increased sinuosity.

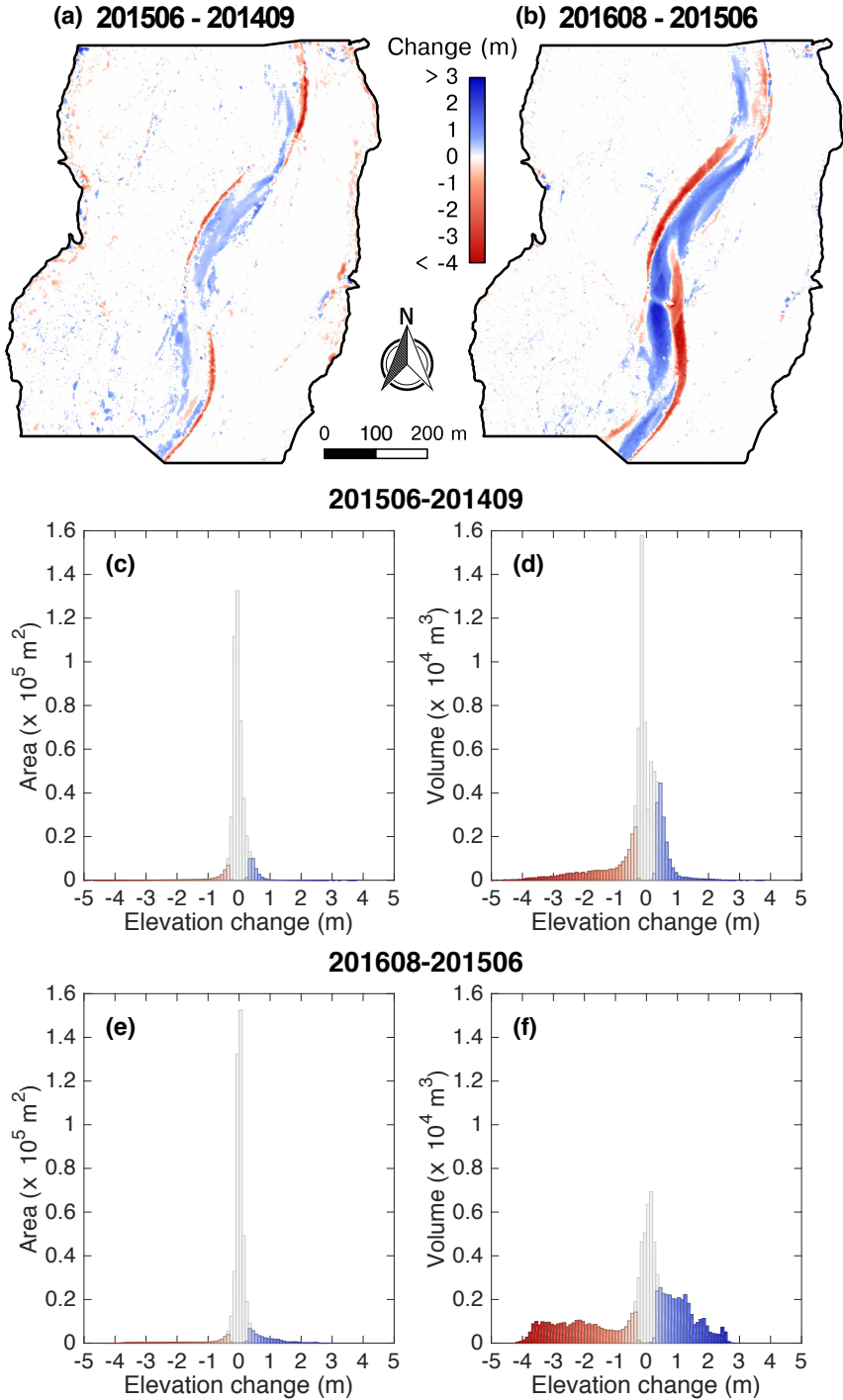


Figure 5.10: (a) and (b) Thresholded difference maps, using geomorphic change detection, covering the spans between the three survey dates. Flow is from bottom to top. (c) Area and (d) volume histograms for the first survey period, showing both raw (gray) and thresholded (colors) values, binned by elevation change. (e) Area and (f) volume histograms for the second survey period, showing both raw (gray) and thresholded (colors) values, binned by elevation change.

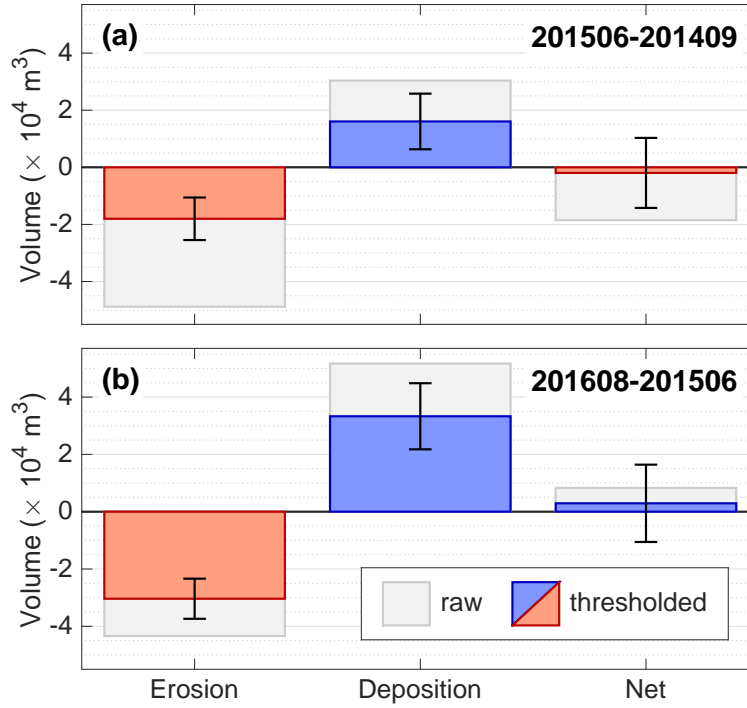


Figure 5.11: Raw and thresholded values of erosion, deposition, and net changes for (a) the first two surveys and (b) the second two surveys.

5.3.3 Aerial imagery surveys

Results from the planform analyses of historic aerial images as well as discharge data over the same time periods are shown in Figure 5.12. Movement of the active channel centerline, delineated from historical aerial images, is shown in Figure 5.13. Historical channel migration rates up to the mid-2000s remained around 0.2-0.4 m/yr. Following the 20060625 image the average migration rate increased to nearly 2 m/yr until 2009 and then decreases to 1 m/yr around the time of dam removal. From 2011 to 2013 the average channel migration rate fell to 0.8 m/yr before increasing again between 2013 and 2014. The rate continued to increase until the final aerial image on 20160728, with a rate of 1.3 m/yr from 2013 to 2014, 2.8 m/yr from 2014 to 2015, and 5.4 m/yr from 2015 to 2016.

Draut et al. (2011) found that due to large floods in 2006 and 2008 their results showed disproportionately rapid rates of channel movement over that short period. Their solution was to exclude images from 2006 and 2008 from their analysis, noting that effects from

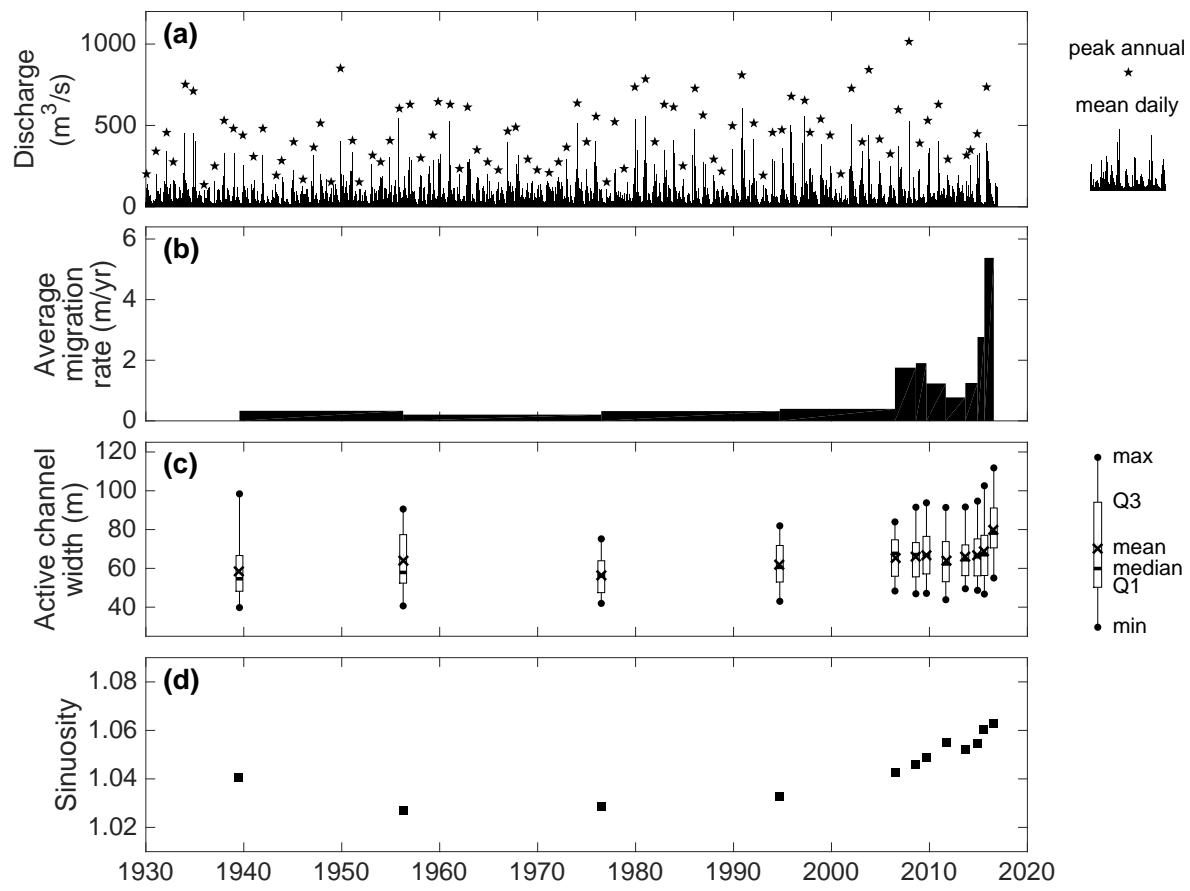


Figure 5.12: (a) Discharge over aerial photo period, (b) average migration rates between aerial photo dates, (c) active channel width distributions from aerial photos, and (d) sinuosity measured from active channel width centerlines.

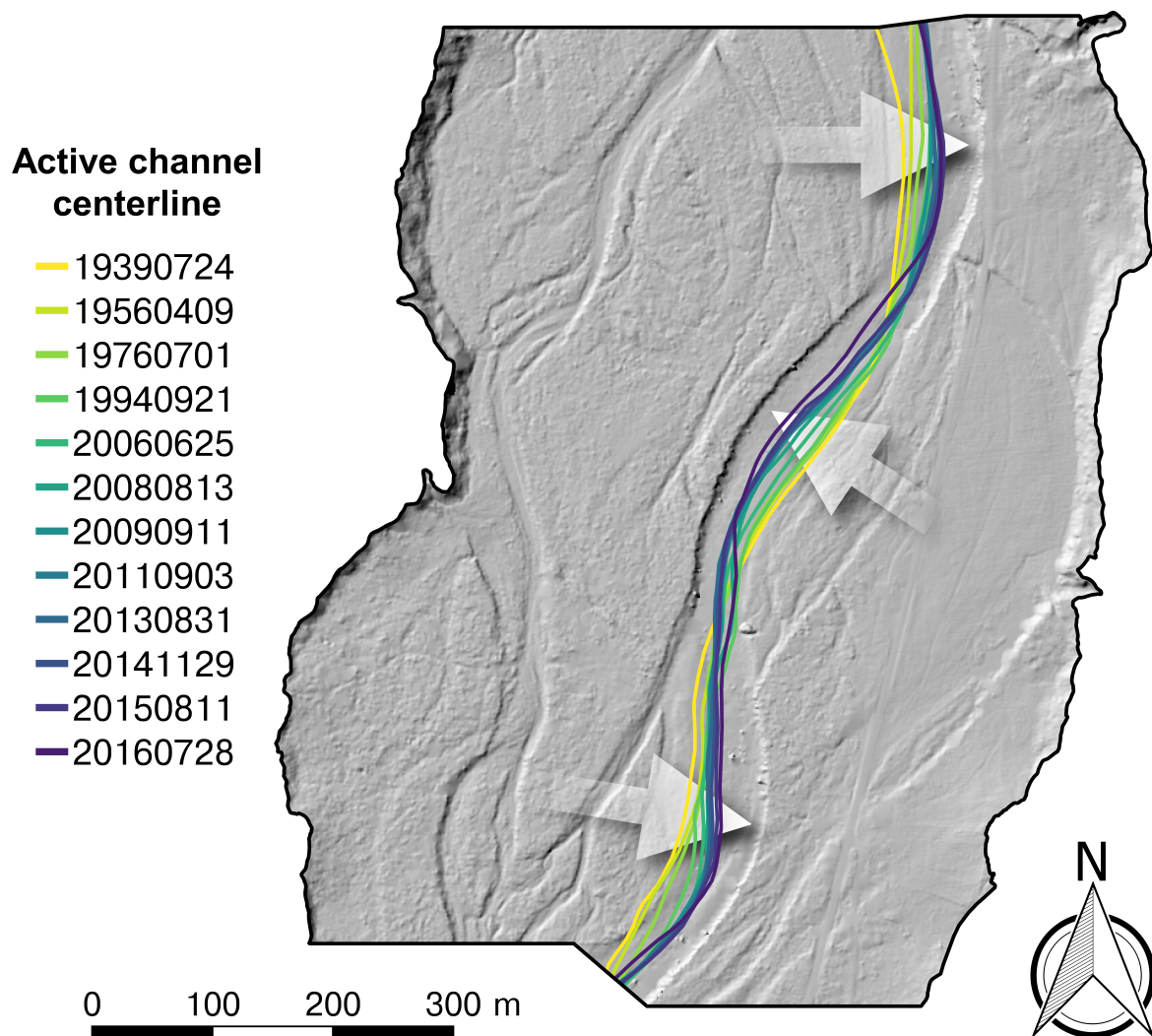


Figure 5.13: Lateral migration of active channel centerlines delineated from aerial photos. Flow is from bottom to top.

extreme events are dampened when averaged over longer periods of time between samples. Due to the limited number of images and the short time since dam removal we have chosen to include all available images and note that shorter periods between sampling times may overestimate channel movement rates.

Mean bankfull channel widths over the aerial image survey period remained relatively consistent until the later surveys. From 1939 to 2014 mean widths ranged from 56-67 m with an average of 64 m. In 2015 the mean channel width increased to approximately 69 m and further increased to 80 m in 2016. There is a noticeable increase in the rate of channel widening in Figure 5.12c from 2015 to 2016. Channel sinuosity has remained more-or-less constant from 1939 to 2016 ranging only from 1.03 to 1.06 with a mean of 1.05. Although there is a trend of increasing sinuosity from 1976 to 2016, the magnitude of changes is trivial.

5.3.4 Hydrodynamic modeling

Two-dimensional modeling calibration resulted in Manning's n values of 0.05, 0.05, and 0.04 for 201409, 201506, and 201608, respectively. Mean errors of the calibrated water surface boundaries were 1.2, 1.3, and 0.8 m for the three surveys, respectively. Statistics for the depth-averaged modeling results for flow depth, shear stress, and velocity magnitude across all of the discharge for each of the survey geometries are summarized in Figure 5.14. For each of the survey geometries the flow depth steadily increases with discharge until around the 10-year return flow ($Q_{10} = 760 \text{ m}^3/\text{s}$), after which maximum and mean flow depths remain relatively consistent up to the 100-year flood ($Q_{100} = 1121 \text{ m}^3/\text{s}$). For each simulated discharge the 201409 and 201506 flow depths are more similar to one another than either are to the 201608 flow depths. In all flow cases the majority of 201608 flow depths are lower than depths for either previous survey geometry for a given discharge. However, 201608 consistently produces higher maximum flow depths across the range of discharges.

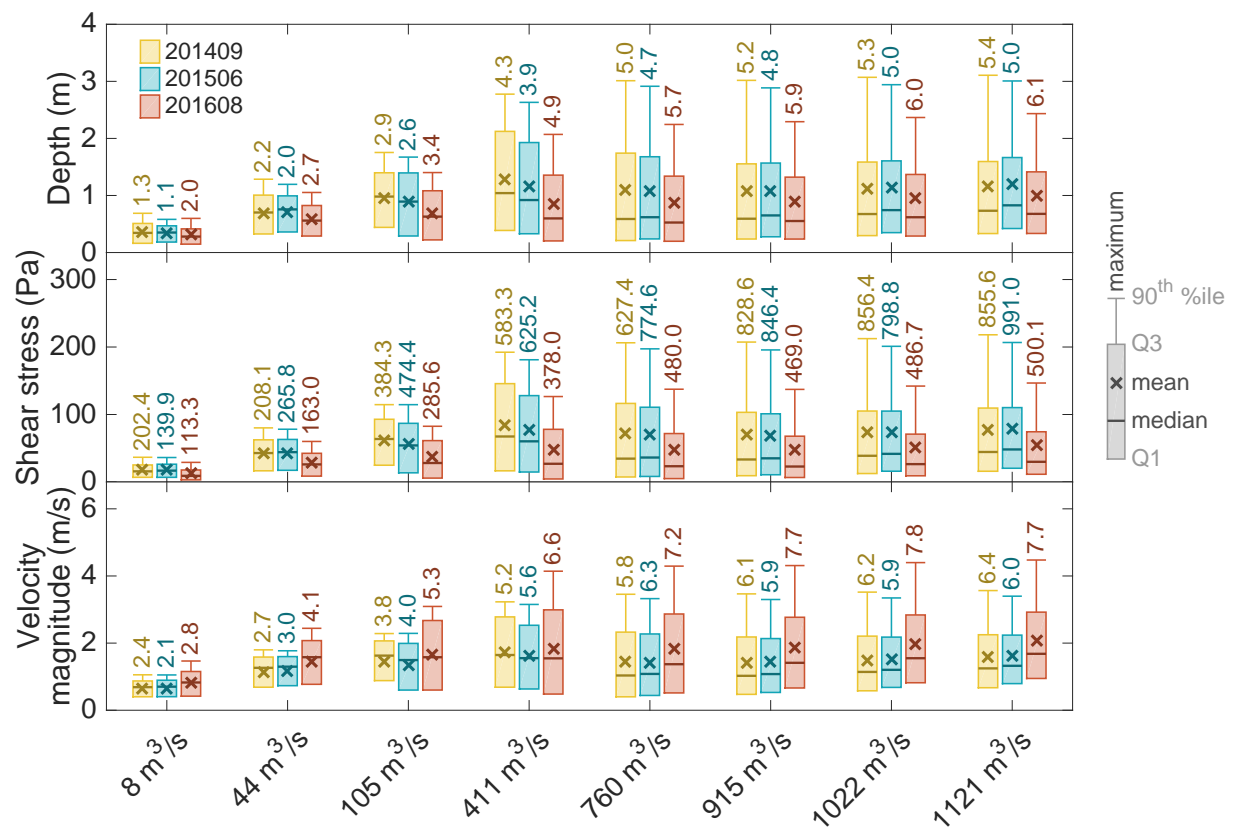


Figure 5.14: Hydrodynamic variable distribution statistics for the modeled discharges through each survey geometry.

5.3.5 Riffle-pool delineation

Geomorphological changes, transmitted through differences in the distribution and magnitude of hydrodynamic variables, result in consequent changes to aerial extents and distribution of in-channel hydro-morphological units. The result from our fuzzy c -means clustering (in variable-space) is shown in Figure 5.15b. The spatial distributions of these clusters for each survey date are shown in Figure 5.15a. In order to aid in the consideration and discussion of these results it was necessary to label each cluster (*Tamminga*, 2016), although this does introduce some degree of subjectivity (*Wallis et al.*, 2012). Intuitively, the cluster with the higher shear stress values (5) was labeled the “riffle” cluster and the cluster with the highest flow depths (4) was labeled the “pool” cluster. The two clusters with the lowest flow depths and shear stresses (1 and 2) generally occur at the channel margins and are not generally associated with primary flow areas. They were labeled as “edge” and “shallow” clusters, respectively. Finally, the last cluster (3) which shares some qualities with pools (shear stress) and others with riffles (flow depth) was labeled the “run/glide” cluster.

Quantitative area calculations for each cluster are summarized in Table 5.2 and Figure 5.15c. Geomorphic unit clusters remained relatively consistent between 201409 and 201506, both geographically and aerially, especially when compared with 201608. From 201409 to 201506 and especially into 201608 channel widening and bar growth has manifested in greater channel edge areas. Between the three surveys, cells that are undefined and those described by shallow cluster points occupy similar amounts of area. Both riffle and pool areas dramatically decrease from 201506 to 201608 (Table 5.2 and Figure 5.15c), and break up, becoming more disconnected (Figure 5.15a).

5.4 Discussion

5.4.1 Effects of increased sediment supply on channel morphology

Previous investigation of channels subject to increased sediment supply, and dam removal in particular, have provided important insight on fluvial response to changing sedimentolog-

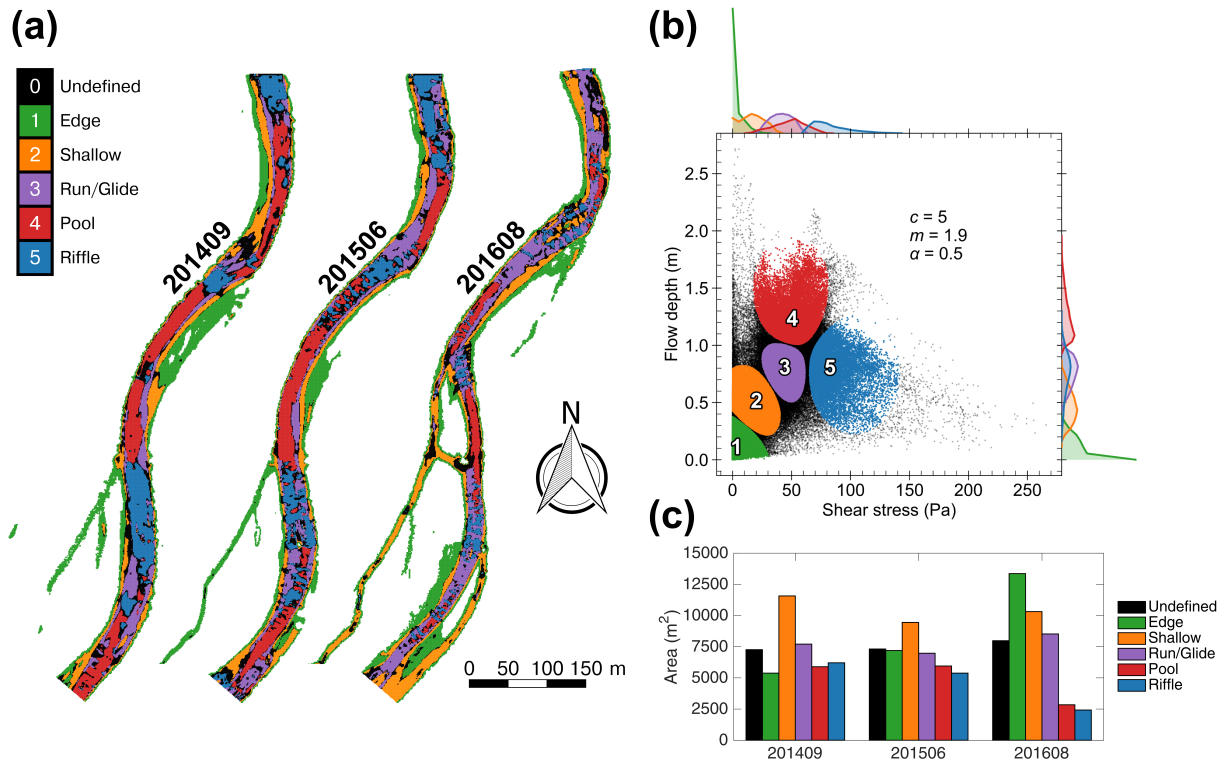


Figure 5.15: (a) Geographical distribution of clusters shown for each survey geometry. Units were numbered by ranking the mean shear stress. Flow is from bottom to top. (b) Results from fuzzy c -means clustering shown in variable-space. Note that all three surveys-worth of velocity and shear data points are included. Clusters were numbered by ranking the mean shear stress. (c) Aerial sums of each cluster for all survey geometries.

Table 5.2: Areas occupied by geomorphic units delineated using fuzzy logic for each survey geometry at the mean annual discharge ($Q_{\text{avg}} = 44 \text{ m}^3/\text{s}$). Units were numbered by ranking the mean shear stress.

#	name	201409		201506		201608	
		area (m ²)	%	area (m ²)	%	area (m ²)	%
0	undefined	7261	16.5	7315	17.3	7979	17.6
1	edge	5380	12.2	7190	17.0	13360	29.4
2	shallow	11570	26.3	9446	22.4	10313	22.7
3	run/glide	7706	17.5	6975	16.5	8520	18.8
4	pool	5893	13.4	5951	14.1	2843	6.3
5	riffle	6208	14.1	5380	12.7	2422	5.3
		$\sum = 44018$		$\sum = 42257$		$\sum = 45437$	

ical regimes. For a channel with riffle-pool morphology subject to a large depositional flood, *Lisle* (1982) observed extreme channel aggradation and widening, as well as significant fining of the surface material. Bars were built and pools were filled and became more riffle-like, creating nearly homogeneous downstream conditions of steeper, shallower flow. The effect of a higher transport capacity (brought on by decreased skin friction and reduced bar-pool relief) allowed for accelerated erosion of aggraded material. He reports periods of five years and greater for channels to achieve some degree of stability. Results of flume experiments by *Jackson and Beschta* (1984) also suggest that riffles and pools adjust to increased sand loading by degrading riffles and aggrading pools, effectively reducing form roughness. Similar findings have been reported by *Madej* (1999, 2001). She found that bedforms in channels of northwestern California became irregular and broke up in response to flooding and increased sediment supplies. Large sediment inputs also resulted in shallower, more longitudinally homogeneous flow conditions. *Nelson and Dubé* (2016) describe increases to channel width, lateral mobility, and bar area following pulsed sediment and flooding.

Free (2015) explicitly studied and quantified changes in elevations and grain size distributions for the middle Elwha River. Using terrestrial laser scanning (TLS) from 2012–2014, he reports very minor geomorphological changes in the area of our study reach (the most downstream area he surveyed). He attributes this partially to the lag time required for sediment to travel farther downstream, but explains it mostly as an effect of the relatively straight, uncomplex channel geometry. It should be noted that his use of TLS precludes his ability to measure bathymetric changes in channel geomorphology. Therefore his quantified survey areas are limited to exposed bars and banks. *Brew et al.* (2015) show that during this same time period notable changes to channel bathymetry do take place. Specifically, from pre-removal conditions in July 2011 to post-sediment release in May 2013 pools filled with sediment, effectively homogenizing the longitudinal profile. Subsequently, by August 2013, following snowmelt runoff, the pools were re-evacuated and the pre-removal longitudinal undulations re-emerged. However, during this same period, there were relatively little change

in channel planform (Figure 5.12). The question remains then, what explains the sudden increase in geomorphic changes revealed by our data, both in terms of elevation changes and channel planform geometry?

We hypothesize at least a few scenarios that may explain the timing of the dramatic increase in channel morphodynamics and lateral channel activity in our study reach. First, the rate of sediment transfer from the reservoir to our study site (approximately 5 km downstream of the location of former Glines Canyon Dam) is likely to be modulated by the size of sediment in question. Sediments composing the bed and delta in the upstream impoundment were composed of mostly sand and finer material, although a considerable volume of coarse material was also present (*Czuba et al.*, 2011). In general, reservoir delta composition is stratified with the coarsest material at the bottom. As the reservoir level receded and the delta prograded toward the dam site the finer material likely constituted the front. When the delta reached the dam removal site and bedload began moving downstream, it was likely the finer bed material that moved through first. Because of this, it is likely that finer material from the reservoir reached our study site before coarser material. Additionally, during periods of bedload transport, it is likely that smaller particles traveled at faster rates, traversing greater distances for a given event. Using the equation of mean travel distance from *Hassan et al.* (1992), regressed using tracer data from a variety of field sites, we can calculate very rough estimates of bedload travel times from the reservoir.

$$L = 2.85 \times 10^{-3} \omega_e^{1.31} D^{-0.94} \quad (5.1)$$

where L is the travel distance, ω_e is the excess unit stream power ($\omega - \omega_{\text{critical}}$), and D is the grain diameter. Unit stream power is calculated as

$$\omega = \frac{\rho g Q S}{B} \quad (5.2)$$

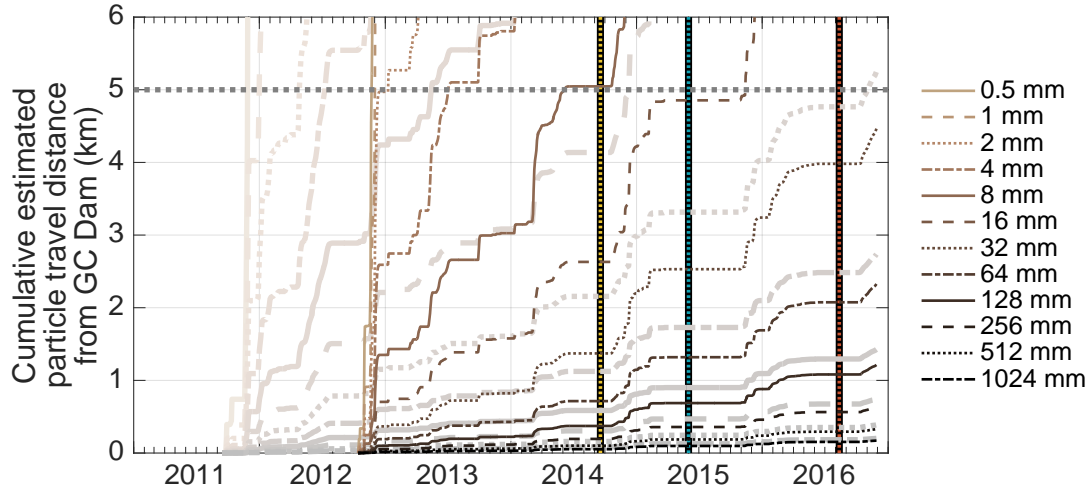


Figure 5.16: Cumulative estimated particle travel distances from Glines Canyon Dam based on grain size. Lighter colored lines represent a starting time of the beginning of dam removal in Sept. 2011 rather than the beginning of bedload passing in Oct. 2012. Dotted horizontal line represents the approximate distance from the site of former Glines Canyon Dam to our study area. Dotted vertical lines represent our surveys reported here.

where ρ is the density of water, g is gravitational acceleration, Q is discharge, S is slope, and B is width. Using some **very** conservative values (ω_{critical} corresponding to $Q_{\text{avg}} = 44 \text{ m}^3/\text{s}$; $S = 2\%$; $B = 50 \text{ m}$) we can estimate travel distances for a range of grain diameters (Figure 5.16). Certainly, without direct tracer data from this system under these circumstances the estimated distances should be viewed skeptically. Primarily, Figure 5.16 highlights the fact that, even supposing all grain sizes left the dam site simultaneously, finer particles would travel the necessary 5 km up to years earlier than coarser material. It is almost certain that these calculations underestimate the particle velocity of finer material as the regressed data were composed of coarser material (Hassan *et al.*, 1992). Nevertheless, coarser material, which likely arrived later, has greater potential for influence on channel morphodynamics and our results may constitute this temporal lag in grain size movement downstream. The rapid fining and subsequent re-coarsening of bar material (Free, 2015) as well as the filling and re-evacuating of pools (Brew *et al.*, 2015; East *et al.*, 2015) were brought on by the influx of only finer bedload material.

Another explanation for the supposed delayed response our data may suggest is the potential for multiphasic response of downstream reaches to upstream sediment supply changes. A first phase may be described by the initial influx of amplified sediment supply. Upstream reaches experience this phase first and begin adjusting. As the pulse disperses and moves downstream the influence of this first phase becomes muted. However, as the upstream reaches become more adjusted to the new supply conditions (e.g., increased dynamism) additional material (and of different composition) may become available for movement downstream. After the initial wave of the sediment pulse has passed downstream reaches this second phase, in the form of bed and bank material from upstream reaches, arrives. The changes to the middle Elwha River in 2013 and 2014, reported, for example, in *East et al.* (2015) and *Free* (2015), may constitute this first phase, while our results reveal the second.

Although long-term flow statistics have not changed considerably in the decades leading up to, or the years after, dam removal (compare our return intervals with *Department of the Interior* (1995b), for example), the temporal pattern of flows since 2011 may also contribute to the results of our study. During dam removal (Sept. 2011 to Sept. 2014), the Elwha experienced a relatively subdued hydrologic regime. Without flows exceeding the 2-year flow recurrence interval, it is possible that no overbank or “channel forming” discharges occurred. The deposition of material reported by *Draut and Ritchie* (2015), *East et al.* (2015), and *Free* (2015) was largely transient and did not have any lasting effects on the middle reach. However, with the newly initiated sediment supply and more “normal” hydrologic years with flows competent to perform geomorphic work the system undergoes lasting changes, and at faster rates than during pre-removal years. If the sediment supply remains elevated due to the movement of reservoir sediment the rates of change may continue to also be increased, but once the excess sediments are depleted and “background” sediment flux rates remain the rates of morphodynamism may relax.

Our data alone do not allow us to quantify large wood, but *Free* (2015) notes fluctuations in both the number of individual logs and of log jams from 2012 to 2014. As wood

from upstream reaches becomes available (either by passing through the former dam site or by increased lateral movement upstream) there is a greater potential for jams to develop downstream. Although the geometry of our study reach does not necessarily lend itself to anchoring instream wood (i.e., no boulders or dramatic bends) an increase in wood loading may also play a role in the measured geomorphic changes.

5.4.2 Dam removal effects on sedimentology

In disrupting the natural longitudinal continuity of sediment movement in river channels, dams have the effect of coarsening the surface texture in downstream reaches (*Kondolf*, 1997). How a river channel adjusts sedimentologically to increased sediment supply, particularly in the changes related to surface texture and particle size distribution, understandably depends on the nature of the incoming sediment load. In cases of dam removal, where reservoir sediments are generally finer than the downstream antecedent surface sediments, a fining trend is common (*Cheng and Granata*, 2007; *Magilligan et al.*, 2016). When coarse sediments are stored in the reservoir, channel coarsening can occur (*Kibler et al.*, 2011). For the Elwha River, pre-dam surface grain distributions for the middle river are not known, but evidence that supports winnowing of finer material from the middle Elwha, resulting in a coarser surface distribution, has been reported (*Kloehn et al.*, 2008). Although *Kloehn et al.* (2008) do not report full grain size distributions or precise locations of their pebble counts, the fact that a number of samples from the middle Elwha contain a higher proportion of coarse material (> 128 mm), than samples from the upper, undammed Elwha, suggests some degree of bed armoring. Grain size distributions reported in *Department of the Interior* (1996), then, represent the coarsened, armored surface. In the first two years of dam removal, considerable fining had occurred on the surface in the middle river (*Draut and Ritchie*, 2015; *East et al.*, 2015; *Free*, 2015; *Peters et al.*, 2017), before coarsening again, although not to pre-removal levels.

Our results point to continued fluctuations in the surface texture in response to dam removal. As discussed above it is entirely possible that the coarser grains from the former Lake Mills bed and delta arrived later than the finer material, and that some coarse material has yet to traverse the 5 km length, supposing it is not stored elsewhere in the channel or on the floodplain for a longer period of time. The net thresholded geomorphic changes from 201506–201409 and 201608–201506 show similar magnitudes, albeit in opposite directions (Figure 5.11). One would expect the case of net degradation (201409–201506) to result in overall surface coarsening and net aggradation (201608–201506) to result in general surface fining, but the opposite occurs. However, with uncertainty taken into account it is difficult to say with confidence whether either period was net aggradational or degradational. The trends in overall grain size may also be viewed in terms of the hydrology between surveys. Between the first two years instantaneous discharges (with a maximum of $447 \text{ m}^3/\text{s}$) only surpassed $Q_2 = 411 \text{ m}^3/\text{s}$ for a total of six hours, versus ~ 2 days above Q_2 between the second two surveys (with a maximum of $881 \text{ m}^3/\text{s}$ exceeding the 10-year recurrence interval). The extended period of time at or above bankfull discharge (assumed to be approximately Q_2) may play an important role in the grain size adjustments we have reported. With finer reservoir sediments, and possibly added finer sediments from bank retreat in upstream reaches, the shorter period of flood conditions during the first period may have only provided enough time to move the material into our study reach without sufficient time for it to pass. However, during the second period the extended time at flood flow, as well as higher flows, may have been more capable of mobilizing the finer grains that had accumulated as well as transporting the material coming in from upstream. Additionally, the higher flows, corresponding to higher levels of transport competence, may have been moving larger material that was able to enter our study reach.

5.4.3 Hydrodynamics and geomorphic units

Researchers have previously shown a tendency for channels that experience increased levels of sediment supply to, at least temporarily, respond through homogenization of the bed and breakup of mesoscale bed forms (*Lisle*, 1982; *Madej*, 1999). In-filling of pools and subsequent channel widening give way to wider, shallower flow (*Madej*, 2001). To a certain extent our results show similar trends, although perhaps not to the degree experienced during dam removal (*Brew et al.*, 2015), when the well-defined riffle-pool profile with undulating flow depth transitioned to nearly plane-bed with homogeneous longitudinal flow. This response, however, was temporary and the pools re-evacuated only months later. Our data do not suggest that deposition from 2014–2016 was limited to, or even focused on, pool locations (Figure 5.10). However, hydrodynamic modeling indicates that overall flow depths have decreased (Figure 5.14). Maximum depths did increase from 201506 to 201608 due to movement of the channel around a large boulder approximately $\frac{1}{3}$ of the way downstream in our study reach. In 201409 and 201506 the boulder was on the edge of the channel at river right, and in 201608 appears on the left side of the main channel with a large scour hole at the base leading to a side channel to left. For a given discharge these decreased flow depths have given way to higher velocity magnitudes (both mean and maxima, Figure 5.14), perhaps supporting the idea that the pools have become more “riffle-like” (*Lisle*, 1982). Generally it is posited that channel adjustment to a more homogeneous bed configuration is the channel’s way of increasing its capacity to accommodate the increased sediment load. Interestingly, from 201506 to 201608 our depth-averaged modeling results show across the board reductions in shear stresses, which is usually considered a good proxy for sediment transport capacity. For some discharges the mean and maximum shear stresses are approximately half what they were in 201409 or 201506.

These temporal hydrodynamic variations manifest themselves into temporal variations in the arrangement of geomorphic units. The effect of bedform breakup is evident in the spatial pattern and distribution of geomorphic units (Figure 5.15a). In 201409 the two

primary units of discussion, riffles and pools, generally have clear longitudinal zones. These spatial distributions were easily confirmed by field experience. Moving into 201506 the units are in roughly the same positions. However, there is a sort of merging of longitudinal zones at the edges of riffles and pools as the units seem to elongate and mix. By 201608 both pool and riffle areas had diminished to half the coverage they had previously occupied. They had also become more broken up, losing nearly all of the longitudinal delineation. Instead of pools becoming more “riffle-like”, it appears that both pools and riffles have become more “run/glide-like” and altogether shallower with lower velocities. The long pool that once occupied the central quarter of the length of the study reach became bisected. Although bankfull channel width increased dramatically between 2015 and 2016 the active wetted channel for the mean annual flow ($44 \text{ m}^3/\text{s}$) has decreased for much of the length of the study reach. The bisection of the central pool and the emergence of a quasi-riffle in between could be an accommodation for a narrower effective width in order to maintain the near-ubiquitous riffle-pool spacing of 5–7 channel widths. Whether the breakup of fluvial landforms is transient or constitutes an altered steady state remains to be seen.

5.4.4 Implications for geomorphic unit maintenance

Because geomorphic units were defined using data from all three surveys it would be circular to compare the distribution of flow variables within those units at that discharge between the surveys. However, we can compare how hydrodynamic variables with each cluster change over different discharges and compare those trends between the surveys. Figure 5.17 shows statistics related to model-predicted shear stress in each geomorphic unit over the range of flows modeled. Unsteady flow is thought to be very important for the maintenance of geomorphic units. The subject of riffle-pool maintenance has had no shortage of attention over the last four decades or more. The first formalized hypothesis for riffle-pool maintenance, the so-called “velocity reversal hypothesis”, postulates that near-bed velocities in pools increase at a higher rate with rising stage than velocities in adjacent riffles (*Keller*,

1971b). At some point the near-bed velocity in the pool overtakes the near-bed velocity in the riffle allowing for net scour of pool and deposition of the riffle at flood-stage. Other researchers have affirmed this pattern (e.g., *Milan et al.*, 2001) or something similar with shear stress (e.g., *Lisle*, 1979). Others have simply reported convergence, rather than reversal (e.g., *Clifford and Richards*, 1992), and yet others have rejected the hypothesis altogether (*Bhowmik and Demissie*, 1982). Such a reversal relationship for shear stress is suggested by our hydrodynamic results (Figures 5.17 and 5.18).

Decades ago, when detailed topographic measurements were not easily collected through lidar and GPS and when multi-dimensional flow measurements and modeling was cost- and time-prohibitive, researchers most commonly used one-dimensional variables (e.g., cross-sectional average velocity) to describe the flow differences between geomorphic units. With increased dimensionality we can look at distributions of flow parameters related to geomorphic unit and discharge. Our numerical modeling results suggest that channel geometry favors shear stress reversal (analogous to velocity reversal) at or above the two-year flood ($Q_2 = 411 \text{ m}^3/\text{s}$) for 201409 and 201608. For 201409, mean pool shear stress converges with mean riffle shear stress at Q_2 . Beyond Q_2 mean pool shear stress surpasses mean riffle shear stress. For 201409, from the 10-year flood ($Q_{10} = 760 \text{ m}^3/\text{s}$) and up, 25th percentile values for pool shear stress exceed mean values for riffle shear stress. A similar trend occurs for 201608 with riffle and pool shear stresses converging at Q_2 and pool shear stresses remaining higher thereafter. For 201506 there is no reversal in mean shear stress magnitudes, although mean values converge around Q_2 . It is interesting to note that at the Q_1 for velocity and Q_2 for shear stress maximum pool values for 201608 equal or exceed maximum riffle values. This may simply be a reflection of homogenization of the channel bed, but may also suggest the potential for maintenance and reconstitution of a more coherent aerial pattern of geomorphic units. It is worth noting also, that neither velocity nor shear stress reversal necessarily implies capacity or transport reversal (*Bayat et al.*, 2017).

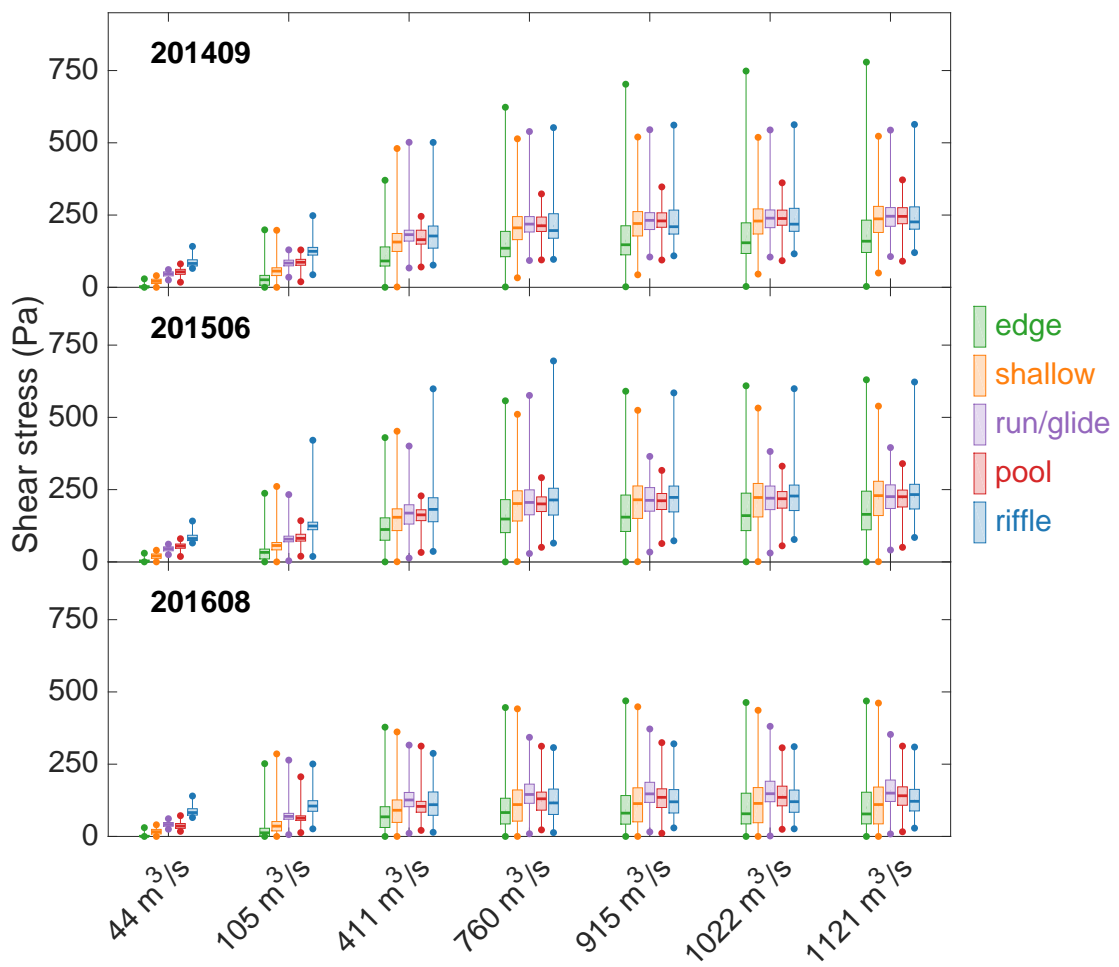


Figure 5.17: Distribution statistics for shear stress grouped by cluster for each discharge and survey geometry. Box bounds represents the inter-quartile range (Q3–Q1), horizontal bar through box represents median, and upper and lower dots represent maximum and minimum, respectively.

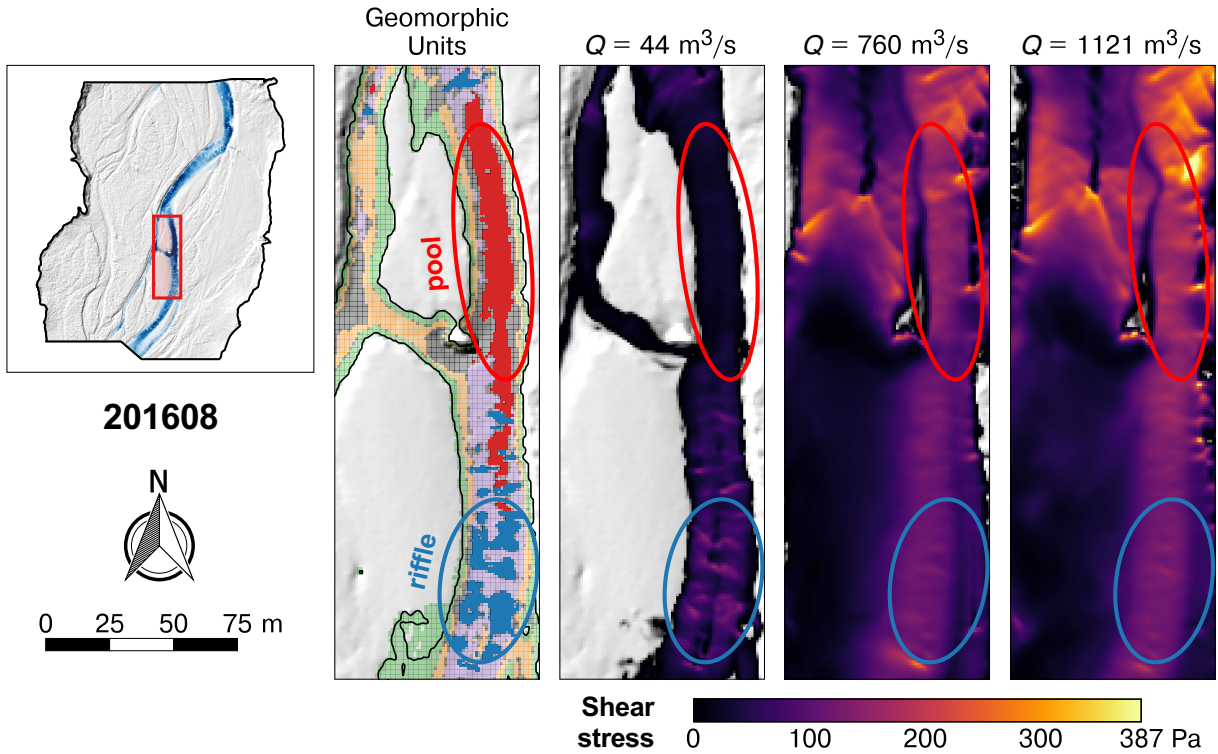


Figure 5.18: Spatial distribution of calculated shear stress in a riffle-pool couplet at increasing discharges. Shear stress increases substantially in the pool from $44 \text{ m}^3/\text{s}$ to $760 \text{ m}^3/\text{s}$, and only moderately in the riffle. Overall pool shear stress values for the higher discharges are greater than overall riffle shear stress values for the same discharges. Flow is from bottom to top.

5.5 Conclusions

Dam removal is becoming a common practice for river restoration and rehabilitation. The recent trends in restoration applications as well as the effects of a warming climate (e.g., more wildfires, landslides, and floods) accentuate the necessity to understand how river systems respond to potentially dramatic changes to sedimentological input, particularly in the form of large sediment pulses and increased sediment supply. We have used the dam removal project that took place on the Elwha River from 2011 to 2014 as a “natural experiment” to explore how a return to a more natural sediment supply regime is affecting a downstream reach. Because Glines Canyon Dam was operated as a “run of the river” facility the removal of the dam effectively increased sediment supply without having an effect on hydrology. Our surveys consisted of bathymetric/topographic measurements as well as grain size distributions. They were conducted in 2014–2016 and were supplemented with a study of aerial photos for the study reach dating from 1939–2016. Hydrodynamic modeling allowed for the estimation of flow conditions given the geometries obtained through our ground surveys for a range of flows. Modeling results were in turn used, along with fuzzy logic, to aid in the identification and delineation of geomorphic units.

Our results show general aggradation of the channel bed, especially on bars, and degradation of outside banks for both survey periods. The coupling of bar building and bank retreat translates into channel migration, and in some places (where bank erosion does not have corresponding inner bar building) channel widening. Aerial photo analyses suggest that although channel migration and widening have been occurring for the last several decades, the rates of both processes have increased dramatically since dam removal, suggesting that the increased sediment supply has led to greater channel dynamism. Hydrodynamic modeling reveals that the wider channel, having experienced widespread channel bed aggradation, conveys discharge with an overall shallower, slower flow. These altered hydro-morphodynamic conditions in turn show in-channel geomorphic units that have broken up. In the first surveys there was a relatively clear longitudinal pattern of riffles and pools, while the third survey

shows diminished areas for both geomorphic units and more disconnected and broken up aerial pattern. There is, however, potential for maintenance, and possibly re-emergence of a more regular configuration with riffle and pool shear stresses and velocities nearly equivalent at higher discharges.

Chapter 6

Summary and Conclusions

In this dissertation, I have presented results from numerical morphodynamic models, flume experiments, and field observations to better understand riffle-pool dynamics in gravel-bed rivers, with a specific focus on understanding how width variations, unsteady flow, and changes in sediment supply affect the morphodynamics of riffle-pool sequences. In Chapter 2 a one-dimensional morphodynamic model was created and used to explore sediment pulse dynamics under various conditions. Results analyzed using a newly introduced pulse dispersion index show that downstream pulse translation is favored for sediment pulses composed of finer material and sediment pulses with lower pulse heights and longer pulse feed times. Calculated pulse dispersion indices range from 0.2–1.2 for different pulse masses/feed times and from 0.3–1.6 for pulses composed of different grain diameters. In contrast, pulse dispersion indices ranged from 0.8–1.1 for unsteady flow simulations and 0.9–1.1 for variable-width geometries. Furthermore, the Froude number, which has been the most commonly used predictor of relative pulse dispersion/translation, was found to be a poor predictor of pulse evolution characteristics for these simulations.

Chapter 3 presents two-dimensional morphodynamic simulations performed using the open-source Delft3D model. The relative effects of the amplitude and wavelength of sinusoidal width variations were systematically explored by creating multiple variable-width geometries used throughout the simulations. Width variation amplitude was found to be the primary control on topographic relief between riffles and pools (with greater amplitudes resulting in greater relief), while width variation wavelength was found to be the primary control on bar mode (with shorter wavelengths resulting in side bars and longer wavelengths producing central bars). Simulations introducing sediment pulses suggest that overall sediment pulse evolution does not differ greatly in variable-width channels when compared to a constant-width channel, although instantaneous pulse evolution is affected by local channel

geometry, with a greater degree of pulse translation occurring at narrower channel sections. Unsteady flow simulations using cycled hydrographs and steady sediment supply in variable width channels show discrete areas of cyclic erosion/deposition referred to here as “structural hydrograph boundary layers”, in reference to the “hydrograph boundary layer” theory of *Parker et al.* (2007). Width variations and associated bed deformation over cycled hydrographs result in a reversal of the location of maximum and minimum bedload transport rates highlighting the importance of higher discharges for riffle-pool maintenance, even in a variable-width channel.

Complementary flume experiments are presented in Chapter 4, where the response of a constant-width channel to unsteady flow and increasing sediment supply rates is compared with the response of a variable-width channel. In the constant-width channel, doubling the sediment supply rate resulted in a 30% increase in bed slope. In the variable-width channel, however, the doubled sediment supply resulted in a much milder increase in bed slope (7%). The variable width channel accommodated the doubled sediment supply by decreasing the topographic relief between bars and pools and decreasing the cross-sectional elevation variability, each of which serve to effectively reduce form drag. This response differs from simulations in Chapter 3, where variable-width channels were predicted to have increased slopes comparable to a constant-width channel following an increase in sediment supply. This discrepancy highlights the need for further research into the interaction between channel geometry and changing sediment supply rates.

Finally, Chapter 5 presents a field study from the Elwha River, a riffle-pool channel that experienced a significant sediment supply increase following a dam removal project in 2011-2014. Analysis of historical aerial imagery dating from 1939-2016 shows that channel dynamism has increased following dam removal, evident in increasing rates of lateral channel migration and channel widening. Average migration rates have increased from approximately 1 m/yr before dam removal to nearly 6 m/yr from 2015-2016. Annual topographic surveys from 2014-2016 confirm substantial lateral channel migration and show that the majority

of deposition has occurred within the channel and on bars. The deposition, coupled with bank degradation, results in negligible net volume changes. Hydrodynamic modeling and associated delineation of geomorphic units shows a decrease in both riffle and pool area from 2014 to 2016, although at higher discharges a reversal in the location of maximum shear stress occurs, suggesting the potential for the re-emergence of a well-defined riffle-pool structure.

Taken together, the work presented in this dissertation provides important insight on the morphodynamics of riffle pool sequences in gravel-bed rivers. My numerical morphodynamic modeling has shown that under steady flow, sinusoidal channel width variations have little impact on the overall evolution of sediment pulses. However, instantaneous pulse evolution is influenced by the local channel width such that greater pulse dispersion occurs at wider sections, indicating riffles are areas of temporary sediment storage in steady flow. Differences in variable-width response to increased sediment supply under unsteady flow between two-dimensional morphodynamic modeling and flume experiments emphasize the need for additional research regarding the interaction of width variations and sediment supply rate changes. However, the response of the variable-width flume, where increased sediment supply is primarily adjusted to by decreasing form drag through the reduction of riffle-pool relief and cross-stream topographic variability, can be seen as an analogue to the response of the middle Elwha River to increased sediment supply following dam removal, where post-dam removal surveys show homogenization of the channel bed and a less definitive sequence of riffles and pools.

References

- Adams, J. (1979), Gravel size analysis from photographs, *Journal of the Hydraulics Division*, 105(HY10), 1247–1255.
- Agisoft (2016), Agisoft PhotoScan Professional Edition, version 1.2.3.2016, <http://www.agisoft.ru/products/photoscan/>, Accessed 30 January 2016.
- Aigner, J., A. Kreisler, R. Rindler, C. Hauer, and H. Habersack (2017), Bedload pulses in a hydropower affected alpine gravel bed river, *Geomorphology*, 291, 116–127, doi:10.1016/j.geomorph.2016.05.015.
- An, C., X. Fu, G. Wang, and G. Parker (2017a), Effect of grain sorting on gravel bed river evolution subject to cycled hydrographs: Bed load sheets and breakdown of the hydrograph boundary layer, *Journal of Geophysical Research: Earth Surface*, 122, 1513–1533, doi:10.1002/2016JF003994.
- An, C., Y. Cui, X. Fu, and G. Parker (2017b), Gravel-bed river evolution in earthquake-prone regions subject to cycled hydrographs and repeated sediment pulses, *Earth Surface Processes and Landforms*, doi:10.1002/esp.4195.
- Andrews, E. D. (1982), Bank stability and channel width adjustment, East Fork River, Wyoming, *Water Resources Research*, 18(4), 1184–1192, doi:10.1029/WR018i004p01184.
- Ashida, K., and M. Michiue (1972), Study on hydraulic resistance and bed-load transport rate in alluvial streams, *Journal of Civil Engineering, Japan Society of Civil Engineers*, 206(10), 59–69.
- Baker, V. R. (1977), Stream-channel response to floods, with examples from central Texas, *Geological Society of America Bulletin*, 88(8), 1057–1071, doi:10.1130/0016-7606(1977)88<1057:SRTFWE>2.0.CO;2.

Bankert, A. R., and P. A. Nelson (2017), Alternate bar dynamics in response to increases and decreases of sediment supply, *Sedimentology*, doi:10.1111/sed.12399.

Bartley, R., and I. Rutherford (2005), Measuring the reach-scale geomorphic diversity of streams: Application to a stream disturbed by a sediment slug, *River research and Applications*, 21(1), 39–59, doi:10.1002/rra.813.

Bayat, E., J. F. Rodríguez, G. A. M. de Almeida, and P. M. Saco (2016), Variation of bed grain size distribution under unsteady flow and its effect on the long-term stability of pool-riffle sequences, in *River Flow 2016*, edited by G. Constantinescu, M. Garcia, and D. Hanes, pp. 1212–1217, Taylor & Francis Group, London.

Bayat, E., J. F. Rodríguez, P. M. Saco, G. A. M. de Almeida, E. Vahidi, and M. H. García (2017), A tale of two riffles: Using multidimensional, multifractional, time-varying sediment transport to assess self-maintenance in pool-riffle sequences, *Water Resources Research*, 53(3), 2095–2113, doi:10.1002/2016WR019464.

Bellmore, J. R., J. J. Duda, L. S. Craig, S. L. Greene, C. E. Torgersen, M. J. Collins, and K. Vittum (2017), Status and trends of dam removal research in the United States, *Wiley Interdisciplinary Reviews: Water*, 4(2), doi:10.1002/wat2.1164.

Benda, L., and T. Dunne (1997), Stochastic forcing of sediment supply to channel networks from landsliding and debris flow, *Water Resources Research*, 33(12), 2849–2863, doi:10.1029/97WR02388.

Benda, L., D. Miller, P. Bigelow, and K. Andras (2003), Effects of post-wildfire erosion on channel environments, Boise River, Idaho, *Forest Ecology and Management*, 178(1), 105–119, doi:10.1016/S0378-1127(03)00056-2.

Bernhardt, E. S., M. A. Palmer, J. D. Allan, G. Alexander, K. Barnas, S. Brooks, J. Carr, S. Clayton, C. Dahm, J. Follstad-Shah, D. Galat, S. Gloss, P. Goodwin, D. Hart, B. Hassett, R. Jenkinson, S. Katz, G. M. Kondlof, P. S. Lake, R. Lave, J. L. Meyer, T. K.

- O'Donnell, L. Pagano, B. Powell, and E. Sudduth (2005), Synthesizing US river restoration efforts, *Science*, 308(5722), 636–637, doi:10.1126/science.1109769.
- Bezdek, J. C. (1981), *Pattern Recognition with Fuzzy Objective Function Algorithms*, 256 pp., Plenum Press, New York, doi:10.1007/978-1-4757-0450-1.
- Bhowmik, N. G., and M. Demissie (1982), Bed material sorting in pools and riffles, *Journal of the Hydraulics Division*, 108(10), 1227–1231.
- Biron, P. M., R. B. Carver, and D. M. Carré (2012), Sediment transport and flow dynamics around a restored pool in a fish habitat rehabilitation project: Field and 3D numerical modelling experiments, *River Research and Applications*, 28(7), 926–939, doi:10.1002/rra.1488.
- Bittner, L. D. (1994), River bed response to channel width variation: Theory and experiments, Master's thesis, University of Illinois at Urbana-Champaign.
- Blom, A., L. Arkesteijn, V. Chavarriás, and E. Viparelli (2017), The equilibrium alluvial river under variable flow and its channel-forming discharge, *Journal of Geophysical Research: Earth Surface*, 122(10), 1924–1948, doi:10.1002/2017JF004213.
- Bombar, G., Ş. Elçi, G. Tayfur, M. Ş. Güney, and A. Bor (2011), Experimental and numerical investigation of bed-load transport under unsteady flows, *Journal of Hydraulic Engineering*, 137(10), 1276–1282, doi:10.1061/(ASCE)HY.1943-7900.0000412.
- Brew, A. K., J. Morgan, and P. Nelson (2015), Bankfull width controls on riffle-pool morphology under conditions of increased sediment supply: Field observations during the Elwha River dam removal project, in *3rd Joint Federal Interagency Conference on Sedimentation and Hydrologic Modeling, Reno, Nev.*
- Brown, A. V., and P. P. Brussock (1991), Comparisons of benthic invertebrates between riffles and pools, *Hydrobiologia*, 220(2), 99–108, doi:10.1007/BF00006542.

Brown, R. A. (2017), Stratigraphic feedbacks on alternate bar morphology, Master's thesis, Colorado State University.

Brown, R. A., and G. B. Pasternack (2017), Bed and width oscillations form coherent patterns in a partially confined, regulated gravel–cobble-bedded river adjusting to anthropogenic disturbances, *Earth Surface Dynamics*, 5(1), 1–20, doi:10.5194/esurf-5-1-2017.

Brown, R. A., G. B. Pasternack, and T. Lin (2016), The topographic design of river channels for form-process linkages, *Environmental Management*, 57(4), 929–942, doi: 10.1007/s00267-015-0648-0.

Brummer, C. J., and D. R. Montgomery (2006), Influence of coarse lag formation on the mechanics of sediment pulse dispersion in a mountain stream, Squire Creek, North Cascades, Washington, United States, *Water Resources Research*, 42(7), doi:10.1029/2005WR004776.

Brunner, G. (2010), HEC-RAS, River Analysis System Hydraulic Reference Manual (Version 4.1), *Report CPD-69*, retrieved from United States Army Corps of Engineers, Hydraulic Engineering Center website: http://www.hec.usace.army.mil/software/hecras/documents/HECRAS_4.1_Reference_Manual.pdf.

Buffington, J. M., and D. R. Montgomery (1999), Effects of sediment supply on surface textures of gravel-bed rivers, *Water Resources Research*, 35(11), 3523–3530, doi:10.1029/1999WR900232.

Bunte, K. (2004), Gravel Mitigation and Augmentation Below Hydroelectric Dams: A Geomorphological Perspective, *US Department of Agriculture, Forest Service, Rocky Mountain Research Station. Report submitted to the Stream Systems Technology Center, Fort Collins, CO*.

Bunte, K., and S. R. Abt (2001), Sampling surface and subsurface particle-size distributions in wadable gravel-and cobble-bed streams for analyses in sediment transport,

hydraulics, and streambed monitoring, in *General Technical Report RMRS-GTR-74*, U.S. Department of Agriculture, Forest Service, Rocky Mountain Research Station, doi: 10.2737/RMRS-GTR-74.

Caamaño, D., P. Goodwin, J. M. Buffington, J. C. Liou, and S. Daley-Laursen (2009), Unifying criterion for the velocity reversal hypothesis in gravel-bed rivers, *Journal of Hydraulic Engineering*, 135(1), 66–70, doi:10.1061/(ASCE)0733-9429(2009)135:1(66).

Caamaño, D., P. Goodwin, and J. M. Buffington (2012), Flow structure through pool-riffle sequences and a conceptual model for their sustainability in gravel-bed rivers, *River Research and Applications*, 28(3), 377–389, doi:10.1002/rra.1463.

Carling, P. A., and H. G. Orr (2000), Morphology of riffle–pool sequences in the River Severn, England, *Earth Surface Processes and Landforms*, 25(4), 369–384, doi:10.1002/(SICI)1096-9837(200004)25:4<369::AID-ESP60>3.0.CO;2-M.

Chartrand, S. M. (2017), Pool-riffle dynamics in mountain streams: implications for maintenance, formation and equilibrium, Ph.D. thesis, University of British Columbia, doi: 10.14288/1.0349138.

Chaudhry, M. H. (2008), *Open-Channel Flow*, Springer Science & Business Media, doi:10.1007/978-0-387-68648-6.

Cheng, F., and T. Granata (2007), Sediment transport and channel adjustments associated with dam removal: Field observations, *Water Resources Research*, 43(3), doi:10.1029/2005WR004271.

Chin, A., and K. J. Gregory (2001), Urbanization and adjustment of ephemeral stream channels, *Annals of the Association of American Geographers*, 91(4), 595–608, doi:10.1111/0004-5608.00260.

Clifford, N. (1993), Differential bed sedimentology and the maintenance of riffle-pool sequences, *Catena*, 20(5), 447–468, doi:10.1016/0341-8162(93)90042-N.

Clifford, N. J., and K. S. Richards (1992), The reversal hypothesis and the maintenance of riffle-pool sequences: a review and field appraisal, in *Lowland Floodplain Rivers: Geomorphological Perspectives*, edited by P. A. Carling and G. E. Petts, pp. 43–70, John Wiley and Sons Ltd., Chichester.

Collins, M. J., N. P. Snyder, G. Boardman, W. S. L. Banks, M. Andrews, M. E. Baker, M. Conlon, A. Gellis, S. McClain, A. Miller, and P. Wilcock (2017), Channel response to sediment release: insights from a paired analysis of dam removal, *Earth Surface Processes and Landforms*, 42(11), 1636–1651, doi:10.1002/esp.4108.

Costa, J. E., and J. E. O'Connor (1995), Geomorphically effective floods, in *Natural and Anthropogenic Influences in Fluvial Geomorphology*, edited by J. E. Costa, A. J. Miller, K. W. Potter, and P. R. Wilcock, Geophysical Monograph 89, pp. 45–56, American Geophysical Union, doi:10.1029/GM089p0045.

Cui, Y., and G. Parker (2005), Numerical model of sediment pulses and sediment-supply disturbances in mountain rivers, *Journal of Hydraulic Engineering*, 131(8), 646–656, doi: 10.1061/(ASCE)0733-9429(2005)131:8(646).

Cui, Y., and A. Wilcox (2008), Development and Application of Numerical Models of Sediment Transport Associated with Dam Removal, in *Sedimentation Engineering: Processes, Measurements, Modeling, and Practice*, pp. 995–1020, ASCE, doi:10.1061/9780784408148. ch23.

Cui, Y., C. Paola, and G. Parker (1996), Numerical simulation of aggradation and downstream fining, *Journal of Hydraulic Research*, 34(2), 185–204, doi:10.1080/00221689609498496.

Cui, Y., G. Parker, J. Pizzuto, and T. E. Lisle (2003), Sediment pulses in mountain rivers: 2. Comparison between experiments and numerical predictions, *Water Resources Research*, 39(9), doi:10.1029/2002WR001805.

Cui, Y., G. Parker, T. E. Lisle, J. Gott, M. E. Hansler-Ball, J. E. Pizzuto, N. E. Allmendinger, and J. M. Reed (2003a), Sediment pulses in mountain rivers: 1. Experiments, *Water Resources Research*, 39(9), doi:10.1029/2002WR001803.

Cui, Y., G. Parker, C. Braudrick, W. E. Dietrich, and B. Cluer (2006a), Dam removal express assessment models (DREAM). Part 1: model development and validation, *Journal of Hydraulic Research*, 44(3), 291–307, doi:10.1080/00221686.2006.9521683.

Cui, Y., C. Braudrick, W. E. Dietrich, B. Cluer, and G. Parker (2006b), Dam Removal Express Assessment Models (DREAM) part 2: Sample runs/sensitivity tests, *Journal of Hydraulic Research*, 44(3), 308–323, doi:10.1080/00221686.2006.9521684.

Cui, Y., J. K. Wooster, J. G. Venditti, S. R. Dusterhoff, W. E. Dietrich, and L. S. Sklar (2008), Simulating sediment transport in a flume with forced pool-riffle morphology: Examinations of two one-dimensional numerical models, *Journal of Hydraulic Engineering*, 134(7), 892–904, doi:10.1061/(ASCE)0733-9429(2008)134:7(892).

Cui, Y., J. K. Wooster, C. A. Braudrick, and B. K. Orr (2014), Lessons learned from sediment transport model predictions and long-term postremoval monitoring: Marmot Dam removal project on the Sandy River in Oregon, *Journal of Hydraulic Engineering*, 140(9), 04014,044, doi:10.1061/(ASCE)HY.1943-7900.0000894.

Czuba, C. R., T. J. Randle, J. A. Bountry, C. S. Magirl, J. A. Czuba, C. A. Curran, and C. P. Konrad (2011), Anticipated sediment delivery to the lower Elwha River during and following dam removal, in *Coastal Habitats of the Elwha River: Biological and Physical Patterns and Processes Prior to Dam Removal*, edited by J. J. Duda, C. S. Magirl, and J. A. Warrick, pp. 27–46, US Department of the Interior, US Geological Survey.

Daniels, M. D., and M. H. McCusker (2010), Operator bias characterizing stream substrates using Wolman pebble counts with a standard measurement template, *Geomorphology*, 115(1), 194–198, doi:10.1016/j.geomorph.2009.09.038.

de Almeida, G. A. M., and J. F. Rodríguez (2011), Understanding pool-riffle dynamics through continuous morphological simulations, *Water Resources Research*, 47(1), doi:10.1029/2010WR009170.

de Almeida, G. A. M., and J. F. Rodríguez (2012), Spontaneous formation and degradation of pool-riffle morphology and sediment sorting using a simple fractional transport model, *Geophysical Research Letters*, 39(6), doi:10.1029/2012GL051059.

Deltares (2014), *Delft3D-FLOW, User Manual: Simulation of Multi-Dimensional Hydrodynamic Flows and Transport Phenomena, Including Sediments*, 684 pp., Deltares, Delft, The Netherlands.

Department of the Interior (1995a), *Elwha River Ecosystem Restoration, Final Environmental Impact Statement*, NPS D-253A, Department of the Interior, National Park Service, Olympic National Park, Port Angeles, Washington.

Department of the Interior (1995b), *Development of Flood Hydrographs*, Elwha Technical Series PN-95-1, U.S. Department of the Interior, Bureau of Reclamation, Pacific Northwest Region, Boise, Idaho.

Department of the Interior (1996), *Alluvium Distribution in the Elwha River Channel Between Glines Canyon Dam and the Strait of Juan de Fuca, Washington*, Elwha Technical Series PN-95-5, U.S. Department of the Interior, Bureau of Reclamation, Pacific Northwest Region, Boise, Idaho.

Deroose, R. C., N. A. Trustrum, and P. M. Blaschke (1993), Post-deforestation soil loss from steepland hillslopes in Taranaki, New Zealand, *Earth Surface Processes and Landforms*, 18(2), 131–144, doi:10.1002/esp.3290180205.

Dethier, E., F. J. Magilligan, C. E. Renshaw, and K. H. Nislow (2016), The role of chronic and episodic disturbances on channel–hillslope coupling: the persistence and legacy of extreme floods, *Earth Surface Processes and Landforms*, 41(10), 1437–1447, doi:10.1002/esp.3958.

Dietrich, W. E., J. W. Kirchner, H. Ikeda, and F. Iseya (1989), Sediment supply and the development of the coarse surface layer in gravel-bedded rivers, *Nature*, 340(6230), 215–217, doi:10.1038/340215a0.

Draut, A. E., and A. C. Ritchie (2015), Sedimentology of New Fluvial Deposits on the Elwha River, Washington, USA, Formed During Large-Scale Dam Removal, *River Research and Applications*, 31(1), 42–61, doi:10.1002/rra.2724.

Draut, A. E., J. B. Logan, and M. C. Mastin (2011), Channel evolution on the dammed Elwha River, Washington, USA, *Geomorphology*, 127(1), 71–87, doi:10.1016/j.geomorph.2010.12.008.

Dunn, J. C. (1973), A fuzzy relative of the ISODATA process and its use in detecting compact well-separated clusters, *Journal of Cybernetics*, 3(3), 32–57, doi:10.1080/01969727308546046.

Duró, G., A. Crosato, and P. Tassi (2016), Numerical study on river bar response to spatial variations of channel width, *Advances in Water Resources*, 93(A), 21–38, doi:10.1016/j.advwatres.2015.10.003.

East, A. E., G. R. Pess, J. A. Bountry, C. S. Magirl, A. C. Ritchie, J. B. Logan, T. J. Randle, M. C. Mastin, J. T. Minear, J. J. Duda, et al. (2015), Large-scale dam removal on the Elwha River, Washington, USA: River channel and floodplain geomorphic change, *Geomorphology*, 228, 765–786, doi:10.1016/j.geomorph.2014.08.028.

Eke, E., G. Parker, and Y. Shimizu (2014), Numerical modeling of erosional and depositional bank processes in migrating river bends with self-formed width: Morphodynamics of bar push and bank pull, *Journal of Geophysical Research: Earth Surface*, 119(7), 1455–1483, doi:10.1002/2013JF003020.

Ferguson, R. I., M. Church, C. D. Rennie, and J. G. Venditti (2015), Reconstructing a sediment pulse: Modeling the effect of placer mining on Fraser River, Canada, *Journal of Geophysical Research: Earth Surface*, 120(7), 1436–1454, doi:10.1002/2015JF003491.

Ferrer-Boix, C., and M. A. Hassan (2015), Channel adjustments to a succession of water pulses in gravel bed rivers, *Water Resources Research*, 51(11), 8773–8790, doi:10.1002/2015WR017664.

Foley, M. M., J. R. Bellmore, J. E. O'Connor, J. J. Duda, A. E. East, G. E. Grant, C. W. Anderson, J. A. Bountry, M. J. Collins, P. J. Connolly, L. S. Craig, J. E. Evans, S. L. Greene, F. J. Magilligan, C. S. Magirl, J. J. Major, G. R. Pess, T. J. Randle, P. B. Shafroth, C. E. Torgersen, D. Tullos, and A. C. Wilcox (2017), Dam removal: Listening in, *Water Resources Research*, 53(7), 5229–5246, doi:10.1002/2017WR02045.

Free, B. J. (2015), Quantifying channel responses to the removal of the Glines Canyon Dam in the middle reach of the Elwha River, Washington, Master's thesis, Central Washington University.

Gath, I., and A. B. Geva (1989), Unsupervised optimal fuzzy clustering, *IEEE Transactions on Pattern Analysis and Machine Intelligence*, 11(7), 773–780, doi:10.1109/34.192473.

Gilbert, G. K. (1914), The transportation of debris by running water, *USGS Professional Paper 86*, p. 221.

Gillespie, B. M., and J. R. Giardino (1996), Determining the migratory activity index for a river: An example from the Brazos River, Texas, *Zeitschrift fur Geomorphologie*, 40(4), 417–428.

Gran, K. B., and J. A. Czuba (2017), Sediment pulse evolution and the role of network structure, *Geomorphology*, 277, 17–30, doi:10.1016/j.geomorph.2015.12.015.

Guney, M. S., G. Bombar, and A. O. Aksoy (2013), Experimental study of the coarse surface development effect on the bimodal bed-load transport under unsteady flow conditions,

Journal of Hydraulic Engineering, 139(1), 12–21, doi:10.1061/(ASCE)HY.1943-7900.0000640.

Gunsolus, E. H., and A. D. Binns (2018), Effect of morphologic and hydraulic factors on hysteresis of sediment transport rates in alluvial streams, *River Research and Applications*, 34(2), 183–192, doi:10.1002/rra.3184.

Halkidi, M., Y. Batistakis, and M. Vazirgiannis (2001), On clustering validation techniques, *Journal of Intelligent Information Systems*, 17(2), 107–145, doi:10.1023/A:1012801612483.

Harman, C., M. Stewardson, and R. DeRose (2008), Variability and uncertainty in reach bankfull hydraulic geometry, *Journal of Hydrology*, 351(1), 13–25, doi:10.1016/j.jhydrol.2007.11.015.

Harrison, L. R., and E. A. Keller (2007), Modeling forced pool–riffle hydraulics in a boulder-bed stream, southern California, *Geomorphology*, 83(3), 232–248, doi:10.1016/j.geomorph.2006.02.024.

Hassan, M. A., and M. Church (2000), Experiments on surface structure and partial sediment transport on a gravel bed, *Water Resources Research*, 36(7), 1885–1895, doi:10.1029/2000WR900055.

Hassan, M. A., M. Church, and P. J. Ashworth (1992), Virtual rate and mean distance of travel of individual clasts in gravel-bed channels, *Earth Surface Processes and Landforms*, 17(6), 617–627, doi:10.1002/esp.3290170607.

Hassan, M. A., R. Egozi, and G. Parker (2006), Experiments on the effect of hydrograph characteristics on vertical grain sorting in gravel bed rivers, *Water Resources Research*, 42(9), doi:10.1029/2005WR004707.

Hicks, B. J., J. D. Hall, P. Bisson, and J. R. Sedell (1991), Responses of salmonids to habitat changes, in *Influences of Forest and Rangeland Management on Salmonid Fishes and Their*

Habitats, edited by W. R. Meehan, Special Publication 19, pp. 483–518, American Fisheries Society.

Hirano, M. (1971), River bed degradation with armouring, *Transactions of the Japanese Society of Civil Engineers*, 3(2), 194–195.

Hodge, R. A., D. A. Sear, and J. Leyland (2013), Spatial variations in surface sediment structure in riffle–pool sequences: a preliminary test of the Differential Sediment Entrainment Hypothesis (DSEH), *Earth Surface Processes and Landforms*, 38(5), 449–465, doi:10.1002/esp.3290.

Hoey, T. B., and R. Ferguson (1994), Numerical simulation of downstream fining by selective transport in gravel bed rivers: Model development and illustration, *Water Resources Research*, 30(7), 2251–2260, doi:10.1029/94WR00556.

Hoffman, D. F., and E. J. Gabet (2007), Effects of sediment pulses on channel morphology in a gravel-bed river, *Geological Society of America Bulletin*, 119(1-2), 116–125, doi:10.1130/B25982.1.

Humphries, R., J. G. Venditti, L. S. Sklar, and J. K. Wooster (2012), Experimental evidence for the effect of hydrographs on sediment pulse dynamics in gravel-bedded rivers, *Water Resources Research*, 48(1), doi:10.1029/2011WR010419.

Ibáñez, A., A. Ollero, D. Ballarín, J. Horacio, D. Mora, A. Mesanza, C. Ferrer-Boix, V. Acín, D. Granado, and J. P. Martín-Vide (2016), Geomorphic monitoring and response to two dam removals: rivers Urumea and Leitzaran (Basque Country, Spain), *Earth Surface Processes and Landforms*, 41(15), 2239–2255, doi:10.1002/esp.4023.

Jackson, W. L., and R. L. Beschta (1984), Influences of increased sand delivery on the morphology of sand and gravel channels, *Water Resources Bulletin*, 20(4), 527–533, doi:10.1111/j.1752-1688.1984.tb02835.x.

Jang, C.-L. (2014), Numerical experiments of the behavior of bars in the channels with periodic variable width, *Journal of Korea Water Resources Association*, 47(1), 37–47, doi:10.3741/JKWRA.2014.47.1.37.

Jowett, I. G. (1993), A method for objectively identifying pool, run, and riffle habitats from physical measurements, *New Zealand Journal of Marine and Freshwater Research*, 27(2), 241–248, doi:10.1080/00288330.1993.9516563.

Juez, C., E. Battisacco, A. J. Schleiss, and M. J. Franca (2016), Assessment of the performance of numerical modeling in reproducing a replenishment of sediments in a water-worked channel, *Advances in Water Resources*, 92, 10–22, doi:10.1016/j.advwatres.2016.03.010.

Kappesser, G. B. (2002), A riffle stability index to evaluate sediment loading to streams, *Journal of the American Water Resources Association*, 38(4), 1069–1081, doi:10.1111/j.1752-1688.2002.tb05547.x.

Kazemipour, A. K., and C. J. Apelt (1980), Resistance to flow in irregular channels, *Tech. Rep. Research Report No. CE7*, University of Queensland, Department of Civil Engineering.

Kazemipour, A. K., and C. J. Apelt (1983), Energy Losses in Irregular Channels, *Journal of Hydraulic Engineering*, 109(10), 1374–1379, doi:10.1061/(ASCE)0733-9429(1983)109:10(1374).

Keller, E. A. (1971a), Pools, riffles, and meanders: Discussion, *Geological Society of America Bulletin*, 82(1), 279–280.

Keller, E. A. (1971b), Areal sorting of bed-load material: the hypothesis of velocity reversal, *Geological Society of America Bulletin*, 82(3), 753–756, doi:10.1130/0016-7606(1971)82[753:ASOBMT]2.0.CO;2.

Keller, E. A., and J. L. Florsheim (1993), Velocity-reversal hypothesis: A model approach, *Earth Surface Processes and Landforms*, 18(8), 733–740, doi:10.1002/esp.3290180807.

Kellerhals, R., and D. I. Bray (1971), Sampling procedures for coarse fluvial sediments, *Journal of the Hydraulics Division*, 97(8), 1165–1180.

Kibler, K., D. Tullos, and M. Kondolf (2011), Evolving expectations of dam removal outcomes: Downstream geomorphic effects following removal of a small, gravel-filled dam, *Journal of the American Water Resources Association*, 47(2), 408–423, doi:10.1111/j.1752-1688.2011.00523.x.

Kieffer, S. W. (1989), Geologic nozzles, *Reviews of Geophysics*, 27(1), 3–38, doi:10.1029/RG027i001p00003.

Kleinhans, M. (2005), Upstream sediment input effects on experimental dune trough scour in sediment mixtures, *Journal of Geophysical Research: Earth Surface*, 110(F4), doi: 10.1029/2004JF000169.

Kleinhans, M. G., A. W. E. Wilbers, A. De Swaaf, and J. H. Van Den Berg (2002), Sediment supply-limited bedforms in sand-gravel bed rivers, *Journal of Sedimentary Research*, 72(5), 629–640, doi:10.1306/030702720629.

Kloehn, K. K., T. J. Beechie, S. A. Morley, H. J. Coe, and J. J. Duda (2008), Influence of dams on river-floodplain dynamics in the Elwha River, Washington, *Northwest Science*, 82(sp1), 224–235, doi:10.3955/0029-344X-82.S.I.224.

Knighton, A. D. (1989), River adjustment to changes in sediment load: the effects of tin mining on the Ringarooma River, Tasmania, 1875–1984, *Earth Surface Processes and Landforms*, 14(4), 333–359, doi:10.1002/esp.3290140408.

Knighton, D. (1998), *Fluvial Forms & Processes: A New Perspective*, 400 pp., Routledge, New York.

Knox, J. C. (2000), Sensitivity of modern and Holocene floods to climate change, *Quaternary Science Reviews*, 19(1), 439–457, doi:10.1016/S0277-3791(99)00074-8.

Kondolf, G. M. (1997), PROFILE: hungry water: effects of dams and gravel mining on river channels, *Environmental Management*, 21(4), 533–551, doi:10.1007/s002679900.

Konrad, C., H. Berge, R. Fuerstenberg, K. Steff, T. Olsen, and J. Guyenet (2011), Channel dynamics in the Middle Green River, Washington, from 1936 to 2002, *Northwest Science*, 85(1), 1–14, doi:10.3955/046.085.0101.

Krapu, G. L., D. E. Facey, E. K. Fritzell, and D. H. Johnson (1984), Habitat use by migrant sandhill cranes in Nebraska, *The Journal of Wildlife Management*, 48(2), 407–417, doi: 10.2307/3801172.

Kuhnle, R. A. (1992), Bed load transport during rising and falling stages on two small streams, *Earth Surface Processes and Landforms*, 17(2), 191–197, doi:10.1002/esp.3290170206.

Lane, E. W. (1955), The importance of fluvial morphology in hydraulic engineering, *Proceedings, American Society of Civil Engineers*, 81(745), 1–17.

Lee, K. T., Y.-L. Liu, and K.-H. Cheng (2004), Experimental investigation of bedload transport processes under unsteady flow conditions, *Hydrological Processes*, 18(13), 2439–2454, doi:10.1002/hyp.1473.

Legleiter, C. J., and M. F. Goodchild (2005), Alternative representations of in-stream habitat: classification using remote sensing, hydraulic modeling, and fuzzy logic, *International Journal of Geographical Information Science*, 19(1), 29–50, doi:10.1080/13658810412331280220.

Leopold, L. B., and M. G. Wolman (1960), River meanders, *Geological Society of America Bulletin*, 71(6), 769–793, doi:10.1130/0016-7606(1960)71[769:RM]2.0.CO;2.

Leopold, L. B., M. G. Wolman, and J. P. Miller (1964), *Fluvial Processes in Geomorphology*, 544 pp., W.H. Freeman and Company, San Francisco.

Lewis, M. (2012), *Applied Statistics for Economists*, 368 pp., Routledge, New York.

Lisle, T. (1979), A sorting mechanism for a riffle-pool sequence, *Geological Society of America Bulletin*, 90(7 Part II), 1142–1157, doi:10.1130/GSAB-P2-90-1142.

Lisle, T. E. (1982), Effects of aggradation and degradation on riffle-pool morphology in natural gravel channels, northwestern California, *Water Resources Research*, 18(6), 1643–1651, doi:10.1029/WR018i006p01643.

Lisle, T. E. (2007), The evolution of sediment waves influenced by varying transport capacity in heterogeneous rivers, in *Gravel-Bed Rivers VI: From Process Understanding to River Restoration*, edited by H. Habersack, H. Piegay, and M. Rinaldi, pp. 443–469, Elsevier, doi:10.1016/S0928-2025(07)11136-6.

Lisle, T. E., and S. Hilton (1992), The volume of fine sediment in pools: An index of sediment supply in gravel-bed streams, *Journal of the American Water Resources Association*, 28(2), 371–383, doi:10.1111/j.1752-1688.1992.tb04003.x.

Lisle, T. E., F. Iseya, and H. Ikeda (1993), Response of a channel with alternate bars to a decrease in supply of mixed-size bed load: A flume experiment, *Water Resources Research*, 29(11), 3623–3629, doi:10.1029/93WR01673.

Lisle, T. E., J. E. Pizzuto, H. Ikeda, F. Iseya, and Y. Kodama (1997), Evolution of a sediment wave in an experimental channel, *Water Resources Research*, 33(8), 1971–1981, doi:10.1029/97WR01180.

Lisle, T. E., J. M. Nelson, J. Pitlick, M. A. Madej, and B. L. Barkett (2000), Variability of bed mobility in natural, gravel-bed channels and adjustments to sediment load at local and reach scales, *Water Resources Research*, 36(12), 3743–3755, doi:10.1029/2000WR900238.

Lisle, T. E., Y. Cui, G. Parker, J. E. Pizzuto, and A. M. Dodd (2001), The dominance of dispersion in the evolution of bed material waves in gravel-bed rivers, *Earth Surface Processes and Landforms*, 26(13), 1409–1420, doi:10.1002/esp.300.

Luce, C. H., and T. A. Black (1999), Sediment production from forest roads in western Oregon, *Water Resources Research*, 35(8), 2561–2570, doi:10.1029/1999WR900135.

Luchi, R., J. M. Hooke, G. Zolezzi, and W. Bertoldi (2010), Width variations and mid-channel bar inception in meanders: River Bollin (UK), *Geomorphology*, 119(1), 1–8, doi: 10.1016/j.geomorph.2010.01.010.

MacVicar, B. J., and A. G. Roy (2007a), Hydrodynamics of a forced riffle pool in a gravel bed river: 1. Mean velocity and turbulence intensity, *Water Resources Research*, 43(12), doi:10.1029/2006WR005272.

MacVicar, B. J., and A. G. Roy (2007b), Hydrodynamics of a forced riffle pool in a gravel bed river: 2. Scale and structure of coherent turbulent events, *Water Resources Research*, 43(12), doi:10.1029/2006WR005274.

MacWilliams, M. L., J. M. Wheaton, G. B. Pasternack, R. L. Street, and P. K. Kitanidis (2006), Flow convergence routing hypothesis for pool-riffle maintenance in alluvial rivers, *Water Resources Research*, 42(10), doi:10.1029/2005WR004391.

Madej, M. A. (1999), Temporal and spatial variability in thalweg profiles of a gravel-bed river, *Earth Surface Processes and Landforms*, 24(12), 1153–1169, doi:10.1002/(SICI)1096-9837(199911)24:12<1153::AID-ESP41>3.0.CO;2-8.

Madej, M. A. (2001), Development of channel organization and roughness following sediment pulses in single-thread, gravel bed rivers, *Water Resources Research*, 37(8), 2259–2272, doi:10.1029/2001WR000229.

Madej, M. A., and V. Ozaki (1996), Channel response to sediment wave propagation and movement, Redwood Creek, California, USA, *Earth Surface Processes and Landforms*, 21(10), 911–927, doi:10.1002/(SICI)1096-9837(199610)21:10<911::AID-ESP621>3.0.CO;2-1.

Madej, M. A., D. G. Sutherland, T. E. Lisle, and B. Pryor (2009), Channel responses to varying sediment input: A flume experiment modeled after Redwood Creek, California, *Geomorphology*, 103(4), 507–519, doi:10.1016/j.geomorph.2008.07.017.

Magilligan, F. J., K. H. Nislow, B. E. Kynard, and A. M. Hackman (2016), Immediate changes in stream channel geomorphology, aquatic habitat, and fish assemblages following dam removal in a small upland catchment, *Geomorphology*, 252, 158–170, doi:10.1016/j.geomorph.2015.07.027.

Mao, L. (2012), The effect of hydrographs on bed load transport and bed sediment spatial arrangement, *Journal of Geophysical Research: Earth Surface*, 117(F3), doi: 10.1029/2012JF002428.

Marcus, W. A., S. C. Ladd, J. A. Stoughton, and J. W. Stock (1995), Pebble counts and the role of user-dependent bias in documenting sediment size distributions, *Water Resources Research*, 31(10), 2625–2631, doi:10.1029/95WR02171.

Mastin, M. C., C. P. Konrad, A. G. Veilleux, and A. E. Tecca (2016), Magnitude, frequency, and trends of floods at gaged and ungaged sites in Washington, based on data through water year 2014, *Tech. rep.*, US Geological Survey, doi:10.3133/sir20165118.

Maturana, O., D. Tonina, J. A. McKean, J. M. Buffington, C. H. Luce, and D. Caamaño (2014), Modeling the effects of pulsed versus chronic sand inputs on salmonid spawning habitat in a low-gradient gravel-bed river, *Earth Surface Processes and Landforms*, 39(7), 877–889, doi:10.1002/esp.3491.

Milan, D. J., G. L. Heritage, A. R. G. Large, and M. E. Charlton (2001), Stage dependent variability in tractive force distribution through a riffle–pool sequence, *Catena*, 44(2), 85–109, doi:10.1016/S0341-8162(00)00155-7.

Milne, J. A. (1982), Bed-material size and the riffle-pool sequence, *Sedimentology*, 29, 267–278, doi:10.1111/j.1365-3091.1982.tb01723.x.

Moody, J. A., and B. M. Troutman (2002), Characterization of the spatial variability of channel morphology, *Earth Surface Processes and Landforms*, 27(12), 1251–1266, doi:10.1002/esp.403.

Morgan, J. A., and P. A. Nelson (2016), Hydro- and morphodynamics of riffle-pool sequences in the middle Elwha River, Washington, USA, in *River Flow 2016*, edited by G. Constantinescu, M. Garcia, and D. Hanes, pp. 1212–1217, Taylor & Francis Group, London.

Morgan, J. A., D. J. Brogan, and P. A. Nelson (2017), Application of Structure-from-Motion photogrammetry in laboratory flumes, *Geomorphology*, 276, 125–143, doi:10.1016/j.geomorph.2016.10.021.

Myers, T. J., and S. Swanson (1997), Stochastic modeling of pool-to-pool structure in small Nevada rangeland streams, *Water Resources Research*, 33(4), 877–889, doi:10.1029/96WR03975.

Nelson, A., and K. Dubé (2016), Channel response to an extreme flood and sediment pulse in a mixed bedrock and gravel-bed river, *Earth Surface Processes and Landforms*, 41(2), 178–195, doi:10.1002/esp.3843.

Nelson, J. M., and J. D. Smith (1989), Mechanics of flow over ripples and dunes, *Journal of Geophysical Research: Oceans*, 94(C6), 8146–8162, doi:10.1029/JC094iC06p08146.

Nelson, J. M., Y. Shimizu, T. Abe, K. Asahi, M. Gamou, T. Inoue, T. Iwasaki, T. Kakinuma, S. Kawamura, I. Kimura, et al. (2016), The international river interface cooperative: Public

domain flow and morphodynamics software for education and applications, *Advances in Water Resources*, 93(A), 62–74, doi:10.1016/j.advwatres.2015.09.017.

Nelson, P. A., and J. A. Morgan (in review), Flow and sediment supply controls on gravel bedform dynamics, *Geomorphology*.

Nelson, P. A., J. G. Venditti, W. E. Dietrich, J. W. Kirchner, H. Ikeda, F. Iseya, and L. S. Sklar (2009), Response of bed surface patchiness to reductions in sediment supply, *Journal of Geophysical Research: Earth Surface*, 114(F2), doi:10.1029/2008JF001144.

Nelson, P. A., D. Bellugi, and W. E. Dietrich (2014), Delineation of river bed-surface patches by clustering high-resolution spatial grain size data, *Geomorphology*, 205, 102–119, doi:10.1016/j.geomorph.2012.06.008.

Nelson, P. A., A. K. Brew, and J. A. Morgan (2015), Morphodynamic response of a variable-width channel to changes in sediment supply, *Water Resources Research*, 51(7), 5717–5734, doi:10.1002/2014WR016806.

Nouh, M. (1990), The self armouring process under unsteady flow conditions, *Earth Surface Processes and Landforms*, 15(4), 357–364, doi:10.1002/esp.3290150406.

Olsen, D. S., B. B. Roper, J. L. Kershner, R. Henderson, and E. Archer (2005), Sources of variability in conducting pebble counts: their potential influence on the results of stream monitoring programs, *Journal of the American Water Resources Association*, 41(5), 1225–1236, doi:10.1111/j.1752-1688.2005.tb03796.x.

O'Neill, M. P., and A. D. Abrahams (1984), Objective identification of pools and riffles, *Water resources research*, 20(7), 921–926, doi:10.1029/WR020i007p00921.

Pace, K. M., D. Tullos, C. Walter, S. Lancaster, and C. Segura (2017a), Sediment pulse behaviour following dam removal in gravel-bed rivers, *River Research and Applications*, 33(1), 102–112, doi:10.1002/rra.3064.

Pace, K. M., D. Tullos, C. Walter, S. Lancaster, and C. Segura (2017b), Sediment pulse behaviour following dam removal in gravel-bed rivers, *River Research and Applications*, 33(1), 102–112, doi:10.1002/rra.3064.

Parker, G. (1990), Surface-based bedload transport relation for gravel rivers, *Journal of Hydraulic Research*, 28(4), 417–436, doi:10.1080/00221689009499058.

Parker, G. (2006), 1D Sediment Transport Morphodynamics with Applications to Rivers and Turbidity Currents, e-book available at http://vtchliuc.edu/people/parkerg/morphodynamics_e-book.htm.

Parker, G. (2008), Transport of gravel and sediment mixtures, in *Sedimentation Engineering: Processes, Measurements, Modeling, and Practice*, vol. 110, edited by M. Garcia, pp. 165–252, ASCE Publications, doi:10.1061/9780784408148.ch03.

Parker, G., and E. Andrews (1985), Sorting of bed load sediment by flow in meander bends, *Water Resources Research*, 21(9), 1361–1373, doi:10.1029/WR021i009p01361.

Parker, G., C. M. Toro-Escobar, M. Ramey, and S. Beck (2003), Effect of floodwater extraction on mountain stream morphology, *Journal of Hydraulic Engineering*, 129(11), 885–895, doi:10.1061/(ASCE)0733-9429(2003)129:11(885).

Parker, G., M. Hassan, and P. Wilcock (2007), Adjustment of the bed surface size distribution of gravel-bed rivers in response to cycled hydrographs, in *Gravel-Bed Rivers VI: From Process Understanding to River Restoration*, edited by H. Habersack, H. Piégay, and M. Rinaldi, pp. 241–285, Elsevier, doi:10.1016/S0928-2025(07)11127-5.

Pasternack, G. B., and R. A. Brown (2013), Ecohydraulic design of riffle-pool relief and morphological unit geometry in support of regulated gravel-bed river rehabilitation, in *Ecohydraulics: An Integrated Approach*, edited by I. Maddock, A. Harby, P. Kemp, and P. Wood, pp. 337–355, John Wiley & Sons, Ltd., Chichester, doi:10.1002/9781118526576.ch20.

Pasternack, G. B., and J. R. Wyrick (2017), Flood-driven topographic changes in a gravel-cobble river over segment, reach, and morphological unit scales, *Earth Surface Processes and Landforms*, 42(3), 487–502, doi:10.1002/esp.4064.

Pearson, A. J., N. P. Snyder, and M. J. Collins (2011), Rates and processes of channel response to dam removal with a sand-filled impoundment, *Water Resources Research*, 47(8), doi:10.1029/2010WR009733.

Peters, R. J., M. Liermann, M. L. McHenry, P. Bakke, and G. R. Pess (2017), Changes in streambed composition in salmonid spawning habitat of the Elwha River during dam removal, *Journal of the American Water Resources Association*, 53(4), 871–885, doi:10.1111/1752-1688.12536.

Phillips, B., and A. Sutherland (1990), Temporal lag effect in bed load sediment transport, *Journal of Hydraulic Research*, 28(1), 5–23, doi:10.1080/00221689009499144.

Pickup, G., R. Higgins, and I. Grant (1983), Modelling sediment transport as a moving wave — the transfer and deposition of mining waste, *Journal of Hydrology*, 60(1), 281–301, doi:10.1016/0022-1694(83)90027-6.

Pitlick, J., E. R. Mueller, C. Segura, R. Cress, and M. Torizzo (2008), Relation between flow, surface-layer armoring and sediment transport in gravel-bed rivers, *Earth Surface Processes and Landforms*, 33(8), 1192–1209, doi:10.1002/esp.1607.

Pizzuto, J. (2002), Effects of dam removal on river form and process, *BioScience*, 52(8), 683–691, doi:10.1641/0006-3568(2002)052[0683:EODROR]2.0.C.

Podolak, C. J. P., and P. R. Wilcock (2013), Experimental study of the response of a gravel streambed to increased sediment supply, *Earth Surface Processes and Landforms*, 38(14), 1748–1764, doi:10.1002/esp.3468.

Poole, G. C., C. A. Frissell, and S. C. Ralph (1997), In-stream habitat unit classification: Inadequacies for monitoring and some consequences for management, *Journal of the American Water Resources Association*, 33(4), 879–896, doi:10.1111/j.1752-1688.1997.tb04112.

x.

Powell, D. M., I. Reid, and J. B. Laronne (2001), Evolution of bed load grain size distribution with increasing flow strength and the effect of flow duration on the caliber of bed load sediment yield in ephemeral gravel bed rivers, *Water Resources Research*, 37(5), 1463–1474, doi:10.1029/2000WR900342.

Pryor, B. S., T. Lisle, D. S. Montoya, and S. Hilton (2011), Transport and storage of bed material in a gravel-bed channel during episodes of aggradation and degradation: a field and flume study, *Earth Surface Processes and Landforms*, 36(15), 2028–2041, doi:10.1002/esp.2224.

Qin, J., T. Wu, and D. Zhong (2015), Spectral behavior of gravel dunes, *Geomorphology*, 231, 331–342, doi:10.1016/j.geomorph.2014.12.023.

Radinger, J., J. Kail, and C. Wolter (2017), Differences among expert judgments of fish habitat suitability and implications for river management, *River Research and Applications*, 33(4), 538–547, doi:10.1002/rra.3109.

Rathburn, S., and E. Wohl (2003), Predicting fine sediment dynamics along a pool-riffle mountain channel, *Geomorphology*, 55(1), 111–124, doi:10.1016/S0169-555X(03)00135-1.

Rathburn, S. L., and E. E. Wohl (2001), One-dimensional sediment transport modeling of pool recovery along a mountain channel after a reservoir sediment release, *River Research and Applications*, 17(3), 251–273, doi:10.1002/rrr.617.

Recking, A. (2014), Relations between bed recharge and magnitude of mountain streams erosions, *Journal of Hydro-Environment Research*, 8(2), 143–152, doi:10.1016/j.jher.2013.08.005.

Repetto, R., M. Tubino, and C. Paola (2002), Planimetric instability of channels with variable width, *Journal of Fluid Mechanics*, 457, 71–76, doi:10.1017/S0022112001007595.

Richards, K. S. (1976a), The morphology of riffle-pool sequences, *Earth Surface Processes*, 1(1), 71–88, doi:10.1002/esp.3290010108.

Richards, K. S. (1976b), Channel width and the riffle-pool sequence, *Geological Society of America Bulletin*, 87(6), 883–890, doi:10.1130/0016-7606(1976)87\$(\$883:CWATRS\$)\$2.0.CO;2.

Rodrigues, S., E. Mosselman, N. Claude, C. L. Wittenberger, and P. Juge (2015), Alternate bars in a sandy gravel bed river: generation, migration and interactions with superimposed dunes, *Earth Surface Processes and Landforms*, 40(5), 610–628, doi:10.1002/esp.3657.

Rodríguez, J. F., F. López, C. García, and M. García (2004), Laboratory experiments on pool-riffle sequences designed to restore channelized low-gradient streams, in *Protection and Restoration of Urban and Rural Streams*, edited by M. Clar, D. Carpenter, J. Gracie, and L. Slate, pp. 339–348, ASCE, Reston, Virginia, doi:10.1061/40695(2004)34.

Roper, B. B., and D. L. Scarneccia (1995), Observer variability in classifying habitat types in stream surveys, *North American Journal of Fisheries Management*, 15(1), 49–53, doi:10.1577/1548-8675(1995)015<0049:OVICHT>2.3.CO;2.

Rubin, D. M., J. C. Schmidt, and J. N. Moore (1990), Origin, structure, and evolution of a reattachment bar, Colorado River, Grand Canyon, Arizona, *Journal of Sedimentary Research*, 60(6), 982–991, doi:10.1306/D426765E-2B26-11D7-8648000102C1865D.

Sawyer, A. M., G. B. Pasternack, H. J. Moir, and A. A. Fulton (2010), Riffle-pool maintenance and flow convergence routing observed on a large gravel-bed river, *Geomorphology*, 114(3), 143–160, doi:10.1016/j.geomorph.2009.06.021.

Schmidt, J. C. (1990), Recirculating flow and sedimentation in the Colorado River in Grand Canyon, Arizona, *The Journal of Geology*, 98(5), 709–724, doi:10.1086/629435.

Schmidt, J. C., D. M. Rubin, and H. Ikeda (1993), Flume simulation of recirculating flow and sedimentation, *Water Resources Research*, 29(8), 2925–2939, doi:10.1029/93WR00770.

Schuerch, P., A. L. Densmore, B. W. McArdell, and P. Molnar (2006), The influence of landsliding on sediment supply and channel change in a steep mountain catchment, *Geomorphology*, 78(3), 222–235, doi:10.1016/j.geomorph.2006.01.025.

Sear, D. A. (1992), Impact of hydroelectric power releases on sediment transport processes in pool-riffle sequences, in *Dynamics of Gravel-Bed Rivers*, edited by P. Billi, R. D. Hey, C. R. Thorne, and P. Tacconi, pp. 629–650, John Wiley & Sons, Ltd., Chichester.

Sear, D. A. (1996), Sediment transport processes in pool-riffle sequences, *Earth Surface Processes and Landforms*, 21(3), 241–262, doi:10.1002/(SICI)1096-9837(199603)21:3<241::AID-ESP623>3.0.CO;2-1.

Singh, V. P., and C. Ojha (2008), Characteristic velocity of stream bed movement, *Journal of Hydrologic Engineering*, 13(2), 96–100, doi:10.1061/(ASCE)1084-0699(2008)13:2(96).

Sklar, L. S., J. Fadde, J. G. Venditti, P. Nelson, M. A. Wydzga, Y. Cui, and W. E. Dietrich (2009), Translation and dispersion of sediment pulses in flume experiments simulating gravel augmentation below dams, *Water Resources Research*, 45(8), doi:10.1029/2008WR007346.

Song, T., and W. H. Graf (1996), Velocity and turbulence distribution in unsteady open-channel flows, *Journal of Hydraulic Engineering*, 122(3), 141–154, doi:10.1061/(ASCE)0733-9429(1996)122:3(141).

Strom, K., A. N. Papanicolaou, N. Evangelopoulos, and M. Odeh (2004), Microforms in gravel bed rivers: Formation, disintegration, and effects on bedload transport, *Journal of Hydraulic Engineering*, 130(6), 554–567, doi:10.1061/(ASCE)0733-9429(2004)130:6(554).

Strom, K. B., R. D. Kuhns, and H. J. Lucas (2010), Comparison of automated image-based grain sizing to standard pebble-count methods, *Journal of Hydraulic Engineering*, 136(8), 461–473, doi:10.1061/(ASCE)HY.1943-7900.0000198.

Strom, M. A., G. B. Pasternack, and J. R. Wyrick (2016), Reenvisioning velocity reversal as a diversity of hydraulic patch behaviours, *Hydrological Processes*, 30(13), 2348–2365, doi:10.1002/hyp.10797.

Struiksma, N., K. W. Olesen, C. Flokstra, and H. J. De Vriend (1985), Bed deformation in curved alluvial channels, *Journal of Hydraulic Research*, 23(1), 57–79, doi:10.1080/00221688509499377.

Sutherland, D. G., M. H. Ball, S. J. Hilton, and T. E. Lisle (2002), Evolution of a landslide-induced sediment wave in the Navarro River, California, *Geological Society of America Bulletin*, 114(8), 1036–1048, doi:10.1130/0016-7606(2002)114\$(\$1036:EOALIS\$)\$2.0.CO;2.

Tamminga, A. (2016), UAV-based remote sensing of fluvial hydrogeomorphology and aquatic habitat dynamics, Ph.D. thesis, University of British Columbia, doi:10.14288/1.0315349.

Thomas, R. J., J. A. Constantine, P. Gough, and B. Fussell (2015), Rapid channel widening following weir removal due to bed-material wave dispersion on the River Monnow, Wales, *River Research and Applications*, 31(8), 1017–1027, doi:10.1002/rra.2803.

Thompson, D. M. (2001), Random controls on semi-rhythmic spacing of pools and riffles in constriction-dominated rivers, *Earth Surface Processes and Landforms*, 26(11), 1195–1212, doi:10.1002/esp.265.

Thompson, D. M. (2002), Geometric adjustment of pools to changes in slope and discharge: a flume experiment, *Geomorphology*, 46(3-4), 257–265, doi:10.1016/S0169-555X(02)00077-6.

Thompson, D. M. (2006), The role of vortex shedding in the scour of pools, *Advances in Water Resources*, 29(2), 121–129, doi:10.1016/j.advwatres.2005.03.015.

Thompson, D. M. (2007), The characteristics of turbulence in a shear zone downstream of a channel constriction in a coarse-grained forced pool, *Geomorphology*, 83(3-4), 199–214, doi:10.1016/j.geomorph.2006.05.001.

Thompson, D. M. (2011), The velocity-reversal hypothesis revisited, *Progress in Physical Geography*, 35(1), 123–132, doi:10.1177/0309133310369921.

Thompson, D. M. (2013), Pool-riffle, in *Treatise on Geomorphology*, vol. 9, edited by E. Wohl, pp. 364–378, Academic Press, San Diego, CA, doi:10.1016/B978-0-12-374739-6.00246-3.

Thompson, D. M., and K. S. Hoffman (2001), Equilibrium pool dimensions and sediment-sorting patterns in coarse-grained, New England channels, *Geomorphology*, 38(3-4), 301–316, doi:10.1016/S0169-555X(00)00100-8.

Thompson, D. M., and C. R. McCarrick (2010), A flume experiment on the effect of constriction shape on the formation of forced pools, *Hydrology and Earth System Sciences*, 14, 1321–1330, doi:10.5194/hess-14-1321-2010.

Thompson, D. M., E. E. Wohl, and R. D. Jarrett (1996), A revised velocity-reversal and sediment-sorting model for a high-gradient, pool-riffle stream, *Physical Geography*, 17(2), 142–156.

Thompson, D. M., J. M. Nelson, and E. E. Wohl (1998), Interactions between pool geometry and hydraulics, *Water Resources Research*, 34(12), 3673–3681, doi:10.1029/1998WR900004.

Thompson, D. M., E. E. Wohl, and R. D. Jarrett (1999), Velocity reversals and sediment sorting in pools and riffles controlled by channel constrictions, *Geomorphology*, 27(3), 229–241, doi:10.1016/S0169-555X(98)00082-8.

Toro-Escobar, C. M., C. Paola, and G. Parker (1996), Transfer function for the deposition of poorly sorted gravel in response to streambed aggradation, *Journal of Hydraulic Research*, 34(1), 35–53, doi:10.1080/00221689609498763.

Trimble, S. W. (1997), Contribution of stream channel erosion to sediment yield from an urbanizing watershed, *Science*, 278(5342), 1442–1444, doi:10.1126/science.278.5342.1442.

Tsujimoto, T. (1987), Non-uniform bed load transport and equilibrium bed profile, in *XXII IAHR Congress, Fluvial Hydraulics (1)*, pp. 177–182.

Tubino, M. (1991), Growth of alternate bars in unsteady flow, *Water Resources Research*, 27(1), 37–52, doi:10.1029/90WR01699.

Tullos, D. D., M. J. Collins, J. R. Bellmore, J. A. Bountry, P. J. Connolly, P. B. Shafroth, and A. C. Wilcox (2016), Synthesis of common management concerns associated with dam removal, *Journal of the American Water Resources Association*, 52(5), 1179–1206, doi:10.1111/1752-1688.12450.

van Rijn, L. C. (1984), Sediment transport, part III: bed forms and alluvial roughness, *Journal of Hydraulic Engineering*, 110(12), 1733–1754, doi:10.1061/(ASCE)0733-9429(1984)110:12(1733).

Venditti, J. G., W. E. Dietrich, P. A. Nelson, M. A. Wydzga, J. Fadde, and L. Sklar (2010a), Effect of sediment pulse grain size on sediment transport rates and bed mobility in gravel bed rivers, *Journal of Geophysical Research: Earth Surface*, 115(F3), doi:10.1029/2009JF001418.

Venditti, J. G., W. E. Dietrich, P. A. Nelson, M. A. Wydzga, J. Fadde, and L. Sklar (2010b), Mobilization of coarse surface layers in gravel-bedded rivers by finer gravel bed load, *Water Resources Research*, 46(7), doi:10.1029/2009WR008329.

Venditti, J. G., P. A. Nelson, J. T. Minear, J. Wooster, and W. E. Dietrich (2012), Alternate bar response to sediment supply termination, *Journal of Geophysical Research: Earth Surface*, 117(F2), doi:10.1029/2011JF002254.

Venditti, J. G., C.-Y. M. Lin, and M. Kazemi (2016), Variability in bedform morphology and kinematics with transport stage, *Sedimentology*, 63(4), 1017–1040, doi:10.1111/sed.12247.

Venditti, J. G., P. A. Nelson, R. W. Bradley, D. Haught, and A. B. Gitto (2017), Bedforms, structures, patches, and sediment supply in gravel-bed rivers, in *Gravel-Bed Rivers: Processes and Disasters*, edited by D. Tsutsumi and J. B. Laronne, pp. 439–466, Wiley Online Library, doi:10.1002/9781118971437.ch16.

Vetter, T. (2011), Riffle-pool morphometry and stage-dependant morphodynamics of a large floodplain river (Vereinigte Mulde, Sachsen-Anhalt, Germany), *Earth Surface Processes and Landforms*, 36(12), 1647–1657, doi:10.1002/esp.2181.

Viparelli, E., R. Haydel, M. Salvaro, P. R. Wilcock, and G. Parker (2010a), River morphodynamics with creation/consumption of grain size stratigraphy 1: laboratory experiments, *Journal of Hydraulic Research*, 48(6), 715–726, doi:10.1080/00221686.2010.515383.

Viparelli, E., O. E. Sequeiros, A. Cantelli, P. R. Wilcock, and G. Parker (2010b), River morphodynamics with creation/consumption of grain size stratigraphy 2: numerical model, *Journal of Hydraulic Research*, 48(6), 727–741, doi:10.1080/00221686.2010.526759.

Viparelli, E., D. Gaeuman, P. Wilcock, and G. Parker (2011), A model to predict the evolution of a gravel bed river under an imposed cyclic hydrograph and its application to the Trinity River, *Water Resources Research*, 47(2), doi:10.1029/2010WR009164.

Wallis, C., I. Maddock, F. Visser, and M. Acreman (2012), A framework for evaluating the spatial configuration and temporal dynamics of hydraulic patches, *River Research and Applications*, 28(5), 585–593, doi:10.1002/rra.1468.

Wang, L., A. J. Cuthbertson, G. Pender, and Z. Cao (2015), Experimental investigations of graded sediment transport under unsteady flow hydrographs, *International Journal of Sediment Research*, 30(4), 306–320, doi:10.1016/j.ijsrc.2015.03.010.

Warrick, J. A., J. A. Bountry, A. E. East, C. S. Magirl, T. J. Randle, G. Gelfenbaum, A. C. Ritchie, G. R. Pess, V. Leung, and J. J. Duda (2015), Large-scale dam removal

on the Elwha River, Washington, USA: source-to-sink sediment budget and synthesis, *Geomorphology*, 246, 729–750, doi:10.1016/j.geomorph.2015.01.010.

Waters, K. A., and J. C. Curran (2015), Linking bed morphology changes of two sediment mixtures to sediment transport predictions in unsteady flows, *Water Resources Research*, 51(4), 2724–2741, doi:10.1002/2014WR016083.

Westerling, A. L., H. G. Hidalgo, D. R. Cayan, and T. W. Swetnam (2006), Warming and earlier spring increase western US forest wildfire activity, *Science*, 313(5789), 940–943, doi:10.1126/science.1128834.

Wheaton, J. M., J. Brasington, S. E. Darby, and D. A. Sear (2010a), Accounting for uncertainty in DEMs from repeat topographic surveys: improved sediment budgets, *Earth Surface Processes and Landforms*, 35(2), 136–156, doi:10.1002/esp.1886.

Wheaton, J. M., J. Brasington, S. E. Darby, J. Merz, G. B. Pasternack, D. Sear, and D. Vericat (2010b), Linking geomorphic changes to salmonid habitat at a scale relevant to fish, *River Research and Applications*, 26(4), 469–486, doi:10.1002/rra.1305.

White, J. Q., G. B. Pasternack, and H. J. Moir (2010), Valley width variation influences riffle–pool location and persistence on a rapidly incising gravel-bed river, *Geomorphology*, 121(3), 206–221, doi:10.1016/j.geomorph.2010.04.012.

Whitman, M. S., E. H. Moran, and R. T. Ourso (2003), Photographic techniques for characterizing streambed particle sizes, *Transactions of the American Fisheries Society*, 132(3), 605–610, doi:10.1577/1548-8659(2003)132<605:PTFCSP>2.0.CO;2.

Wijbenga, J. H. A., and G. J. Klaassen (1983), Changes in bedform dimensions under unsteady flow conditions in a straight flume, in *Modern and Ancient Fluvial Systems*, edited by J. D. Collinson and J. Lewin, Special Publication Number 6 of the International Association of Sedimentologists, pp. 35–48, John Wiley & Sons, doi:10.1002/9781444303773.ch3.

Wilcock, P. R., and J. C. Crowe (2003), Surface-based transport model for mixed-size sediment, *Journal of Hydraulic Engineering*, 129(2), 120–128, doi:10.1061/(ASCE)0733-9429(2003)129:2(120).

Wilkinson, S. N., R. J. Keller, and I. D. Rutherford (2004), Phase-shifts in shear stress as an explanation for the maintenance of pool–riffle sequences, *Earth Surface Processes and Landforms*, 29(6), 737–753, doi:10.1002/esp.106.

Wohl, E., and C. J. Legleiter (2003), Controls on pool characteristics along a resistant-boundary channel, *The Journal of Geology*, 111(1), 103–114, doi:10.1086/344667.

Wohl, E. E., and D. A. Cenderelli (2000), Sediment deposition and transport patterns following a reservoir sediment release, *Water Resources Research*, 36(1), 319–333, doi:10.1029/1999WR900272.

Wohl, E. E., D. M. Thompson, and A. J. Miller (1999), Canyons with undulating walls, *Geological Society of America Bulletin*, 111(7), 949–959, doi:10.1130/0016-7606(1999)111<0949:CWUW>2.3.CO;2.

Wolman, M. G. (1954), A method of sampling coarse river-bed material, *EOS, Transactions American Geophysical Union*, 35(6), 951–956, doi:10.1029/TR035i006p00951.

Wolman, M. G., and J. P. Miller (1960), Magnitude and frequency of forces in geomorphic processes, *The Journal of Geology*, 68(1), 54–74, doi:10.1086/626637.

Wolman, M. G., and A. P. Schick (1967), Effects of construction on fluvial sediment, urban and suburban areas of Maryland, *Water Resources Research*, 3(2), 451–464, doi:10.1029/WR003i002p00451.

Wong, M., and G. Parker (2006), One-dimensional modeling of bed evolution in a gravel bed river subject to a cycled flood hydrograph, *Journal of Geophysical Research: Earth Surface*, 111(F3), doi:10.1029/2006JF000478.

Wood, P. J., and P. D. Armitage (1997), Biological effects of fine sediment in the lotic environment, *Environmental Management*, 21(2), 203–217, doi:10.1007/s002679900019.

Woolpert, Inc. (2013), Airborne LiDAR Report: Elwha River, WA LiDAR, Englewood, Colo.

Wu, F.-C., and T.-H. Yeh (2005), Forced bars induced by variations of channel width: Implications for incipient bifurcation, *Journal of Geophysical Research: Earth Surface* (2003–2012), 110(F2), doi:10.1029/2004JF000160.

Wu, F.-C., Y.-C. Shao, and Y.-C. Chen (2011), Quantifying the forcing effect of channel width variations on free bars: Morphodynamic modeling based on characteristic dissipative Galerkin scheme, *Journal of Geophysical Research: Earth Surface* (2003–2012), 116(F3), doi:10.1029/2010JF001941.

Wyrick, J. R., and G. B. Pasternack (2014), Geospatial organization of fluvial landforms in a gravel–cobble river: beyond the riffle–pool couplet, *Geomorphology*, 213, 48–65, doi: 10.1016/j.geomorph.2013.12.040.

Xie, X. L., and G. Beni (1991), A validity measure for fuzzy clustering, *IEEE Transactions on Pattern Analysis and Machine Intelligence*, 13(8), 841–847, doi:10.1109/34.85677.

Yarnell, S. M., J. F. Mount, and E. W. Larsen (2006), The influence of relative sediment supply on riverine habitat heterogeneity, *Geomorphology*, 80(3), 310–324, doi:10.1016/j.geomorph.2006.03.005.

Zahid, N., M. Limouri, and A. Essaid (1999), A new cluster-validity for fuzzy clustering, *Pattern Recognition*, 32(7), 1089–1097, doi:10.1016/S0031-3203(98)00157-5.

Zeug, S. C., K. Sellheim, C. Watry, B. Rook, J. Hannon, J. Zimmerman, D. Cox, and J. Merz (2014), Gravel augmentation increases spawning utilization by anadromous salmonids: a case study from California, USA, *River Research and Applications*, 30(6), 707–718, doi: 10.1002/rra.2680.

Zinger, J. A., B. L. Rhoads, and J. L. Best (2011), Extreme sediment pulses generated by bend cutoffs along a large meandering river, *Nature Geoscience*, 4(10), 675–678, doi: 10.1038/ngeo1260.

Zolezzi, G., R. Luchi, and M. Tubino (2012), Modeling morphodynamic processes in meandering rivers with spatial width variations, *Reviews of Geophysics*, 50(4), doi: 10.1029/2012RG000392.

Zunka, J. P., D. D. Tullos, and S. T. Lancaster (2015), Effects of sediment pulses on bed relief in bar-pool channels, *Earth Surface Processes and Landforms*, 40(8), 1017–1028, doi:10.1002/esp.3697.

Appendix A

Riffle-pool delineation details

A.1 Fuzzy c -means clustering

The fuzzy c -means (FCM) concept was introduced by *Dunn* (1973) and generalized by *Bezdek* (1981). The FCM clustering method is based upon the minimization of the objective function, J_m ,

$$J_m = \sum_{i=1}^D \sum_{j=1}^N \mu_{ij}^m \|x_i - c_j\|^2 \quad (\text{A.1})$$

where i is the index of data points, D is the total number of data points, j is the index of cluster centers, N is total number of clusters, x_i is the i th data point, c_j is the center of the j th cluster, μ_{ij} is the degree of membership of x_i in the j th cluster, and m is a matrix exponent controlling the degree of fuzzy overlap ($1 \leq m < \infty$, generally $m < 3$). The input data, $X = \{x_1, x_2, \dots, x_D\}$, is a matrix of finite dimensions with the number of rows corresponding to the number of data points, D , and the number of columns corresponding to the number parameters associated with each data point, P (in our case $P = 2$, flow depth and shear stress). The FCM procedure begins by randomly initializing membership values for all data points in all clusters. The cluster centers are calculated as

$$c_j = \frac{\sum_{i=1}^D \mu_{ij}^m x_i}{\sum_{i=1}^D \mu_{ij}^m} \quad (\text{A.2})$$

From the cluster center locations, the fuzzy membership values can be updated.

$$\mu_{ij} = \frac{1}{\sum_{k=1}^N \left(\frac{\|x_i - c_k\|}{\|x_i - c_j\|} \right)^{\frac{2}{m-1}}} \quad (\text{A.3})$$

The objective function, J_m , is then recalculated and the calculations for the cluster center locations and fuzzy membership values are iterated until J_m is changed by less than a specified

value or after a specified number of iterations. See *Bezdek* (1981) for more details on this and other fuzzy recognition methods.

A.2 Cluster validity

A plethora of fuzzy cluster validity techniques have been developed and proposed over the last few decades (*Halkidi et al.*, 2001). Some of the early validation parameters, such as the partition coefficient and the partition entropy suggested by *Bezdek* (1981), prove to be unhelpful as they have a monotonic relationship with the number of clusters and the fuzzy weighting exponent. For our purposes, validation of FCM clusters was performed using two parameters: SC (*Zahid et al.*, 1999) and XB (*Xie and Beni*, 1991). Both SC and XB are “compactness-separation” functions that incorporate the fuzzy membership matrix, $U = [\mu_{ij}]$ ($1 \leq i \leq D, 1 \leq j \leq N$), and cluster centers, $C = [c_{jn}]$ ($1 \leq j \leq N, 1 \leq n \leq P$), as well as the structure of the input data, X . SC is defined as

$$SC = SC_1 - SC_2 \quad (\text{A.4})$$

where

$$SC_1 = \frac{\sum_{j=1}^N \|c_j - \bar{X}\| / N}{\sum_{j=1}^N \left(\sum_{i=1}^D \mu_{ij}^m \|x_i - C_j\|^2 / \sum_{i=1}^D \mu_{ij} \right)} \quad (\text{A.5})$$

and

$$SC_2 = \frac{\sum_{j=1}^{N-1} \sum_{r=1}^{N-j} \left(\sum_{i=1}^D (\min(\mu_{ij}, \mu_{ik})^2) / n_{ij} \right)}{\sum_{i=1}^D (\max_j \mu_{ij})^2 / \sum_{i=1}^D \max_j \mu_{ij}} \quad (\text{A.6})$$

where $k = r + 1$ and $n_{ij} = \sum_{i=1}^D \min(\mu_{ij}, \mu_{ik})$. XB is defined as

$$XB = \frac{\sum_{i=1}^D \sum_{j=1}^N \mu_{ij}^m \|x_i - C_j\|^2}{n \min_{i,j} \|C_i - C_j\|^2} \quad (\text{A.7})$$

The optimum fuzzy c -partition corresponds to a maximum of SC and a minimum for XB .

Cluster validity was tested by varying both the number of clusters ($2 \leq c \leq 10$) and the weighting exponent ($1.2 \leq m \leq 2.9$). Both validity indices mentioned above were calculated for each combination of c and m . Unfortunately, neither validation index used provided a global optimum for both c and m . However, by considering both indices we were able to arrive at values corresponding to local optimums. Figure A.1 shows the validation indices, SC and XB , plotted against the number of clusters, c , and the weighting exponent, m , respectively. Based on the results from the compactness-separation index, SC (Figure A.1a), we determined a value for the number of clusters of $c = 5$. Based on the results from the validation index of *Xie and Beni* (1991), XB (Figure A.1b), we decided to use a weighting exponent value of $m = 1.9$.

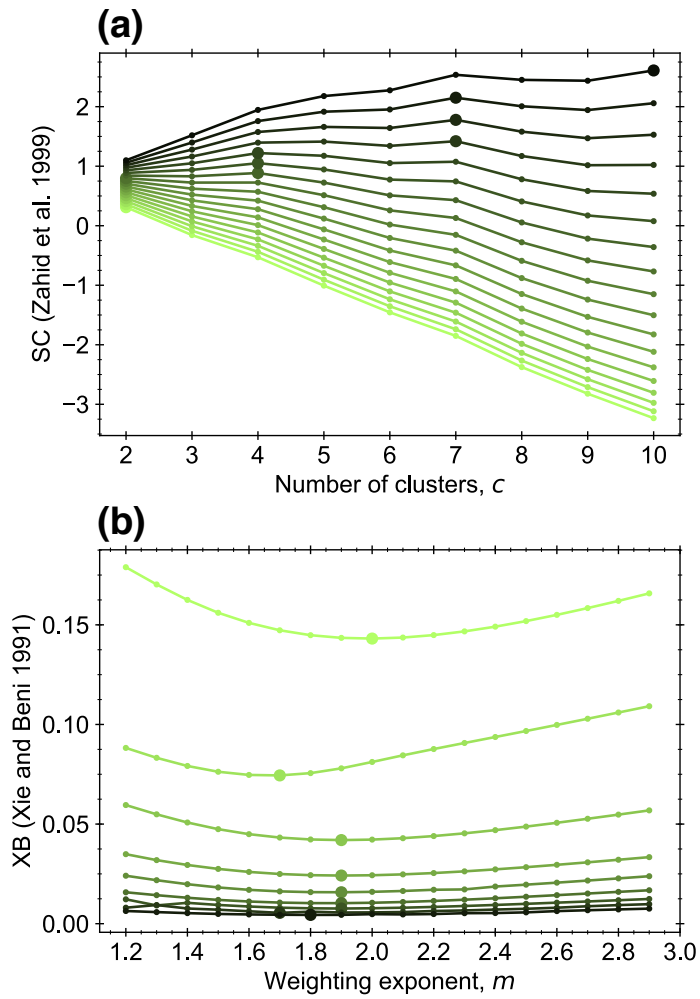


Figure A.1: FCM clustering validation, where larger markers correspond to optimum values for the curve. (a) Separate-compactness index of Zahid *et al.* (1999), where darker colors correspond to higher m weighting exponents; (b) Cluster validity index of Xie and Beni (1991), where darker colors correspond to a higher number of clusters.